Life of a Photon in X-ray Spectroscopy

Uhlig, Jens

2011

Document Version:
Other version

Life of a Photon in X-ray Spectroscopy

Jens Uhlig

Doctoral Thesis
2011

Lund University

Life of a Photon in X-ray Spectroscopy

Printed in Sweden by Media-Tryck, Lund, 2011

Division of Chemical Physics
Department of Chemistry
Lund University
P.O. Box 124
SE–221 00 Lund
Sweden

http://www.chemphys.lu.se

ISBN 978-91-7422-284-5

"The beginning is the most important part of the work."
Plato
The Republic

Abstract

This thesis summarizes the experimental work in which an ultrafast X-ray laser plasma source was combined with various scalable direct detection schemes to test a novel approach for lab-based time-resolved X-ray absorption spectroscopy. A laser plasma source based on a water jet target was built and commissioned. X-ray and electron emissions of this source were characterized with various direct detection schemes. The procedures for spectral retrieval with direct detection CCD's were optimized with regard to the laser plasma source. The novel approach of using a single photon measuring cryogenic microcalorimeter array as a high-resolution ($\Delta E/E \approx 2000$ @ 6 keV) energy-dispersive detector was investigated. The potentially very high quantum efficiency, large detection angle and straightforward scalability make this device an interesting photon analyzer for low photon yield experiments. In this thesis a prototype version of this detector was built (in cooperation), implemented and commissioned into the laser plasma setup. With this combination of a lab-based broad-band source and the free standing microcalorimeter spectrometer high resolution X-ray absorption spectra in transmission mode were achieved. The thesis presents the first hard X-ray absorption fine structure (XAFS) spectrum taken with this novel approach and discusses further improvements and applications.

Populärvetenskaplig sammanfattning

Denna avhandling ger en introduktion till laser-plasma-röntgenkällor och olika direkta detektionsmetoder sammankopplade till en laboratoriebaserad uppställning för tidsupplöst röntgenabsorptionsspektroskopi. Molekylär funktion innebär att molekyler uträttar arbete genom strukturförändringar. Tidsupplöst röngtenabsorption kan i realtid följa dessa sturkturförändringar och därmed bidra till förståelse och optimering av processer och material. Tillämpningarna sträcker sig från organiska solceller över artificiell fotosyntes till ljusaktiverade kemiska reaktioner.

I många storskaliga faciliteter (tex synkrotronanläggningar) över hela världen används röntgenabsorptionspektroskopi som ett verktyg för att undersöka molekylära strukturer. Antalet anläggningar som erbjuder ultrasnabb tidsupplöst spektroskopi för studier av kemisk dynamik är mycket begränsat. Detta skapar ett stort behov av laboratoriebaserad utrustning som medger sådana experiment.

Intensiva laserpulser fokuserade på ytan av ett material genererar kortvariga pulser av högenergetisk, s.k. hård, röntgenstrålning med ett brett spektrum. Braggreflektion, den klassiska metoden för att analysera ett röntgenspektrum, ger med dess smala energiacceptans mycket låg transmission av röntgenfotonerna och är därmed en mycket ineffektivt analysmetod. Detta blir särskilt problematiskt för den lågintensiva isotropa röntgenstrålningen genererad med vår laserplasma källa. För att förbättra effektiviteten undersöktes och optimerades olika direkta detektionsmetoder med fokus på absorptionsspektroskopi.

I avhandlingen introduceras en ny typ av supraledande detektor som registrerar enskilda röntgenfotoner genom att mäta den värme de utvecklar. Med denna detektor uppmättes de första röntgenspektra med hög upplösning. Framtida utveckling och förbättring av denna nya detektor presenteras och visar lovande framtidsutsikter.

List of Publications

This thesis is based on the following papers, which will be referred to by their Roman numerals in the text.

I **A broadband laser plasma x-ray source for application in ultrafast chemical structure dynamics.**
W. Fullagar, M. Harbst, S. Canton, J. Uhlig, M. Walczak, C.-G. Wahlström, V. Sundström.
Review of Scientific Instruments **78(11)**, 115105 (2007).

II **The use and characterization of a backilluminated charge-coupled device in investigations of pulsed x-ray and radiation sources.**
W. Fullagar, J. Uhlig, M. Walczak, S. Canton, I. Maasilta, V. Sundström.
Review of Scientific Instruments **79(10)**, 103302 (2008).

III **Lab-based Ultrafast Molecular Structure**
W. Fullagar, J. Uhlig, N. Gador, K. Kinnunnen, I. Maasilta, C.-G. Wahlström, V. Sundström.
AIP Conference Proceedings **1234(1)**, 919-922 (2010).

IV **Laser generated 300 keV electron beams from water**
J. Uhlig, C.-G. Wahlström, M. Walczak, V. Sundström, W. Fullagar.
Laser and particle beams **29-4**, 415-424(2011).

V **Table-top ultrafast x-ray microcalorimeter spectrometry for molecular structure**
J. Uhlig, W. Fullagar, J. Ullom, W.B. Doriese, N. Gador, S. Canton, K. Kinnunen, J. Fowler, C. Reintsema, D. Swetz, D. Bennett, G. Hilton, K. Irwin, D. Schmidt, V. Sundström.
Physical Review Letter **110(13)**, 138302(2013).

Contents

Papers

Chapter 1

Introduction

The life of a photon spans its "birth", or generation, over its "working life" during sample interaction, to its "death", resulting in observable consequences in a detector. This thesis introduces a highly efficient new way to analyze photons in ultrafast table top X-ray schemes, with a prototypical application in X-ray absorption spectroscopy. It discusses some of the consequences for the source, the interaction and the detection.

The optical, electrical and mechanical properties of any material are determined by its internal structure. Activating materials with light and understanding its effects is one of the big scientific challenges of these days. Breaking and formation of chemical bonds upon light activation is a very dynamic process involving the motion of electrons and nuclei. Brief pulses of light can freeze and temporally resolve these events and allow us a snapshot of an evolving structure[1]. Investigating the evolution of molecular structures in real-time will aid the understanding of the properties and function of these materials, both in ordinary fundamental chemical processes, and when under coherent optical control. Figure 1.1 shows a schematic with a brief overview

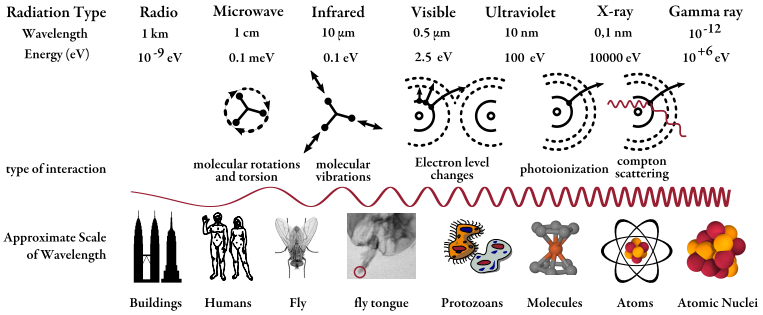

Figure 1.1. *First row shows a schematic with length scales and corresponding photon energies. The next row gives the symbolic interactions that are typically excited by photons of this wavelength. That last row depicts objects with the typical size of this length.*[2]

of the typical interactions excited by different wavelengths and some objects that show these length scales. Interatomic distances in condensed matter and molecules are of the order of Ångströms (1 Å= 10^{-10} m). To probe structural changes in molecules wavelength of similar dimensions are needed [3,4]. X-rays can be used to explore such molecular structures. In pump probe techniques a brief first pulse starts a reaction. Then after a period of evolution a second brief pulse takes a snapshot of the current state. This process is typically repeated in a stroboscopic experiment to acquire data of adequate quality. Laboratory based ultra-fast pump-probe capability is a particular incentive in this work. A variety of time resolved X-ray based techniques have been and are being developed to probe structural changes in matter [5–10]. This thesis focuses on X-ray absorption fine structure spectroscopy.

In chapter 2 sources for ultra-fast X-rays are presented. Large facilities were also visited and used in course of this work, whose operation is briefly described. The chapter also describes this work's development of a setup with a laser plasma X-ray source based on a water jet target for the generation of ultra-brief pulses of hard X-ray broadband radiation.

The characteristics of the source were chosen to match the direct detection approach in the novel combination of this "hot" source with a "cold" micro calorimetric direct detection array. Such detectors are in a rapidly maturing stage of international development, and our particular array is the focus of chapter 4.

In the closing months of this work the detector and the source were married for the first time. Chapter 3 presents the first promising results of this novel combination, as the "working life" aspect of the X-ray photon, and as the central aspect of this work.

This work started under the framework of the European MAXLAS project whose aim was to stimulate the cooperation between the different institutions of the MAX-lab synchrotron facility and the Lund Laser Centre. At the commencement of the presented thesis, X-rays had already been produced from metal target plasma sources at the Lund High-Power Laser Facility [11–14], the first versions of the water jet source were recently built and work to characterize it were underway (paper **I**). During my time systematic studies of the source emission and its optimization were carried out. A backilluminated CCD was used very extensively which in due course became the subject of a manuscript (paper **II**). The High Power Laser Facility had been carefully designed to have an excellent temporal contrast [15–17] and this fact enabled a number of useful studies of electron beam generation and its relation to prepulses using the water jet source (paper **IV**). The perspective of high repetition rate readout with a simultaneously limited need of X-rays motivated the development of the new system designed to work together with a microcalorimeter based detection system. The microcalorimeter detector array

was built in cooperation with the Quantum Device Group at the National Institute of Standards and Technology in Boulder Colorado. The incentive brought by this thesis led to a new collaboration between this group, a research group in Jyväskylä (Finland) developing similar detectors and several groups within the JILA initiative in Boulder (USA) , resulting in a similar laser plasma microcalorimeter setup that will be built in early 2012.

Throughout this work, substantial time was devoted to the design, building, characterization and commissioning of the new plasma setup. This work also led to the design, building and commissioning of the detector periphery in Lund. It further developed part of the control and analysis techniques and codes for the cryostat and calorimeter. In addition, it measured and analyzed samples using the plasma source as well as potential samples at a few large scale facilities. The blend of optics, particle acceleration, chemistry, plasma physics, detector development and spectroscopy is highly multidisciplinary! This is reflected in this thesis, which had to deal with all those aspects. The unifying feature in this work is the "life" of the photon and the steps that can be taken to put them to use. An effort is made to present the life of the photon from its generation (birth), through the time it interacts with a sample to its detection (demise).

Paper **I** describes the stable X-ray emissions from our water plasma source. Paper **II** describes how a direct detection charge coupled device (CCD) can be used to calibrate, characterize and measure emissions from a laser plasma source. In paper **IV** a presentation of fast electron beams using a double pulse or temporally impaired pulse is given; this impacted the further developments of the X-ray source and also suggests new application based on the fast electrons. Paper **III** develops the idea of a microcalorimeter based setup and outlines some new ideas that will become possible with this unique combination. Manuscript **III** is still in preparation and presents the "first light" XAS spectrum measured using a laser-plasma and a microcalorimeter array.

Chapter 2

X-ray Generation

This chapter presents the generation or birth of ultrafast X-rays. Beginning with a general discussion about ultrafast X-ray generation the specific systems used will be investigated. The last sections are the theory, present status and some prospective developments for the laser plasma setup that was built during this thesis.

2.1 Basic principles of X-ray generation

X-rays were discovered by Wilhelm Conrad Röngten in 1895[18]. He observed a penetrating radiation from the anode of a discharge tube, using a fluorescent screen and later photographic film. Most modern sources of hard radiation work on a similar principle. Charged particles are made to interact with strong electrical and/or magnetic fields to achieve a strong acceleration. Electrons have a favorable charge/mass ratio and most technical sources of hard X-ray radiation are based on them.

The emission of X-rays can be understood as a transition of a charged particle from a higher energetic state to a lower state. In a simple picture a free electron being decelerated from a high kinetic energy to a lower kinetic energy performs such a transition and emits a photon. If both states correspond to bound states the emitted spectrum will have a discrete and narrow distribution. The transition energies are characteristic for the emitting atoms. X-ray emission spectroscopy uses these spectra to obtain information about the energetic levels of bound states. Vacancies in deeply bound states of atoms are generated by ionizing radiation (e.g. X-rays or electrons see chapter 3), multiphoton absorption (see section 2.5.1) or capture of an electron in the nucleus during a radioactive decay process (see section 4.5.12). If an unbound electron in a material is captured into a bound state the emitted excess energy is the characteristic

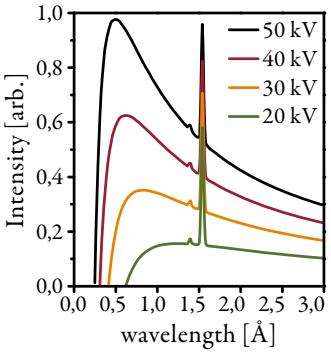

Figure 2.1. *Simulated copper bremsstrahlung spectrum with artificially broadened characteristic lines.*

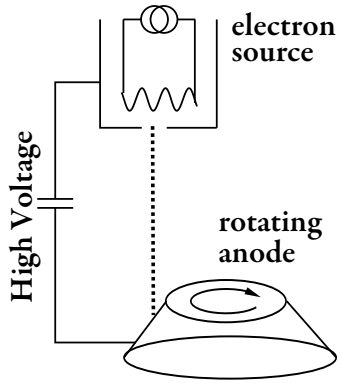

Figure 2.2. *Principle of rotation anode X-ray tube. Constantly replacing the target material increased the power densities on the target before the structures started to melt. Even smaller target sizes can be achieved by using liquid targets like laser plasma sources* [11–13].

line energy broadened by the thermal electron distribution and phononic/electronic excitations.

A fast electron striking a thick material undergoes a cascade of stochastic processes and transfers most of its energy into material excitations and finally the lattice (see section 4.3). During each step a part or all of the energy can be emitted as photon forming the so called "bremsstrahlung" (braking radiation) spectrum. The initially fast electrons can excite core electrons which give rise to characteristic line emission. The observable spectrum is the sum of both bremsstrahlung and line spectra (figure 2.1). The efficiencies depend on material, electron energy, temperature and have been studied since the early days of X-ray spectroscopy [19–25].

Most of the electron energy is converted into heat in this cascade. Medical or scientific applications which desire high fluxes on small foci need to dissipate higher power densities then any solid material can withstand. Examples of schemes to relieve the target material are to rotate the anode (figure 2.2) and give it time to cool, to use liquid metal target jets hit by electron guns [26;27] or to use a variety of other movable target systems and a laser plasma source.

X-ray tubes are the most widespread sources for hard X-ray generation. We will revisit them while discussing table top sources of pulsed X-rays in section 2.5.4. In contrast to these stochastic processes the electron trajectory and angular acceleration is highly controlled in modern large scale research facilities (section 2.2).

2.2 Ultra short X-ray pulses produced in large scale facilities

Gaining control over the path of the charged particles and its acceleration enabled a huge jump in the quality and amount of emitted radiation. Electrons are accelerated to relativistic energies and guided once or repetitively through a bent trajectory. The acceleration during the bend stimulates the emission of radiation. The very first of these devices synchronously accelerated an electron beam in a circular motion in a permanent magnetic field, with the constant emission of radiation. The next generation of ring shaped storage facilities introduced local magnetic fields breaking up the circular motion into several smaller bends linked by straight sections (figure 2.3 a). In the straight sections the electron bunch can be accelerated to compensate for the radiation loss, reshaped in chicanes for recompression, or guided through the insertion devices. During the bends controlled emission occurs [28;29].

Electron bunches can be generated by many methods including emission from hot cathodes (the classical glowing wire), field

emission from a cold cathode or via photoemission from a photocathode excited by an optical pulse. The latter method is often preferred by modern facilities built to generate very short and temporally controlled pulses for femtosecond X-ray sources[30]. After extraction the electrons are rapidly accelerated to relativistic energies. Once at relativistic speed the electron bunch has (in its own frame of reference) not much time to feel the Coulomb repulsion and so remains compressed as seen in the laboratory frame. The acceleration is often done in radio frequency resonant structures as shown in figure 2.4. A radio wave is coupled into the cavities in the device so that energy is synchronously transferred as it moves along. A detailed description of the methods used to accelerate, shape and re-compress the bunches can be found in reference[31].

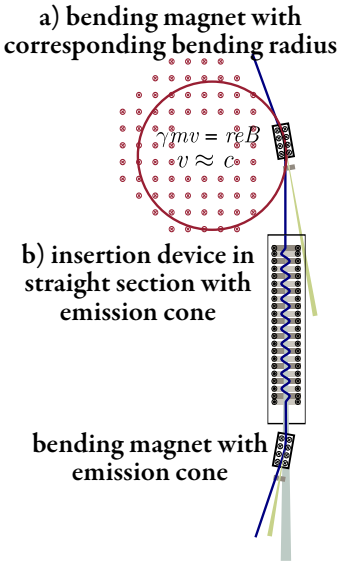

Figure 2.3. *The original round synchrotron is broken up in bent and straight sections.*

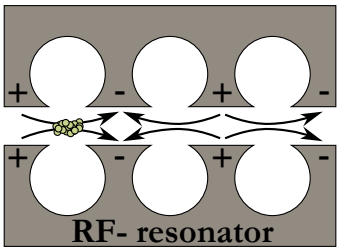

Figure 2.4. *Schematic of radio frequency (RF) resonator for electron acceleration (Klystron). The surface charge inside the structure changes synchronously with the electron movement.*

2.2.1 Bending magnets and wigglers

The breakup of the circular electron motion into many small angular bends allows the use of stronger and smaller superconducting magnets and higher electron energy. Both lead to more intense and harder radiation. The schematic of the electron trajectory in figure 2.3 shows a section of a synchrotron ring. To each of the small bends an effective radius r can be assigned (figure 2.3 a):

$$r = \frac{\gamma m_0 v}{eB} \quad \text{with} \quad v \approx c\,, \tag{2.1}$$

where m_0 is the classical mass of the electron, v its speed, e the elementary charge and B the magnetic field that asserts the Lorentz-force. For a correct description the relativistic energies require the correction factor γ.

$$\gamma = \frac{E_{electron}}{m_0 c^2} = \frac{1}{\sqrt{1-(v/c)^2}} \tag{2.2}$$

In the observation plane of the synchrotron the electron moves in a straight line emitting linearly polarized light. Perpendicular to the plane the radiation has a circularly polarized component. The relativistic movement of the electron has the following effect. A electron on a linear path emits an energy flux density S shown in figure 2.5 a. For particles at relativistic velocities the Doppler shift introduced for observations in the laboratory frame of reference compresses the emitted radiation into a small cone with a total opening angle $\Phi \sim 1/\gamma$.

A typical bending magnet spectrum was generated for different field strength and electron energies in figure 2.6. The energy of maximum emission is often called the characteristic energy and is approximated by[4]:

$$E_{characteristic}\,[keV] = 0,665 \cdot E^2_{electron}\,[GeV] \cdot B\,[T] \tag{2.3}$$

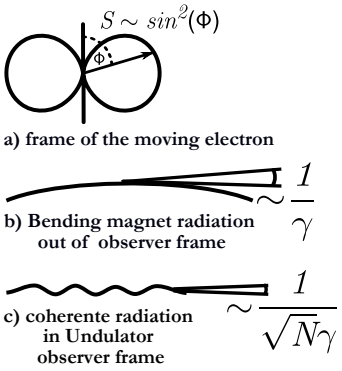

Figure 2.5. *The relativistic Doppler effect*[32] *compresses the wavefront in the frame of the observer along the direction of the moving electron. The resulting emission cone shows a strong compression in the forward direction. The coherent X-ray generation in an undulator compresses the cone even further.*

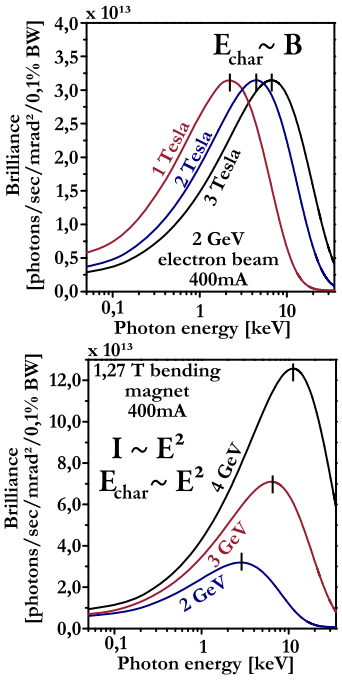

Figure 2.6. *Emission from a bending magnet as function of energy and current*

Numerical example: *Typical numbers are ≈ 100 magnets and 10^{11} electrons for a 1.2 km long ring with 100 mA and 24 equal bunches.*

Bending magnets produce a broad spectrum with temporal duration only slightly longer than the electron bunch.

Since most experiments at synchrotrons use monochromatic radiation a convenient unit to compare the emission of different devices is the brilliance which is often stated in units of photons/second mrad mm^{-2} 0.1% bandwidth.

Many small bending magnets brought close together force the electrons to execute a wiggling motion in the straight sections of the ring (figure 2.3 b). Modern wigglers use strong, often superconducting magnets and produce a broad spectrum. In figure 2.7 the path of the electron bunch through the wiggler follows several small bends. Considering only the emission of a single electron, at the same point of observation and energy we can write the phase information of the emitted electric field and the intensity in a qualitative way as follows:

$$E_{single\ electron} = \sum_{i=1}^{N_{magnets}} cos(\omega t + \phi_i)$$

$$I_{single\ electron} = E^2 = \sum_{i=1}^{N_{magnets}} cos(\omega t + \phi_i)^2 + \sum_{i \neq j}^{N_{magnets}} cos(\omega t + \phi_i) cos(\omega t + \phi_j) \qquad (2.4)$$

There is no controlled relation between the position of the electron in the bends and the wavelength of the emitted hard radiation within the coherence length. The phase ϕ_i between the magnets and the radiation will therefore vary over 2π and the cross products vanish. Different electrons in the bunch have no fixed phase relation either and are therefore adding linearly to the summed intensity. Wigglers are built to produce a smooth and broadband radiation that scales like

$$I_{wiggler} \sim N_{magnets} * N_{electrons} \qquad (2.5)$$

and offer a wide stable spectrum which extends often well beyond 20 keV. They are often the preferred choice in these energy regions.

2.2.2 Undulator, the "coherent" wiggler

In an undulator the electron pathlength is matched to multiples of the emitted wavelength. To fullfill this condition the (n-th multiple) wavelength λ_n of the emitted radiation must be on the order of the Doppler corrected undulator wavelength $\lambda_u/2\gamma^2 n$. The electron follows a curved trajectory which is often described by its maximum angular deviation

$$K = eB_0\lambda_u/2\pi m_e c, \qquad (2.6)$$

with the electron charge e, the magnetic field B_0 and the electron mass m_e. In an undulator the relative oscillatory amplitude A is smaller, and the bending radius larger, than in a wiggler. This leads to softer and less intens emitted radiation from each bend.

The often stated undulator coherence condition for the first order on the undulator axis is then:

$$\lambda = \frac{\lambda_u}{2\gamma^2}(1 + K^2/2) \tag{2.7}$$

The undulator wavelength λ_u is mechanically fixed but B_0 and consequently also K can be adjusted by varying the gap between the two magnet poles[34]. For photons at the fundamental wavelength (or multiples of it) the phase factor in equation 2.4 is resonant.

$$I^h_{single\,electron} = \sum_{i,j}^{N_{magnets}} cos(h\omega t + n_i h\pi) cos(h\omega t + n_j h\pi) \tag{2.8}$$

For all uneven harmonics (n=1,3,5) the photons interfere constructively and lead to a $sin(Nx)/sin(x)$ interference envelope where N is the number of magnets. The even harmonics vanish (figure 2.7c). The intensity in this case scales as:

$$I_{undulator} \sim N^2_{magnets} * N_{electrons} \tag{2.9}$$

This spectrally narrow flux can be guided though a monochromator to further limit the bandwidth. The opening angle is compressed to $1/\sqrt{N_{magnets}}$ compared to the natural linewidth $1/\gamma$ (figure 2.5 c). Variations like "tempering" (tuning to different wavelength at the begin and at the end of an undulator), circular polarized undulators and asymmetric magnetic structures are discussed in textbooks[4;35].

Note that the resonance wavelength has a squared dependence on the electron energy γ^{-2} (formula 2.7). A small change in the electron energy observed at the end of linear accelerators can result in a substantial shift of the center wavelength in the undulator. After the narrow bandpass of a monochromator the fluctuations are in the range of several percent and in many cases pose demand on the detector to resolve single pulses for normalization (see also chapter 4).

2.2.3 Short pulses at large scale facilities

In a classical storage ring the electron bunch is ≈ 3 cm long, corresponding to a duration of ≈ 100 ps. Several techniques have been developed to shorten the pulse duration of the generated X-rays to sub ps pulses.

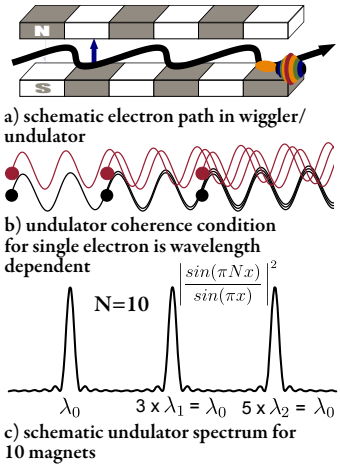

Figure 2.7. *a: Oscillating movement of an electron through a periodic magnetic field. b: The coherence condition between electron movement and emitted radiation of periodic wavelength. c: schematic undulator spectrum for N magnets. Several codes like SPECTRA[33] are used to simulate the emission*

Comment: *The amplitude A of the oscillation and the smallest bending radius can be estimated by:*

$$A = \frac{K\lambda_u}{2\pi\gamma}$$

$$r = \frac{\gamma\lambda_u}{K2\pi}$$

Numerical example: *Assuming a 6 GeV electron beam the order of magnitudes are:*

γ	$\approx$	10^4
K	$\approx$	*1 for undulator,*
K	$\geq$	*10 for wiggler,*
	For K=1	
λ_u	$\gtrsim$	1.5 cm
λ	$\approx$	0.8 Å
A	$\approx$	0.2 µm
r	$\approx$	28 m

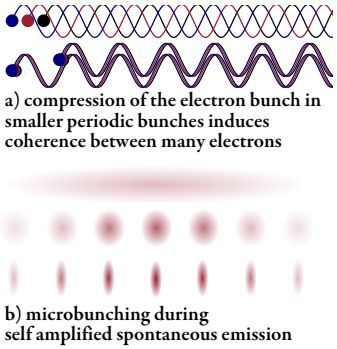

Figure 2.8. *a: Applying a coherence condition to the electron distribution within the bunch leads to constructive superposition of the emitted radiation. b: The induced electric field leads to a micro bunching and local compression of the electron bunch.*

Energy can be transferred from or into a strong optical laser field by parts of the electron bunch during the oscillatory movement in an insertion device. The small section (typically 100 µm) of the several cm long electron bunch has for a short time a slightly higher/lower energy and can be spatially separated in a dispersive section. The time and spatial structure of the electron bunch is then mimicked in a radiator into a X-ray pulse containing an ultrashort part in the wings[36]. The flux achievable with these tunable sources is proportional to the fraction of "sliced" electrons.

Another approach for synchrotron based short pulses is a clever way to rotate the electron bunch by Zholents[37]. In a time dependent field the horizontally stretched electron bunch is rotated, guided through an insertion device, and then rotated back. In the insertion device the temporal spread of the electron bunch is encoded in the divergence of the emitted X-ray beam. The X-ray beam is re-collimated and the resulting tilted wavefront is corrected in an asymmetric Bragg reflection. This device is currently implemented at the Advanced Photon Source (APS) in Argonne/USA[38] and a pulse duration as short as 1 ps at very high X-ray flux is expected.

Recently a new generation of X-ray facilities became available[39–41]. Just as the optical laser could transfer energy to the electron bunch in an insertion device, the self generated radiative field can transfer energy into the electron bunch. The originally random emission of each electron in the bunch now becomes concentrated in these micro bunches (figure 2.8). The coherence condition of the emitted radiation is now met by a part of the electrons and very high emitted intensities can be reached[42]. For a perfectly compressed micro bunch the intensity would scale as $N^2_{electrons}$. Since the electron bunches vary slightly in phase the intensity scales:

$$I_{undulator+modulated\,electron\,bunch} \sim N^2_{magnets} * N^{1<x<2}_{electrons}. \qquad (2.10)$$

Self amplified spontaneous emission (SASE) electron bunches with typically 300 fs duration are guided into the undulator. The micro bunching effect is stronger with higher electron density. The compressing effect emphasizes therefore the central part of the bunch. The emitted pulse shows a central part as short as 50 fs on a broader background. The jitter between laser and X-ray pulse arrival is recorded for every shot. An overview over the available large scale facilities can be found in reference[43].

2.3 Pulsed lasers

A wave packet can be described as the sum of many modes with their wavevectors **k** and the polarization σ whose phases overlap only during a short period of time:

$$\vec{E}(\vec{x},t) = \sum_{\vec{k}\sigma} \hat{E}_{\vec{k}\sigma}(\vec{x},t) e^{i(\vec{k}\vec{x}-\omega(\vec{k})t)}. \tag{2.11}$$

The summed electrical field has the fast oscillatory frequency of the center wavelength and with an overall envelop temporal and spectral shape. It is often assumed that the temporal envelope has the form of a Gaussian or hyperbolic secant (sech) function. The shortest possible temporal width τ of a pulse with these shapes is related to the bandwidth $\delta\omega$ by the time-bandwidth product (compare also figure 2.9):

$$\tau \cdot \Delta\omega \geq 2\pi c_B \quad with\, c_B \begin{cases} 0.441 & \text{for Gaussian shape} \\ 0.315 & \text{for Hyperbolic secant} \end{cases} \tag{2.12}$$

The electrical field for a linearly polarized, cylindrically symmetric pulse with temporal and spatial gaussian shape can be written:

$$E(t,r) = E_0 \cdot e^{-2ln2(t/\Delta t)^2} \cdot e^{-(r/\Delta r)^2} \cdot e^{i\omega t + iC(t)}. \tag{2.13}$$

Here Δt is the temporal width, Δr the cylindrical Gaussian width. C(t) is generally called the chirp and represents the temporal distribution of the frequency components within the pulse. Many commercial laser systems designed for high power, short pulses use the very broad gain bandwidth of titanium doped sapphire (Ti:Saph) to amplify selected modes in a laser cavity. Double prism or dispersive mirror constructions allow a certain bandwidth to be amplified. An intensity dependent index of refraction changes the path in the cavity depending on the strength of the electric field and is used in our system to passively mode lock the cavity[44]. The process of mode-locking is either started from noise or with help of "artificial noise" introduced by modulating optics[45;46]. The output of these so called oscillators is a continuous train of pulses with relatively low energy (several nJ/pulse) and a repetition rate defined by twice the length of the cavity, usually on the order of 80 MHz.

The maximum power of pulsed laser systems increased dramatically when the chirped pulse amplification scheme was developed[47;48]. The chirp in equation 2.13 is altered and the pulses are stretched in time (typically several hundred ps). The combination of a Pockels cell (see comment) and polarizing optics selects a few pulses from the pulsetrain into a second cavity.

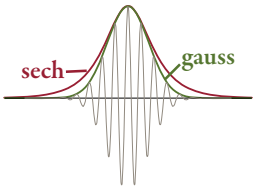

Figure 2.9. *Fast oscillating electric field with Gaussian carrier function in comparison to hyperbolic-secant envelope*

***Q-switched** or giant pulse lasers use a variable attenuator in the cavity that damps the spontaneous radiation below the lasing level. At one point in time the damping is removed and the built up population inversion can cause much stronger lasing than in a continues wave laser with the same pump intensity*

***A Pockels cell** is an electro optical module acting as a switchable half wave plate, which rotates a linear polarized laser pulse of the particular wavelength by 90 deg. For broadband pulses only a part of the pulse is rotated perfectly*

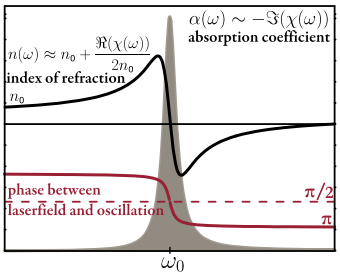

Figure 2.10. *Principle behavior of the Lorentz oscillator model for the index of refraction(black), the phase between exciting wave and oscillator (red) and the absorption (grey)*

***Comment**: indeed thin slices of light would be better since the bunches are typically* 0.5 cm *wide and only as thick a hair (*30 µm *for a* 100 fs *bunches)*

The peak intensity of the stretched pulses is below the damage threshold of optics in the laser system, allowing optical amplification up to this point. Within the cavity each pulse is amplified over several round-trips in a second Ti:Saph crystal which is pumped by a Q-switched laser (see comment). After the pulse is coupled out by a second Pockels cell it is sometimes amplified further in multi-pass systems. In the last stage the introduced chirp is reversed to generate a short pulse of extreme intensity.

2.3.1 Oscillator model

A monochromatic light wave of angular frequency $\omega = 2\pi f$ transverses a material with the phase velocity $v_p = c/n(\omega)$, where n is the refractive index of the material and c the speed of light in vacuum. Each electron in the material acts as a forced resonator, oscillating in the external field (Lorentz oscillator model). In a non magnetic medium the index of refraction is $n(\omega) = \sqrt{1+\chi(\omega)}$. The electric susceptibility χ combines the electrical field **E** and the polarization density **P** of an isotropic medium according to $\mathbf{P} = \epsilon_0 \chi \mathbf{E}$. Consider a dielectric medium where the oscillation of the electrons has its own resonance frequency ω_0 and is linearly damped by a factor σ. The susceptibility for this resonant system can be expressed as:

$$\chi(\omega) = \left(\frac{Ne^2}{\epsilon_0 m \omega_0}\right) \frac{\omega_0^2}{\omega_0^2 - \omega^2 + i\omega\sigma}. \tag{2.14}$$

N is the number of oscillators (dipoles), m the mass and e the elementary charge. In the vicinity of the resonance frequency the imaginary part of the susceptibility becomes large and with it the absorption. The width of the Lorentzian shaped absorption depends on the damping factor in the oscillatory system. The relative phase between the excitation and the polarization response shows a frequency dependent phase shift with a sharp step at the resonance. Already from this simple model (Figure 2.10) it is obvious that every material shows a dispersion ($dn/d\omega$). Short laser pulses have a spectral width around the center wavelength (e.g. $\Delta\lambda$ =35 nm for our pulses). The different components of the bunch travel with the group velocity:

$$v_g(\omega) = \frac{d\omega}{dk} = \left(\frac{n}{c} + \frac{2\pi}{\lambda_0}\frac{dn}{d\omega}\right)^{-1} \tag{2.15}$$

Dispersion in the group velocity will change the chirp in the pulse, meaning that the phases of different wavelength walk apart and the pulse can stretch non linearly. The typical method of calculating the linear dispersion in media is by use of the Sellmeier equations. The empirical relationship between wavelength

and refractive index is tabulated for most commonly used materials. Table 2.1 shows literature values for the materials relevant in the table top plasma source.

The effect is strong for the coherence length in non linear crystals like $\beta - BaB_2O_4$ (BBO). In the case of frequency doubling in BBO from 800 nm to 400 nm the walk off is in the order of 15 fs per 100 µm crystal and strongly limits the usable gain length. The efficiency of second harmonic generation in non linear crystals can be expressed $\eta_{SHG} = C^2L^2P/A$, where P is the power per area A, L is the crystal length, and C is a constant that depends on the active mode area. For higher intensities this linear model does not hold and non linear effects with an intensity dependent index of refraction n(I) like the Kerr effect[46] and relativistic effects (see also section 2.5) have to be considered.

Table 2.1. *Sellmeier equations for the materials relevant in this thesis*

Material	Sellmeier equations wavelength $[\mu m]$	range $[\mu m]$
Fused Silica[46]	$n^2=1+\frac{0.6962\lambda^2}{\lambda^2-(0.06840)^2}+\frac{0.4079\lambda^2}{\lambda^2-(0.1162)^2}+\frac{0.8975\lambda^2}{\lambda^2-(9.8962)^2}$	0.21-3.71
BBO[46]	$n_o^2=2.7359+\frac{0.01878}{\lambda^2-0.01822}-0.01354\lambda^2$ $n_e^2=2.3753+\frac{0.01224}{\lambda^2-0.01667}-0.01516\lambda^2$	0.22-1.06
HPLC water at 20°C[49]	$n^2=1+\frac{0.5684\lambda^2}{\lambda^2-(0.005101)^2}+\frac{0.1726\lambda^2}{\lambda^2-(0.01821)^2}$ $+\frac{0.02086\lambda^2}{\lambda^2-(0.02621)^2}+\frac{0.1131\lambda^2}{\lambda^2-(10.697)^2}$	0.182-1.12

2.4 Lasers and optical setups used in experiments

The measurements presented in this thesis were performed using different laser systems.

2.4.1 High contrast, high power laser system

The development, calibrations and effects around the laser plasma source were done using a parasitic beam of the multi-terawatt laser of the Lund Laser Center (LLC)[15]. This system has an 80 MHz Ti-Sapphire mode-locked oscillator with preamplifier, spectral cleaning with an acoustic wave pulse shaper (Dazzler) and extra Pockels cells outside the regenerative amplifier for additional temporal contrast improvements. After the regenerative amplifier the pulse is guided through a multipass amplifier. At this stage the parasitic beam used by us was coupled out and compressed. The output to our setup was 800 nm, 40 fs, 80 mJ, 10 Hz and a very high contrast ratio $>10^6$: 1 towards the leaked amplified spontaneous emission (ASE) background and pre-pulses. The system has been described in greater detail elsewhere[16;17;50–52].

2.4.2 Laser used in the high repetition rate laser plasma source

The system built by "Spectra Physics" is based on a short pulse Kerr lense modelocked Ti:sapphire "Tsunami" oscillator. The "Tsunami" is pumped by 4 W CW 532 nm generated by a frequency doubled LiB_3O_3 (LBO), diode pumped $Nd : YVO_4$ (Neodynium doped yttrium vanadate) laser (market name "Millenia"). The oscillator output is 80 MHz, 500 mW, 55 nm wide and chirped to 500 fs. The amplifier system is sketched in figure 2.11. The Tsunami output is stretched to 200 ps and a 1 kHz sub multiple of the 80 MHz is coupled into the regenerative amplifier.

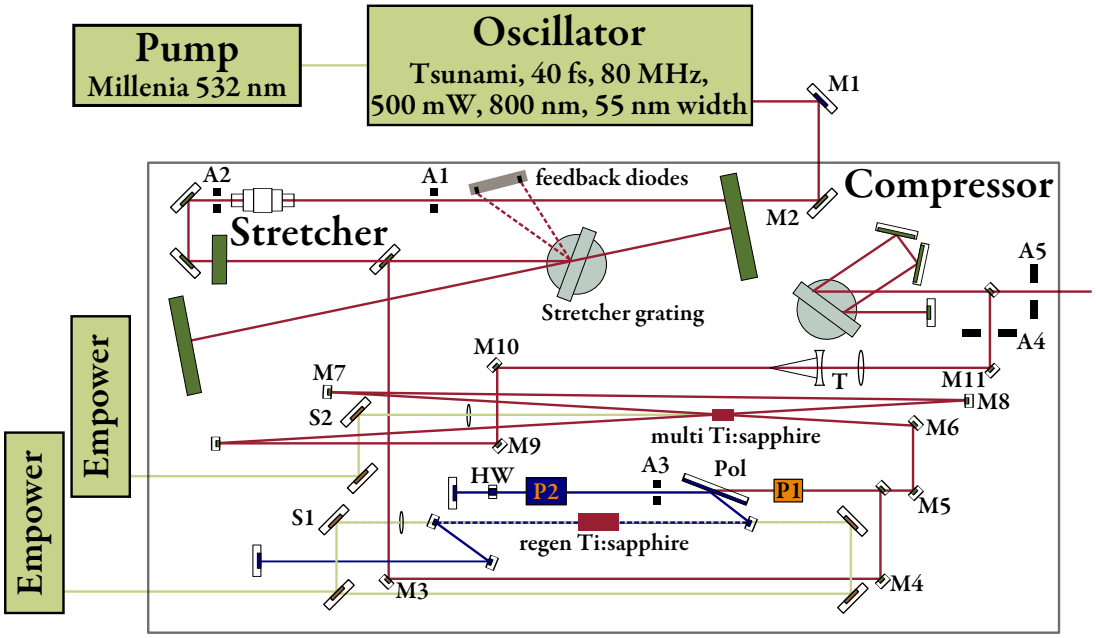

Figure 2.11. *Amplified laser system used for the table top X-ray source. The regenerative amplifier (blue beampath) is built with a half wave plate (Pol) one Pockels cell (P2) and a half wave plate (HW). The amplifier is seeded by a Spectra Physics Tsunami Ti:Sapphire oscillator (red path) and pumped by two doubled Nd:YLF Empower diode lasers (green path). For more details see text.*

The regenerative amplifier (blue beampath) is built with a polarizer (Pol), one Pockels cell (P2) and a half wave plate (HW). By switching the polarization within the Pockels cell (P2) the cavity can be closed and opened. The reflectivity of the polarizer, the effect that the a half wave plate is only optimal for the center wavelength and the quality and alignment of these elements define the temporal contrast ratio in this amplifier. The Ti:sapphire crystal is pumped by a frequency doubled Q-switched 1053 nm

Nd:YLF laser. During the time of the described experiments the crystal was pumped from two sides.

In an optimally aligned system we reach contrast ratios of 1:10^3 towards ASE and prepulses (a damaged or missaligned Pockels cell can lead to a decreased contrast ratios of about 1:10). The pulse is further amplified in a separately pumped double pass amplification system to 6.8 mJ (before compression). The beam diameter is adjusted in the lens telescope T and the previously introduced chirp is reversed. The total output of the system is $\approx$ 6 mJ, 40 fs at 800 nm. The contrast ratio, quality of the beam and stability is of huge importance for the intended usage. Internal beam movements due to damaged optics and thermal instabilities introduced the misalignment of Pockels cells, astigmatism generated in the optics and crystals, power and beam pointing fluctuations. A big challenge and still work in progress was to stabilize this commercial system. Since the processes during the X-ray generation are highly non-linear all fluctuations are amplified and can lead to noise in the best, hazardous situations in the worst case (see section 2.5.4 and paper **IV**).

2.4.3 Optical setup for time resolved absorption experiments

The optical components after the amplifier are shown in figure 2.12. The polarization of the main 800 nm beam is adjusted in a rotatable quartz $\lambda_{1/2}$ waveplate and split by two Brewster type polarizers. The polarization separation is better then 1:100 for the transmitted beam (pump beam) and 1:500 for the reflected beam (X-ray generating beam). The pump beam is delayed on a 13 ns delay line with 5 fs step size and $\pm$40 fs hysteresis. The full size beam is frequency doubled in a 200 µm thick BBO crystal and cleaned with two dichroic mirrors (high reflector for 400 nm and very weak reflector for 800 nm) to less then 5 % remaining IR radiation and focused on the sample. The transmitted infrared beam after the first dichroic mirror is used to record the presence of the pump beam.

The probe beam is expanded through a 1:2.5 telescope and focused by a 90° off axis parabolic mirror (made by Janos Inc.) onto the water jet target. The off axis parabolic mirror has two foci if not perfectly aligned or if the beam shows astigmatism[13]. Two close foci can generate conditions similar to temporal double pulse structures and can give rise to the generation of high energetic electron beams (see paper **IV**).

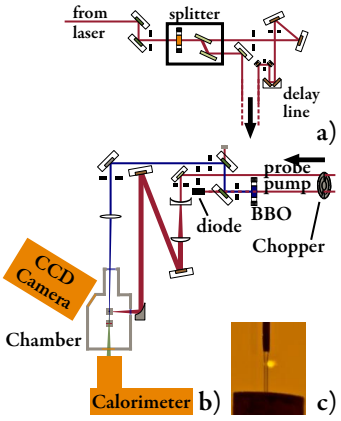

Figure 2.12. *Optics setup for the table top XAS. a)The laser beam is split with a variable beam splitter. b) The repetition rate can be adjusted by a coupled chopper for pump and probe beam. The pump beam is converted into* 400 nm*, cleaned by two dichroic mirrors and focused into the chamber. The leakage from the first mirror is measured by a photodiode that will be fed into the detector to link pump and un-pumped datapoints. The X-ray generating beam is reflected over a* 90° *off axis parabolic mirror onto the water jet. c) The plasma is formed tangentially on a* 160 µm *water jet.*

2.5 Laser-plasma X-ray source

Photon densities and electrical fields in the focal point of the pulsed laser reach intensities only found in extreme environments like lightning or centers of stars. At these intensities atoms and molecules are nearly instantaneously ionized. In this highly non linear regime particles are accelerated and can undergo a variety of processes including harmonic generation, the driving of plasma wakes, and different scattering processes. A number of recent textbooks[53–58] and review articles[8;59–62] cover the wide field of ultra fast laser-matter interaction and X-ray generation. I will focus on some interactions and aspects relevant for the work with a laser plasma X-ray source that is used for X-ray absorption spectroscopy. A quick and incomplete overview of laser driven X-ray sources would include the following:

Wake field acceleration A high intensity laser can generate collimated and mono energetic electron beams and particle beams[61;63]. The accelerated electrons can be trapped in the plasma wake, wiggle in the driving laser field and generated table top synchrotron radiation[64]. It was suggested and shown that these mono energetic electrons[65] and fast particles can be injected in small undulators[66;67] or be used to drive Compton[68] or Thomson[69] sources.

Plasma source Intense laser fields interact with steep plasma density gradients to generate and heat plasma. The electrons in this plasma interact with matter to form bremsstrahlung or characteristic line radiation.

Laser driven X-ray diode A small bunch of electrons is generated by a short laser pulse from a photocathode. These are then accelerated by a strong electric field onto a classical anode[70;71].

High harmonic generation A strong laser field distorts the potential of an atom so that at a controlled point electrons lost by the atom are returned to the atom when the field reverses. The electrons gain energy in the laser field, fall back in their ground state and emit a photon having the energy of the ionization potential, plus the energy gained in the field. The process repeats itself with the emitted photon. With strong laser pulses photons well beyond 2000 times the fundamental wavelength have been observed[72–75].

Compton scattering The inverse Compton effect can transfer energy to optical photons scattered on fast electrons generated at synchrotron or laser sources and high energy x- and gamma radiation can be emitted. The efficiency is low and very large photon densities are needed[68;76–78].

Thomson scattering This source works in the low energy limit of Compton scattering. The oscillatory field of a strong laser pulse interacts directly with an intense electron beam. The oscillating electrons emit radiation similar to a wiggler. The achievable flux is very small, but the reported emission is on the order of the laser pulse duration[79].

2.5.1 Ionization

The energy of an 800 nm photon is often not sufficient to ionize an atom or lift an electron from the valence (or highest occupied level) to the conduction band (lowest unoccupied level) in an isolator. Electrons in the conduction band or free electrons with sufficient energy can ionize molecules and excite further electrons into the conduction band. This collisional ionization can lead to an avalanche effect when the sum of field ionization rate and collision rate is larger than the recombination rate[54].

For the initial ionization the two main models are multi photon ionization and field ionization. Which of the two processes dominates is determined by how much energy the electron gains during its oscillation in the laser field (and is related to the resonance absorption discussed above in section 2.3.1). The average oscillatory energy (ponderomotive energy[81]) one electron has if its resonance frequency in the atom field is ω_e is:

$$U = e^2E^2/4m_e^2\omega_e^2. \tag{2.16}$$

To determine which process is dominating, one has to consider the ionization potential I_p of the atom. The dimensionless Keldysh parameter[82] $\Gamma = \sqrt{I_p/4U}$ is an estimate of the threshold between the two effects. For high frequencies and/or low electric field strength the ponderomotive energy is small and $\Gamma \gg 1$. Multiphoton ionization is the dominant absorption process in this regime. At high intensities many photons can simultaneously interact with the atom and the electric field can be understood as a distortion of the potential barrier (see figure 2.13 and the comment under to it). The electron can tunnel through the barrier or if the distortion is large enough and the barrier is suppressed go "over-the-barrier"[54;83].

Tunnel ionization is the basis for the coherent generation of high harmonics. The electrons tunneling through the barrier can gain energy from the laser field and be recaptured, and emit a photon of higher energy. The process inherits the coherence of the driving laser field. This is a very active area of research and the control of phase and ionization has enabled groups to generate harmonics in the hard X-ray range[72].

Numerical example: *A pulse of 30 fs with 3 mJ, focused to a waist diameter of 10 µm has* $\approx 10^{17}\ W/cm^2 = 10^{21}\ W/m^2$ *compared to 1 kW/m² of average sunlight and contains* $\approx 10^{16}$ *photons, assuming a wavelength of 800 nm or 1.5 eV photons energy. For linearly polarized light the electrical field is:*

$$E = \sqrt{2I/\epsilon_0 c} \approx 1 \cdot 10^{12}\ V/m$$

with c the speed of light and ϵ_0 *the permittivity in vacuum. Compared to this the Coulomb field of the first Bohr radius of hydrogen*[80] *is*

$$E_{bohr} = \frac{e}{a_0^2} \cdot \frac{1}{4\pi\epsilon_0} \approx 5 \cdot 10^{11}\ V/m$$

where e is the elementary charge and a_0 *the first Bohr radius*

$$a_0 = 4\pi\epsilon_0(\hbar^2)/(me^2) = 5.3 \cdot 10^{-11}\ m$$

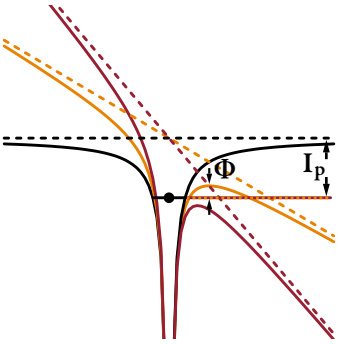

Figure 2.13. *Schematic drawing of the tunnel ionization process.* I_p *is the ionization potential for the undistorted potential (black). Under the electrical field the potential distortion generates a potential well of height* Φ *through which the electron can tunnel (gold). For an even stronger electrical field the potential distortion might become large enough that no potential barrier remains and the electrons then can flow freely (red).*

Comment figure 2.13 *An estimate for the electric field can be made by a linear Coulomb potential:*

$$V_{coul}(x) = (-Ze^2)/(4\pi\epsilon_0 x)$$

modified by a homogeneous electrical field to:

$$V_{total}(x,t) = V_{coul}(x) - eE(t)x$$

The barrier is the ionization potential (I_p) minus the maximum of this curve. Here one can define an apparent laser intensity for each bound state at which this barrier would be low enough for direct ionization[53]*:*

$$Int_{app} = \frac{\pi^2 c \epsilon_0^3 I_p^4}{2Z^2 e^6}$$

, where Z is the charge of the generated ion, e the elementary charge and c the speed of light. For typical gases:

Ion generated	I_p *[eV]*	Int_{app} *[Wcm^{-2}]*
He^+	*24.59*	1.4×10^{15}
N^+	*14.53*	1.8×10^{14}
N^{5+}	*97.9*	1.5×10^{16}
O^+	*13.6*	1.3×10^{14}
O^{6+}	*138.1*	4.0×10^{16}

2.5.2 Plasma oscillation

In the laser focus of a plasma source the ionized particles form a strongly inhomogeneous plasma with a high degree of ionization. The strong electric fields locally disturb the condition of neutrality. The mobile and light electrons, once ionized, oscillate in the Coulomb potential of the heavier and less mobile ions with the (Langmuir) oscillation frequency[53]:

$$\omega_p^2 = \frac{e^2 n_e}{m_e \epsilon_0}. \tag{2.17}$$

Here n_e is the free electron density, m_e the electron mass and e the elementary charge. The energy transfer from the driving electrical field to the oscillator is maximum at the resonance frequency (see oscillator model section 2.3.1) and due to the phase shift this layer acts as a perfect mirror. Assuming the existence of a density gradient, a laser can penetrate the plasma until the critical density, where $\omega_p(n_e) = \omega_{laser}$ is reached.

2.5.3 Propagation in under-dense plasma

Several other important effects can be understood from the Langmuir frequency. For the experiment the index of refraction is:

$$n \approx \sqrt{1 - \omega_0^2/\omega_{laser}^2}. \tag{2.18}$$

By considering also equation 2.17 we see that with increasing ionization the index of refraction decreases in regions with higher intensity (higher degree of ionization). Assuming a spatial intensity variation like described in equation 2.13, the effective higher speed in the middle of the beam turns the wavefront and leads to de-focusing. Focusing optics with focal length f and an initial beam diameter of R normally have a minimal possible focal diameter of $D = 2f\lambda/\pi R$. Intensity de-focusing limits this focal parameter further if the ionization threshold is reached. This motivates the use of gases with lower ionization threshold, or evacuation leading to a reduction of the attainable electron density (see comment in section 2.5.1). This effect decreases the area of the confocal parameter $\sim (4\pi f/R)^2$ and with this the interaction length.

In the water plasma source presented here the vacuum pressure is limited by the water vapor pressure. The water is degassed and in some cases cooled below room temperature to be able to further reduce the pressure. During the experiments the chamber is constantly flushed with helium to obtain a higher ionization threshold. Plasma sources based on materials with lower vapor pressures can reach higher laser intensities in the focal area and generate higher electron temperatures (see section 2.5.4).

The quiver movement of electrons in a very strong electric field can require a relativistic correction of the electron mass if the laser field is intense enough. The effective resonance frequency becomes $\omega_{corr}(I) = \omega_0/\gamma$ and is higher in areas with larger field strength. Following a similar argument as before, this process may generate a self focusing effect[84]. Balancing these and several other not previously mentioned effects like (Raman and Thomson light scattering[12]), light can be guided in a self generated plasma channel over long distances[85]. Processes like white light generation[55;86–88], self compression[89], guiding of electrical discharges and lightning[90] and laser driven plasma waves in self guided channels or capillaries[61;91;92] use these effects.

2.5.4 Plasma heating and generation of bremsstrahlung

The laser heating of a plasma has been studied for many years[53;54;58]. In laser plasma sources the plasma is generated at the steep interface between a high density target and an area of lower density. A gradient of temperatures and densities is formed. The leading edge of the laser pulse hits an intact surface and starts the partial ionization. Nuclei in the plasma move roughly with the speed of sound in practical units[53]

$$c_{ion} \simeq 0,31\sqrt{(T_e/keV)\cdot(Z_{eff}/A)}\ \mu m\ ps. \tag{2.19}$$

Here T_e is the electron temperature in keV and Z_{eff} the effective charge normalized by the atomic number. The expansion resulting from this speed is small during a single high contrast pulse of 50 fs. For optically impaired temporal contrast (see section 2.4) or deliberately generated pre-pulses with several picosecond delay (paper **IV**), the heavier particles in the plasma have time to expand and generate a plasma and temperature gradient spreading, over a much wider range (plasma scaling length)[53;93–96]. At the intact plasma surface collisional absorption processes dominate the energy absorption at lower intensities of $\approx\ 10^{12} - 10^{14}\,W/cm^2$ [53;58]. Several collisionless absorption mechanisms are suggested for higher laser intensities[53;54;58;97–99]. One dominant process at the undisturbed density surface is the vacuum heating mechanism named after Brunel[100–102] which was extended to shorter pulses by Gibbon[99]. In this mechanism the p-polarized field extracts electrons from areas with high electron density and accelerates them during the opposite electric cycle back into the area of high density. Complex collective events for p-polarized light have been calculated using particle in cell (PIC) codes that can generate a superheated fraction of electrons. The total intensity spectrum is often presented with a bi-Maxwellian distribution[53;103]. A common feature for many theoretical findings is that the hot electron temperature scales as

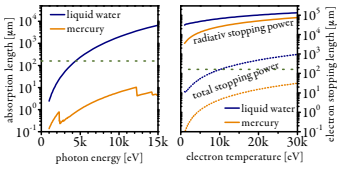

Figure 2.14. *Left figure: Photon attenuation length in water and mercury*[104]*. The green line indicates the jet thickness. Right figure: Electron stopping power of water and mercury, normalized to the density of the material and photon energy. The stopping power for radiative energy loss and total energy loss was transformed into a stopping length assuming the continuous slowing down approximation. The spectra were calculated using the ESTAR database*[105] *which does not consider shell correction. The corrections are necessary if the electron energy comes of the order of the inner shell binding energy.*

$$T \sim c \cdot \left(\frac{I}{[10^{16}\, W/cm^2]} \frac{\lambda^2}{[\mu m^2]} \right)^{2/9<\alpha<1} . \qquad (2.20)$$

Details of the proposed theories for different intensity ranges, materials and angles of incidence can be found in a number of textbooks, recent articles and references therein (e.g.[21;24;53;54;58;93;95;106–111]). Fast electrons are stopped in the material and release their energy as bremsstrahlung. Several studies have investigated the conversion efficiency for laser plasma generated fast electrons for different intensities, geometries and target materials[23;24;93;112;113]. Target ablation at the high laser intensities requires replacement of the target material between shots with precision in the order of the focal dimension of a few micrometers. The ablated material has to be controlled to avoid coverage of optics. Different target/debris handling systems have been developed over the years for flat polished discs[13;23;24;94;114–120], wires[121;122], tapes[123;124], drums[125;126], cluster[127–130], droplets[131;132], pulsed gas nozzles[133] and liquid jets[103;134–141]. Many of the early systems were developed to study laser plasma interactions. Later developments aimed at the application of the generated intense characteristic line emission to study structural changes in ordered systems. It was proposed and shown that a near edge spectrum (see chapter 3) can be extracted using the overlap of characteristic emission lines with specific absorption edges[142;143]. Several groups showed steady state and time resolved X-ray absorption fine structures using laser plasma sources in the soft X-ray regime (e.g.[120;126;144;145]). Sources for lab based time-resolved hard X-ray spectroscopy based on these constructions have been build and time resolved measurements been presented[103;124;141;146–151]. All of those studies use flat or bent analyzer crystals with their low efficiency (see section 4.4.3) to disperse the X-ray probe radiation.

The choice of target material depends on many different aspects: while high-Z materials stop electrons more efficiently (figure 2.14) the reabsorption within the material is also much higher. The conversion efficiency into bremsstrahlung is higher the faster the electrons are. The electron speed depends on the electron density and the maximal achievable power density[152].

The photon flux achieved in the range $5 - 10\,\mathrm{keV}$ (presented in papers **I** and **II**) is comparable with fluxes achieved from other sources[103;151;152] and sufficient to limit the detection rate to the detector (see also section 2.5.6 and section 4.5.6). In future iterations X-ray optical elements might be introduced in the system (see section 2.5.7 and 4.4.3). This first version however was designed to run without any optical elements. This work developed the use of single X-ray photon measuring detectors in combination with a plasma source for X-ray absorption spectroscopy, in

particular with the view to enable ultrafast pump-probe and lab-based X-ray absorption studies. Without the possibility to spatially filter characteristic emission lines close to the area of interest (see also comment in section 4.4.3) thick metallic filters would have to be used to suppress the intense emission or the counted background radiation would substantially increase. Partly for this reason, the target material was selected for its lack of observable emission lines.

2.5.5 Sample chamber, water jet target, debris protection and sample jet

Simplicity and long term stability are among the advantages of micro-jet targets. Experiments in this work mostly used a jet apparatus based on a long stainless steel syringe orifice with sharpened edges and an inner diameter of 210 µm a self contracted[153] jet with 160 µm. The jet apparatus is operated under laminar flow conditions with $\approx 5\,\mathrm{m/s}$. The focal spot is set $\approx 2\,\mathrm{mm}$ under the nozzle (see inset figure 2.12). The characteristic scaling length after the Rayleigh-theory predicts the earliest breakup of the jet after:

$$L \approx \cdot\sqrt{\frac{\rho * d^3}{\sigma}}. \tag{2.21}$$

c_{jet} is the jetspeed, ρ the density, d the real jet diameter and σ the surface tension. This length is however only an estimate[153] and with the carefully designed laminar flow conditions the scaling length does reach several cm. Deionized water is used for the jet and a mesh filter with 60 µm opening prevents clogging of the jet. The stable X-ray production and tests with synchronous stroboscopic illumination of the plasma focus area using the second arm of the laser at different relative arrival times similar to the work from Thoss[113] confirm a stable surface at the interaction region. The fairly large jet diameter enables the control of the angle of incidence on the surface (see figure 2.12 c). If the sample chamber is operated under 1 atmosphere helium the jet is produced using a small centrifugal pump whose already very small pressure fluctuations are further damped by long, elastic tubing.

The rough vacuum in the evacuated setup was chosen to be limited to water vapor pressure to avoid boiling of the jet. A water aspirator pump (buffered over two water filled gas ballast containers) provides a simple and stable pumping system that is not sensitive to the humidity. An external water reservoir is filled with helium under atmospheric pressure and the pressure difference between the chamber and the reservoir drives the water jet.

Several sample chambers were used during the thesis work. The initial work for papers **I**, **II** and **IV** was done in a modular

lead chamber presented in paper **I**. To be able to automate and feedback the movement of the chamber and its contents with standard motorized linear optical delay stages a new, light weight, modular and compact chamber was developed. This most recent chamber was built from aluminium and designed to provide sufficient absorption to satisfy the safety regulations under stable X-ray emissions. Additional external lead shielding can be added in case of laser instabilities and hazards from high energy electron emissions discussed in paper **IV**. The chamber has two for antireflection coated 1 inch windows, one large observation window and two beryllium windows mounted on aluminium carriers. All windows are sealed with rubber gaskets and can be exchanged. The holder, wall and lid are separate units designed to be opened and modified.

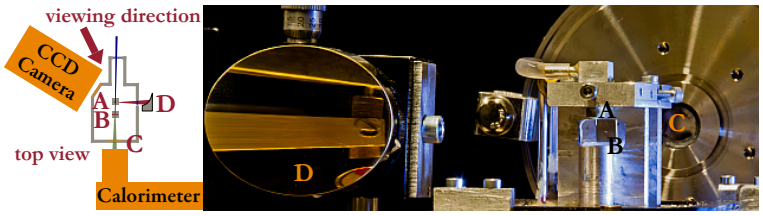

Figure 2.15. *Magnified sample chamber and photograph of the setup. Debris protection and outer chamber walls have been removed. A is the water nozzle producing the water jet. B is an alignment pinhole in the place where the sample jet is placed. C is the entrance window of the Detector. D is the off axis parabolic mirror focusing the laser.*

Figure 2.15 presents the sample chamber without the outer walls. The holder for the water jet A and the nozzle for the sample jet are aligned on flat surfaces and can be easily exchanged. The whole chamber is $8 \times 10\,\text{cm}$ with an extension for the entrance window of the pump beam. To commence an experiment the system is aligned for maximum X-rays (using the CCD camera, see chapter 4). The detector is aligned on the X-rays that pass through the alignment pinhole. The pump laser is aligned on the pinhole and the transmitted intensity measured. A first indication of the temporal overlap is measured by introducing a scattering element near the nozzle A and measuring the scattered light with a fast photodiode (the pump-beam traverses a fixed distance past the water jet, see also figure 2.19). Improved time-zero alignment might be found by measuring the pump beam scattering from the generated plasma plume (in which the critical density acts like a plasma mirror). The alignment pinhole is then replaced by the nozzle that replaces the sample jet.

During the operation under aspirator vacuum pressure, a small amount of helium can be constantly lead into the chamber and onto windows and other surfaces where condensation might cause problems. A small splatter protection with holes for the two laser beams is placed in the gap between the holder and the catch tube of the water jet to minimize the open area. The constant gas stream purges the chamber effectively from the

water splatter and steam generated by the plasma explosion. Water and sample outlets are tapped with screw threads and can house changeable stainless steel catch tubes. The chamber rests on three custom built adjustable legs with ball heads that each sit under tension in a v-shaped groove providing a stable 6 point kinematic design with very low slip [154–156].

For pump probe measurements the sample is a free flowing jet with $\approx 0.6\,\mathrm{m/s}$, produced by two conically wedged flat stainless steel plates with 6 mm length and adjustable gap beginning from a few micrometers. The pressure difference is generated by a small chemically resistant pumps (e.g. micro gear pump from MZR Inc. or small diaphragm pumps from Xavitech).

Future improvements on the jet system could include separation of the sample environment from the X-ray generation environment using thin membranes or break through nozzles [157]. The sample environment could be decoupled from the X-ray chamber with broadband X-ray optics (see section 2.5.7), though this would introduce alignment difficulties, questions of X-ray temporal dispersion in the optics.

2.5.6 X-ray flux considerations

X-ray absorption spectroscopy measures the spectral variation of the absorption cross-section. The important task is to achieve a flux on the sample area that:

has known spectral composition This can be achieved by either using a monochromatic beam and normalizing on the incoming and outgoing intensity, or by using a beam of the full spectral width and analyzing its spectral components with and without the sample.

is as stable as possible For monochromatic beams with large fluctuations an effective normalization is needed which has a signal to noise ratio similar to the actual measurement. If spectral fluctuations do not include sharp features they can be normalized by a system with worse spectral resolution than would be needed to retrieve the spectrum.

is as high as possible to measure with the desired signal to noise and readout capabilities of the detector. Every photon in XAS carries information and the signal to noise statistics is often limited by the number of photons collected. In our single photon counting experiments this rate is limited by the number of microcalorimeter pixels and their individual countrate.

does not damage the sample In most ultra-fast time-resolved experiments the sample is replaced before each X-ray expo-

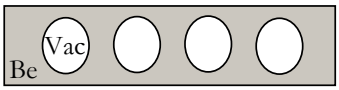

Figure 2.16. *Beryllium lenses using the diffractive index $n(Z) = 1 - \alpha Z$ typical focus length of several meters*

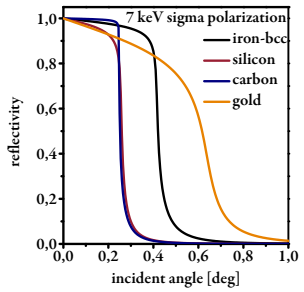

Figure 2.17. *Relative reflectivity as function of incident angle measured from grazing incidence. Generated with with the database*[158]

sure. The pump beam often curses as much sample damage as the X-ray probe.

must not produce radiation hazard In large scale facilities radiation safety for users is often excellent. In small experimental table top setups radiation hazards like the described electron beams need to be recognized, monitored and eliminated by the experimentalist.

2.5.7 X-ray optics with potential use in tabletop absorption spectroscopy with direct detection

The index of refraction for X-rays is calculated and experimentally proven to be less then unity in materials[159].

$$n = 1 - (\frac{e^2}{mc^2})\frac{N\lambda^2 Z}{2\pi} \tag{2.22}$$

where N is the number of atoms per unit volume and Z the atomic number. This fact enables the interesting construction of beryllium lenses with vacuum/air as the material with higher index of refraction (figure 2.16)[160]. The kinematic theory of reflection after Darwin/Prins describes the angular dependence of the total reflection in a Bragg peak with polarization perpendicular to the scattering plane and negligible absorption as:

$$|\theta - \theta_0| < \left(\frac{e^2}{mc^2}\right)\frac{N\lambda^2}{\pi sin(2\theta)}f. \tag{2.23}$$

Here N is the number of atoms per unit volume and the angle θ_0 is the Bragg angle corrected for refraction derived for small n from

$$\lambda_{vacuo} = \lambda_f\left(1 - \frac{1-n}{sin^2(\theta_0)}\right)$$

and the false uncorrected Bragg glanzing angle for this order

$$\lambda_f = (2d \cdot sin(\theta_0)).^{161}$$

If we neglect effects of absorption, material density and the dispersion corrections f' and f'', the width of the total reflection scales as: $f^0 \sim \rho/q$ with the density ρ and momentum transfer Q[159;162]:

$$Q = |K_f - K_i| = \frac{4\pi sin(\theta)}{\lambda}.$$

For heavier and less ordered materials the absorption in top layers can not be neglected and the initially perfect reflected intensity is attenuated faster (figure 2.17).

Regardless of these absorption effects, the very small acceptance angle associated with Bragg diffraction amounts to a very

narrow bandpass behavior when using crystal diffraction as the basis of an energy analyzer. There can be corresponding losses of flux. Reflection under very small angles has a similar angle dependence being in effect zero order diffraction. Nevertheless energy dependence for reflection can effectively cover a larger wavelength range. The emission of a point source like a plasma source is in principle isotropic in the full solid angle 4π (see also paper **I**), which is a problem when designing or considering X-ray optics.

Using a larger solid angle without smearing the time resolution requires a careful design of the experiment. Optics for broadband reflection suitable for tabletop XAS include:

toroidal mirrors figure 2.18 a) Elliptical design guides the reflected rays with one reflection into a good focal spot. The material is usually as heavy as possible or covered with a high Z material, or can consist of multilayers in which the d-spacing may be tapered [160;163].

poly capillary lens figure 2.18 b) Many small capillaries made e.g. from lead glass or silicon guide the beam over several internal total reflections. These optics can have stronger bends than optics based on single reflection and therefore capture a larger solid angle. With each reflection the penetration depth smears the time-resolution and the difference in the pathlength allows only the use of a small outer ring. There are many different designs using single or multiple diameters. [164;165].

lobster eye lens figure 2.18 c) A multifoil optics with rectangular or axial symmetric cross section. The foils are covered with multilayers or high-Z materials like gold to give better performance at shorter wavelength. The design offer a large solid angle of capture (several 10s of mrad) [166].

bent mirror system figure 2.18 d) Bent gold or multi layer covered systems. Two bent mirrors coated with high Z material or wavelength adjusted multilayers are arranged at 90 degrees and have a two bounce focal path. The perfection of the surface can be made very high. Such Kirkpatrick-Baez systems are among the achromatic standard techniques used at synchrotron sources [160;167;168].

With each reflection the temporal broadening can be increased and pathlength differences have to be considered carefully for each design. Bargheer [169] presents some considerations for the use of optics in table top diffraction experiments which are valid for the broadband capable devices. The solid angle for a circular

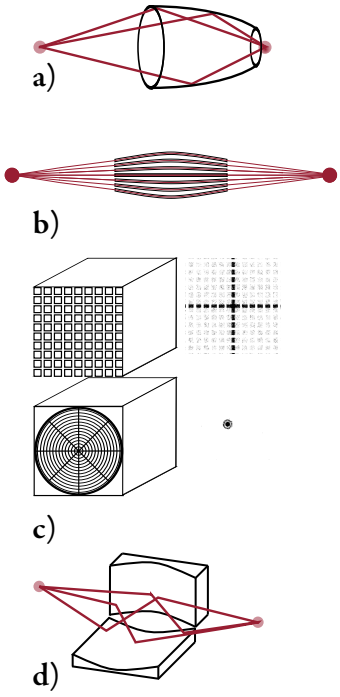

Figure 2.18. *a: toroidal shaped single reflective optics, b: poly-capillary lenses, c: lobster eye multifoil optics, d: bend mirror systems*

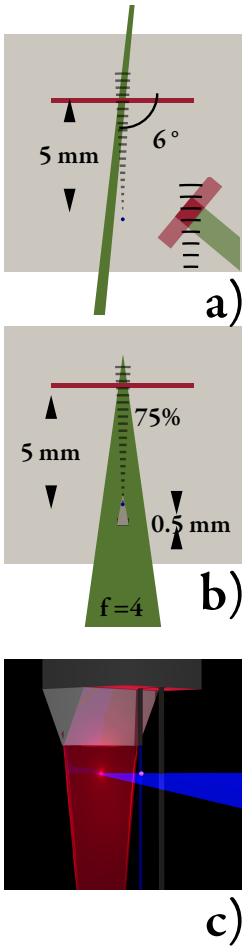

Figure 2.19. *a: At reduced source-sample distances the temporal smearing is increased due to the different wavefront projection on thick samples. Differences in the speed of light in thick samples can be compensated by wavefront tilting. b: a different perpendicular nozzle design with a small beam-block in front of the water jet and strong focusing can simplify the use of small distances. c: 3d sketch of the design.*

cross-section with the full opening angle ω is

$$\Omega = 4 * \pi sin^2(\frac{\omega}{4}) \tag{2.24}$$

In the presented tabletop XAS setup the use of optics was avoided by bringing the sample close the source. This avoids the necessarily careful mechanical alignment, spectral filtering qualities, temporal dispersion considerations and expense of X-ray optics. In the currently implemented prototype the source-sample distance was chosen to be 2 cm = 1.7×10^{-4} sr (assuming a 300 µm probed spot) for simple access and testing. Without major reconstruction a source sample distance of 0.5 cm = 2.8×10^{-3} sr (for a 300 µm diameter probed spot) is possible by replacing the current nozzle with the design described in figure 2.19.

In this simple design the path differences for the bent wavefronts is $\approx$ 15 fs and only the walk off due to dispersion in the sample gives a strong contribution to the time smearing ($\approx$ 1 fs per 1 µm pumped sample in water). To reduce this walk-off one would either limit the sample thickness or could adjust the angle between X-ray beam and the exciting laser pulse (additionally wavefront adjustment and control might be needed). It should be borne in mind that the X-ray pulse duration is expected to be a few hundred fs with the current implementation of the source (see paper **I**).

The use of reflecting X-ray optics could increase the total X-ray flux on the sample (at the cost of additional temporal smearing)[169]. It would however ease the access for excitation by enlarging the free distance before the sample and it would enable the possibility to separate the sample environment from the X-ray source. In combination with a stronger and especially harder source the detector development would enable us to measure time resolved table top emission spectra. This possibility to spectrally filter the emission would reduce the measurement time and might ease the use of high-Z target elements by suppression of emission lines (see also section 4.4.3 and 3.4).

óá

Chapter 3

Interaction

In this central chapter the working life of X-ray photons is presented, after their birth in a "hot" source (chapter 2) and before their demise in a "cold" detector (chapter 4). Compared to the source and detector, foreseeable chemical samples are "warm". X-ray absorption spectroscopy is a well established molecular structure approach applicable to disordered samples. Laboratory based ultra-fast stroboscopic pump-probe capability is a particular incentive in this work. To develop a new technique for transmission X-ray absorption spectroscopy at energies up to and exceeding 10 keV was a goal of this work. The physics of this technique is outlined. The "hot" source and "cold" detector were married for the first time in the closing months of this work. A few of its first resulting transmission X-ray absorption fine structure spectra are presented.

3.1 Main interactions

X-rays interact primarily with the electrons in a material. Electrons have a much higher charge-to-mass ratio than atomic nuclei. This makes them much more responsive to the oscillating electric field of photons. In addition, electrons are usually much more numerous than nuclei in materials.

X-rays that interact with matter can be absorbed, or have their energy altered, or their phase shifted. Absorption will be the focus of this chapter. Energy shifts are the symptom of inelastic processes, and include X-ray fluorescence, Compton scattering[76], and phonon interactions (which require extremely high X-ray energy resolution). Of these, X-ray fluorescence is an important and easily detectable consequence of absorption, requiring its brief discussion in this chapter. Phase shifts are the basis of the X-ray diffraction methods, of which crystallography and holography are just two well-known examples. It is worth mentioning that

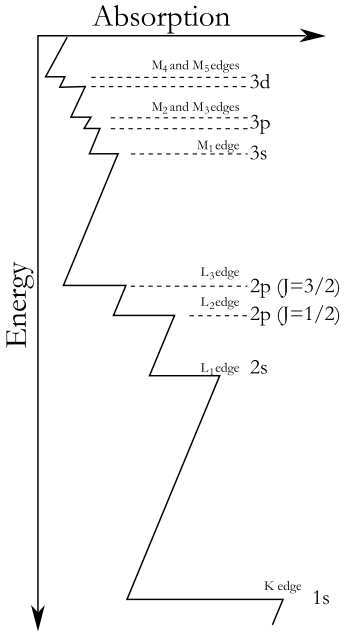

Figure 3.1. *Absorption edges for most standard materials are tabulated*[34;104;171].

Comment to equation 3.1: The integrated transmitted intensity is equivalent to the Beer - Lambert law in the visible range:

$$I(z) = I_0 e^{-\mu(E)z}$$
$$\mu = ln(I_0/I_T)/z$$

phase shifts and absorption are intimately related. Their common ground has its roots in the Lorentz driven oscillator model that was presented in section 2.3.1, while the quantitative relationship is expressed by the so-called Kramers-Krönig equations[4].

When absorption of an X-ray photon occurs, an electron is elevated to a higher energy state. The excited electron might still occupy a bound state of the atom or molecule. Alternatively, the electron might have sufficient energy to escape the atom or molecule altogether, and radiate as a photoelectron wave (with an energy-dependent de Broglie wavelength $\lambda = h/p$[170], and a symmetry depending on the parent orbital). These two situations correspond to different features in X-ray absorption spectra. In the first case, the available bound states give a spectroscopist's assessment of the atoms and geometry of the molecule. In the second case the free photoelectron wave can serve as a probe of neighboring atoms, by reflecting from and among them in a way that modulates the X-ray absorptivity. Either way, the absorption of X-rays can serve as a probe of the structure of molecules. This structure can be decoded from the X-ray absorbance if one understands the electron's behavior.

3.2 X-ray Absorption processes in spectroscopic methods

X-ray absorption spectroscopy (XAS) probes the absorption probability of photons as a function of their energy. The absorption in an infinitesimal thin sheet of material is given by[172;173]:

$$-dI_{trans} = I_{trans}(z)\mu dz \tag{3.1}$$

with μ the linear absorption coefficient, I the intensity and z the pathlength in the material. Ignoring resonant absorption energies the absorption cross section for a free atom follows

$$\mu(E) \approx \frac{\rho Z^4}{AE^3} \tag{3.2}$$

with a strong dependency on the atomic number Z and the energy E; ρ is the density and A the atomic mass[80]. The strong Z dependence gives element specific contrast which can be further enhanced by using differential absorption above and below resonances[13]. The probability for a photon to be absorbed can be theoretically derived from the transition moment between the initial ψ_i and the final states ψ_f and the density of states ρ[168;174;175].

$$\mu \propto \left|\left\langle \psi_f | H' | \psi_i \right\rangle\right|^2 \rho(E_f - E_i - \hbar\omega). \tag{3.3}$$

If the energy of the photon is sufficient to excite a filled electronic state into a continuum state the sudden rise in the absorption probability is called absorption edge (see figure 3.1). The excited atom/molecule undergoes different radiating and non radiating relaxation processes which are shown in figure 3.2. The two main deactivation channels are the fluorescence decay and the Auger decay. For hard X-rays (above 2 keV) the fluorescence decay process is more likely [176]. During the fluorescence decay an electron at a higher energetic state fills the core hole and a photon of characteristic energy is emitted. The emitted photon energies are element specific and are used in X-ray emission spectroscopy (XES). The energy of the emitted photon can be analyzed for chemical shifts in both the final core hole state and the emitting originating state. The width of the absorption crossection is broadened by the the uncertainty principle $\Delta E\tau \geq \hbar$ due to a very short lifetime τ of the core excitation. The lifetime broadening of the K-absorption edge of iron is 1.25 eV and 1.6 eV for the Kα_1 emission [177]. Resonant scattering processes from core states over one or several bound intermediate states can overcome this limitation, but require highly tunable monochromatic excitations [178].

The theory of X-ray absorption [168;176;179–182] and emission [178;183–185] spectroscopy is well established and for details the reader is referred to these recent review articles and text books. The photon emission is related to the density of occupied states while absorption spectroscopy probes the density of unoccupied states. Both show strong chemical sensitivity and can be used to identify changes in chemical structure [178]. The high quantum efficiency of the developed microcalorimeter detectors offer promising features for both X-ray absorption and emission techniques. Non resonant X-ray emission spectroscopy does not rely on monochromaticity of the exciting radiation and would be easily installed in a plasma source setup. Planned ultrafast facilities like the short pulse facility at MAX IV in Lund expect 1×10^7 photons/pulse at 100 Hz and would benefit from quantum efficient detectors with the features discussed in section 4.5.3. The current prototypical laser plasma arrangement and presented measurements are geared towards X-ray absorption fine structure (XAFS) spectroscopy, which and will be the focus of the following discussion.

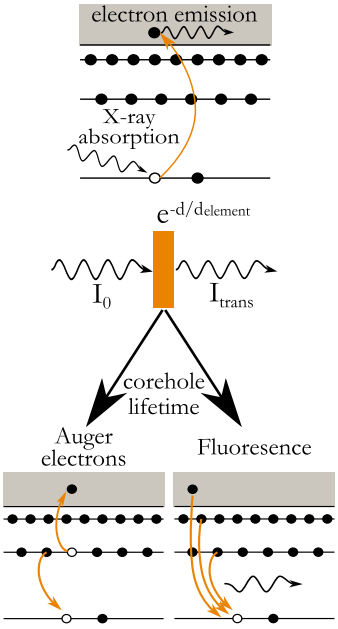

Figure 3.2. *Cartoon with the main processes triggered by X-ray absorption.*

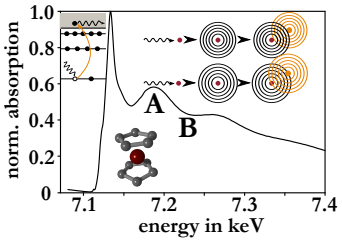

Figure 3.3. *X-ray absorption measurement of a complex based on ferrocene. The oscillatory EXAFS patterns from equation 3.4 can be analyzed to retrieve the Fe-C bondlength. EXAFS offers a local molecular structure probe in a potentially complex or disordered molecular environment.*

3.3 X-ray Absorption fine structure (XAFS) spectroscopy

It is common to differentiate between the X-ray Absorption near edge structure (XANES) and the extended X-ray absorption fine structure (EXAFS). The difference is how much the description of the transition probability (equation 3.3) can rely on semi classical scattering theory. The emitted electron can be scattered from the neighboring atoms and by a process of interference gives rise to modulations in the absorption pattern. In the EXAFS region approximations to single and multiple scattering path can be made and the absorption coefficient $\mu(E)$ can be expressed as $\mu(E) = \mu_0(E)(1 + \chi(E))$. The correction factor $\chi(E)$ is called EXAFS function and can be expressed[168]:

$$\chi(k) = -\sum_j \underbrace{\frac{N_j}{kR_j^2}}_{A} \underbrace{\left|f_j(k)\right|}_{B} \underbrace{e^{-R_j/\lambda_e}}_{C} \underbrace{e^{-2k^2\sigma_j^2}}_{D} \cdot sin(\underbrace{2kR_j}_{E} + \underbrace{2\delta_1}_{F} + \underbrace{arg(f_j(k))}_{G}) \tag{3.4}$$

$$\text{with } k = \sqrt{2m(E - E_0)/\hbar^2}. \tag{3.5}$$

The sum goes over all possible scattering paths j with N_j multiplicity and the electron wave vector k. The prefactor A contains the scaling factor due to the expanding spherical surface at distance R_j of the scatterer and the return path. Terms B and G are the amplitude and phase shift from the atomic scattering factor $f_j(k)$. The variable λ_e in term C is the mean free electron path, and term D is a Debye-Waller factor that describes the average displacement of the scatterers. Term E originates from the wave nature of the emitted electron and can be understood as interference between the arriving and returning wave packet. It gives rise to the oscillatory part in figure 3.3 and F is a phase shift arising from the delocalized nature of the orbital of the emitting atom. For experiments in the EXAFS region the edge jump is normalized, the background subtracted and the modulations of $\chi(k)$ are analyzed. The main information of the EXAFS region is the extraction of interatomic distances. The number and type of ligand atom can be determined, and with improving data quality, multiple scattering paths and can be refined that reveal local structure. Low lying electronic states, the valence of the atom and multiple scattering events contribute to the signal in the XANES region. The analysis often requires complex model calculation and a variety of codes are available to perform such calculation. FEFF, FDMNES, GNXAS, EXCURV and MXAN are some of these codes which are implemented in a number of software packages with fitting routines like IFEFFIT, EXAFSPAK or

Viper[168;180]. A qualitative approach to XANES involving comparison to reference spectra, can often satisfactory answer the basic chemical questions. One interesting example for this method is the following measurement.

3.3.1 Evolution of Ru-Pt and Ru-Pd catalysts upon optical excitation

In the context of photocatalytic splitting of water it was shown that the dinuclear ruthenium-palladium complex $[(tbbpy)_2Ru(tpphz)Pd(Cl)_2]^{2+}$ (RutpphzPd) with tbbpy = 4,4′-di-tert.-butyl-2,2′-bipyridine and tpphz = tetrapyrido[3,2-a:2′3′-c:3″,2″-h:2‴,3‴-j]phenazine) forms hydrogen in the presence of an electron donor and is able to hydrogenate alkynes (see figure 3.4)[186]. Hammarström[187] suggested that a similar ruthenium-palladium complex is destroyed during the reaction cycle and that the colloidal particles that result function as reaction centers for further hydrogen production. Sakai[188] showed that the related complex with platinum is stable during hydrogen formation. A manuscript under preparation[189] will present more experimental and theoretical details of the photophysical and poisoning processes.

The optical spectra show a significant absorption of the (RutpphzPd)[186;190] between 350 nm and 400 nm which is lacking in the (RutpphzPt). The absorption in this area is dominated by n-$\pi*$ and $\pi - \pi*$ transitions which are centered on the (tpphz) ligand and might point to a coupling of electronic states of Pt to the ligand. Any photocatalysis in both RutpphzPd and RutpphzPt follows electron transfer from the light-absorbing Ru-center of the complex to the catalytically active metal species.

This experiment was performed at the XAS beamline at the ANKA Synchrotron Radiation facility. Both catalysts were dissolved in a mixture of acetonitrile, water and triethylamine and were irradiated for different times. Comparison of the absorption spectra with reference spectra in figure 3.5 suggests that RutpphzPd decomposes to colloidal metal upon irradiation like the similar complex. While RutpphzPt is not significantly changed upon irradiation. This suggest a different reaction mechanism for the hydrogen evolution in the two complexes. Monitoring the electron transfer during the metal to ligand charge transfer might illuminate this process. The characteristic timescales for the three stage excitation decay in RutpphzPd are 0.8 ps, 5 ps and 310 ps[190]. The ruthenium L edges, the palladium L edges and the platinum M edges are reachable with the energies present in the plasma source and their spectrum could be accumulated simultaneously for each molecule. The field of biomimetic hydrogen producing compounds is of great scientific interest and some recent reviews can be found in these references[191;192].

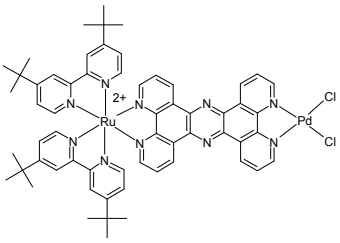

Figure 3.4. *Chemical structure of: $(tbbpy)_2Ru(tpphz)Pd(Cl)_2](PF_6)_2$ The structure of RutpphzPt is similar.*

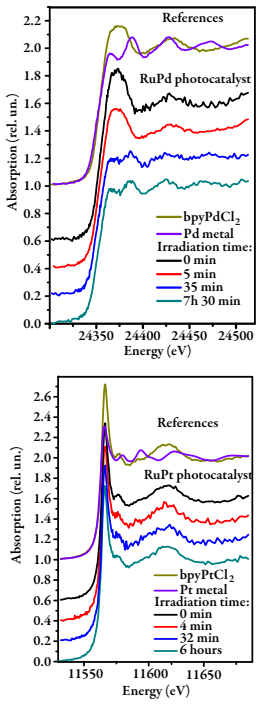

Figure 3.5. *NEXAFS of RutpphzPd and RutpphzPt for different optical irradiation periods. Each compared to reference compounds. The RutpphzPd complex shows decomposition and formation of metal like features.*

3.4 Ultra fast experiments, filters and examples

In recent years a rapidly increasing number of ultrafast X-ray absorption experiments with sub picosecond time-resolution have been performed at the facilities discussed in the previous chapter. A number of reviews have been published describing their similarities and differences[8;9;59;193;194]. This section will discuss the choice of filters for a laser plasma source and the performance of the system in relation to them. The transmitted X-ray intensity is the product of absorption in the solvent A_{solv}, sample A_{sample}, and filters A_{filt}, each with its own crossection $\sigma(k)$ concentration n_i and thickness d. The integrated absorption for each is then according to equation 3.1 $A_i(E) = exp(-n_i\sigma_i(E)d)$. The information we try to extract is the difference $\Delta\sigma(E)$ of the absorption crossection in the sample of excited and ground state molecules. The signal scales with the excited fraction f, the concentration n and the sample thickness d.

Broadband transmission experiments based on direct detecting single photon measuring exploits the natural beam divergence to spatially separate X-ray photons in a given shot, which have different energies. The total number of photons that have to be collected depends on the exclusion from the detector of photons whose energies lies outside the spectral range of interest. This energy range might cover several absorption edges simultaneous (see section 3.3.1). The shot noise in single photon counting is Poisson distributed with width $\sqrt{N_s + N_b}$, with N_s being the signal and N_b the background. The square of the signal to noise ratio is also called number of effective counts:

$$N_{eff} = \frac{N_s}{1 + \frac{N_b}{N_s}} \tag{3.6}$$

The optimal filter solution would be a neutral bandpass filter limiting the transmitted photons to the area of interest. In principle, reflective grating like structures could function like this (see section 4.4.3). In the current experiment available transmission filters were used to reduce the number of photons outside the spectral region of interest. For the high energy range a thin material with a suitable absorption edge and a thick low Z filter using the E^{-3} dependence of the absorption (equation 3.2) for the energy range below the absorption edge.

Two or more low energy photons whose summed intensity results in the area of interest contribute to the background signal. The probability for two simultaneous events within the same laser pulse is reduced by suppressing low energy photons as aggressive as possible and sparse the distribution over a higher repetition rate to avoid this pileup. Indeed all photons outside the range of interest simply reduce the maximum attainable

countrate for useful photons. Bunker[168] derives a formula for the selection of the optimal filter thickness that allows tabulated values to be used for the optimization. He defines a filter quality Q=μ_{sample}/μ_{back} where μ_i is the linear absorption coefficient in the sample or background energy area. A similar approach with a small difference can be taken here. In his formula the fluorescence of the filters is considered a negative effect. For the microcalorimeter it is indeed very useful for energy calibrating of the detector during operation and the placement of the filters can be used to enhance this aspect. A wider selection of filters is therefore also preferable over a single element filter. A computer routine based on the emission characteristic of the source, the rate at which photons can be accepted (see section 4.5.10), the filter materials tabulated data[104;171] and the stopping function of the detector can be used to optimize the filter selection and positioning. Crosstalk between pixels at higher count rates and enhancing the prominence of certain features for detector corrections (see section 4.5.13) have to be considered.

The present state of the system and the path for future development can be best illustrated by an example. This example calculates the measurement times for the two spin states of iron-tris(bipyridine)Cl_2 dissolved in water using tabulated values[104] and loosely following the calculations of Gawelda[195]. From the total absorption in the aqueous complex at 7.2 keV, every 545 th X-ray photon in a 1 mM solution and every 23 rd X-ray photon in a 25 mM solution is absorbed by the iron atom. Assuming a 300 µm thick sample jet, the total absorption I/I_0 is ≈ 0.36 for both solutions. The fine structure modulation χ is ≈ 0.55 and the maximum change in X-ray absorbance at full excitation $\Delta\chi$ is ≈ 0.12 normalized to the edge jump[195]. Using 1 mJ/pulse of 800 nm excitation in BBO ≈ 200 µJ of 400 nm can be generated for the excitation of the sample. Focused on 300 µm the fluence is 0.28 Jcm^{-2}. With 3.1 eV per photon $\approx 6 \times 10^{14}$ photons are available for the excitation of $\approx 1 \times 10^{13}$ molecules in a solution with 1 mM concentration and 3×10^{14} molecules in a solution with 25 mM concentration. Using the optical cross sections given by Gawelda[195] ≈ 50 % of the molecules would be excited in 1 mM and 22 % of the molecules in 25 mM. The maximum signal is therefore 2.6 % of the edge jump and the background absorption 545:1 in the 1 mM solution and 23:1 in the 25 mM solution. N_{eff} of equation 3.6 is therefore 4.7×10^{-5} and 1.1×10^{-3}. The minimum number of measured photons necessary to reach N/N_{eff}=1 is 4.5×10^8 photons/bin and 8×10^5 photons/bin respectively.

The microcalorimeter offers at the moment ≈ 3 eV energy resolution. Assuming a mild over sampling with 1 eV bin sizes in a 1 keV wide range, a total of 1000 bins would have to be filled. By using simple absorption filters 1/5 of the recorded

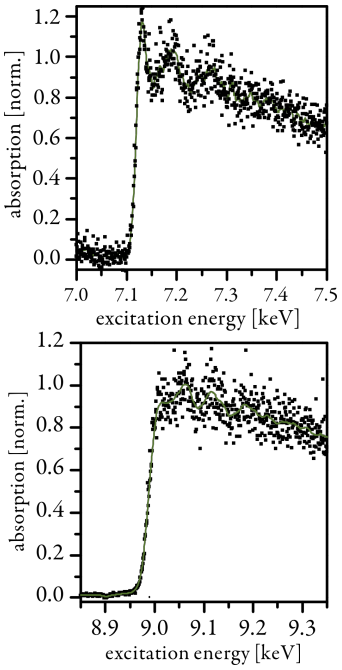

Figure 3.6. *Transmission absorption fine structure spectrum of ferrocene. The transmission data was binned to 0.5 eV bins and a 20 points floating average added to guide the eye. As background for the normalization on the edge jump the smooth free atom fit discussed in the text and paper* **V** *was used. Both, the iron K-edge of the ferrocene sample (right frame) and the copper K-edge of the filter material show fine structure modulations and suggest the possibility for simultaneous observation of multiple absorbers in a wide range.*

photons lay within the 1 keV area of interest. This rough estimate suggests that for each of the 5000 bins 0.45×10^9 photons would have to be collected and with the consideration from above a total of 2×10^{12} photons for a 1 mM solution and 4×10^9 photons for 25 mM to reach a signal to noise of one. A more aggressive clipping of the spectrum would be the the most immediate practical approach to enhancing the experiment but could not improve matters by more than a factor of 5.

The following numbers are explained in chapter 4 but they offer a perspective on further short term developments. The detector has a optimum countrate of ~ 1 kHz at the moment. When the array is fully built it will offer ~ 4 kHz with the same record length (shaping time, time needed to measure one photons with the optimum energy resolution). A new room temperature component in the system that is currently tested at NIST and improvements of the temperature modeling in the pixel could allow for higher fluxes in each pixel that would improve the countrate by a factor of 2-4 without changing the detector setup. However, the detector development is a rapidly developing field as will be discussed in chapter 4 (see especially figure 4.11) and the straight forward scalability of this approach suggest interesting future possibilities beyond the capabilities of this prototype. Instabilities in the laser system together with the expected record times for this prototype prevented us from recording pump-probe spectra at this stage of development. But the following section shows some promising first results, that are the basis for paper **V**, which is still in preparation.

3.5 First results

The combination of source and detector has to date recorded a number of absorption spectra in transmission mode. The very first spectrum was of ferrocene powder and will be briefly presented here. Several other spectra including a spectrum of a free running jet with a 300 mmol iron-tris(bipyridine)Cl_2 solution in water and cobalt compounds were recorded. The ferrocene dataset with a total of $\approx 15 \times 10^6$ recorded events is the smallest of these data sets and was used to develop a semi automated code to analyze the recorded data. It was the "first light" for this source-detector combination. The steps necessary to extract the correct energy of every recorded pulse are discussed in section 4.5.13. The automated code and data extraction is still work in progress but is essential for analyzing large data sets.

This steady state experiment used a thin layer of powdered ferrocene between two layers of "Kapton" foil. The materials in the ~ 30 cm between the source and the detector array consisted of powdered ferrocene with approximately one absorption

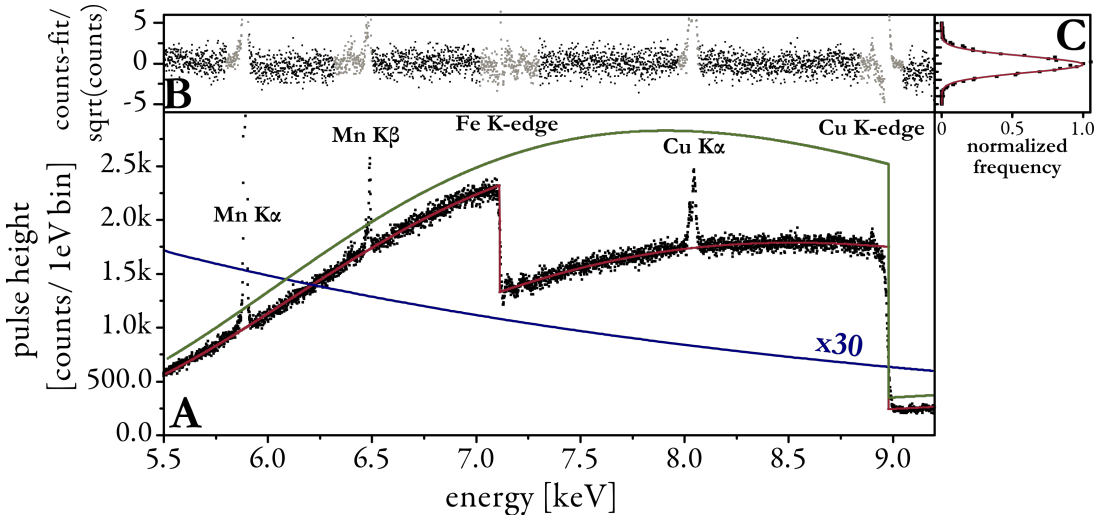

Figure 3.7. *A) Laser plasma absorption spectrum in transmission mode of ferrocene. Including emission lines and absorption edges of metal filters and calibration sources (see text), B) baseline fit base on emitted spectrum and reference data of all involved materials. Areas of emission lines and fine structure modulation were excluded (grey). C) A histogram normalized to the poisson error of the total number of counts. A Gaussian curve with σ=1 is superimposed. The red line is a fit based on free atom reference data on the baseline of the spectrum. The green line is the same fit without the ferrocene absorption and is used as I_0 in the analysis. The blue line is the fitted emission of the plasma source. (see text)*

length thickness, 50 µm "Kapton", 136 µm beryllium, ∼ 36 µm aluminium, ∼ 20 cm air and ∼ 6 µm copper. The filters and the sample were placed approximately half way between source and detector. The spectrum was accumulated using the 22 pixels available at the time, and with an approximate total countrate of 330 Hz. More experimental details can be found in paper **V**.

The recorded absorption spectrum is shown in figure 3.7 A. The absorption coefficients for the transmitted materials were retrieved from available sources[104]. The data set was fitted with these coefficients (assuming atoms) and under the assumptions that the source emission that can be modeled with a single electron temperature following an exponential emission characteristics (see paper **I**). The only variables in this fit were the total flux of the source and its effective temperature (blue line), the thickness of the transmitted filter materials, the thickness of the bismuth absorber and the ferrocene thickness. The residuals are plotted in figure 3.7 B. The grey areas were excluded from the fit due to sharp and known features in, or superimposed on, the absorption spectrum. The optimized fit free atom (red curve) shows excellent agreement between the measured spectrum the one one expected from the reference data. The histogram of the residuals was normalized by the expected Poisson error for the number of

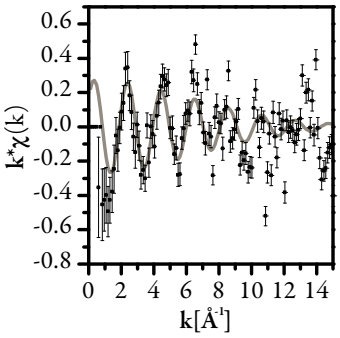

Figure 3.8. *Extracted fine structure modulation from the iron K-edge presented in figure 3.6. The data was binned in quadratically scaled energy bins and the free atom fit (see text) was chosen as background function. Without further data treatment a single path length EXAFS pattern after equation 3.4 was fitted on the data.*[198]

recorded events. Figure 3.7 C shows this normalized histogram overlayed with a Gaussian distribution function with σ=1. Their very close agreement indicates that shot noise is the dominant noise contribution in this measurement. From this measurement the region of the iron and the copper K-edge are presented in figure 3.6. The fine structure modulations are apparent. The two edges and their XAFS features visible in figure 3.6 in fact represent well known standards[168;196;197] and could have been used to extract structural information. Figure 3.8 shows the extraction of the χ(k) function from this dataset. From the modulation it is possible to determine the Fe-C bondlength (see equation 3.4). As new and better data is obtained from more interesting compounds, and in pump-probe experiments, the measurement technique developed in this thesis is likely to become a powerful tool in chemistry.

Chapter 4

X-ray Detection

In this chapter the physics behind X-ray detection will be introduced with the focus on energy resolving detectors in the first part. The second part presents and discusses the detection schemes developed for lab-based direct detection X-ray absorption spectroscopy.

4.1 Introduction

The main difference between detectors built for photons in the visible range and the hard X-ray range is the energy carried by a single photon and combined with this the cross section for interactions. Especially in time resolved measurements the number of available photons is also rather small, so that every measured photon has a relatively large statistical significance. A large variety of interactions can be used to detect hard X-rays. Beside the possibility to disperse the energy of photons spatially before or after the interaction, some material excitations have suitable symptoms to serve as the basis of X-ray detection. This is because X-ray photon energies are much larger than most familiar electronic, translational and rotational transition energies in chemistry. Thus, in the course of thermalization by a cascade of different pathways, many different material and electronic excitations, with various longevity, can be produced by a single X-ray photon. The precision that can be obtained depends on the elimination of mechanistic channels that lead to energy trapping in high energy metastable states (which are the basis of many conventional X-ray detectors). Equally important, the precision depends on the energy of the final excitations being as small as possible. Together, these two considerations motivate ultracryogenic micro-calorimeter arrays.

4.2 Overview of X-ray detection schemes

Fluorescent screens and photographic film were the first detectors used by Becquerel and Röngten. In these, and the much later image plate technology, the X-ray photon energy either drives a chemical reaction or leads to emission of an optical photon during the decay. These are still popular choices for large area detectors[199–202]. However they use only a very small fraction of the photon energy ($3 - 10\,\%$) and their intrinsic energy resolution is poor compared to other techniques discussed below. Semiconductor, photocathode or gas based detectors are also based on the ionizing abilities of hard X-rays. Photons generate a charge cloud that is electrically read with or without prior amplification. Applied strong electric fields can transfer enough energy to the generated electrons that an avalanche kind of amplification can occur within the detection volume e.g. in Geiger tubes and spark chambers. A controlled electron multiplication after the same mechanism occurs in photomultiplier tubes and multichannel plates, avalanche photodiodes and electron multiplying charge coupled devices. The charge cloud and ionized molecules can act as condensation points in supersaturated environments like cloud chambers. Some techniques measure directly the energy of a generated photoelectron with different techniques like time of flight for soft X-rays, or by using the Cherenkov effect in the range of several MeV. X-ray streak cameras decode the time structure of the arriving photons into a spatial coordinate. The generated electron cloud is then manipulated with a changing strong electric field.

The very stable flux generated during most steady state experiments allows the use of integrating detectors in monochromatic experiments. The low repetition rates and large fluctuations present in most ultrafast time resolved experiments often require either the resolution of every single experiment (shot) and/or the recording of the whole spectral range simultaneously, depending on how stable the spectral distribution is.

Two different types of detector types which were used in the presented experiments shall be discussed further. The first are semiconductor detectors, whose detection principle is based on the generation of a charge cloud in a zone with no free charge carriers. The second are cryogenic single photon counting detectors (section 4.5). Both can be constructed as arrays that provide a very efficient photon energy to signal conversion at low noise levels, with the convenience of electronic data collection and management. In them, individual pixels can determine single X-ray photons with less or more energy resolving ability. And the array size is scalable.

4.3 Excitation cloud generation and energy resolution limit

As discussed in chapter 3 the main absorption mechanisms for photons between 1 keV and 15 keV is photo ionization. The Compton cross section also becomes important as the energy increases. In silicon it becomes dominant above $\approx 60\,\mathrm{keV}$ [171], with the changeover moving to higher energies for higher-Z elements. With photoionization being the dominant interaction mechanism, the initial result of both mechanisms is the partial or complete energy transfer from the photon to one electron. This electron can have energy up to the initial X-ray photon energy, and/or leaves a highly excited ion. The ionized atom can generate further charge carriers via Auger or shake up processes if the electron was absorbed in deeper bound levels. The highly energetic electrons distribute their energy in several steps. The initial interactions are collisions with nuclei and (primarily) electrons, during which additional, lower energy electrons and some new, lower energy photons (bremsstrahlung) are generated [171;203;204] (see also figure 2.14).

In metallic systems the free charge carriers absorb the energy and couple it efficiently to the lattice, which results in a fast thermalization of the excitation. In superconductors the barrier for free charge generation is the Cooper pair binding energy on the order of several meV (see equation 4.10 and 4.5.3). The principle energy breakdown process is similar to semiconducting/insulating materials that have a larger bandgap. The main energy loss mechanism for electrons with energies close to the bandgap is electron - hole generation. For silicon at room temperature this process substantially accounts for photoelectrons with energy greater than the bandgap ($\approx 1.2\,\mathrm{eV}$) and up to $\approx 10\,\mathrm{eV}$ [205–208]. Electrons with less energy excite primarily optical and acoustical phonons and in this way couple their energy to the lattice. Especially for superconducting absorbers the coupling processes and energy down conversion is under active discussion [209–213].

Non-equilibrium detectors (e.g. charge coupled devices, photodiodes or superconducting tunnel junctions) rely on generated excitations whose number fluctuate for a fixed X-ray photon energy [214]. Phonons can also be generated during each ionization step in the cascade described above. At the end of the cascade the electrons have a thermally distributed energy below the X-ray photon energy and have a energy above the energy gap (roughly 1700 ionizations are generated for a single photon with 6 keV in silicon). Van Roosbroeck compared this randomized distribution to a simple model called crazy carpentry [215]. The total number of generated excitations is much smaller than is expected from the

Numerical example: *Non equilibrium detectors rely on on the fact that the thermal excitations are small compared to the signal. The thermal energy is with the Boltzmann constant* $k_B T \approx 26\,meV$ *for* 300 K. *To reach a energy resolution of* 2 eV *for* 6 keV *photons the gap energy would have to be* $(E_{SI}/E_{gap})^{1/2} \approx 65$ *and therefore* $E_{gap} \approx 0.3\,meV$. *Assuming the condition* $E_{gap} > 10 \cdot k_B T$ *the temperature of the device would have to be* $T < 3.5K$, *at a still significant dark current.*

excitation energy $N_{excitations} < E_{photon}/E_{Gap}$, which would apply if jumping the gap was the only channel for the redistribution of the X-ray photons energy.

The minimum energetic fraction needed to generate a single excitation is dependent on:

- the materials gap energy and type of excitation[208]
- the temperature, since it varies the gap energy and electron-phonon interactions[216]
- the initial photon energy since it plays a role for the initial cross-sections and nonlinear effects due to high electron densities[216;217]
- the kind of device, since some devices use high electric fields to extract the charge carriers which raises the device dependent possibility of avalanche gain processes.[217;218]

If one assumes a Poisson distribution of the total number of generated electrons, and tries to measure the energy of a single absorbed photon by counting the N excitations generated for every energetic fraction ϵ, we would expect:

$$\langle \Delta E_{measured} \rangle = \epsilon \sqrt{N} = \sqrt{\epsilon E_{photon}} \tag{4.1}$$

Fano showed, that if the ionization events along the cascade could be treated as independent events, then fluctuation in the total number of charges partially average out. With the so called Fano-factor[214] $F < 1$ the fluctuations are smaller than a pure Poisson distribution would predict[219]:

$$\langle \Delta E_{measured} \rangle = \sqrt{F\,\epsilon E_{photon}} \tag{4.2}$$

The Fano-factor and the energy fraction ϵ for the generation of one excitation can be simulated or measured. For a cooled silicon detector and 6 keV photons they are $F \approx 0.1$ and $\epsilon \approx 3.6\,\text{eV/electron}$[208;216;217]. Neglecting other loss or gain processes in the device. The fundamental resolution limit for silicon, which is often called Fano-limit, with these values would be:

$$\langle \Delta E^{silicon}_{measured} \rangle = \sqrt{F\,\epsilon\,6\,keV} < \sqrt{E_{Gap} 6\,keV} < \sqrt{\epsilon\,6\,keV} \tag{4.3}$$

and assuming a Gaussian distribution

$$\Delta E_{FWHM} \approx 2.355 \cdot \langle \Delta E^{silicon}_{measured} \rangle \approx 109\,eV \text{ and}$$
$$N_{excitations} \approx 1666 \text{ e-h pairs}$$

From equation 4.2 it is obvious that the energy resolution improves with smaller ϵ.

4.4 Semiconductor detectors

There are a large variety of semiconductors actively used for X-ray detection. The absorption length of silicon (figure 4.1) for photons above 5 keV is larger then the depletion length of most depleted areas in p-n junctions, so many X-ray detectors use scintillator screens to stop the X-rays and convert them to visible wavelength. The conversion and optical capture efficiency are poor and effectively scramble the observable energy of the original X-ray photon. However, the X-ray stopping efficiency of the scintillator can be made almost 100 %. Devices with several hundred micrometer thick depleted areas have become available since. These direct detection devices alleviate the need for the separate scintillator (except at high X-ray energies), and the X-ray energy scrambling problem that it causes.

Common to most types of detectors is that the generated electron-hole cloud is separated by an applied or internal electric field and guided into a charge sensitive preamplifier where it is quantitatively amplified an ultimately digitized. In some cases an electric field chosen to transfer sufficient energy to the generated excitations to further ionize and generate an intrinsic gain by an avalanche process. Since this statistical process is often non-linear it amplifies existing noise and degrades the intrinsic energy resolution. It is however preferred for low energetic photons and when the application aims at speed and counting the number of photons but not resolving their energy[220]. Devices using this effect are e.g. electron multiplying charge coupled devices (EMCCD)[221], or avalanche photodiodes (APD)[222]. Drift diodes offer excellent single photon resolution and have been built as multi element devices with resolutions close to the Fano limitation presented above[223]. When operated as drift diodes they can accept only one photon per element and pulse. In a different mode of operation they work as fully depleted charge coupled devices described below. The stopping power of common semiconductor materials requires thick depleted areas from which the charges can be collected. A variety of materials have found use in single pixel detectors[224;225]. The majority of large scale semiconductor area detectors, however, are based on doped silicon.

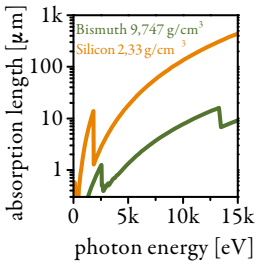

Figure 4.1. *X-ray absorption length for silicon and bismuth.*[104]

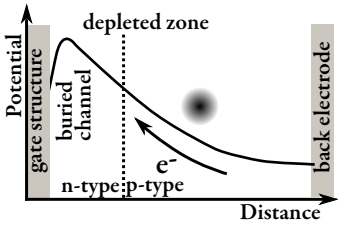

Figure 4.2. *Schematic electric potential in the depleted zone of a PN-CCD. With buried transfer channel, symbolized gate structures and transport direction.*

4.4.1 Charge coupled devices (CCD)

X-ray energy resolution can be achieved with spatially dispersed Bragg diffraction (see section 4.4.3). The narrow band pass condition of the Bragg reflection however makes inefficient use of broadband radiation and experiments are time consuming. The use of the intrinsic energy resolution in direct detection devices improves the quantum efficiency dramatically. Charge coupled

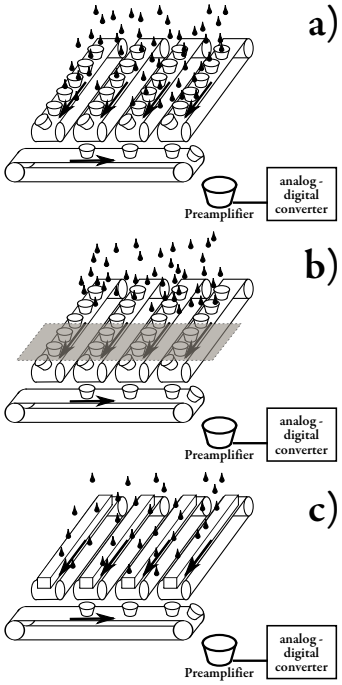

Figure 4.3. *Conveyor belt analogy*[226] *for the different modes of operation. a: in the standard operation mode the charges are shifted on row at a time with the vertical shift speed into the transfer channel and read out through a pre-amplified analog-digital converter. b: fast kinetic or frame transfer readout mode uses part of the CCD as physical information storage. c: fully vertically binned mode, a whole vertical column is coupled as a single pixel.*

devices (CCD) have found widespread use in the scientific community and are frequently used for a large number of different purposes. The high demands for low defect densities and challenges concerning scalability and price has led to a silicon dominated technology. To obtain sufficient stopping power in the active area the dopant densities are arranged to extend the device depth that is totally depleted from charge carriers to several tens of microns[227](indeed scientific fully depleted devices with several hundred micron depletion depth have been produced[228]). Excitations generated in this area are separated and the electrons are transferred into a buried transport channel (figure 4.2). The buried channel close to the gate structure is generated by selective doping. It collects the charges and keeps them physically separate from surface imperfections, where recombination and trapping can occur.

The potential in the three or four step gate structure on one surface is sequentially reduced and raised to transport the cloud charge into the next pixel[219;229]. From the variety of readout modes three are particulary useful in the context of pulsed plasma sources and shall be discussed a little bit further. During a full frame readout the pixels are shifted one row at a time with the vertical shift speed into the horizontal shift register (figure 4.3a). This register is read pixel by pixel with the horizontal clocking frequency through a charge sensitive preamplifier and an analog to digital converter. The typical full frame readout frequencies are on the order of a few Hertz depending on the array size and choice of clocking speed. Higher speeds reduce the separating voltages and lead to additional noise sources and potential loss of electrons due to recharging effects[219;230]. The fast kinetic (or frame transfer) mode (figure 4.3b) uses a part of the CCD *hidden* behind a sufficiently thick block as physical storage. A reduced number of rows can be shifted very quickly behind a blocking layer, since nothing is read during the transfer time. The stored frames are read afterwards in the normal way. In this mode the camera can be operated at the repetition rate of the laser without the use of a shutter. A full frame is accumulated over several shots. All or part of the array can be hardware binned to columns and read out with kHz repetition rate to give a realtime feedback of moderate to fast repetition rate pulsed sources (figure 4.3c).

In front illuminated CCD the photons have to penetrate the thin gate structures. If the charge cloud is generated close to the gate structure it directly feels the strong confining electric field. Our commercially available CCD has a fully depleted depth of $\approx 40\,\mu m$[231] (in silicon the absorption length is $\approx 30\,\mu m$ at 6 keV) and can contain a maximum of 2.5×10^5 electrons/pixel[227], which corresponds to ≈ 150 photons of 6 keV. This number is important if the device is operated in the fully vertical binned

mode, or while measuring energetic particles like the electron beams discussed in paper **IV**. These kind of chips are usually not fully depleted and have areas with no confining field deeper in the structure. Back illuminated, back thinned chips have a weaker confining field close to the back electrode and charges can more easily spread in this region. Special fully depleted chips with low conductance are available but are not usually included in commercial cameras[219;228;231–234]. Paper **II** discusses various effects and consequences if the initial charge cloud distribution spreads over the borders of a single pixel or at different depth in the CCD and how such a device can be used to analyze laser plasma sources[152]. It was possible to evaluate the charge cloud radius as function of the X-ray photon energy by suitable analysis. At very low exposures which guarantee sparse enough event densities to separate each single absorption event spatially, CCDs have frequently been used as multi element single photon counters[50;152;235].

In figure 4.4 the emission of a ^{55}Fe source (see section 4.5.12) was recorded on a $256 \times 1\,024$ pixel, 40 µm deep depleted front illuminated CCD[227] cooled to −65 °C. 10000 frames with each ≈ 900 absorption events were recorded and analyzed. All pixels below a chosen threshold were set to zero and events spread over more then 2 pixels discarded. Figure 4.4 a shows the pulse height spectrum separated into absorption events contained within a single pixel and spread over two pixels. The deconvolution for single pixel events gave an energy resolution of 150 eV for 2.5 MHz pixel readout. If the readout is slowed down the optimal resolution is 138 eV. From charge clouds spread over two pixels spectral information can still be extracted. They need a separate background treatment (not applied in this figure) and with this correction broadened the observed spectral line by 40 eV. The threshold has to be chosen with care and optimized for every set of shift speed, exposure time, gain settings, chip temperature and total recorded flux. A threshold below the actual noise level rejects a large number of pulses and leads to poor counting statistics (figure 4.4 b). A high threshold neglects the spectral redistribution (figure 4.4 c). High level programming languages like Matlab, Pylab and Labview, which are often used to automate such analysis, are especially efficient and fast if their optimized matrix subroutines are used for such data analysis. In the appendix B a simple matrix algorithm, which was developed to reduce the processing time of such an analysis, is explained.

Figure 4.5 presents a single shot spectrum from a collimated X-ray beam generated by electron oscillations in a laser wakefield accelerator. The experiment was performed at the high power branch of the multi Tera-watt laser of the Lund Laser Centre and is described in references[50;91]. The CCD was used to optimize and study the X-ray emission in more detail. For this measure-

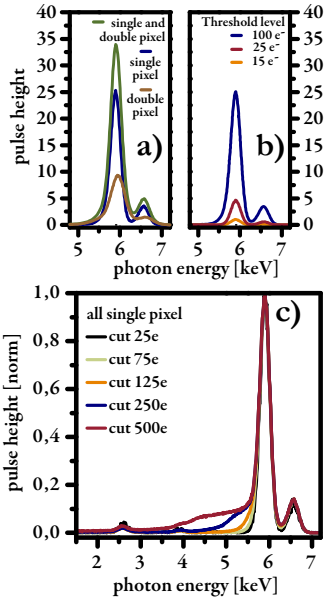

Figure 4.4. *Pulse height spectrum of ^{55}Fe line emission. a: after a threshold of 100 electrons was applied, events were sorted into event located in a single pixel and events spread over two pixels b: suppression of events for to low threshold c: at a high threshold the spectral redistribution is not sufficiently suppressed*

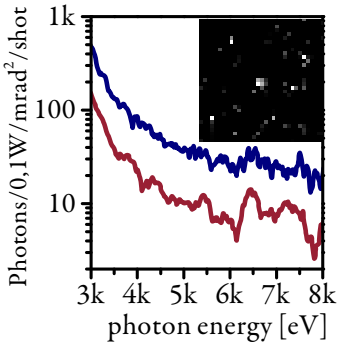

Figure 4.5. *Histogram of a single shot from a collimated X-ray beam generated by electron oscillations in a laser wakefield accelerator. The red line shows absorption events spread over a single pixel, the blue line a histogram of all exposed pixels.*

ment two 15 µm thick nickel sieves with 5×5 µm openings were aligned and placed in front of the camera. The 25 µm pitch of the sieve matches the camera pitch. Even with this reduced intensity a larger than expected fraction of neighboring pixels show excitations above the chosen threshold level. The histogram is corrected for additional absorption in filter materials and the thickness of the active silicon.

In complementary metal oxide semiconductor (CMOS) detectors every pixel drives a small individual processing circuit. A parallel bus system enables the read-out of every single pixel separately[229;230;236;237]. Hybrid sensors like the commercially available Pilatus[238] are built to offer the possibility to gate pixels to bunches of high repetition rate sources[239]. An intrinsic threshold can be set to suppress readout noise. They are used as spatial detectors in scattering experiments or as detectors for Bragg type analyzers (see also section 4.4.3)[240]. A very interesting recent development in back illuminated back thinned CMOS with depleted zones of several microns, readout noise and very fast readout speeds shall be mentioned[241;242]. The device has 10.8 µm$\times$10.8 µm pixels with selectable areas readout and up to 2400 Hz readout for 1 28 $\times$ 128 pixels. The depletion thickness is 1.5 µm and the expected resolution for 10 ms exposure and at this readout speed is 250 eV.

For many specialized applications hybrid detectors based on CMOS or depleted P-channel field effect transistors (DEPFET) readout and other principles like avalanche photo detection are under development and it will be interesting to follow this rapidly growing field. I had the privilege to work with the XPAD (hybrid CMOS photon counting)[243–245] at the linear accelerator in Stanford recording pump-probe liquid scattering. The high repetition rate and numbers of pixels will bring future challenges for on-line data processing. A small selection of other actual projects in this field: MEDIPIX (hybrid CMOS photon counting)[246], AGIPD (hybrid CMOS integrating)[247;248], ASCI (APD-array)[249], ATLAS (hybrid CMOS Photon counting)[250]. A recent summary was give in the resumé[251] to the PIXEL conference in 2010.

4.4.2 Application of CCDs in the laser-plasma setup

Figure 4.6 shows several ways that a CCD can be used with a laser plasma source, which have been applied at different times in this work. A more detailed description can be found in paper **II**. The main adjustment and feedback detector in the laser-plasma setup that was built during this work is an X-ray CCD camera in an Andor-Newton housing. The front illuminated deep depletion 30-11 CCD from the company e2v[227] is mounted on a -60 °C cold stage in an argon environment. The camera is operated either

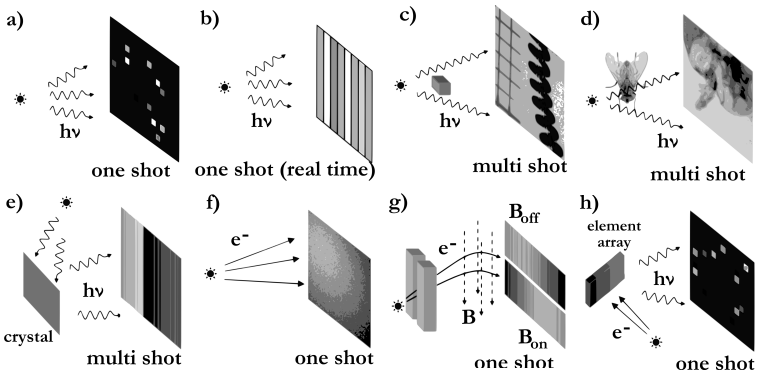

Figure 4.6. *Frequent modes of CCD use: a) a parallel array of energy-dispersive point detectors for determination of source spectra; b) aggressive hardware binning allows realtime optimization; c) shadow edge from high contrast objects for source size determination; d) contrast imaging of suitable samples; e) crystal dispersed spectral X-ray measurements; f) direct observation of high energy electron beams; g) particle charge and energy measurements by deflection; h) indirect measurement of particle beams by observation of induced X-ray fluorescence from element arrays.*[252]

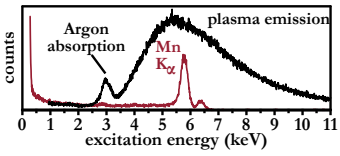

Figure 4.7. *Spectra taken of the water jet laser plasma source at* 3 mJ *pulse energy (black) also* ^{55}Fe *emission spectrum (wine). The smooth plasma spectrum is shaped by the strong absorption from* 250 µm *Beryllium,* 5 mm *Argon,* 30 cm *air, as well as by its absorption in the silicon of the CCD.*

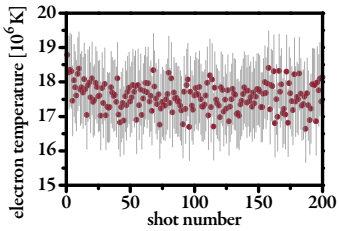

Figure 4.8. *The electron temperature was retrieved from the emitted spectrum for 200 consecutive shots. The grey background shows the* 95 % *confidence level of the temperature fit. The shot to shot variation shown here are clearly dominated by the uncertainty within the single shot measurement. The stability of the total flux and and accumulated spectra suggest a more stable emission. However, the tracking of the spectrum does reveal alignment problems and the appearance of high energetic electron beams.*

synchronously to the laser pulses for single shot operation, or in a free running internal triggered mode for multiple shot exposures. Figure 4.7 shows the emission histogram of our plasma source "as measured". The spectral redistribution and features from the protecting gas clearly show the need to apply the corrective calculations discussed above but also the smooth emission of our plasma source in the full spectral range. The black spectrum was generated from 200 single shots with an average of 900 absorbed events and 30 cm of air between camera and source. A detailed analysis and discussion the plasma source and the electron beams measured are presented in the papers **I**,**II** and **IV**.

4.4.3 Bragg optics

In this section we discuss briefly optical elements based on Bragg reflection which are used in the context of ultrafast spectroscopy. Probing the crystalline structures with X-rays has a long history[253] and only a few basic relations shall be mentioned. The momentum $\mathbf{Q}$ transferred from a elastically scattered quantum may be written $\mathbf{Q} = \mathbf{k} - \mathbf{k}'$. If this momentum transfer corresponds to a vector of the reciprocal lattice $\mathbf{G}$ the scattered light will interfere constructively[159]. The formulation of the Laue condition $\mathbf{Q} = \mathbf{G}$ is shown in figure 4.9 and is equivalent to the Bragg condition for crystalline layers $n\lambda = 2d\,sin(\Theta)$. The acceptance angle for each reflex was stated in section 2.5.7. The very

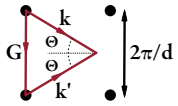

Figure 4.9. *Laue condition for constructive interference. The dots represent points in the reciprocal lattice.*

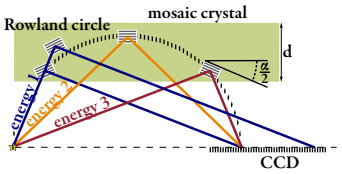

Figure 4.10. *A thick polycrystalline layer with small angular distribution of the crystallites reflects.*

narrow bandpass nature of Bragg reflections makes experiment with flat analyzing crystals inefficient. The use of bent periodic structures increase the volume of the sampled Ewald sphere and is a standard technique used today. The stress introduced in bent single crystals limits the achievable bending radius to the order of meter. Many X-ray plasma sources emit pseudo isotropically in the full 4π solid angle. The solid angle which can be collected from single crystalline devices is therefore very limited if no further optical elements are used [169;254](see also section 2.5.6). Optics with polycrystalline or multilayered optics can be deposited on templates suited to the experiment and these collect larger solid angles. A spherically bent Johann type spectrometer uses a larger part of the Ewald sphere and focus photons emitted from a point source onto a point like detector. Each set of bent crystals are scanned in a small range to analyze the energy. High resolution X-ray emission spectrometers are often based on this concept [178;240;255]. Cylindrical [256;257], conical [258;259] and toroidal [260–262] bent analyzer crystals focus a broad bandwidth source onto a line focus. They can be used for a wider energy range and have been tested in laser plasma sources. The line focus allows the use of a linear or low dimensional detector array with higher readout speed for recording the whole spectrum at once. A useful overview of the energy resolution and efficiency achievable with Johann type of analyzer optics can be found in references [160;263].

Poly-crystalline structures with low mosaicity have been proposed to increase the scattering efficiency [257]. Photons penetrate the small differently oriented crystallites until the Bragg condition is met or it is finally absorbed (figure 4.10). If the angular distribution (rocking curve, indicated in figure 4.10 by α) is slightly larger than the acceptance angle of each crystallite an increased diffraction can be observed under some condition. This is called mosaic focusing. The crystallite size and material has to be chosen so that the efficiency for reflection is much larger than for absorption in same crystallite and the angular distribution is just wide enough that a larger part of the Rowland circle contributes to the intensity [264]. The energy resolution is reduced compared to a single crystallite of the same material and thickness since several wavelengths are reflected into the same point in the detection plane. The spread of the energy can be estimated by simple geometric considerations [264]. Legall reached $E/\Delta E$ of 1800 for the (002) reflection and 2900 for the (004) reflection of a thin film of highly oriented pyrolytic graphite [265]. The surface and structural quality is essential for a high energy resolution.

Multilayered or grating optical elements could however be used as wide bandpass filters in the laser plasma source [160;266]. In the soft X-ray region periodic structures for the energy analysis can be artificially constructed [126;267–269]. Structured optics for the

interatomic wavelengths in the $5 - 10$ keV energy range are very challenging for the precision needed in their construction[270] at the same time that their cross section for interaction with very small structures becomes low.

4.5 Cryogenic photon detection

Chapter 3 motivated energy resolutions of $\Delta E \leq\sim 5\,eV$ for time resolved X-ray absorption studies. This resolution needs to be accomplished for photon energies in the $\sim 5 - 10$ keV range. As presented in the numerical example below figure 4.15, cryogenic detectors with resolutions meeting and exceeding these criteria are becoming available. A core part of this thesis work was the development of a microcalorimeter detector in collaboration with the Quantum Device group at the National Institute of Standard and Technology in Boulder Colorado (USA). It was based on a design of Ullom[271], for use in an electronically noisy lab environment. Personal contributions included discussions and planning of the detector design, coordination of the construction, building parts of the detector and peripherical components, system assembly in Boulder and Lund, testing and installation of the electronics in Lund and development of the calibration, readout and measurement procedures in cooperation with the group in Boulder. In addition contributions were made to the development of the pulse analysis, supervision and guidance of a thesis study to develop a parallelized pulse analysis and development of major parts of the controlling software and routines in Lund.

In this section the physics of cryogenic detectors are introduced. The system construction is presented and the features and challenges of these detectors are discussed. The section closes with a description of the analysis and corrections of the recorded data that was necessary to extract the spectra presented in paper **V**.

Several other types of cryogenic detectors using the thermal energy of the particle shower or charge cloud generated by the high energy photon will be mentioned in the next sections. The focus will be on the calorimetric photon detection. A short introduction to the physics of superconductivity and its role for this detector will also be given. As with the single particle CCD detectors described earlier the essential performance criteria are:

spectrum accumulation time For detectors based on pixels, the relevant attributes are how many pixels they have, how fast is each and whether they are read synchronously or each individually. Also, how good is the multi event suppression and how critical is this. Spectral filtering at the experiment level has of course a positive influence. One important factor here is the dead time. Detector dead time may come

after each event or only after events of a certain kind (see section 4.5.6). At the time of writing the maximum count-rate in our detector array reaches ≈ 1000 counts/s. With successive upgrades planned and with ongoing developments, this will increase dramatically. During the "Low temperature detector conference" 2011 the numbers of pixels per device was presented to follow a "Moores law"[272] (see figure 4.11). Devices with capabilities above 10^5 photons/second at slightly lower energy resolution at 6 keV are being developed[273]. As a comparison, the single channel readout of commercial scientific charge coupled devices with deep depleted chips offer up to $\approx 5 \times 10^6$ pixel/sec. In either case, data processing may become the eventual bottleneck if every pixel is analyzed.

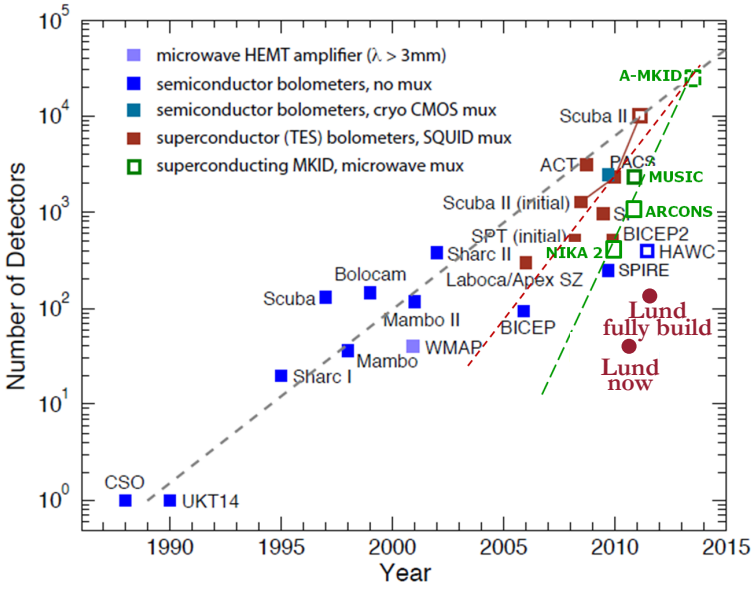

Figure 4.11. *Development of the number of detectors as function of time. The abbreviations in the plot are instrument names. HEMT - High electron mobility transistor, MKID - multiple kinetic inductance detector, mux - multiplexing, SQUID superconducting quantum interference device, TES - transition edge sensor.*[274]

energy resolution Until the shaping time (build-up and decay of a signal) becomes less than the laser repetition interval, there is a trade off for the data acquisition speed. Longer readout per pixel increases the energy resolution performance but reduces the maximum readout speed[275]. The achievable energy resolution is often not only determined by the machine resolution itself but also by the computation afterwards. The estimated (see section 3.4) 2×10^{12} recorded events for realistic samples have to be corrected for additional fluctuations in the measurement conditions introduced in the detectors. Often spectra are combined from many different detectors with different calibrations.

Optimizing the automation and improving the computational data treatment was one major improvement achieved towards the end of this project.

flux and fill factor, partial registry Since single photon counting can only process a certain rate of counts the total source flux and detector fill factor are only of importance for later improvements involving increasingly accurate measurements. For the transmission based experiments pioneered in this work, more flux from a source only means a larger fraction of X-ray photons would be "wasted", since the bottleneck for the data collection is the detector. Finding more effective experiment-level approaches to X-ray filtering can very usefully reduce the number of photons not contributing to the spectrum. The demands on detectors built for the International X-ray Observatory[276] aim to reach fill factors close to 100 % with mushroom shaped absorbers for a similar energy range[277]. The fill factor during the experiment presented in paper **V** was 2 %. As more pixels are commissioned the fill factor of the existing detector is increasing. Once this array is fully constructed it will offer a 20 % fill factor. Considering also the ≈ 50 % quantum efficiency of the absorber at 6 keV, this might be considered as ≈ 10 % detection quantum efficiency for the solid angle subtended by the array.

4.5.1 Low temperature effects

Electrons in a metal scatter inelastically with each other, lattice imperfections, impurities and phonons. If the electrons are accelerated by a potential difference the originally random energy transfer will be changed into an energy flow from the electrons to the lattice. The scattering of the electrons is the origin of the resistivity. Electrons are Fermions and follow the Pauli exclusion principle, meaning that they will not occupy the same state. A consequence is that the number of particles $\bar{n}_i$ in a single-particle state of energy ϵ_i is (with k_B the Boltzmann constant and T the temperature):

$$\bar{n}_i = \frac{1}{e^{(\epsilon_i - \epsilon_f)/k_B T} + 1} \tag{4.4}$$

The fraction of thermally excited electrons above the Fermi level ϵ_f is of the order of $k_B T/\epsilon_f$ and is the fraction of electrons contributing to heat and thermal conductivity. The electrical conductivity σ is linked to the thermal conductivity κ by the "Wiedemann-Franz Law":[278]

$$\kappa = (\pi^2 T/3e^2)\sigma \tag{4.5}$$

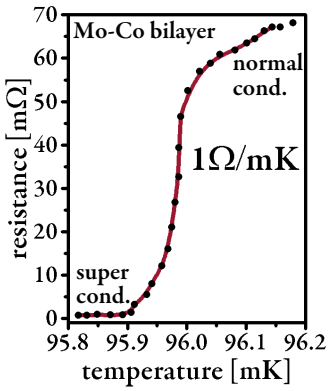

Figure 4.12. *Electrical resistance as function of temperature. The very steep transition is the basis of the transition edge senor as temperature sensor. The natural transition temperature T_c can be chosen to be close to the desired working point.*

In pure metals the heat conduction is mainly carried by electrons since the electronic speed on the Fermi surface v_F is much larger then the speed of phonons (speed of sound u). An estimate[278] for the speed ratio of v_F to u can be found with the Fermi energy ϵ_F, the effective electron mass m^*, the lattice constant d and the atom mass M:

$$\epsilon_F \sim v_F p_F \sim \hbar^2/m^* d^2 \qquad (4.6)$$
$$u \sim v_F \sqrt{m^*/M}.$$

The effective mass m^* is the mass of an electron close to the band gap and can be derived from $1/m^* = \hbar^{-2}(d^2E/dk^2)\epsilon_F$. While this is equivalent to the electron mass for a free atom it can vary strongly in crystals depending on the electric field. For metals one can assume the fraction of excited electrons to be k_BT/ϵ_F. Let N be the total number of electrons with the approximate energy k_BT. The total (thermally) excited energy is then:

$$U_{el} = N \cdot (k_BT/\epsilon_F)k_BT \qquad (4.7)$$

the heat conductivity dU/dT carried by the electrons is then,

$$c_{el} = (2k_B^2/\epsilon_F) \cdot NT \qquad (4.8)$$

With decreasing temperature the number of free electrons reduces and less phonon modes are excited. The remaining electrical resistance called rest resistance is dominated by lattice and impurity scattering. The total resistivity ρ is simply additive and could be written $\rho(T) = \rho_0 + \rho_{electron\ phonon}(T)$. The second temperature dependent part scales roughly linearly with temperature at room temperature and $\rho(T) \sim T^5$ for $T \ll \Theta_{Debye}$ (Bloch law). $\Theta_{debye} \sim \epsilon_F\sqrt{m^*/M}$ is the Debye temperature at which all possible phonon frequencies are occupied. The energy dissipation is a random process and the fluctuation dissipation theorem leads to a fundamental relationship between electrical noise and electrical resistance. The mean square of voltage fluctuation $\overline{V^2}$ is called Johnson noise and is related to the Ohmic resistance R, the temperature T and the Boltzmann constant k_B by[278–281]:

$$\overline{V^2} = 4k_BTR \qquad (4.9)$$

and is one of the fundamental noise terms in the detector.

4.5.2 Superconductivity

After the original discovery of superconductivity by Heike Kamerlingh Onnes in 1911[282] superconductivity was observed in a wide selection of materials including most metals[283–287]. In the previous section it was noted that metals at cold temperature have a

finite rest resistance originating in the electron scattering from defects and impurities. Onnes however discovered that once a certain temperature is reached the specific resistivity of the material makes a very fast transition between a finite value and exactly 0 Ω. This transition is one of the strongest temperature dependencies known and is used in our setup as a very sensitive temperature sensor. The second basic effect of superconductors is the perfect diamagnetic reaction of a superconductor called the Meissner Ochsenfeld effect[288]. A superconducting material of type I expels a magnetic field perfectly from its bulk material by inducing a shielding current. The macroscopic Ginzburg-Landau[289;290] theory of superconductivity[285;287] describes a penetration length λ_L of a magnetic field into a superconductor, according to $B(x) = B(x = 0)exp(-x/\lambda_L)$. If the magnetic field exceeds a critical field the superconductivity is suppressed. The critical magnetic field has a temperature dependence similar to figure 4.13 following $B(T) = B(T = 0)(1 - (T/T_0)^2)$. Superconductors of type II reduce the free energy by allowing flux vortices into the bulk material[291] in the intermediary Shubnikov phase. The vortices are small normally conducting regions shielded by ring currents in the superconducting area. At high vortex density the superconductivity is suppressed. Since the magnetic field around a current is proportional to the electrical current a critical current j_c can be defined accordingly. This dependence is used in the superconducting transition edge sensor. In this thermometer the critical temperature at zero field and current is above the working point and the critical current is used to suppress the superconductivity and keep the sensor in the transition. In the theory of Bardeen, Cooper and Schrieffer (BCS)[292] the reduced lattice vibration and attraction from the nuclei can lead to a net attractive force between two electrons. The two electrons are called a Cooper pair and have either a spin of 0 or +1. They no longer obey the Fermionic law of exclusion, but have all the exactly same bosonic energy state. To break up a Cooper pair at T=0 and form a pair of free electrons (now called quasi particles) a minimum energy of

$$\Delta(T = 0) = 1,76 k_B T_c \tag{4.10}$$

is needed which is called the gap energy. The gap energy for the system shown in figure 4.12 would be 15 µeV and for pure molybdenum 140 µeV. The gap energy decreases with increasing temperature. At T_c the Cooper pairs break up and form again a Fermi distribution. The assumption of an energy gap has many interesting effects. The energy portion ϵ needed to break up one cooper pair is small. The number of excitations is therefore large and the Fano resolution limit (equation 4.2) small. For pure molybdenum the thermal energy $k_B T$ is at 100 mK very small compared to the gap energy and the fraction of electrons

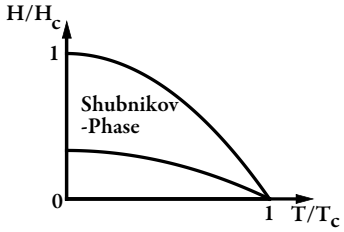

Figure 4.13. *The critical magnetic field strength as function of the critical temperature.*

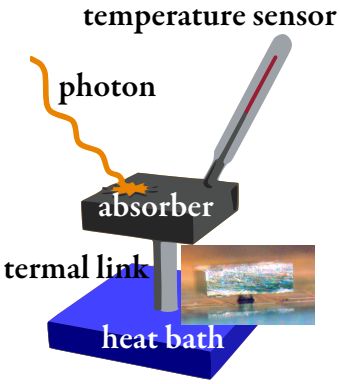

Figure 4.14. *Sketch of basic bolometric/calorimetric principle. The small inset shows an actual absorber used in gamma ray spectroscopy (curtesy Dan Schmidt, NIST). A thick tin absorber is glued on a thin film structure similar to Figure 4.16.*

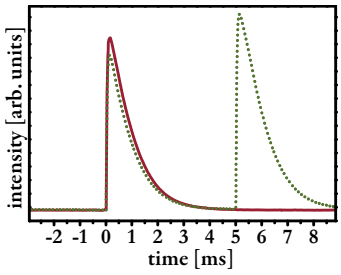

Figure 4.15. *Measured pulses from the laser plasma source. A single pulse (red) with several decay times gives a response that returns to the baseline before the next photon arrives. If the density of arriving photons is gets too high, two photons can be absorbed in the same trigger event and the calculation of the integrated intensity becomes difficult.*

Numerical example: *For the microcalorimeter array used in the presented experiments (details in the sections below) the estimated C ≈ 1.8 pJ/K and G ≈ 58 pW/K. A 6 keV photon would raise the temperature of the absorber by 0.5 mK; the signal fall time τ_0 would be ≈ 0.03 s and with the bath temperature of 85 mK the ultimate energy resolution would be 2.6 eV. The electro thermal feedback generates a faster decay time (see section 4.5.5).*

which are excited and could contribute to heat conduction or heat capacity is determined by a Boltzman distribution with $-\Delta/k_BT \approx -16$ in the exponent. The heat capacity of the material is now dominated by the much smaller phonon heat capacity which in the Debye model at the low temperature limit is:

$$c_p h \approx \frac{12\pi^4 k_B}{5} N_{atom} (T/\Theta_{Debye})^3 \tag{4.11}$$

If a normal contacting material comes in contact with a superconducting material some quasi particles diffuse from the normal conductor into the superconductor and lower its critical temperature in the vicinity of the contact area. The thickness of this influenced area depends on the charge diffusion constant of the normal conducting material and the temperature[287]. Typically the thickness reaches from a few tens of nanometers up to several micrometers. Using thin film technology the critical temperature of the whole film can be adjusted to exploit this proximity effect.

4.5.3 Microcalorimeter array basic principle

In a simple model of a bolometric/calorimetric photon detector the arriving photon of energy E_0 generates a particle shower that is fully thermalized in the absorber with heat capacity C. The temperature changes by $\Delta T = E_0/C$ which is measured by a sensitive thermometer. The absorber is reset with a time constant C/G via a heat bridge with thermal conductivity G to the temperature of the "cold bath" T. A constant photon flux would generate the temperature difference $\Delta T = Input\ power/G$. Devices operating in this steady state regime are in general called bolometers and are widely used in applications with high photon fluxes like laser power meters. Calorimeters shows a dynamic temperature response to a sudden input of energy. The X-ray photon energy is derived from the integral of the single photon thermal response plotted in red in Figure 4.15. All the following descriptions are based on this principle. Assuming an ideal behavior of the system, the ultimate sensitivity ΔE would be limited by the thermal fluctuations[293]:

$$\Delta E_{rms} = \sqrt{kT^2C}. \tag{4.12}$$

The need for low temperatures and low heat capacity is clear from equation 4.12. Since we are measuring dynamic signals and shall assume a constant signal shape the energy resolution can be somewhat higher then this[294;295]. Equation 4.12 shows one problem with these devices. To thermalize the particle shower generated by hard X-rays and the successive fast electrons, a high charge density is desirable without the rise in heat capacity shown in equation 4.8. Many absorbers are therefore chosen to be either superconducting or "poor" metals.

4.5.4 Types of thermometers

The absorber is coupled into a thermometer of different kinds. Some of the main kinds are outlined below:

- Semiconducting thermistors consist of a current biased high impedance thermistor and show a temperature dependence[296] of $R(T) = R_0 exp\left(\sqrt{T_0/T}\right)$.
- Transition edge sensors (TES) will be covered in greater detail in section 4.5.5.
- Metallic magnetic calorimeters use the temperature dependence of the magnetic susceptibility of a material. Their advantage is a contact free readout and no energy dissipation into the absorber. A variation of this principle is the use of the flux change due to the Meissner effect in a superconducting absorber which is used in magnetic penetration detectors.

In non thermal cryogenic detection mechanisms that are suitable for array type detectors, X-ray photons generate a cloud of quasiparticles and their sensitivity is based on the low binding energy of the Cooper pairs (see also section 4.3).

- On one side of a superconducting/insulator/superconducting tunnel junction (STJ) a photon is absorbed and its energy is sufficient to split a large number of Cooper pairs. The gap energy is on the order of a few meV like in niobium with 1.47 meV or aluminium with 0.17 meV for T=0[295]. The excited electrons carry a quasi particle tunnel current through the insulator that can be measured. Since the original response from the material is close to 800 electrons per 1 eV of the original photon energy the energy resolution due to statistical fluctuations is high. These kind of detectors has been used successfully for XAS at low energies[297–299](see comment below).
- Transition edge sensors can absorb photons in their active zone directly and act then as non thermal detectors. The total current transported through them is only partially carried by Cooper pairs. The absorbed X-ray photon reduces the number of available Cooper pairs and a larger fraction of the current is carried by quasi particles what produces a increased voltage drop over the material[295].
- Kinetic inductance detectors could be called "pair breaking detectors". The (mainly inductive) impedance of a tuned electrical resonator is $Z_S = R + i\omega L$. Quasi particles generated by an absorbed photon alter the resistance and detune the high Q resonant circuit. An advantage of

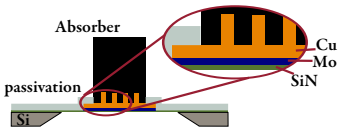

Figure 4.16. *The transition edge sensor is a* 2.5 µm *bismuth absorber on* 0.2 µm *Copper and* 0.1 µm *molybdenum bilayer. A meander structure of* 0.5 µm *copper bars strengthens the proximity effect in the molybdenum locally. The structure is deposited on a thin freestanding silicon nitride membrane supported by deep etched silicon. The copper bars affect the excess noise and were extensively discussed in reference*[301] *and chapter 2.7 of reference*[295].

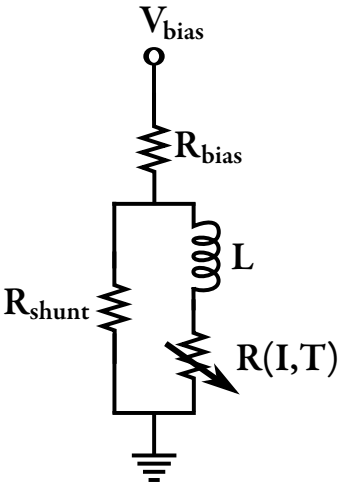

Figure 4.17. *A typical readout circle for a voltage biased transition edge sensor. The parameters for the system used are given in table 4.1. A shunt resistor* R_{shunt} *parallel to the out-coupling inductance L and the temperature and current dependent resistance of the TES builds the Loop. A large bias resistor (typically a few* kΩ*) decouples the total current from the temperature variations in the TES.*

these systems is the intrinsic possibility for frequency domain multiplexing of many pixels. Since this detector uses the same efficient pair breaking mechanism the number of electrons generated is high[300].

Thermal detectors are slower in their response time compared to detectors based on "quasi" particle generation. But since the radiation loss is very small they do not show charge losses due to recombination. Non thermal detectors using the small binding energy of Cooper pairs suffer from the possibility to use thick absorbers or the high voltages used in CCDs to extract the charge carriers. At the recent Low Temperature Detector conference in Heidelberg LTD-14 (proceedings are not yet published but will appear as a special issue in the "Journal of Low Temperature Physics" shortly after the print of this thesis) sensors built with most of these principles and energy resolutions better then 5 eV for the MnK_α emission lines were presented.

Which detector principle is optimal depends on the specific application. Readout speed, multiplexing, resolution, scalability, the energy range and many more factors will make one or other principle appear optimal. A good overview is given in reference[295], and in the tutorial section of the proceedings of the series of conferences named above.

4.5.5 Transition edge sensor (TES)

The temperature sensor for the detector used in the experiment of this thesis is a transition edge sensor built using thin film technology (figure 4.16). The copper-molybdenum bilayer is adjusted to have a T_C well above the desired working point (summarized in table 4.1). The thin layer is then brought into the transition phase by applying a bias current (in form of a bias voltage V_{bias} over a high resistance, see figure 4.17). The transition is very steep and offers a very sensitive temperature sensor. The simplified thermal differential power equation for the sensor can be written as (ignoring noise terms):

$$C(T)\frac{dT}{dt} = -P_{bath}(\Delta T) + P_{joule}(T, I) + P_{photon} \tag{4.13}$$

The heat flow from the detector to the bath $P_{bath}(\Delta T)$ is dependent on the temperature difference and is defined in a linear model by the G in the numerical example in section 4.5.3. The joule heating $P_{joule}(T, I)$ by the detector bias is for a static model $\sim R(I, T) \cdot I(R)^2$. The temperature changes generated in TES exceed the small signal limit and their extensive theoretical treatment is beyond the scope of this work. The solution of the differential equations including some nonlinear contributions

can be found in the thesis from Lindeman[302], in[295;303] and citations therein. The TES is used in a voltage biased scheme ($R_{bias} \gg R_{loop} = 1/(1/R_{shunt} + 1/R_{TES})$ and the Joule heating becomes:

$$P_{joule}(T, I) \sim RI^2 \sim V^2/R_{TES}. \tag{4.14}$$

This effect gives a stabilizing negative electro-thermal feedback since with increasing temperature the resistance in the sensor increases[303] (figure 4.12). The feedback reduces the Joule heating and with this reduces the total "fall" time of the signal. This is the reason why the estimated excitation decay time in the numerical example differed from the observed time (figure 4.15). A crude approximation for the correction factor can be made by assuming small and slow signals. The effective fall time would then be on the order of[295;303]:

$$\tau_{eff} \approx \frac{\tau_0}{1 + LG}. \tag{4.15}$$

LG is the "loop gain" and is locally defined(for a constant total current) as:

$$LG = \frac{P_{joule} \cdot \alpha}{G\, T_0}. \tag{4.16}$$

Here α is a dimensionless parameter describing the resistance change of the TES as a function of the temperature at the working point with current I_0, $\alpha_{I_0} = \partial log(R)/\partial log(T)$, G is the thermal conductance and T_0 the critical temperature (see table 4.1 and the numerical example in section 4.5.3). The loop gain can be understood as the gain of the readout circuit.

Irwin[304] found for the energy resolution of a TES the simplified expression:

$$\Delta E_{FWHM} = 2\sqrt{2ln2}\sqrt{4k_B T_0^2 \frac{C}{\alpha}\sqrt{n/2}}. \tag{4.17}$$

A high α parameter would therefore be desirable for fast and accurate photon detection. Restrictions in fabrication and the multiplexed readout, however, limit the possible values. The factor n in this formula is derived from considerations including coupling constants and excess noise and are discussed in this reference[295]. More on this topic in the discussion at the end of section 4.5.13.

Table 4.1. *The estimated parameters for the TES used (at a bias point of 20 % R_{normal})*

G	58 pW/K
C	1.8 pJ/K
$\alpha_{I_0} = \frac{\partial log(R)}{\partial log(T)}$	400
$\beta_{T_0} = \frac{\partial log(R)}{\partial log(I)}$	2
R_{shunt}	240 µΩ
R_{normal}	10.7 mΩ
n	3.2
T_c	117 mK
T_{bath}	85 mK

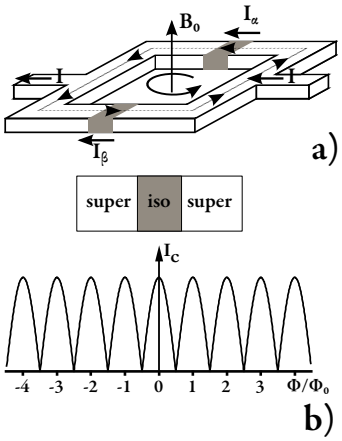

Figure 4.18. *a Schematic of a SQUID including both partial currents I_α and I_β and the induced ring shielding current. b Modulation of the maximum current that can flow through the SQUID as function of the flux through the loop.*

4.5.6 TES readout

The current going through the transition edge sensor (TES) is coupled inductively into the readout system. Each coil used in this sensitive step is wound in a complex gradiometer structure to suppress stray field with up to octapole symmetry and is shielded by superconducting layers. The current readout is done in a superconducting quantum interference device (SQUID) which consists of a superconducting loop with two interruptions in each arm called weak links (figure 4.18). Each of these weak links is a Josephson contact and can be modeled like a superconductor-isolator-superconductor tunneling contact. The maximum tunnel current through this contact which can be carried losslessly by the Cooper pairs depends strongly on the phase difference of the wave functions on both sides of the contact[285]. A field Φ_{extern} within the loop will generate a shielding ring current (dotted line) which in the simplest model generates a phase difference in each contact (D.C. Josephson effect). Let $i_n = I_C sin\varphi_n$ be the current through each of the contacts then the total current through both contacts is:

$$i = i_1 + i_2 = 2\, I_c\, cos((\varphi_1 - \varphi_2)/2)\, sin((\varphi_1 + \varphi_2)/2) \qquad (4.18)$$

Only considering the ring current with the inductance L and a symmetric driving current the total flux in the loop would be

$$\Phi = \Phi_{extern} + LI_{circular} = \Phi_{extern} + L(i_1 - i_2)/2.$$

The phase difference $\varphi_2 - \varphi_1$ can often be assumed to be

$$n \cdot 2\pi + 2\pi\Phi/\Phi_0,$$

for integer n the total current through the contacts is then

$$i = 2I_c cos(\pi\Phi/\Phi_0) sin(\varphi_1 + \pi\Phi/\Phi_0).$$

Without any self inductance the maximum current flowing through the loop corresponds to $di/d\varphi_i = 0$, giving

$$i_{max} = 2I_c|cos(\pi\Phi_{ext}/\Phi_0)| \qquad (4.19)$$

like shown in figure 4.18b. Since the loop is a macroscopic structure, field variations below the magnetic flux quantum Φ_0 can be measured. Minute current changes in an inducing loop can induce multiple flux quanta, so techniques based on such SQUID measurements can enjoy exquisite sensitivity. SQUIDs are frequently used as sensitive current sensors, especially in systems which already provide low temperatures[285;305;306]. In the present work SQUIDs function as current comparators. The current of two opposite wound coils is fed into one arm of the loop and the difference of the induced flux is measured[305].

4.5.7 Multiplexing

Multiplexing is employed to read large arrays of detectors. Three types of multiplexing for low temperature detectors are commonly employed[307]. In frequency-division multiplexing (FDM) all pixels within one channel are sampled with a different frequency simultaneously. In time domain multiplexing (TDM) every pixel within one channel is switched on sequentially. In code division multiplexing (CDM)every pixel is sampled constantly but the sign of the bias modulates with a unique code. The readout electronic for the presented array was designed and fabricated in the facilities of the Quantum Devices Group at the National Institute of Standard and Technology (NIST) Boulder, Colorado US in close collaboration with their personnel. The room temperature components are presented elsewhere[308]. The cold stage multiplexed readout system has several channels of microcalorimeters (columns). Within each column, several pixels (rows) are time division multiplexed. In figure 4.19 a two pixel multiplexing system is sketched. The basic idea for the multiplexing is to couple the TES (A) inductively into a current comparator (SQUID) for each pixel (B), which may be switched on or off for the purpose of multiplexing. The outputs are summed and after some amplification and impedance matching brought to an output amplifier at room temperature (C). The signal is digitized, analyzed in a digital proportional integral derivative (PID) controller which provides the feedback voltage (E) of the close loop amplifier.

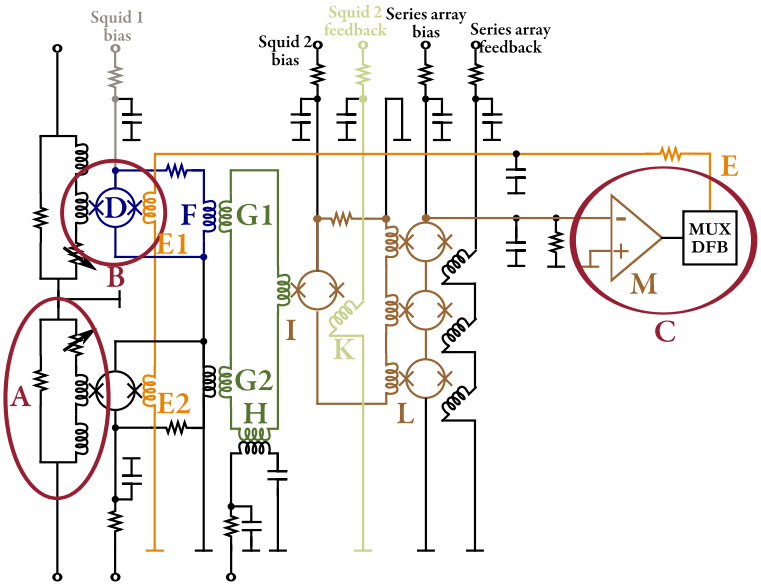

Figure 4.19. *Schematic of the readout for a two pixel multiplexed system. Red rings A:TES readout loop B:SQUID current comparator C:Room temperature electronics with preamplifier and digitizer. Blue, Green, Brown amplification circuit reading the change of current through the first SQUID which is the error signal Gold:feedback current for current comparison in B, for a detailed description see text*

Some further itemization of the circuit components follows:

TES readout loop (red ring A) The current through the transition edge sensor (TES) is coupled inductively to the readout loop as described in figure 4.17. The sketched primary readout loop has an additional series inductance to slow down the rising current edge of the pulse and enable the feedback loop to follow the signal development and stay locked on the working point of the SQUID (see discussion at the end of this section).

Tuned current comparison (red ring B) As described in the previous sections the current through the TES is inductively coupled into the first superconducting quantum interference device (SQUID) (blue D) over a gradiometer loop structure designed to suppress stray fields with up to octupole symmetry. Into the same coupling loop, but with opposite polarization and different inductance, a feedback channel (Gold E1) is coupled.

Current feedback (gold line) The feedback line couples into each SQUID of this column and is synchronously switched to the value that was calculated in the previous cycle to compensate for the flux induced by the TES readout loop. The signals in the SQUID (Blue D) are kept close to the working point if the feedback is fast enough. Fast rising error currents (which are then uncompensated) can induce a flux that rises a full magnetic flux quantum in the SQUID which the jumps through one full current period (equation 4.19). The feedback then stabilized on the new current. To avoid this effect the earlier mentioned additional inductance was introduced. (see also discussion at the end of this section)

Multiplexing Each first stage SQUID is voltage biased (grey line). The bias is switched on for one SQUID at a time and the current of only one SQUID is coupled over a coupling coil (Blue F -> Green G1) into the superconducting summing loop (green loop). The summing loop is damped by a pickup coil (green H).

Amplification The summing coil is fed into a tuned current comparator (Brown I). Since the system is tuned to compensate the flux in the first stage SQUID (red ring B) the induced signal is the error signal. The tuning provided by the light green line K is setting the working point and is not changed during the multiplexing. The whole system has two SQUID-based amplification stages. In the first stage SQUID, and the second is in the readout of the summing

coil (brown I). The relative inductance in each SQUID's coupling coils determines the amplification.

Impedance matching SQUIDS are low impedance devices. A tuned multi stage serial SQUID array is used to match the impedance of the circuit to the room temperature electronics (red circle C).

Error preamplification The error signal is amplified and digitized in the room temperature electronics.

Feedback and mux The digitized error signal is converted into a feedback signal in a digital proportional-integral-derivative (PID) controller[309–311]. The acquired feedback signal is stored and used the next time this pixel is measured. The previous feedback signal together with the measured error signal and several flags to assure synchronous data transfer are sent digitally over an optical fiber to the PC.

One readout cycle for a single pixel in the current configuration takes 640 ns. The sequence is outlined in figure 4.21:

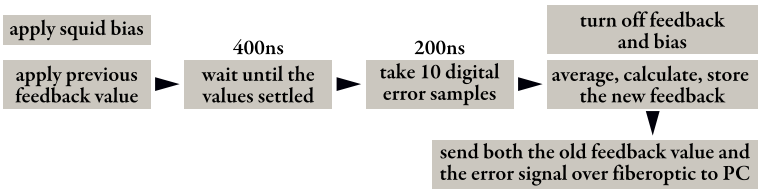

Figure 4.21. *Step diagram for a single pixel. A single pixel readout cycle takes in the current configuration 640 ns (including 40 ns delay for signal transport).*

In the current configuration ten pixels (rows) are multiplexed in four of the possible eight channels (columns), so that each of the pixels is sampled every 6.4 µs. The excising array has 160 pixels and is shown in figure 4.20. During the steep signal rise after the photon absorbtion the feedback has to be able to follow the signal (figure fig:photonarrival). The sampling frequency limits the number of pixels that can be multiplexed. The additional inductance introduced in the TES readout loop slows down the signal transients, enabling this multiplexing scheme. If the SQUID switches over one Φ_0 into the next current oscillation the feedback follows new current at the same error value, the gain factor is different, dynamic range is lost and the energy calibration is wrong (more on this in section 4.5.13). A program is testing the current values constantly and sets the loop back to its calibration values in regular intervals. However, to not interfere with the system readout this check can only

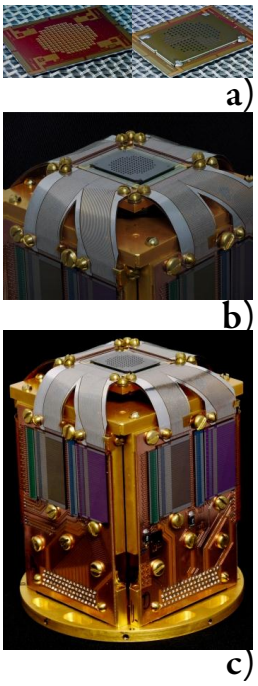

Figure 4.20. *Figure A shows the installed array without (left) and with the collimator (right) in a transfer pad (courtesy Dan Schmidt NIST). The pixels are arranged in a square grid with an even 665 µm pitch but cover a circular crossection, to optimize the overlap with the round X-ray window. A 275 µm thick deep etched silicon collimator (right figure) with 320 µm by 305 µm openings is aligned 20 µm distant from the pixels and minimizes the photons being absorbed in the bulk silicon near the superconducting leads. Figure B shows the mounted array with flexible bent aluminium leads. The shunt resistor, inductive loads and first and second stage squids are mounted at the sides of the three dimensional structure (figure C). All four sides of the structure are connected via a flexible circuit board. The base of the structure is made of copper and covered with gold to ensure good heat contact and minimize radiative emission.*

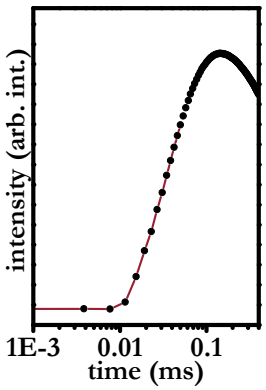

Figure 4.22. *The signal change between two sampling points can be several percent for rapid changes and sparse sampling in large systems. This demands fast dynamic response for the amplifying system and induces errors in measured photon arrival time (which is a important parameter in the discrete data treatment).*

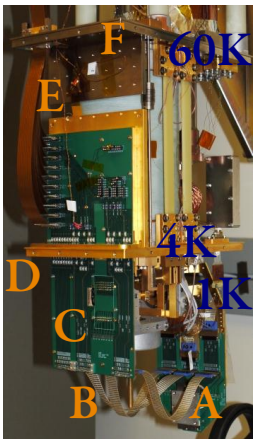

Figure 4.23. *After the first two amplifications on the low temperature stage in figure 4.20 c the signal is filtered and amplified in an intermediate stage at* 1 K *(board A), transported over superconducting cables B to the transfer board C which is thermally located on the* 4 K *stage D. From where it is guided out with flexible copper leads E into the* 60 K *area of the cryostat F.*

happen in long intervals and the time after each unlocking event is lost for data collection. The next generation room temperature readout electronics is in the final testing state and will offer a $\approx 10\times$higher clocking speed, which will enable a larger number of multiplexed pixels. The heat capacity of the absorber and the other parameters (see table 4.1) were adjusted for a maximum photon energy of 10 keV. Above this limit the relative sensitivity of the sensor is reduced and often the feedback can not follow the signal changes (see section 4.5.13).

4.5.8 Signal transport and amplification

The eight separate columns are arranged in the physical array as 45 degree pie sections. Four of those columns, each with 10 multiplexed pixels (rows) are wire bound to a flexible superconducting connector (aluminium at 80 mK). The construction is mounted on a gold covered three dimensional copper construct with the readout and multiplexing electronics glued and wire bonded on a foldable circuit board on the four sides. The whole complex is held at the base temperature of 85 mK. The signal is transferred over long superconducting wires (see figure 4.27 G2) to a circuit board at the intermediate 1 K level (figure 4.23 A). The long superconducting wires ensure good thermal isolation at the same time as a near lossless signal transport. At the 1 K level a set of low power filters and the series array are located. Again a set of long superconducting cables transports the signal and bias currents to a transfer circuit board at the 4 K stage (figure 4.23 C). This board contains the main isolation and noise filter into the upper part of the vacuum vessel with less shielding. Flexible copper wires (figure 4.23 E) transport the signals and bias currents through the 60 K shields (figure 4.23 F) and the vacuum feedthrough into a small rack mounted on top of the cryostat. The circuits providing the bias voltages are battery driven. The amplified data is transferred via high quality coaxial cables to the readout system. The power for the readout electronics is galvanically separated from the 240 VAC power and cleaned in several band pass filters. The whole system is heavily grounded and all possible strong radio frequency noise sources in the lab have extra shielding or are disabled during the measurement. The communication with the PC is carried solely via optical cables to a custom built PCI card.

4.5.9 Temperature and noise shielding

A blackened aluminium shield mounted on the 4 K and 60 K stage together with the vacuum shield isolates the bulk of the cryostat from electro-magnetic fields present in the laser laboratory and reduces the radiation load from all but the next

cold stage. The detector package is shielded in four layers (see figure 4.24). The innermost aluminium shielding is mounted directly on the 85 mK detector package. The second and third layers (one at 4 K and another at 60 K) are made from annealed "Amumetal 4K" from the company "Amuneal". This material is designed to yield a high magnetic permeability. The outermost layer is a modified ISO 100KF vacuum flange with a standard KF port to enable the coupling to standard vacuum systems and a 25 µm Duraberyllium window. The three inner shields are closed with an exchangeable windows. Without this shielding the detector would be saturated with IR photons. In the current configuration two layers of 1 µm aluminium are mounted on each of the successive three windows on the three inner levels. For better transmission at very soft X-ray energies other radiation filter materials such as aluminium covered polymers (e.g. from companies like "Lebow Company" or Lexan) can be chosen.

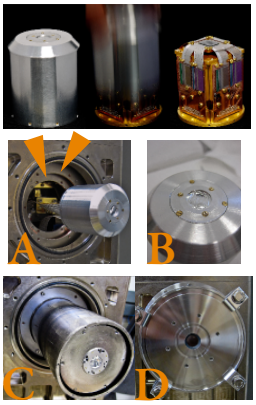

Figure 4.24. *The detector package is shielded with a superconducting 1 mm aluminium cover which is mounted directly on the 85 mK copper construct and suspended outside the cryostat body (A). The arrows mark the inner 4 K and 60 K aluminium shielding. (B) Depending on the application different window materials can be chosen (see text). Annealed magnetic shielding (A4K material produced by Amuneal) is mounted on the two inner shields and extends over the detector package. Each shield is closed with a small exchangeable window. The outer vacuum shield has a removable ISO 100 KF flange. For freestanding operation a 25 µ m Duraberyllium window is glued behind the 10.2 mm diameter opening in a modified ISO 100 flange and offers a ISO KF 40 connection to standard vacuum systems.*

4.5.10 Data recording and synchronization

The data stream in the PC is separated into the different channels belonging to each pixel. Software constantly analyzes this stream and writes a fixed data section onto the disk in a case a chosen trigger condition corresponding to photon arrival is met. This approach is based on prior developments and has some advantages over simply streaming the data to disk. During the data analysis each pulse can be treated separately and statistical exclusion criteria can be used to minimizing the processing time. Real time processing capabilities are under development and will allow flexible record length for each pulse[312;313] (see also section 4.5.13 for more details). The length of the recorded pulse is optimized according to the expected signal decay time[275]. A longer recording is beneficial for the energy resolution since the pulse can be fitted over a longer period of time and the absorber can cool down to its base temperature (figure 4.25) but it also limits the possible maximum count rate and with this increases the measurement time. For the current setup a minimum record length of $\sim$ 12 ms has been chosen, corresponding to a maximum pixel count rate of $\approx$ 80 Hz. In the initial (and still applicable) algorithm, records are discarded if they contain two ore more distinguishable events. The probability for exactly one photon to be absorbed within one record length is follows a Poisson distribution[80]. With 80 Hz maximal trigger rate the optimal event "survival" rate v_{opt} for exactly one photon per record length is:

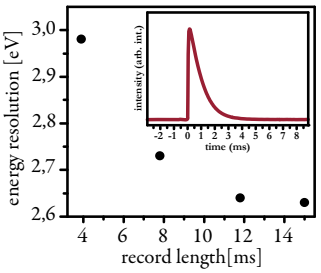

Figure 4.25. *The energy resolution in dependence of the recorded pulselength for a typical pixel. The inset shows the typical detector response on a* 6 keV *photon.*

$$f_{poisson}(k;\lambda) = \frac{\lambda^k e^{-\lambda}}{k!} \Rightarrow \lambda_{k=1}^{max} = 1 \tag{4.20}$$

$$f(1;\lambda_{max}) = 1/e \qquad v_{opt}^{80Hz} = 29,4Hz \tag{4.21}$$

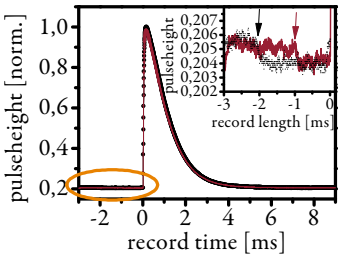

Figure 4.26. *Simultaneous arrival of photons induces crosstalk between different pixels. The direction of the signal could point to an inductive origin of this signal.*

The signal between two different pixels does show crosstalk features if a photon is simultaneously absorbed in a second pixel which is thermally or electrically close. An increased total flux adds to this problem and a sparse excitation with only slightly less effective counts is beneficial for the energy resolution. In the current detector module pixels with minimal crosstalk among those available were chosen. Nevertheless, it does contribute to the total noise level and needs to be addressed in the next generation of detectors. The crosstalk is best visible in the recorded calmer region just before the rise of the signal (figure 4.26).

The two biggest uncertainties left in the measurement are baseline/gain shifts due to variations of the base temperature (see section 4.5.11) and the asynchronous arrival of the photos as measured by the discrete sampling points. The large intensity change between two of the sparse points especially for large areas on the rising edge has a significant influence on the integrated signal. In future iterations of the electronics this could be addressed by recording the laser arrival time.

This
ning machine. Laser on - laser off information can currently be included by modulating the total incoming X-ray flux to signal a change in experimental conditions (blocking the X-ray generation process by e.g. blocking the laser beam) in later iteration this information might be written into the data stream.

4.5.11 Temperature control system

The cryostat is based on a design from NIST and was built by High Precision Devices Inc. in Boulder, Colorado. Driving and control electronics were purchased separately or built as part of this thesis work. The controlling software was also partly written in the course of this work. The detector operating at the bath temperature of 85 mK is mechanically supported in several stages from the casing of the room temperature cryostat. Each stage has its own cooling and the weight is carried by materials with low heat conductivity. The cryostat is evacuated to pressures below 4×10^{-7} mbar before cooling. The large cold areas of the shielding materials described in the previous chapter act as a cryopump[154] and further reduce the pressure. The first two stages are carried by glass fiber constructs and are cooled by a two stage pulse tube cooler. The cooling concept is sketched in figure 4.27. An external water cooled compressor generates a pressure difference between two long pressurized gas lines. An external rotating valve converts this pressure difference into a 1 Hz pulsating pressure (A). The separation of valve and pulse tube reduces the mechanical vibration transmitted into the cryostat. The pulsating pressure wave drives a two stage pulsation cooler based on a Stirling process inside the vacuum

vessel. The cooling medium used is 99.9995 % pure helium. The whole cryostat is supported by a highly adjustable table separated from the optical laser and X-ray table. Part B and C of figure

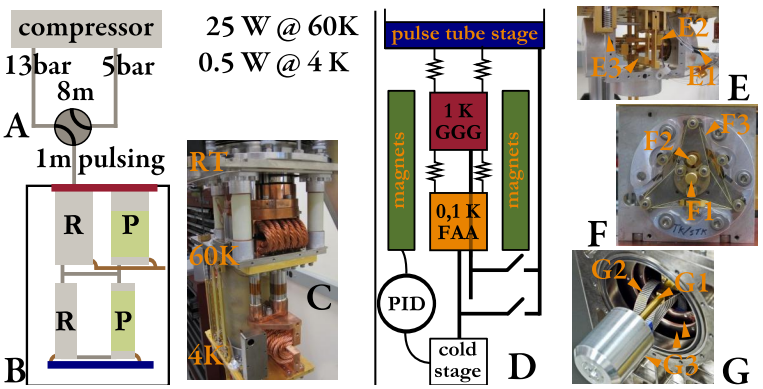

Figure 4.27. *Cryostat cooling system A) an external compressor and motor driven valve generates a pulsating pressure difference that drives a two stage pulse tube cooler in the cryostat B) in which each tube is split in two parts, consisting of a regenerator R and the pulse tube P. The cold stages are thermally attached to the respective pulse-tube stage. C) Photograph of the system with indicated temperature stages. D) Sketch of the adiabatic demagnetization refrigerator with the indicated pulse tube end stage at 4 K and two heat switches, superconducting magnets and paramagnetic salt pills. E) Close up of the heat switches. F) Close up of the suspended attachment of the copper rods carrying the detector package. G) Close up of the protruding detector package with indicated superconducting connections G2 and the thermal and electric shields G3 (see text)*

4.27 show a simplified sketch of the pulse tube and a photograph of the system. The gas pulsation drives a heat transfer between the cold section of the regenerator R and both ends of the tube. The principle was described by Gifford[314] and has the advantage of removing all moving parts but the gas from the cryostat. An overview and comprehensive description of the cooling principle can be found in references[315;316].

The first pulse tube cold stage is at $\approx 60\,\mathrm{K}$ and the second stage slightly below 4 K. To minimize the transmitted vibrations and allow for thermal expansion the intermediate cryostat stages are coupled to the pulse tube via annealed flexible copper wires.

The second cooling stage is an adiabatic demagnetization refrigerator[317–319] based on the magneto-caloric effect. The system is sketched in figure 4.27 D. The two active materials gadolinium gallium garnet (GGG) and ferric ammonium alum (FAA) are strongly coupled to their respective cold stages on the detector side, but only weakly coupled to the 4 K cold stage. An externally controllable heat switch (E2 and E3) can generate a good thermal connection to the pulse tube end stage. The magnetic field used in the magnetization process is generated by a superconducting solenoid with $\approx 4.2\,\mathrm{T}$ at 9.3 A driving current. The driving current of the magnet is close to the critical current of the coil. This and the thermal/physical stress generated during the magnetization cycle limits the possible rate of magnetization and demagnetization. At the end of the cooling cycle a residual (weak) magnetic field is used to control the cooling power of the

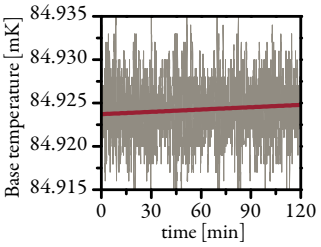

Figure 4.28. *Base temperature fluctuation vs time. The oscillations are with 15 µ K smaller than the long term temperature drift over* 14 h *operation time.*

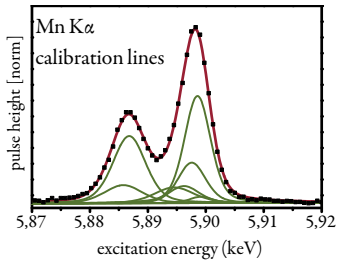

Figure 4.29. *Fitted calorimetric spectrum of a single pixel. This spectral quality was obtained after compensating for the artificially introduced temperature fluctuations as described in section 4.5.13. The fit uses the parameters given in table 4.2 with the total intensity, a linear shift and a gaussian broadening function as free parameters.*

Table 4.2. *Fit parameters for the manganese Kα fine structure assuming a gaussian line shape after Hölzer*[320] *modified by Porter*[321].

Int[rel]	E[eV]	FWHM[eV]
1.000	5898.853	1.715
0.649	5887.743	2.361
0.399	5897.867	2.043
0.312	5886.495	4.216
0.224	5894.829	4.499
0.187	5896.532	2.663
0.0510	5899.417	0.969
0.0113	5902.712	1.5528

cryostat and adjust the temperature. Temperatures above 1 K are measured with silicon diodes. The low temperature 85 mK sensor is a ruthenium oxide thermistor read with a resistor bridge. The output of the resistor bridge is the input to an analogue proportional-integral-derivative (PID)[309–311] controller (Stanford research system). Its output is amplified by a voltage controlled high current analogue amplifier that is used to drive the magnet.

Vibrations caused by the pulse tube also the slow and nonlinear thermal response of the system and the limited available cooling power make the tuning of the feedback loop challenging. Standard tuning techniques like the Ziegler Nichols tuning method[309;311] led to system instabilities. The temperature stabilization achieved is nevertheless sufficient to run the system with some additional correction in the data analysis. Figure 4.28 shows the fluctuations and long time temperature drifts in the system which need to be considered in the data analysis (see section 4.5.13.

The detector package is mounted on a gold coated copper rod (E1, F1 and G1) at 85 mK protruding horizontally from the cryostat axis (figure 4.27 G). The rod is suspended by fine Kevlar fibers (F3) that are attached to the second rod at 1 K (E2 and F2). This second rod is in turn suspended by similar fibers that are attached to the copper structure at 4 K. All electrical connections to the cold stages are superconducting and therefore have a low heat conductivity. This isolated construction enables a total standing time of up to 16 h without any bias currents in the detector and $12 - 14$ h under operating conditions. After this time the adiabatic demagnetisation refrigeration process must be performed again.

4.5.12 Calibration lines

Two radioactive materials were used for energy calibration of both the CCD and the microcalorimeter detectors. The decay from $^{241}_{95}$Am and $^{55}_{26}$Fe are given in the database from Chechev[322] and listed in table 4.3. During the experiment fluorescence lines of the sample and filter materials are excited which appear at known energies throughout the whole spectrum (see section 4.5.13).

Table 4.3. *The decay from $^{241}_{95}Am$ and $^{55}_{26}Fe$[322] with the energy in keV and the probability for the particular transition after a disintegration event in percent.*

$^{241}_{95}Am \xrightarrow{\alpha} {}^{237}_{93}Np$			$^{55}_{26}Fe \rightarrow {}^{54}_{25}Mn^*$		
	E keV	prob. %		E keV	prob. %
Np L1	11.89	0.848	Mn Kα_2	5.8877	8.45
Np Lα	13.9	13.03	Mn Kα_1	5.8988	16.56
Np Lη	15.86	0.31	Mn Kβ	6.4905	3.4
Np Lβ	17.81	18.55			
Np Lγ	20.82	4.81			
γ	26.3446	2.4			
γ	59.54	35.78			

4.5.13 Data extraction, energy calibration and drift correction

The principle behind the data extraction was discussed in a paper by Doriese et al.[275]. The recorded signal for each event is composed of the sum from feedback signal and error signal, since the response is faster than the feedback can follow. The signal is sampled at discrete intervals and shows a complicated decaying function. The extraction and noise reduction of every event is based on the optimal filter[294] algorithm. The assumption is that every pulse (close to the calibrated energy) is of the same shape, discrete and homogeneously sampled. Some pulses that are assumed to be perfect are selected, averaged and analyzed in the Fourier space according to their power spectrum. A filter template is generated using the optimal frequency cutoff which is then transformed back into the time domain. The product between the filter template and the original pulse in the time domain was shown to be proportional to the energy of the event[302].

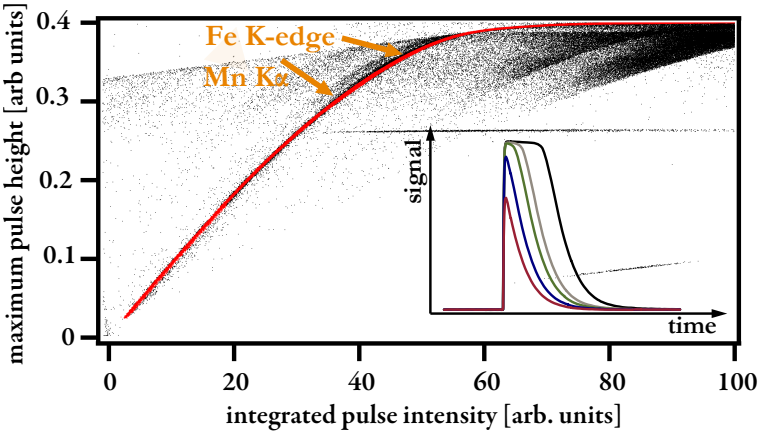

Figure 4.30. *The maximum signal deviation vs integrated peak intensity for all recorded events of a single pixel during the collection of the ferrocene X-ray absorption spectrum. Statistical selection processes rejected those recorded events containing more then one photon or other additional noise contributions. The remaining events are marked in red. The orange arrows show the approximate position of the manganese K_α radiation and the iron K-edge. At large deposited energies (ordinate) the sensor becomes normally conducting and loses its sensitivity. The lost sensitivity of the detector results in a flattening of the pulse shape for increasing photon energies as shown in the inset.*

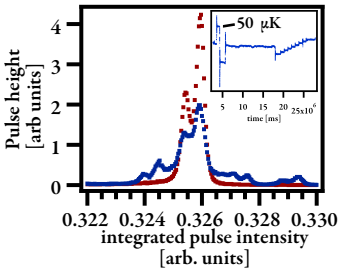

Figure 4.31. *Pulse height spectrum of ^{5}5Fe emission data using artificially introduced temperature fluctuations of up to ±50 µK shown in the inset before (blue line) and after correction red (red line).*

A bachelor project was supervised during this work to develop a parallelized implementation of this code for graphical processing units. A spectrum for time resolved measurements contains more then 1×10^{10} absorption events. The filter template is specially generated for each detector but assumed to be constant for all events recorded with the same detector. Graphical processing units offer a large number of parallel nodes (processing units) that have to access a constant stream of adjacent data storage. The results of this project will be published separately[323] and showed a significant acceleration in the application of this filter step. The this project will contribute to the development of realtime data processing.

The bias settings of the SQUID amplification and the PID settings controlling the signal feedback are tuned after every cooling cycle. The magnetic flux trapped in the superconducting elements and variations in the laboratory conditions make these adjustments necessary. The detector response function is linear only in small regions. The phonon transport conditions inside the absorber, between the contact layers and into the thermometer and heat bath are the object of very active research[324] and difficult to model. Figure 4.30 shows the peak value of the response of a single pixel as function of the integrated value, where the latter is assumed to be closely related to the deposited energy. The compromise of speed and energy resolution that had to be taken operates this detector in a regime where the maximum pulse height is no longer strictly proportional to the integrated intensity. In practice this requires is a calibration for every run on every pixel using radiation of known and discrete spectral distribution.

Temperature fluctuations and drift induced by the cryostat or the heating of electrical elements, laboratory conditions and the photon flux do change local temperature off each pixel during one day of operation. The nonlinear temperature response generates a temperature dependence of the detector gain. Fluctuations as low as 20 µK result in a significant reduction of the energy resolution. Since the TES is in principle a very sensitive thermometer we can use its recorded baseline level before every pulse to track the temperature fluctuations and generate, using artificially induced temperature fluctuations during each measurement cycle, a correction function for every pixel (figure 4.31).

Figure 4.32 contains the filtered pulse-height spectrum of the ferrocene sample recorded with the micro-calorimeter detector array and the laser-plasma source including the ^{55}Fe calibration data. Several prominent features originating from material in or close to the beam-path like the copper, aluminium and silicon Kα emission (fluorescence from filters and detector mask) or the strongest absorption edges. Each of those features is added to a separate spline generated for each pixel. The splines are then

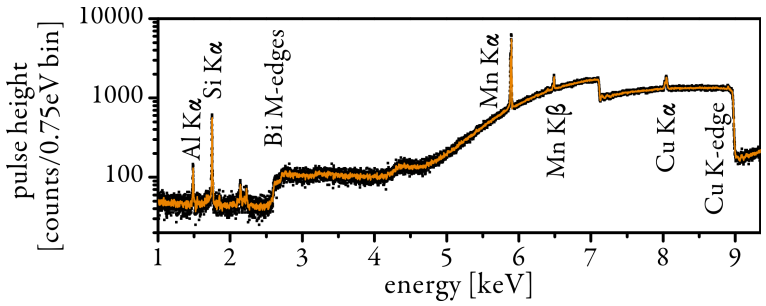

Figure 4.32. *Pulse-height dataset containing the X-ray transmission spectrum of ferrocene powder on Kapton tape spectra recorded with the microcalorimeter array and the laser plasma source. The main spectral features used for calibrating are outlined.*

used to calibrate the filtered and integrated arrays response to a corresponding energy. Events can then be binned in whatever way is deemed suitable. For example, presentations on an energy scale would typically use a constant energy interval binning scheme whose interval accommodates the average energy resolution of the pixels. Alternatively for EXAFS analysis one seeks a constant binning interval in the photoelectron's k (momentum) space. This amounts to binning in intervals that increase quadratically in energy above the absorption edge (equation 3.5). The possibility of arbitrarily binning multiple, simultaneously acquired spectral features either during or after the data collection is a particular strength of this technique.

It can be surmised that in time, and with ongoing developments, it will be possible to fit molecular structures during collection, terminating the data collection when the desired structural accuracy has been attained.

Abbreviations

AES	Auger electron spectroscopy
APD	avalanche photodiodes
APS	Advanced Photon Source
BBO	$\beta - BaB_2O_4$
BCS	Bardeen, Cooper and Schrieffer
CCD	charge coupled devices
CMOS	complementary metal oxide semiconductor
eV	electron volt
EXAFS	extended X-ray absorption fine structure
KID	kinetic inductance detector
NIST	National Institute of Standard and Technology
RIXS	resonant inelastic X-ray scattering
SASE	self amplified spontaneous emission
SQUID	superconducting quantum interference device
TDM	time domain multiplexing
TES	transition edge sensors
Ti:Saph	titanium doped sapphire
XAFS	X-ray absorption fine structure
XANES	X-ray absorption near edge structure
XAS	X-ray absorption spectroscopy
XPS	X-ray photoelectron spectroscopy

Appendix

Vectorized single pixel analysis method

Most advanced codes for particle tracking and analysis are very expensive in computing power. In high level programming languages codes become fast if the optimized and built in matrix routines are used. The code described here accelerated the processing on a 2 GHz double core processor from 500 ms/frame to 20 ms/frame. Which was limited by the data transfer from the storage medium and might be accelerated further. The algorithm

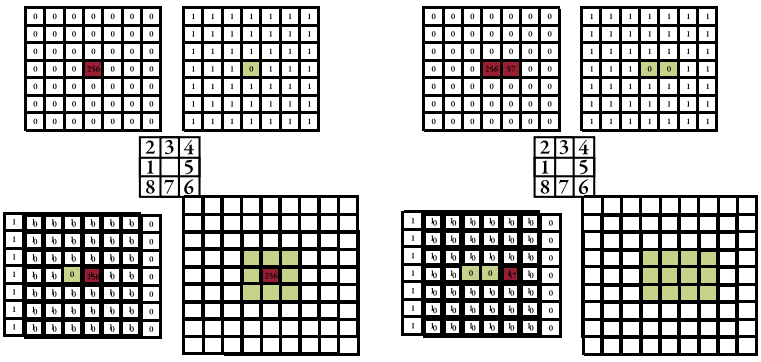

Figure 1. *Fast matrix based single pixel analysis method. The left hand side shows the structure if only a single pixel has a non zero entry. On the right hand side two neighboring cells are filled. The algorithm is described in the text.*

is: Take the original data matrix, apply the desired threshold and generate two matrices. The first matrix contains the data, and zeros where the data is below the threshold. The second matrix has a zero in pixels above the threshold, and 1s elsewhere. Now the contents of this second matrix is successively multiplied with the thresholded matrix containing the data with a shift of one step in all 8 directions. If two adjacent pixels were exposed above threshold both will be multiplied by zero in this procedure and erased. The new matrix contains only the necessary amount of data and can be stored space optimized or further processed.

Laser alignment procedure by Jens Uhlig January 2012

Since this is a commercial system which was designed to be "hands off" no alignment instructions are available. During the course of this work the optimization of the contrast ratio and the minimization of abberations introduced into the beam played a crucial role. This procedure is designed to give a brief account of the every day alignment procedures necessary to operate the laser plasma source.

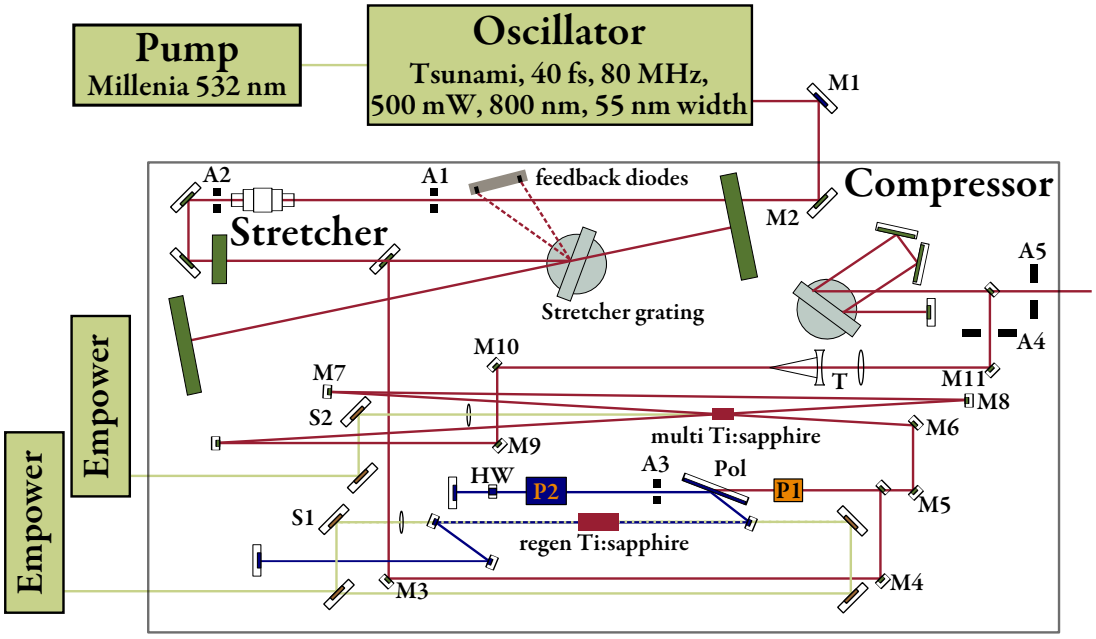

Figure 2. *Laser amplifier used in the Chemical Physics Millenia laser lab, 2011 (see text for details)*

(i) Match the spectrum and the power with prism only, if possible. For this shine the Tsunami output on the power meter and use the fiber optics and the saved spectrum as reference. Note that the spectrum differs from different reflective surfaces. From time to time check with a single shot auto-correlator for the variations in the timing and wavefront tilt (rotate auto-correlator by 90 deg). They are an indication for damages in the crystal.

(ii) If there is a problem to reproduce the spectrum or if the total power suddenly drops play with the alignment slits to check if the beampath has changed and iterate with the

prim. (560 mW output is normal, with time and dirt above 400 mW is fine). Below 150 mW is not enough to seed the regenerative amplifier.

(iii) If the spectrum is still not matching the reference or the mode-locking is lost easily, carefully adjust the end mirrors (one at a time and as little as possible) If you continue to have problems to mode-lock at a chosen position you may play with the acoustic modulator. If in doubt, start in the middle of its range.

(iv) align with M1 and M2 on A1 and A2 (Stretcher alignment) If everything is fine the two feedback diodes should see the second order reflection from the stretcher grating. If not, repeat the alignment and use the milled green alignment tool to check the whole path. Measure the spectrum after the stretcher at this point. It should not be clipped. The grating is a bit too narrow (there is a small clip on both sides) but we should get $55 - 60$ nm bandwidth through the system.

(v) In the spectra control software open Pockels cell P1 (channel 1) to admit the seed beam and close the cavity (open channel 2 but keep channel 3 off!)

(vi) Use M3 and M4 to get the earliest build up.

(vii) Align the Pockels cell P2 to get a symmetric "Isogyre" picture with 4 poles centered on A4. The beam passes the polarizer several times and should be isolated in the center part (dark with blocked Pockels cell). This alignment is one of the crucial steps if everything else is fine.

(viii) Check the power and contrast with the multipass amplifier off and on. With the pump laser for the regenerative amplifier pump at 17 A and for the multipass at 16 A the out coupled pulse should have 3 mJ with the regenerative amplifier only and 5.8 mJ with both amplifiers. The averaged leak power should be below 200 µJ. If these conditions are not met continue try the instructions below this section.

(ix) Check that the Isogyre picture is centered on A4 (flip up with blocked beam) and A5, if this was still fine nothing did move and the laser should be aligned. If this is not aligned adjust M9 and M10 to go centered through the telescope (use the back reflection of the lens surfaces and bring it through A4 then use M11 to go through A5.

(x) Fine tune the two gratings start by adjusting only one of them. It is better to tune the compressor grating at the beginning, assuming that the everything else didn't move.

During adjustments, keep the previous settings. Turn a quarter turn, re-compress and check the output on the autocorrelator again. If the pulse cannot be made briefer then 50 fs with this method check the spectrum inside the laser to get an indication for where the limitation is originated.

(xi) Check with the Pulsescout autocorrelator for side peaks which might point to damaged optics.(there is a internal reflection at 2.16 ps)

(xii) check the full output on a photodiode for the achieved contrast ratio

- The contrast to leaked peaks (other round trips) should be at least 1:10^3
- The timing of the Pockels cells P2 channel 3 is the first point to check for leaks. Then channel 2 and the alignment.

- If the output of the regenerative amplifier with 17.0 A gives < 2.8 mJ play with the seed pulse again and optimize the buildup
- iterate with S1 if necessary
- If the output is still not sufficient one roundtrip of 10 ns The added dispersion will change the compression needed (the cavity should only be touched by experts who do not need this manual)
- With a pump beam of 16 A in the regenerative amplifier the output should be at least 5.8 mJ.
- Check with S2 the overlap of the pump laser. If this was not sufficient the multipass will need a new alignment with the milled alignment tool. (marked positions inside the laser) check if you get the beam with M6 only aligned before and after the crystal. if not you will have to use M5 too but this means the 3mJ option is lost and needs to be realigned later. M7 should be hit a little bit to the lower left side. M7 and M8 bring you through the second pass. You have to bring the beam again centered trough the telescope and the compressor.
- The power before the compressor should be 4.2 mJ without the multipass amplification at 17 A and above 6.8 mJ with Multipass pump laser at 17 A and you should have a nice spectrum there. Check the upper right corner of the Stretcher grating for damage (that is the last point the compressed pulse is hitting and the one getting damaged first)

qn

References

1. Norrish, R. G. W. ; Porter, G.: Chemical Reactions Produced by Very High Light Intensities. in: *Nature* 164 (1949), October, nr. 4172, p. 658–658

2. *partly taken from Wikipedia, idea based on NASA The electromagnetic Spectrum*. http://en.wikipedia.org/wiki/File:EM_Spectrum_Properties_edit.svg, last checked: 2011-11-24

3. Shannon, Claude ; Weaver, Warren: *The mathematical theory of communication*. Urbana : University of Illinois Press, 1998. – ISBN 9780252725463

4. Als-Nielsen, J. ; McMorrow, Des: *Elements of modern X-ray physics*. Wiley Chichester, 2001. – ISBN 9780471498582

5. Zewail, Ahmed H.: Femtochemistry. Past, present, and future. in: *Pure and Applied Chemistry* 72 (2000), nr. 12, p. 2219–2231

6. Rousse, Antoine ; Rischel, Christian ; Gauthier, Jean-Claude: Femtosecond x-ray crystallography. in: *Reviews of Modern Physics* 73 (2001), January, nr. 1, p. 17–31

7. Chergui, Majed ; Zewail, Ahmed H.: Electron and X-ray methods of ultrafast structural dynamics: advances and applications. in: *Chemphyschem : a European journal of chemical physics and physical chemistry* 10 (2009), January, nr. 1, p. 28–43

8. Bressler, C ; Chergui, Majed: Ultrafast X-ray absorption spectroscopy. in: *Chemical Reviews* 104 (2004), nr. 4, p. 1781–1812

9. Bressler, Christian ; Chergui, Majed: Molecular structural dynamics probed by ultrafast X-ray absorption spectroscopy. in: *Annual review of physical chemistry* 61 (2010), March, p. 263–82

10. Bargheer, Matias ; Zhavoronkov, N ; Woerner, M ; Elsaesser, Thomas: Recent progress in ultrafast X-ray diffraction. in: *Chemphyschem : a European journal of chemical physics and physical chemistry* 7 (2006), April, nr. 4, p. 783–92

11. Grätz, Matthias: *Characterisation and Application of a Laser-Based Hard X-Ray Source*. Lund, Lund University, PhD Thesis, 1998

12. Sjögren, Anders: *Laser-Matter Interactions at Extreme Irradiance: X-ray Generation and Relativistic Channelling*, Lund University, PhD Thesis, 2002

13. Tillman, Carl: *Development and Characterisation of a Laser-Based Hard X-ray Source*, Lund University, PhD Thesis, 1996

14. Harbst, Michael: *Generation and Applicatioins of Short-Pulse X-ray Radiation*. Lund, Lund University, PhD, 2005

15. *Lund Laser Center (LLC)*. http://www-llc.fysik.lth.se/, last checked: 2011-12-03

16. Lundh, Olle: *Laser-driven beams of fast ions, relativistic electrons and coherent x-ray photons*, Lund University, PhD Thesis, 2008. – Lund Reports on Atomic Physics LRAP-391

17. Lindau, Filip: *Laser-driven particle acceleration: Experimental investigations*, Lund University, Doctoral Thesis, 2007. – 211 S. – Lund Reports on Atomic Physics LRAP-378

18. Röntgen, Wilhelm C.: Über eine neue Art von Strahlen: vorläufige Mitteilung. (1895)

19. Koch, H. ; Motz, J.: Bremsstrahlung Cross-Section Formulas and Related Data. in: *Reviews of Modern Physics* 31 (1959), October, nr. 4, p. 920–955

20. Pratt, R H.: Bremsstrahlung energy spectra from electrons of kinetic energy 1 keV < T1 < 2000 keV incident on neutral atoms 2 < Z < 92*. in: *Atomic Data and Nuclear Data Tables* 20 (1977), August, nr. 2, p. 175–209

21. McCall, G H.: Calculation of X-ray Bremsstrahlung and characteristic line emission produced by a maxwellian electron-distribution. in: *Journal of Physics D-Applied Physics* 15 (1982), nr. 5, p. 823–831

22. Seltzer, S ; Berger, M: Bremsstrahlung spectra from electron interactions with screened atomic nuclei and orbital electrons. in: *Nuclear Instruments and Methods in Physics Research Section B: Beam Interactions with Materials and Atoms* 12 (1985), August, nr. 1, p. 95–134

23. Lamoureux, M ; Waller, P ; Charles, P ; Avdonina, N B.: Bremsstrahlung from thick targets and a diagnostic for electron energy distributions. in: *Physical Review E* 62 (2000), nr. 3, p. 4091–4095

24. Chen, Z L. ; Zhang, J ; Liang, T J. ; Teng, H ; Dong, Q L. ; Li, Y T. ; Sheng, Z M. ; Zhao, L Z. ; Tang, X W.: Z-dependence of hot electron generation in femtosecond laser interaction with solid targets. in: *Journal of Physics B-Atomic Molecular and Optical Physics* 37 (2004), nr. 3, p. 539–546

25. Galy, J ; Maučec, M ; Hamilton, D J. ; Edwards, R ; Magill, J: Bremsstrahlung production with high-intensity laser matter interactions and applications. in: *New Journal of Physics* 9 (2007), February, nr. 2, p. 23–23

26. Hemberg, O ; Otendal, M ; Hertz, Hans M.: Liquid-metal-jet anode X-ray tube. in: *Optical Engineering* 43 (2004), nr. 7, p. 1682–1688

27. Tuohimaa, Tomi: *Spontaneous and stimulated X-ray Raman scattering*. Stockholm, KTH Stockholm, PhD Thesis, 2011

28. Wiedemann, Helmut: *Synchrotron Radiation (Advanced Texts in Physics)*. Springer, 2010. – 274 S. – ISBN 3642077773

29. Duke, Philip: *Synchrotron Radiation: Production and Properties (Oxford Series on Synchrotron Radiation)*. Oxford University Press, USA, 2009. – 251 S. – ISBN 0199559090

30. Werin, Sverker ; Thorin, Sara ; Eriksson, Mikael ; Larsson, Jörgen: Short pulse facility for MAX-lab. in: *Nuclear Instruments and Methods in Physics Research Section A: Accelerators, Spectrometers, Detectors and Associated Equipment* 601 (2009), nr. 1-2, p. 98–107

31. Khan, Shaukat: *Collective Phenomena in Synchrotron Radiation Sources: Prediction, Diagnostics, Countermeasures (Particle Acceleration and Detection)*. Springer, 2011. – 203 S. – ISBN 364207068X

32. Jones, R.Clark: On The Relativistic Doppler Effect. in: *Journal of the Optical Society of America* 29 (1939), August, nr. 8, p. 337

33. Tanaka, Takashi ; Kitamura, Hideo: *Spectra - a synchrotron radiation calculation code*. http://radiant.spring8.or.jp/spectra/. Version: 2011, last checked: 2011-12-03

34. Thompson, A. C. (Publ.) ; Vaughan, D. (Publ.): *X-ray Data Booklet*. Second. Lawrence Berkeley National Laboratory, University of California, 2001

35. Clarke, James A.: *The Science and Technology of Undulators and Wigglers*. vol. 1. Oxford, England : Oxford University Press, 2004. – ISBN 9780198508557

36. Schoenlein, R. W.: Generation of Femtosecond Pulses of Synchrotron Radiation. in: *Science* 287 (2000), March, nr. 5461, p. 2237–2240

37. Zholents, A. ; Heimann, P. ; Zolotorev, M. ; Byrd, J.: Generation of subpicosecond x-ray pulses using RF orbit deflection. in: *Nuclear Instruments and Methods in Physics Research Section A: Accelerators, Spectrometers, Detectors and Associated Equipment* 425 (1999), nr. 1-2, p. 385–389

38. Waldschmidt, Geoff J. ; Borland, Michael ; Chae, Yong-Chul ; Harkay, KKatherine C. ; Horan, Douglas ; Nassiri, Alireza: Status of RF Deflecting Cavity Design for the Generation of Short X-ray Pulses in the Advanced Photon Source Storage Ring. in: *Proc of the 10th European Particle Accelerator Conference*. Edinburgh, 2006, 3460

39. *Free electon laser FLASH*. http://flash.desy.de/, last checked: 2011-12-03

40. *Free electron laser SACLA*. http://xfel.riken.jp/eng/index.html, last checked: 2011-12-03

41. *Free electron laser SLAC*. https://slacportal.slac.stanford.edu/sites/lcls_public/Pages/Default.aspx, last checked: 2011-12-03

42. Galayda, John N. ; Arthur, John ; Ratner, Daniel F. ; White, William E.: X-ray free-electron lasers present and future capabilities [Invited]. in: *Journal of the Optical Society of America B* 27 (2010), October, nr. 11, p. B106

43. *Ligthsources.org*. www.lightsources.org, last checked: 2011-12-03

44. Spence, D. E. ; Evans, J. M. ; Sleat, W. E. ; Sibbett, W.: Regeneratively initiated self-mode-locked Ti:sapphire laser. in: *Optics Letters* 16 (1991), November, nr. 22, p. 1762

45. Hilborn, Robert C.: Einstein coefficients, cross sections, f values, dipole moments, and all that. in: *American Journal of Physics* 50 (1982), nr. 11, p. 982

46. Saleh, Bahaa E. A. ; Teich, Malvin C.: *Fundamentals of Photonics*. 2nd. New York, USA : John Wiley & Sons, Inc., 2007 (Wiley Series in Pure and Applied Optics). – ISBN 0471839655

47. Strickland, Donna ; Mourou, Gerard: Compression of amplified chirped optical pulses. in: *Optics Communications* 55 (1985), October, nr. 6, p. 447–449

48. Backus, Sterling ; Durfee, Charles G. ; Murnane, Margaret M. ; Kapteyn, Henry C.: High power ultrafast lasers. in: *Review of Scientific Instruments* 69 (1998), nr. 3, p. 1207

49. Daimon, Masahiko ; Masumura, Akira: Measurement of the refractive index of distilled water from the near-infrared region to the ultraviolet region. in: *Applied Optics* 46 (2007), nr. 18, p. 3811

50. Genoud, Guillaume: *Laser-Driven Plasma Waves for Particle Acceleration and X-ray Production*, Lund University, PhD Thesis, 2011. – 214 S. – Lund Reports on Atomic Physics LRAP-443

51. Svanberg, S ; Larsson, J ; Persson, A ; Wahlström, Claes-Göran: Lund high-power laser facility-systems and first results. in: *Physica Scripta* 49 (1994), February, nr. 2, p. 187–197

52. Genoud, Guillaume ; Wojda, F ; Burza, M ; Persson, A ; Wahlström, Claes-Göran: Active control of the pointing of a multi-terawatt laser. in: *The Review of scientific instruments* 82 (2011), March, nr. 3, p. 033102

53. Gibbon, P.: *Short Pulse Laser Interactions with Matter: An Introduction*. World Scientific Publishing Company, 2005. – ISBN 1860941354

54. Mulser, Peter ; Bauer, Dieter: *Springer Tracts in Modern Physics*. vol. 238: *High Power Laser-Matter Interaction*. Berlin, Heidelberg : Springer Berlin Heidelberg, 2010. – 424 S. – ISBN 978–3–540–50669–0

55. Menzel, Ralf: *Photonics: linear and nonlinear interactions of laser light and matter*. vol. 24. 1st. Springer Verlag, 2001. – ISBN 3540670742

56. Eliezer, Shalom: *Interaction of High Power Lasers with Plasmas (Series in Plasma Physics)*. Taylor and Francis, 2001. – 304 S. – ISBN 0750307471

57. Jaroszynski, Dino A. ; Bingham, R. ; Cairns, R A. ; Jaroszynski, Dino A. (Publ.): *Laser-Plasma Interactions*. Taylor and Francis Group, 2009. – ISBN 1584887788

58. Kruer, William: *The Physics Of Laser Plasma Interactions (Frontiers in Physics)*. Westview Press, 2003. – 202 S. – ISBN 0813340837

59. Guo, T.: More power to X-rays: New developments in X-ray spectroscopy. in: *Laser & Photonics Review* 3 (2009), November, nr. 6, p. 591–622

60. Mourou, Gerard ; Tajima, Toshiki ; Bulanov, Sergei: Optics in the relativistic regime. in: *Reviews of Modern Physics* 78 (2006), April, nr. 2, p. 309–371

61. Esarey, E. ; Schroeder, C. ; Leemans, W.: Physics of laser-driven plasma-based electron accelerators. in: *Reviews of Modern Physics* 81 (2009), August, nr. 3, p. 1229–1285

62. Teubner, U. ; Gibbon, P.: High-order harmonics from laser-irradiated plasma surfaces. in: *Reviews of Modern Physics* 81 (2009), nr. 2, p. 445–479. – ISSN 0034–6861

63. Tajima, T. ; Dawson, J.: Laser Electron Accelerator. in: *Physical Review Letters* 43 (1979), July, nr. 4, p. 267–270

64. Rousse, Antoine ; Phuoc, Kim ; Shah, Rahul ; Pukhov, Alexander ; Lefebvre, Eric ; Malka, Victor ; Kiselev, Sergey ; Burgy, Fréderic ; Rousseau, Jean-Philippe ; Umstadter, Donald ; Hulin, Daniéle: Production of a keV X-Ray Beam from Synchrotron Radiation in Relativistic Laser-Plasma Interaction. in: *Physical Review Letters* 93 (2004), September, nr. 13

65. Faure, J ; Glinec, Y ; Pukhov, A ; Kiselev, S ; Gordienko, S ; Lefebvre, E ; Rousseau, J-P ; Burgy, F ; Malka, V: A laser-plasma accelerator producing monoenergetic electron beams. in: *Nature* 431 (2004), September, nr. 7008, p. 541–4

66. Schlenvoigt, H.-P. ; Haupt, K. ; Debus, A. ; Budde, F. ; Jäckel, O. ; Pfotenhauer, S. ; Schwoerer, H. ; Rohwer, E. ; Gallacher, J. G. ; Brunetti, E. ; Shanks, R. P. ; Wiggins, S. M. ; Jaroszynski, D. A.: A compact synchrotron radiation source driven by a laser-plasma wakefield accelerator. in: *Nature Physics* 4 (2007), December, nr. 2, p. 130–133

67. Malka, Victor ; Faure, Jérôme ; Gauduel, Yann A. ; Lefebvre, Erik ; Rousse, Antoine ; Phuoc, Kim T.: Principles and applications of compact laser-plasma accelerators. in: *Nature Physics* 4 (2008), nr. 6, p. 447–453

68. Hartemann, FV ; Gibson, DJ ; Brown, WJ ; Rousse, Antoine ; Phuoc, K. ; Mallka, V. ; Faure, J. ; Pukhov, A.: Compton scattering x-ray sources driven by laser wakefield acceleration. in: *Physical Review Special Topics - Accelerators and Beams* 10 (2007), January, nr. 1

69. Schwoerer, H. ; Liesfeld, B. ; Schlenvoigt, H.-P. ; Amthor, K.-U. ; Sauerbrey, R.: Thomson-Backscattered X Rays From Laser-Accelerated Electrons. in: *Physical Review Letters* 96 (2006), nr. 1

70. Schulze, K. S. ; Kaämpfer, T. ; Uschmann, I. ; Höfer, S. ; Loetzsch, R. ; Förster, E.: Laser-excited acoustical phonons probed by ultrashort pulses from a laser-driven x-ray diode. in: *Applied Physics Letters* 98 (2011), nr. 14, p. 141109

71. Egbert, A ; Chichkov, B. N. ; Ostendorf, A: Ultrashort X-ray source driven by femtosecond laser pulses. in: *Europhysics Letters (EPL)* 56 (2001), October, nr. 2, p. 228–233

72. Seres, E ; Seres, J ; Spielmann, C: Time resolved spectroscopy with femtosecond soft-x-ray pulses. in: *Applied Physics a-Materials Science & Processing* 96 (2009), nr. 1, p. 43–50

73. Brabec, Thomas ; Krausz, Ferenc: Intense few-cycle laser fields: Frontiers of nonlinear optics. in: *Reviews of Modern Physics* 72 (2000), nr. 2, p. 545–591

74. Krausz, Ferenc ; Ivanov, Misha: Attosecond physics. in: *Reviews of Modern Physics* 81 (2009), nr. 1, p. 163

75. Swoboda, Marko: *Attosecond Wave Packet Metrology*, Lund University, PhD Thesis, 2010. – Lund Reports on Atomic Physics LRAP-443

76. Compton, Arthur: The Spectrum of Scattered X-Rays. in: *Physical Review* 22 (1923), November, nr. 5, p. 409–413

77. Gunst, S B. ; Page, L A.: Compton scattering of 2.62-MeV gamma-rays by polarized electrons. in: *Physical Review* 92 (1953), nr. 4, p. 970–973

78. Priebe, G. ; Laundy, D. ; Macdonald, M.A. ; Diakun, G.P. ; Jamison, S.P. ; Jones, L.B. ; Holder, D.J. ; Smith, S.L. ; Phillips, P.J. ; Fell, B.D. ; Sheehy, B. ; Naumova, N. ; Sokolov, I.V. ; Ter-Avetisyan, S. ; Spohr, K. ; Krafft, G.A. ; Rosenzweig, J.B. ; Schramm, U. ; Grüner, F. ; Hirst, G.J. ; Collier, J. ; Chattopadhyay, S. ; Seddon, E.A.: Inverse Compton backscattering source driven by the multi-10 TW laser installed at Daresbury. in: *Laser and Particle Beams* 26 (2008), November, nr. 04, p. 649

79. Schoenlein, R. W. ; Leemans, W. P. ; Chin, A. H. ; Volfbeyn, P. ; Glover, T. E. ; Balling, P. ; Zolotorev, M. ; Kim, K.-J. ; Chattopadhyay, S. ; Shank, C. V.: Femtosecond X-ray Pulses at 0.4 A Generated by 90 Thomson Scattering: A Tool for Probing the Structural Dynamics of Materials. in: *Science* 274 (1996), October, nr. 5285, p. 236–238

80. Vogel, Helmut ; Gerthsen, Christian ; Meschede, Dieter (Publ.): *Gerthsen Physik*. Berlin/Heidelberg : Springer-Verlag, 1999 (Springer-Lehrbuch). – ISBN 3–540–25421–8

81. Bucksbaum, P. H. ; Freeman, R. R. ; Bashkansky, M. ; McIlrath, T. J.: Role of the ponderomotive potential in above-threshold ionization. in: *Journal of the Optical Society of America B* 4 (1987), May, nr. 5, p. 760

82. Keldysh, LV: Ionization in the field of a strong electromagnetic wave. in: *Soviet Physics JETP* 20 (1965), nr. 5, p. 1307–1314

83. Mézel, C. ; Bourgeade, A. ; Hallo, L.: Surface structuring by ultrashort laser pulses: A review of photoionization models. in: *Physics of Plasmas* 17 (2010), nr. 11, p. 113504

84. Boyd, Robert W. (Publ.) ; Lukishova, Svetlana G. (Publ.) ; Shen, Y.R. (Publ.): *Topics in Applied Physics*. vol. 114: *Self-focusing: Past and Present*. New York, NY : Springer New York, 2009. – ISBN 978–0–387–32147–9

85. Delfin, C. ; Lokhnygin, V. ; Mauritsson, J. ; Sjoegren, A. ; Wahlstroem, C.-G. ; Pukhov, A. ; Tsakiris, G. D.: Influence of laser pulse duration on relativistic channels. in: *Physics of Plasmas* 9 (2002), nr. 3, p. 937

86. Schmidt, Bruno E.: *White Light Filamentation: Tailoring & Application for Charge Reversal of Ag3-*, Freie Universitaet Berlin, PhD Thesis, 2008

87. Dharmadhikari, Aditya K. ; Mathur, Deepak ; Yamanouchi, Kaoru (Publ.) ; Giulietti, Antonio (Publ.) ; Ledingham, Kenneth (Publ.): *Springer Series in Chemical Physics*. vol. 98: *Progress in Ultrafast Intense Laser Science-White light generation and filamentation*. Berlin, Heidelberg : Springer Berlin Heidelberg, 2010. – 81–108 S. – ISBN 978–3–642–03824–2

88. Xi, Ting-Ting ; Lu, Xin ; Zhang, Jie: Interaction of Light Filaments Generated by Femtosecond Laser Pulses in Air. in: *Physical Review Letters* 96 (2006), nr. 2, p. 25003

89. Wagner, N L. ; Gibson, E A. ; Popmintchev, T ; Christov, I P. ; Murnane, M M. ; Kapteyn, H C.: Self-compression of ultrashort pulses through ionization-induced spatiotemporal reshaping. in: *Physical Review Letters* 93 (2004), nr. 17. ISBN 0031–9007

90. Zhang, Zhe ; Lu, Xin ; Liang, Wen-Xi ; Hao, Zuo-Qiang ; Zhou, Mu-Lin ; Wang, Zhao-Hua ; Liu, Xun ; Zhang, Jie: Triggering and guiding HV discharge in air by filamentation of single and dual fs pulses. in: *Optics Express* 17 (2009), nr. 5, p. 3461–3468

91. Genoud, Guillaume ; Cassou, K. ; Wojda, F. ; Ferrari, H. E. ; Kamperidis, C. ; Burza, M. ; Persson, A. ; Uhlig, J. ; Kneip, S. ; Mangles, S. P. D. ; Lifschitz, A. ; Cros, B. ; Wahlström, Claes-Göran: Laser-plasma electron acceleration in dielectric capillary tubes. in: *Applied Physics B* (2011)

92. Ehrlich, Y. ; Cohen, C. ; Zigler, A. ; Krall, J. ; Sprangle, P. ; Esarey, E.: Guiding of High Intensity Laser Pulses in Straight and Curved Plasma Channel Experiments. in: *Physical Review Letters* 77 (1996), November, nr. 20, p. 4186–4189

93. Courtois, C ; La Fontaine, A C. ; Landoas, O ; Lidove, G ; Meot, V ; Morel, P ; Nuter, R ; Lefebvre, E ; Boscheron, A ; Grenier, J ; Aleonard, M M. ; Gerbaux, M ; Gobet, F ; Hannachi, F ; Malka, G ; Scheurer, J N. ; Tarisien, M: Effect of plasma density scale length on the properties of bremsstrahlung x-ray sources created by picosecond laser pulses. in: *Physics of Plasmas* 16 (2009), nr. 1, p. 13105–13112

94. Andiel, U ; Eidmann, K ; Witte, K: Time-resolved x-ray K-shell spectra from high density plasmas generated by ultrashort laser pulses. in: *Physical Review E* 63 (2001), January, nr. 2, p. 0–26407

95. Rousse, Antoine ; Audebert, P. ; Geindre, J. ; Falliès, F. ; Gauthier, J. ; Mysyrowicz, A. ; Grillon, G. ; Antonetti, A.: Efficient Kα x-ray source from femtosecond laser-produced plasmas. in: *Physical Review E* 50 (1994), nr. 3, p. 2200–2207

96. Steingruber, J ; Borgstrom, S ; Starczewski, T ; Litzen, U: Prepulse dependence of X-ray emission from plasmas created by IR femtosecond laser pulses on solids. in: *Journal of Physics B-Atomic Molecular and Optical Physics* 29 (1996), nr. 2, p. 0

97. Estabrook, Kent ; Kruer, William L.: Properties of Resonantly Heated Electron Distributions. in: *Physical Review Letters* 40 (1978), January, nr. 1, p. 42–45

98. Forslund, D. D. ; Kindel, JM ; Lee, K: Theory of Hot-Electron Spectra at High Laser Intensity. in: *Physical Review Letters* 39 (1977), August, nr. 5, p. 284–288

99. Gibbon, P. ; Bell, A.: Collisionless absorption in sharp-edged plasmas. in: *Physical Review Letters* 68 (1992), March, nr. 10, p. 1535–1538

100. Brunel, F: Not-so-resonant, resonant absorption. in: *Physical Review Letters* 59 (1987), July, nr. 1, p. 52–55

101. Brunel, F: Anomalous absorption of high intensity subpicosecond laser pulses. in: *Physics of Fluids* 31 (1988), nr. 9, p. 2714

102. Grimes, M. ; Rundquist, A. ; Lee, Y.-S. ; Downer, M.: Experimental Identification of Vacuum Heating at Femtosecond-Laser-Irradiated Metal Surfaces. in: *Physical Review Letters* 82 (1999), May, nr. 20, p. 4010–4013

103. Jiang, Y ; Lee, T ; Rose-Petruck, Christoph G.: Generation of ultrashort hard-x-ray pulses with tabletop laser systems at a 2-kHz repetition rate. in: *Journal of the Optical Society of America B-Optical Physics* 20 (2003), nr. 1, p. 229–237

104. Henke, B: X-Ray Interactions: Photoabsorption, Scattering, Transmission, and Reflection at E = 50-30,000 eV, Z = 1-92. in: *Atomic Data and Nuclear Data Tables* 54 (1993), July, nr. 2, p. 181–342

105. Berger, M J. ; Coursey, J S. ; Zucker, M A. ; Chang, J: *ESTAR: Electron Stopping-Power and Ranges*. http://physics.nist.gov/PhysRefData/Star/Text/ESTAR.html. Version: 2005, last checked: 2011-12-02

106. Gibbon, P. ; Mašek, M. ; Teubner, U. ; Lu, W. ; Nicoul, M. ; Shymanovich, U. ; Tarasevitch, A. ; Zhou, P. ; Sokolowski-Tinten, K. ; Linde, D.: Modelling and optimisation of fs laser-produced K α sources. in: *Applied Physics A* 96 (2009), March, nr. 1, p. 23–31

107. Zastrau, U. ; Audebert, P. ; Bernshtam, V. ; Brambrink, E. ; Kämpfer, T. ; Kroupp, E. ; Loetzsch, R. ; Maron, Y. ; Ralchenko, Yu. ; Reinholz, H. ; Röpke, G. ; Sengebusch, A. ; Stambulchik, E. ; Uschmann, I. ; Weingarten, L. ; Förster, E.: Temperature and Kα -yield radial distributions in laser-produced solid-density plasmas imaged with ultrahigh-resolution x-ray spectroscopy. in: *Physical Review E* 81 (2010), February, nr. 2

108. Chen, H ; Wilks, Scott C. ; Kruer, William L. ; Patel, P K. ; Shepherd, R: Hot electron energy distributions from ultraintense laser solid interactions. in: *Physics of Plasmas* 16 (2009), nr. 2, p. 020705

109. Anand, M ; Gibbon, P. ; Krishnamurthy, M: Hot electrons produced from long scale-length laser-produced droplet plasmas. in: *Laser Physics* 17 (2007), nr. 4, p. 408–414

110. Giulietti, Antonio ; Gamucci, Andrea ; Yamanouchi, Kaoru (Publ.) ; Giulietti, Antonio (Publ.) ; Ledingham, Kenneth (Publ.): *Springer Series in Chemical Physics*. vol. 98: *Progress in Ultrafast Intense Laser Science-Propagation of high intensity laser pulses in plasma*. Berlin, Heidelberg : Springer Berlin Heidelberg, 2010. – 139–163 S. – ISBN 978–3–642–03824–2

111. Wilks, Scott C. ; Kruer, William L.: Absorption of ultrashort, ultra-intense laser light by solids and overdense plasmas. in: *Ieee Journal of Quantum Electronics* 33 (1997), nr. 11, p. 1954–1968

112. Rettig, C. L. ; Roquemore, W. M. ; Gord, J. R.: Efficiency and scaling of an ultrashort-pulse high-repetition-rate laser-driven X-ray source. in: *Applied Physics B* 93 (2008), August, nr. 2-3, p. 365–372

113. Thoss, Andreas: *X-ray Emission and Particle Acceleration from a Liquid Jet Target Using a 1-kHz Ultrafast Laser System*, PhD Thesis, 2003. http://www.diss.fu-berlin.de/2003/240/thoss.pdf

114. Murnane, M M. ; Kapteyn, H C. ; Rosen, M D. ; Falcone, R W.: Ultrafast X-ray Pulses from Laser-Produced Plasmas. in: *Science (New York, N.Y.)* 251 (1991), February, nr. 4993, p. 531–6

115. Teubner, U ; Gibbon, P. ; Altenbernd, D ; Oberschmidt, D ; Forster, E ; Mysyrowicz, A ; Audebert, P ; Geindre, J P. ; Gauthier, J C.: Plasma frequency and harmonic emission from fs-laser plasmas. in: *Laser and Particle Beams* 17 (1999), nr. 4, p. 613–619

116. Ziener, C ; Uschmann, I ; Stobrawa, G ; Reich, C ; Gibbon, P. ; Feurer, T ; Morak, A ; Dusterer, S ; Schwoerer, H ; Forster, E ; Sauerbrey, R: Optimization of K alpha bursts for photon energies between 1.7 and 7 keV produced by femtosecond-laser-produced plasmas of different scale length. in: *Physical Review E* 65 (2002), nr. 6

117. Sjögren, Anders ; Harbst, M ; Wahlström, C.-G. ; Svanberg, S ; Olsson, C: High-repetition-rate, hard x-ray radiation from a laser-produced plasma: Photon yield and application considerations. in: *Review of Scientific Instruments* 74 (2003), nr. 4, p. 2300

118. Hagedorn, M. ; Kutzner, J. ; Tsilimis, G. ; Zacharias, H.: High-repetition-rate hard X-ray generation with sub-millijoule femtosecond laser pulses. in: *Applied Physics B: Lasers and Optics* 77 (2003), August, nr. 1, p. 49–57

119. Hou, B. ; Nees, J. ; Mordovanakis, A. ; Wilcox, M. ; Mourou, G. ; Chen, L.M. ; Kieffer, J.-C. ; Chamberlain, C.C. ; Krol, A.: Hard X-ray generation from solids driven by relativistic intensity in the lambda-cubed regime. in: *Applied Physics B* 83 (2006), January, nr. 1, p. 81–85

120. Dorchies, F. ; Harmand, M. ; Descamps, D. ; Fourment, C. ; Hulin, S. ; Petit, S. ; Peyrusse, O. ; Santos, J. J.: High-power 1 kHz laser-plasma x-ray source for ultrafast x-ray absorption near-edge spectroscopy in the keV range. in: *Applied Physics Letters* 93 (2008), nr. 12, p. 121113

121. Zhavoronkov, Nickolai ; Gritsai, Yuri ; Bargheer, Matias ; Woerner, Michael ; Elsaesser, Thomas ; Zamponi, Flavio ; Uschmann, Ingo ; Förster, Eckhart: Microfocus Cu Kα source for femtosecond x-ray science. in: *Optics Letters* 30 (2005), nr. 13, p. 1737

122. Zamponi, F. ; Ansari, Z. ; Woerner, M. ; Elsaesser, Thomas: Femtosecond powder diffraction with a laser-driven hard X-ray source. in: *Optics Express* 18 (2010), January, nr. 2, p. 947

123. Rose-Petruck, Christoph ; Jimenez, Ralph ; Guo, Ting ; Cavalleri, Andrea ; Siders, Craig W. ; Rksi, Ferenc ; Squier, Jeff A. ; Walker, Barry C. ; Wilson, Kent R. ; Barty, Christopher P. J.: Picosecond-milliångström lattice dynamics measured by ultrafast X-ray diffraction. in: *Nature* 398 (1999), March, nr. 6725, p. 310–312

124. Chen, J ; Zhang, H ; Tomov, I V. ; Wolfsherg, M ; Ding, X L. ; Rentzepis, P.M.: Transient structures and kinetics of the ferrioxalate redox reaction studied by time-resolved EXAFS, optical spectroscopy, and DFT. in: *Journal of Physical Chemistry A* 111 (2007), nr. 38, p. 9326–9335

125. Beck, Michael: *Characterisation of an XUV laser driven plasma source and its application to NEXAFS-spectroscopy of organic molecules*, Technische Uni Berlin, PhD Thesis, 2002. http://opus.kobv.de/tuberlin/volltexte/2002/396/

126. Vogt, Ulrich ; Wilhein, Thomas ; Stiel, Holger ; Legall, Herbert: High resolution x-ray absorption spectroscopy using a laser plasma radiation source. in: *Review of Scientific Instruments* 75 (2004), nr. 11, p. 4606

127. Larsson, J ; Sjögren, Anders: Evaluation of laser-irradiated Ar clusters as a source for time-resolved x-ray studies. in: *Review of Scientific Instruments* 70 (1999), nr. 5, p. 2253

128. Issac, R. ; Wirthig, J. ; Brunetti, E. ; Vieux, G. ; Ersfeld, B. ; Jamison, S.P. ; Jones, D. ; Bingham, R. ; Clark, D. ; Jaroszynski, D.A.: Bright source of K[alpha] and continuum X rays by heating Kr clusters using a femtosecond laser. in: *Laser and Particle Beams* 21 (2004), March, nr. 04

129. Dorchies, F: *Ultra short x-ray source from laser-clusters interaction*. vol. 5975. SPIE, 2006. – 597501–597501–6 S. – ISBN 0277–786X

130. Chakravarty, U. ; Naik, P.A. ; Kumbhare, S.R. ; Gupta, P.D.: Efficient keV X-ray Generation from Irradiation of in-situ Produced Silver Clusters by Ti:sapphire Laser Pulses. in: *Journal of the Optical Society of Korea* 13 (2009), March, nr. 1, p. 80–85

131. Rymell, L ; Hertz, H: Droplet target for low-debris laser-plasma soft X-ray generation. in: *Optics Communications* 103 (1993), November, nr. 1-2, p. 105–110

132. Anand, M ; Safvan, C P. ; Krishnamurthy, M: Hard X-ray generation from microdroplets in intense laser fields. in: *Applied Physics B-Lasers and Optics* 81 (2005), nr. 4, p. 469–477

133. Kugland, N. L. ; Constantin, C. G. ; Neumayer, P. ; Chung, H.-K. ; Collette, A. ; Dewald, E. L. ; Froula, D. H. ; Glenzer, S. H. ; Kemp, A. ; Kritcher, A. L. ; Ross, J. S. ; Niemann, C.: High Kα x-ray conversion efficiency from extended source gas jet targets irradiated by ultra short laser pulses. in: *Applied Physics Letters* 92 (2008), nr. 24, p. 241504

134. Thoss, Andreas ; Richardson, M ; Korn, G ; Faubel, M ; Stiel, H ; Vogt, U ; Elsaesser, Thomas: Kilohertz sources of hard x rays and fast ions with femtosecond laser plasmas. in: *Journal of the Optical Society of America B* 20 (2003), nr. 1, p. 224–228

135. Tompkins, R J. ; Mercer, I P. ; Fettweis, M ; Barnett, C J. ; Klug, D R. ; Porter, L G. ; Clark, I ; Jackson, S ; Matousek, P ; Parker, A W. ; Towrie, M: 5-20 keV laser-induced x-ray generation at 1 kHz from a liquid-jet target. in: *Review of Scientific Instruments* 69 (1998), nr. 9, p. 3113–3117

136. Vogt, Ulrich: Scaling-up a liquid water jet laser plasma source to high average power for extreme-ultraviolet lithography. in: *Proceedings of SPIE* vol. 4343, SPIE, 2001, p. 535–542

137. Korn, Georg ; Thoss, Andreas ; Stiel, Holger ; Vogt, Ullrich ; Richardson, Martin ; Faubel, Manfred ; Elsaesser, *Thomas: Ultrashort 1-kHz laser plasma hard x-ray source. in: *Optics Letters* 27 (2002), May, nr. 10, p. 866

138. Li, Y. ; Zhang, J. ; Sheng, Z. ; Teng, H. ; Liang, T. ; Peng, X. ; Lu, X. ; Tang, X.: Spatial Distribution of High-Energy Electron Emission from Water Plasmas Produced by Femtosecond Laser Pulses. in: *Physical Review Letters* 90 (2003), April, nr. 16

139. Hansson, B A M. ; Berglund, M ; Hemberg, O ; Hertz, Hans M.: Stabilization of liquified-inert-gas jets for laser-plasma generation. in: *Journal of Applied Physics* 95 (2004), nr. 8, p. 4432–4437

140. Hatanaka, K ; Miura, T ; Fukumura, H: White X-ray pulse emission of alkali halide aqueous solutions irradiated by focused femtosecond laser pulses: a spectroscopic study on electron temperatures as functions of laser intensity, solute concentration, and solute atomic number. in: *Chemical Physics* 299 (2004), April, nr. 2-3, p. 265–270. ISBN 0301–0104

141. Reich, Christian ; Laperle, Christopher M. ; Li, Xiaodi ; Ahr, Brian ; Benesch, Frank ; Rose-Petruck, Christoph G.: Ultrafast x-ray pulses emitted from a liquid mercury laser target. in: *Optics Letters* 32 (2007), nr. 4, p. 427

142. Shan, Fang ; Guo, Ting: Ultrafast selected energy x-ray absorption spectroscopy investigations of Ni and Zn species. in: *The Journal of chemical physics* 122 (2005), June, nr. 24, p. 244710

143. Cheng, Guangjun ; Shan, Fang ; Freyer, A ; Guo, Ting: Ultrafast x-ray absorption spectroscopy using laser-driven electron x-ray sources (LEXS). in: *Proceedings of SPIE* vol. 4504, SPIE, 2001, p. 1–7

144. Fourmaux, S ; Lecherbourg, L ; Harmand, M ; Servol, M ; Kieffer, J C.: High repetition rate laser produced soft x-ray source for ultrafast x-ray absorption near edge structure measurements. in: *The Review of scientific instruments* 78 (2007), November, nr. 11, p. 113104

145. Eason, R W. ; Bradley, D K. ; Kilkenny, J D. ; Greaves, G N.: Improved laser-EXAFS studies of aluminium foil. in: *Journal of Physics C: Solid State Physics* 17 (1984), October, nr. 28

146. Tomov, I: Ultrafast X-ray determination of transient structures in solids and liquids. in: *Chemical Physics* 299 (2004), April, nr. 2-3, p. 203–213

147. Tomov, Ivan V. ; Rentzepis, Peter M.: Ultrafast time-resolved transient structures of solids and liquids by means of extended X-ray absorption fine structure. in: *Chemphyschem : a European journal of chemical physics and physical chemistry* 5 (2004), January, nr. 1, p. 27–35

148. Ráksi, Ferenc ; Wilson, Kent R. ; Jiang, Zhiming ; Ikhlef, Abdelaziz ; Côté, Christian Y. ; Kieffer, Jean-Claude: Ultrafast x-ray absorption probing of a chemical reaction. in: *The Journal of Chemical Physics* 104 (1996), nr. 15, p. 6066

149. Oulianov, D A.: Structures of bromoalkanes' photodissociation in solution by means of ultrafast extended x-ray absorption fine-structure spectroscopy. in: *Proceedings of the National Academy of Sciences* 99 (2002), September, nr. 20, p. 12556–12561

150. Lee, T ; Jiang, Y ; Rose-Petruck, C G. ; Benesch, F: Ultrafast tabletop laser-pump-x-ray probe measurement of solvated Fe(CN)(6)(4-). in: *Journal of Chemical Physics* 122 (2005), nr. 8, p. 084506

151. Benesch, Frank ; Lee, Taewoo ; Jiang, Yan ; Rose-Petruck, Christoph G.: Ultrafast laser-driven x-ray spectrometer for x-ray absorption spectroscopy of transition metal complexes. in: *Optics Letters* 29 (2004), nr. 9, p. 1028

152. Fourment, C ; Arazam, N ; Bonte, C ; Caillaud, T ; Descamps, D ; Dorchies, F ; Harmand, M ; Hulin, S ; Petit, S ; Santos, J J.: Broadband, high dynamics and high resolution charge coupled device-based spectrometer in dynamic mode for multi-keV repetitive x-ray sources. in: *The Review of scientific instruments* 80 (2009), nr. 8, p. 083505

153. Eggers, J ; Villermaux, E: Physics of liquid jets. in: *Reports on Progress in Physics* 71 (2008), nr. 3, p. 036601

154. Strong, John: *Procedures in Experimental Physics*. Lindsay Pubns, 1986. – 642 S. – ISBN 0917914562

155. Pollard, Alan Faraday C.: *The kinematical design of couplings in instrument mechanisms*. Hilger Division, Hilger & Watts, 1951

156. Furse, J E.: Kinematic design of fine mechanisms in instruments. in: *Journal of Physics E: Scientific Instruments* 14 (1981), March, nr. 3, p. 264–272

157. Vig, Asger L.: *Pinched Flow Fractionation - Technology and Application*, Technical University of Denmark, PhD Thesis, 2010

158. Sergey, Stephanov: *TER_sl online tool from Stephanovs X-ray server*. http://sergey.gmca.aps.anl.gov/TER_sl.html#TER_sl, last checked: 2011.10.14

159. Warren, B E.: *X-Ray Diffraction*. Dover Publications, 1990. – ISBN 0–486–66317–5

160. Erko, A ; Idir, M ; Krist, T ; Michette, AG: *Springer Series in optical science*. vol. 137: *Modern Developments in X-Ray and Neutron Optics*. Berlin, Heidelberg : Springer Berlin Heidelberg, 2008. – ISBN 978–3–540–74560–0

161. Ewald, P. P.: The so-called correction of Bragg's law. in: *Acta Crystallographica Section A Foundations of Crystallography* 42 (1986), November, nr. 6, p. 411–413

162. Chantler, C.T ; Olsen, K. ; Dragoset, R.A. ; Kishore, A.R. ; Kotochigova, S.A. ; Zucker, D.S.: *X-Ray Form Factor, Attenuation and Scattering Tables*. http://www.nist.gov/pml/data/ffast/index.cfm, last checked: 2011-12-12

163. Uhlig, Jens ; Fullagar, Wilfred K. ; Svensson, C. ; Cerenius, Y: Microfocus Tube Source Recommissioning. in: *Maxlab Activity Report*, 2006, p. 343–343

164. *Use of a Kumakhov lens in analytic instruments*. 1996. – US patent no. 5497008 filed 1995

165. Schields, Paul J. ; Gibson, David M. ; Gibson, Walter M. ; Gao, Ning ; Huang, Huapeng ; Ponomarev, Igor Y.: Overview of polycapillary X-ray optics. in: *Powder Diffraction* 17 (2002), nr. 2, p. 70

166. Putkunz, Corey T. ; Peele, Andrew G.: Detailed simulation of a Lobster-eye telescope. in: *Optics Express* 17 (2009), July, nr. 16, p. 14156

167. Kirkpatrick, Paul ; Baez, A. V.: Formation of Optical Images by X-Rays. in: *Journal of the Optical Society of America* 38 (1948), September, nr. 9, p. 766

168. Bunker, Grant: *Introduction to XAFS-A practical guide to X-ray absorption fine structure Spectroscopy*. Illinois Institute of Technology, 2010. – ISBN 978–0521767750

169. Bargheer, M. ; Zhavoronkov, N. ; Bruch, R. ; Legall, H. ; Stiel, H. ; Woerner, M. ; Elsaesser, T.: Comparison of focusing optics for femtosecond X-ray diffraction. in: *Applied Physics B* 80 (2005), April, nr. 6, p. 715–719

170. Broglie, Louis D.: The wave nature of the electron. in: *Nobel lecture 12 December 1929.*, 1929

171. Berger, M.J. ; Hubbell, J.H. ; Seltzer, S.M. ; Chang, J. ; Coursey, J.S. ; Sukumar, R. ; Zucker, D.S. ; Olsen, K.: *NIST XCOM: Photon Cross Sections Database*. http://www.nist.gov/pml/data/xcom/index.cfm. Version: 2010, last checked: 18/11/11

172. Lambert, I.H.: Lambert law of absorption. Version: 1760. http://imgbase-scd-ulp.u-strasbg.fr/displayimage.php?pos=-16594. in: *Photometria sive de mensura et gradibus luminis, colorum et umbrae*. Eberhardt Klett, Germany, 1760, chapter 5, 391

173. Beer, August: Bestimmung der Absorption des rothen Lichts in farbigen Flüssigkeiten. in: *Annalen der Physik und Chemie* 86 (1852), p. 78–88

174. Landau, Lew D. ; Lifschitz, Ewgeni M. ; Ziesche, Paul. (Publ.): *Quantenmechanik, Lehrbuch der theoretischen Physik, 10 Bde.*. vol. 3. reprint 9th edition. Deutsch (Harri), 1992. – 142–152 S. – ISBN 3817113285

175. Rehr, J J. ; Albers, R C.: Theoretical approaches to x-ray absorption fine structure. in: *Reviews of Modern Physics* 72 (2000), nr. 3, p. 621–654

176. Newville, Matthew: Fundamentals of XAFS. in: *Consortium for Advanced Radiation Sources, University of Chicago (USA)[http://xafs. org]* (2004). http://streaming.lehigh.edu/rm/dept/IMI/VirtualGlassCourse/SuppReading/Tutorials.pdf

177. Krause, M. O. ; Oliver, J. H.: Natural widths of atomic K and L levels, Kα X-ray lines and several KLL Auger lines. in: *Journal of Physical and Chemical Reference Data* 8 (1979), nr. 2, p. 329

178. Bergmann, Uwe ; Glatzel, Pieter: X-ray emission spectroscopy. in: *Photosynthesis research* (2009), August

179. Brown, Frank L. H. ; Wilson, Kent R. ; Cao, Jianshu: Ultrafast extended x-ray absorption fine structure (EXAFS)-theoretical considerations. in: *The Journal of Chemical Physics* 111 (1999), nr. 14, p. 6238

180. Groot, Frank de ; Vankó, György ; Glatzel, Pieter: The 1s x-ray absorption pre-edge structures in transition metal oxides. in: *Journal of Physics: Condensed Matter* 21 (2009), March, nr. 10, p. 104207

181. Yano, Junko ; Yachandra, Vittal K.: X-ray absorption spectroscopy. in: *Photosynthesis research* 102, nr. 2-3, p. 241–54

182. Stöhr, Joachim: *NEXAFS Spectroscopy (Springer Series in Surface Sciences)*. Springer, 1992. – ISBN 3540544224

183. Glatzel, Pieter ; Bergmann, U: High resolution 1s core hole X-ray spectroscopy in 3d transition metal complexes: electronic and structural information. in: *Coordination Chemistry Reviews* 249 (2005), January, nr. 1-2, p. 65–95

184. Groot, Frank de: Multiplet effects in X-ray spectroscopy. in: *Coordination Chemistry Reviews* 249 (2005), January, nr. 1-2, p. 31–63

185. Hennies, Franz ; Pietzsch, Annette ; Berglund, Martin ; Föhlisch, Alexander ; Schmitt, Thorsten ; Strocov, Vladimir ; Karlsson, Hans O. ; Andersson, Joakim ; Rubensson, Jan-Erik: Resonant Inelastic Scattering Spectra of Free Molecules with Vibrational Resolution. in: *Physical Review Letters* 104 (2010), May, nr. 19

186. Schwalbe, Matthias: *Heterosupramolekulare Oligometallkatalysatoren: Synthese und Reaktivitätssteuerung durch Photoelektronentransfer*, Friedrich Schiller Universitaet Jena, PhD Thesis, 2007

187. Lei, Pengxiang ; Hedlund, Maria ; Lomoth, Reiner ; Rensmo, Hå k. ; Johansson, Olof ; Hammarström, Leif: The role of colloid formation in the photoinduced H2 production with a Ru(II)-Pd(II) supramolecular complex: a study by GC, XPS, and TEM. in: *Journal of the American Chemical Society* 130 (2008), January, nr. 1, p. 26–7

188. Ozawa, Hironobu ; Haga, Masa-aki ; Sakai, Ken: A photo-hydrogen-evolving molecular device driving visible-light-induced EDTA-reduction of water into molecular hydrogen. in: *Journal of the American Chemical Society* 128 (2006), April, nr. 15, p. 4926–7

189. Smolentsev, G. ; Uhlig, J. ; Nazarenko, E. ; M., Pfeffer ; B., Dietzek ; Rau, S.: *working title: Evolution of Ru-Pt and Ru-Pd catalysts upon optical excitation*. Manuscript in preparation,

190. Tschierlei, Stefanie ; Presselt, Martin ; Kuhnt, Christian ; Yartsev, Arkady ; Pascher, Torbjörn ; Sundström, Villy ; Karnahl, Michael ; Schwalbe, Matthias ; Schäfer, Bernhard ; Rau, Sven ; Schmitt, Michael ; Dietzek, Benjamin ; Popp, Jürgen: Photophysics of an intramolecular hydrogen-evolving Ru-Pd photocatalyst. in: *Chemistry (Weinheim an der Bergstrasse, Germany)* 15 (2009), August, nr. 31, p. 7678–88. – ISSN 1521–3765

191. Magnuson, Ann ; Anderlund, Magnus ; Johansson, Olof ; Lindblad, Peter ; Lomoth, Reiner ; Polivka, Tomas ; Ott, Sascha ; Stensjö, Karin ; Styring, Stenbjörn ; Sundström, Villy ; Hammarström, Leif: Biomimetic and microbial approaches to solar fuel generation. in: *Accounts of chemical research* 42 (2009), December, nr. 12, p. 1899–909

192. Gordon, John C. ; Kubas, Gregory J.: Perspectives on How Nature Employs the Principles of Organometallic Chemistry in Dihydrogen Activation in Hydrogenases â€ . in: *Organometallics* 29 (2010), November, nr. 21, p. 4682–4701

193. Chen, Lin X. ; Zhang, Xiaoyi ; Lockard, Jenny V. ; Stickrath, Andrew B. ; Attenkofer, Klaus ; Jennings, Guy ; Liu, Di-Jia: Excited-state molecular structures captured by X-ray transient absorption spectroscopy: a decade and beyond. in: *Acta crystallographica. Section A, Foundations of crystallography* 66 (2010), March, nr. Pt 2, p. 240–51

194. Johnson, S.L. ; Milne, C.J.: Ultrafast X-ray science: structural transients in solution. in: *TrAC Trends in Analytical Chemistry* 29 (2010), June, nr. 6, p. 497–507

195. Gawelda, Wojciech: *Time-resolved x-ray absorption spectroscopy of transition metal complexes*, École Polytechnique Fédérale de Lausanne, PhD Thesis, 2006

196. Materials, Exafs: *EXAFS materials reference spectra*. http://exafsmaterials.com/ReferenceSpectra.html, last checked: 18/12/12

197. Absorption Society, International X.: *IXAS database*. http://ixs.iit.edu/database/, last checked: 18/12/11

198. *With friendly permission from Wilfred Fullagar*. 2011

199. Ponchut, Cyril: Characterization of X-ray area detectors for synchrotron beamlines. in: *Journal of synchrotron radiation* 13 (2006), March, nr. Pt 2, p. 195–203

200. Howe, J. ; Chambers, D. M. ; Courtois, C. ; Förster, E. ; Gregory, C. D. ; Hall, I. M. ; Renner, O. ; Uschmann, I. ; Woolsey, N. C.: Comparison of film detectors, charged-coupled devices, and imaging plates in x-ray spectroscopy of hot dense plasma. in: *Review of Scientific Instruments* 77 (2006), nr. 3, p. 036105

201. Hall, C: 2D detectors for synchrotron X-ray sources, some comparative tests. in: *Nuclear Instruments and Methods in Physics Research Section A: Accelerators, Spectrometers, Detectors and Associated Equipment* 310 (1991), nr. 1-2, p. 215–219

202. Hall, C. J. ; Lewis, R. A. ; Parker, B. ; Worgan, J. S.: The secret life of image plate phosphors. in: *Review of Scientific Instruments* 63 (1992), nr. 1, p. 697

203. Kim, Yong-Ki ; Rudd, M.: Binary-encounter-dipole model for electron-impact ionization. in: *Physical Review A* 50 (1994), November, nr. 5, p. 3954–3967

204. Carron, N: *An introduction to the passage of energetic particles through matter*. Boca Raton : Taylor & Francis, 2007. – ISBN 9780750309356

205. Fano, U.: On the Theory of Ionization Yield of Radiations in Different Substances. in: *Physical Review* 70 (1946), July, nr. 1-2, p. 44–52

206. Tung, C. ; Ashley, J. ; Ritchie, R.: Electron inelastic mean free paths and energy losses in solids II: Electron gas statistical model. in: *Surface Science* 81 (1979), March, nr. 2, p. 427–439

207. Vavilov, V: On photo-ionization by fast electrons in germanium and silicon. in: *Journal of Physics and Chemistry of Solids* 8 (1959), January, p. 223–226

208. Bichsel, Hans: Straggling in thin silicon detectors. in: *Reviews of Modern Physics* 60 (1988), July, nr. 3, p. 663–699

209. Barends, R. ; Baselmans, J. J. A. ; Yates, S. J. C. ; Gao, J. R. ; Hovenier, J. N. ; Klapwijk, T. M.: Quasiparticle Relaxation in Optically Excited High-Q Superconducting Resonators. in: *Physical Review Letters* 100 (2008), June, nr. 25

210. Timofeev, A. ; García, C. ; Kopnin, N. ; Savin, A. ; Meschke, M. ; Giazotto, F. ; Pekola, J.: Recombination-Limited Energy Relaxation in a Bardeen-Cooper-Schrieffer Superconductor. in: *Physical Review Letters* 102 (2009), January, nr. 1

211. Kozorezov, A. ; Wigmore, J. ; Martin, D. ; Verhoeve, P. ; Peacock, A.: Electron energy down-conversion in thin superconducting films. in: *Physical Review B* 75 (2007), March, nr. 9

212. Kozorezov, A. ; Pepe, G. ; Golubov, A. ; Martin, D. ; Wigmore, J. K.: Thermalisation in metals on a sub-picosecond time scale, American Institute of Physics (AIP), 2009, 298–301

213. Kozorezov, A.: Energy down-conversion and thermalization in metal absorbers. in: *To be published as special issue in in the Journal of Low Temperature Physics*, 2011

214. Fano, U: Ionization Yield of Radiations. II. The Fluctuations of the Number of Ions. in: *Physical Review* 72 (1947), July, nr. 1, p. 26–29

215. Roosbroeck, W. van: Theory of the Yield and Fano Factor of Electron-Hole Pairs Generated in Semiconductors by High-Energy Particles. in: *Physical Review* 139 (1965), August, nr. 5A, p. A1702–A1716

216. Mazziotta, M.: Electron-hole pair creation energy and Fano factor temperature dependence in silicon. in: *Nuclear Instruments and Methods in Physics Research Section A: Accelerators, Spectrometers, Detectors and Associated Equipment* 584 (2008), January, nr. 2-3, p. 436–439

217. Fraser, G. ; Abbey, A. ; Holland, A. ; McCarthy, K. ; Owens, A ; Wells, A: The X-ray energy response of silicon Part A. Theory. in: *Nuclear Instruments and Methods in Physics Research Section A: Accelerators, Spectrometers, Detectors and Associated Equipment* 350 (1994), October, nr. 1-2, p. 368–378

218. Harrison, M. ; McGregor, D. ; Doty, F.: Fano factor and nonuniformities affecting charge transport in semiconductors. in: *Physical Review B* 77 (2008), May, nr. 19

219. Janesick, James: *Scientific charge-coupled devices*. Bellingham, Wash : SPIE Press, 2001. – ISBN 0819436984

220. Robbins, M S. ; Hadwen, B J.: The noise performance of electron multiplying charge-coupled devices. in: *Ieee Transactions on Electron Devices* 50 (2003), p. 1227–1232

221. inc e2v: *e2v datasheet L3C216 electron multiplying CCD*, http://www.e2v.com/products-and-services/high-performance-imaging-solutions/datasheets/ccd-selector/, last checked: 2011-11-22

222. Lima, Frederico A. ; Milne, Christopher J. ; Amarasinghe, Dimali C V. ; Rittmann-Frank, Mercedes H. ; Veen, Renske M. d. ; Reinhard, Marco ; Pham, Van-Thai ; Karlsson, Susanne ; Johnson, Steven L. ; Grolimund, Daniel ; Borca, Camelia ; Huthwelker, Thomas ; Janousch, Markus ; Mourik, Frank van ; Abela, Rafael ; Chergui, Majed: A high-repetition rate scheme for synchrotron-based picosecond laser pump/x-ray probe experiments on chemical and biological systems in solution. in: *The Review of scientific instruments* 82 (2011), June, nr. 6, p. 063111

223. Lutz, G: Silicon drift and pixel devices for X-ray imaging and spectroscopy. in: *Journal of synchrotron radiation* 13 (2006), March, nr. Pt 2, p. 99–109

224. Owens, Alan: Semiconductor materials and radiation detection. in: *Journal of synchrotron radiation* 13 (2006), March, nr. 2, p. 143–50

225. Ahmed, Syed: *Physics and engineering of radiation detection*. San Diego London : Academic Press, 2007. – ISBN 0120455811

226. Richmond, Michael: *Modiefied from: Introduction to CCDs*. http://spiff.rit.edu/classes/phys445/lectures/ccd1/ccd1.html, last checked: 2011-12-03

227. inc e2v: *e2v datasheet 30-11 deep depletion front illuminated CCD AIMO*, http://www.e2v.com/products-and-services/high-performance-imaging-solutions/datasheets/ccd-selector/, last checked: 2011-11-22

228. Holland, S.E. ; Groom, D.E. ; Palaio, N.P. ; Stover, R.J.: Fully depleted, back-illuminated charge-coupled devices fabricated on high-resistivity silicon. in: *IEEE Transactions on Electron Devices* 50 (2003), January, nr. 1, p. 225–238

229. Burke, Barry ; Jorden, Paul ; Vu, Paul: CCD Technology. in: *Experimental Astronomy* 19 (2005), nr. 1-3, p. 69–102

230. Holst, Gerald: *CMOS/CCD sensors and camera systems*. Winter Park, FL Bellingham, Wash : JCD Pub. SPIE, 2007. – ISBN 0819467308

231. inc. e2v ; Brown, P.: *technical support*. – Private communication

232. Pavlov, G. ; Nousek, J.: Charge diffusion in CCD X-ray detectors. in: *Nuclear Instruments and Methods in Physics Research Section A: Accelerators, Spectrometers, Detectors and Associated Equipment* 428 (1999), nr. 2-3, p. 348–366

233. Bautz, M: X-ray CCD response functions, front to back. in: *Nuclear Instruments and Methods in Physics Research Section A: Accelerators, Spectrometers, Detectors and Associated Equipment* 436 (1999), nr. 1-2, p. 40–52

234. Prigozhin, G. ; Butler, N.R. ; Kissel, S.E. ; Ricker, G.R.: An experimental study of charge diffusion in the undepleted silicon of X-ray CCDs. in: *IEEE Transactions on Electron Devices* 50 (2003), nr. 1, p. 246–253

235. Prigozhin, Gregory Y.: X-ray absorption near edge structure in the quantum efficiency of x-ray charge-coupled devices. in: *Optical Engineering* 37 (1998), nr. 10, p. 2848

236. Hoffman, Alan ; Loose, Markus ; Suntharalingam, Vyshnavi: CMOS Detector Technology. in: *Experimental Astronomy* 19 (2006), nr. 1-3, p. 111–134

237. Rogalski, Antoni: Infrared detectors: status and trends. in: *Progress in Quantum Electronics* 27 (2003), January, nr. 2-3, p. 59–210

238. *DECTRIS Ltd.* http://www.dectris.com/sites/products.html, last checked: 2011-11-24

239. Ejdrup, T ; Lemke, H T. ; Haldrup, K ; Nielsen, T N. ; Arms, D A. ; Walko, D A. ; Miceli, A ; Landahl, E C. ; Dufresne, E M. ; Nielsen, M M.: Picosecond time-resolved laser pump/X-ray probe experiments using a gated single-photon-counting area detector. in: *Journal of synchrotron radiation* 16 (2009), p. 387–90

240. Kleymenov, Evgeny ; Bokhoven, Jeroen A. ; David, Christian ; Glatzel, Pieter ; Janousch, Markus ; Alonso-Mori, Roberto ; Studer, Marco ; Willimann, Markus ; Bergamaschi, Anna ; Henrich, Beat ; Nachtegaal, Maarten: Five-element Johann-type x-ray emission spectrometer with a single-photon-counting pixel detector. in: *The Review of scientific instruments* 82 (2011), June, nr. 6, p. 065107

241. Inc., Intevac: *MicroVista Back illuminated CMOS*. online. http://www.intevac.com/uploads/datasheets/MicroVistaNIR.pdf. Version: 2011, last checked: 2011-11-24. – data sheet

242. Inc., Intevac ; True, Bruce: *back illuminated and back thinned CMOS build for near infrared*. – Private communication

243. Soleil, Synchrotron: *XPAD*. http://www.synchrotron-soleil.fr/images/File/instrumentation/XPAD/ArticlesRS/XPAD.pdf. Version: 2011, last checked: 2011-11-24

244. Hustache-Ottini, S. ; Bérar, J.-F. ; Boudet, N. ; Basolo, S. ; Bordessoule, M. ; Breugnon, P. ; Caillot, B. ; Clemens, J.-C. ; Delpierre, P. ; Dinkespiler, B. ; Koudobine, I. ; Medjoubi, K. ; Meessen, C. ; Menouni, M. ; Morel, C. ; Pangaud, P. ; Vigeolas, E.: The Hybrid Pixel Single Photon Counting Detector XPAD. in: *AIP Conference Proceedings* vol. 879, AIP, 2007, p. 1087–1090

245. Medjoubi, K ; Hustache, S ; Picca, F ; Bérar, J F. ; Boudet, N ; Bompard, F ; Breugnon, P ; Clémens, J C. ; Dawiec, A ; Delpierre, P ; Dinkespiler, B ; Godiot, S ; Logier, J P. ; Menouni, M ; Morel, C ; Nicolas, M ; Pangaud, P ; Vigeolas, E: Performance and Applications of the CdTe- and Si-XPAD3 photon counting 2D detector. in: *Journal of Instrumentation* 6 (2011), January, nr. 01, p. C01080–C01080

246. Ballabriga, R. ; Campbell, M. ; Heijne, E. ; Llopart, X. ; Tlustos, L. ; Wong, W.: Medipix3: A 64k pixel detector readout chip working in single photon counting mode with improved spectrometric performance. in: *Nuclear Instruments and Methods in Physics Research Section A: Accelerators, Spectrometers, Detectors and Associated Equipment* 633 (2011), May, p. S15–S18

247. Henrich, B. ; Becker, J. ; Dinapoli, R. ; Goettlicher, P. ; Graafsma, H. ; Hirsemann, H. ; Klanner, R. ; Krueger, H. ; Mazzocco, R. ; Mozzanica, A. ; Perrey, H. ; Potdevin, G. ; Schmitt, B. ; Shi, X. ; Srivastava, A.K. ; Trunk, U. ; Youngman, C.: The adaptive gain integrating pixel detector AGIPD a detector for the European XFEL. in: *Nuclear Instruments and Methods in Physics Research Section A: Accelerators, Spectrometers, Detectors and Associated Equipment* 633 (2011), May, p. S11–S14

248. Potdevin, Guillaume ; Graafsma, Heinz: Analysis of the expected AGIPD detector performance parameters for the European X-ray free electron laser. in: *Nuclear Instruments and Methods in Physics Research Section A: Accelerators, Spectrometers, Detectors and Associated Equipment* 659 (2011), December, nr. 1, p. 229–236

249. Thil, Ch. ; Baron, A.Q.R. ; Fajardo, P. ; Fischer, P. ; Graafsma, H. ; Rüffer, R.: Pixel readout ASIC for an APD based 2D X-ray hybrid pixel detector with sub-nanosecond resolution. in: *Nuclear Instruments and Methods in Physics Research Section A: Accelerators, Spectrometers, Detectors and Associated Equipment* 628 (2011), February, nr. 1, p. 461–464

250. Backhaus, M. ; Barbero, M. ; Gonella, L. ; Knetter, J. Groß e. ; Hügging, F. ; Krüger, H. ; Weingarten, J. ; Wermes, N.: Development of a versatile and modular test system for ATLAS hybrid pixel detectors. in: *Nuclear Instruments and Methods in Physics Research Section A: Accelerators, Spectrometers, Detectors and Associated Equipment* 650 (2011), September, nr. 1, p. 37–40

251. Wermes, N.: PIXEL 2010 Resumé. in: *Nuclear Instruments and Methods in Physics Research Section A: Accelerators, Spectrometers, Detectors and Associated Equipment* 650 (2011), September, nr. 1, p. 245–252

252. Fullagar, Wilfred ; Uhlig, Jens ; Walczak, Monika ; Canton, Sophie ; Sundström, Villy: *The use and characterization of a backilluminated charge-coupled device in investigations of pulsed x-ray and radiation sources.*, 2008. (10) . – 103302 S. – This content was modified and reprinted with permission from this source. Copyright 2008 American Institute of Physics

253. Lalena, John N.: From quartz to quasicrystals: probing nature's geometric patterns in crystalline substances. in: *Crystallography Reviews* 12 (2006), nr. 2, p. 125–180

254. Tommasini, R ; Bruch, R ; Fill, E ; Bjeoumikhov, A: Convergent-beam diffraction of ultra-short hard X-ray pulses focused by a capillary lens. in: *Applied Physics B-Lasers and Optics* 82 (2006), nr. 4, p. 519–522

255. Thoe, Robert: High-resolution spectrometer design using spherically curved crystals. in: *Journal of the Optical Society of America A* 3 (1986), September, nr. 9, p. 1407

256. Hall, T A.: A focusing X-ray crystal spectrograph. in: *Journal of Physics E: Scientific Instruments* 17 (1984), February, nr. 2, p. 110–112

257. Kopietz, P ; Scharf, P ; Skaf, MS ; Chakravarty, S: A focusing Crystal von Hamos Spectrometer for X-ray Spectroscopy and X-ray Fluorescence Applications. in: *Advances in Laboratory-based X-Ray Sources and Optics* 4144 (1989), p. 148–154

258. Martinolli, E. ; Koenig, M. ; Boudenne, J. M. ; Perelli, E. ; Batani, D. ; Hall, T. A.: Conical crystal spectrograph for high brightness x-ray Kα spectroscopy in subpicosecond laser-solid interaction. in: *Review of Scientific Instruments* 75 (2004), nr. 6, p. 2024

259. Levy, A ; Dorchies, F ; Fourment, C ; Harmand, M ; Hulin, S ; Santos, J J. ; Descamps, D ; Petit, S ; Bouillaud, R: Double conical crystal x-ray spectrometer for high resolution ultrafast x-ray absorption near-edge spectroscopy of Al K edge. in: *The Review of scientific instruments* 81 (2010), June, nr. 6, p. 063107

260. Shymanovich, U ; Nicoul, M ; Lu, W ; Kähle, S ; Tarasevitch, A ; Sokolowski-Tinten, K ; Linde, D von d.: Toward ultrafast time-resolved Debye-Scherrer x-ray diffraction using a laser-plasma source. in: *The Review of scientific instruments* 80 (2009), August, nr. 8, p. 083102

261. Hauer, A. ; Kilkenny, J. D. ; Landen, O. L.: Toroidally curved crystal for time-resolved x-ray spectroscopy. in: *Review of Scientific Instruments* 56 (1985), nr. 5, p. 803

262. Missalla, T. ; Uschmann, I. ; Foörster, E. ; Jenke, G. ; Linde, D. von d.: Monochromatic focusing of subpicosecond x-ray pulses in the keV range. in: *Review of Scientific Instruments* 70 (1999), nr. 2, p. 1288

263. Stepanenko, M.: A spectral resolution of Johann-type X-ray spectrometers. in: *Plasma Devices and Operations* 17 (2009), September, nr. 3, p. 191–200

264. Shevelko, A P. ; Kasyanov, Y S. ; Yakushev, O F. ; Knight, L V.: Compact focusing von Hamos spectrometer for quantitative x-ray spectroscopy. in: *Review of Scientific Instruments* 73 (2002), nr. 10, p. 3458–3463

265. Legall, H. ; Stiel, H. ; Arkadiev, V. ; Bjeoumikhov, A. A.: High spectral resolution x-ray optics with highly oriented pyrolytic graphite. in: *Optics Express* 14 (2006), nr. 10, p. 4570

266. Bilderback, D. ; Lairson, B. ; Barbee Jr., T. ; Ice, G. ; Sparks Jr., C. J.: Design of doubly focusing, tunable (5-30 keV), wide bandpass optics made from layered synthetic microstructures. in: *Nuclear Instruments and Methods in Physics Research* 208 (1983), nr. 1-3, p. 251–261

267. Erko, A. ; Firsov, A. ; Holldack, K. ; Garrett, R. ; Gentle, I. ; Nugent, K. ; Wilkins, S.: New Developments in Femtosecond Soft X-ray Spectroscopy. in: *SRI 2009, 10TH international conference on radiation instrumentation*, SRI, 2010, p. 177–180

268. Wilhein, T. ; Rehbein, S. ; Hambach, D. ; Berglund, M. ; Rymell, L. ; Hertz, H. M.: A slit grating spectrograph for quantitative soft x-ray spectroscopy. in: *Review of Scientific Instruments* 70 (1999), nr. 3, p. 1694

269. Daido, Hiroyuki: Review of soft x-ray laser researches and developments. in: *Reports on Progress in Physics* 65 (2002), October, nr. 10, p. 1513–1576

270. Heimann, Philip A. ; Koike, Masato ; Padmore, Howard A.: Dispersive x-ray absorption spectroscopy with gratings above 2 keV. in: *Review of Scientific Instruments* 76 (2005), nr. 6, p. 063102

271. Ullom, J. N. ; Beall, J. A. ; Doriese, W. B. ; Duncan, W. D. ; Ferreira, L. ; Hilton, G. C. ; Irwin, K. D. ; Reintsema, C. D. ; Vale, L. R.: Optimized transition-edge x-ray microcalorimeter with 2.4 eV energy resolution at 5.9 keV. in: *Applied Physics Letters* 87 (2005), nr. 19, p. 194103

272. Moore, Gordon E.: Cramming more components onto integrated circuits, Reprinted from Electronics, volume 38, number 8, April 19, 1965, pp.114 ff. in: *IEEE Solid-State Circuits Newsletter* 20 (2006), September, nr. 3, p. 33–35

273. Irwin, Kent D. ; Young, Betty ; Cabrera, Blas ; Miller, Aaron: Shannon Limits for Low-Temperature Detector Readout. in: *The thirteenth international workshop on low temperature detectors -LTD13* vol. 1185, 2009. – ISBN 978–0–7354–0751–0, p. 229–236

274. *reproduced with permission from Jochem Baselmans (LTD-14 conference, Heidelberg 2011), with minor modification*

275. Doriese, W. B. ; Adams, J. S. ; Hilton, G. C. ; Irwin, K. D. ; Kilbourne, C. A. ; Schima, F. J. ; Ullom, J. N. ; Young, Betty ; Cabrera, Blas ; Miller, Aaron: Optimal filtering, record length, and count rate in transition-edge-sensor microcalorimeters. in: *The thirteenth international workshop on low temperature detectors -LTD13* vol. 1185, 2009. – ISBN 978–0–7354–0751–0, p. 450–453

276. *International X-ray Observatory (IXO)*. http://ixo.gsfc.nasa.gov/whatIsIxo.html, last checked: 2011.12.05

277. Kilbourne, Caroline A. ; Doriese, W. B. ; Bandler, Simon R. ; Brekosky, Regis P. ; Brown, Ari-David ; Chervenak, James A. ; Eckart, Megan E. ; Finkbeiner, Fred M. ; Hilton, Gene C. ; Irwin, Kent D. ; Iyomoto, Naoko ; Kelley, Richard L. ; Porter, F. S. ; Reintsema, Carl D. ; Smith, Stephen J. ; Ullom, Joel N.: Multiplexed readout of uniform arrays of TES x-ray microcalorimeters suitable for Constellation-X. in: *Proceedings of SPIE* vol. 7011, SPIE, 2008, p. 701104–701104–12

278. Landau, Lew D. ; Lifschitz, Ewgeni M.: *Physikalische Kinetik, Lehrbuch der theoretischen Physik, 10 Bde.*. vol. Bd.10. Berlin : Akademie-Verlag Berlin, 1990. – ISBN 3055000749

279. Nyquist, H.: Thermal Agitation of Electric Charge in Conductors. in: *Physical Review* 32 (1928), July, nr. 1, p. 110–113

280. Kittel, Charles: *Einführung in die Festkörperphysik*. München : Oldenbourg, 2006. – ISBN 3486577239

281. Johnson, J.: Thermal Agitation of Electricity in Conductors. in: *Physical Review* 32 (1928), July, nr. 1, p. 97–109

282. Delft, Dirk van ; Kes, Peter: The discovery of superconductivity. in: *Physics Today* 63 (2010), nr. 9, p. 38

283. Buzea, Cristina ; Robbie, Kevin: Assembling the puzzle of superconducting elements: a review. in: *Superconductor Science and Technology* 18 (2005), January, nr. 1, p. R1–R8

284. Seidel, P. ; Schmidl, F. ; Wald, H. ; Mans, M. ; Peiselt, K. ; Baldeweg, U. ; Beck, M. ; Biering, S. ; Becker, C. ; Uhlig, Jens ; Groszlige, V.: Thin-Film Technology for HTSC Josephson Devices. in: *IEEE TRANSACTIONS ON APPLIED SUPERCONDUCTIVITY* 15 (2005), nr. 2, p. 161–164

285. Buckel, Werner: *Supraleitung (German Edition)*. Wiley-VCH, 2004. – 496 S. – ISBN 3527403485

286. Tinkham, Michael ; Physics: *Introduction to Superconductivity: Second Edition (Dover Books on Physics) (Vol i)*. Dover Publications, 2004. – 480 S. – ISBN 0486435032

287. Poole, Charles P. J. ; Farach, Horacio A. ; Creswick, Richard J. ; Prozorov, Ruslan: *Superconductivity, Second Edition*. Academic Press, 2007. – ISBN 0120887614

288. Meissner, W. ; Ochsenfeld, R.: Ein neuer Effekt bei Eintritt der Supraleitfaehigkeit. in: *Die Naturwissenschaften* 21 (1933), November, nr. 44, p. 787–788

289. Ginzburg, Vitaly L.: On superconductivity and superfluidity (what I have and have not managed to do), as well as on the 'physical minimum' at the beginning of the 21 st century. in: *Chemphyschem : a European journal of chemical physics and physical chemistry* 5 (2004), July, nr. 7, p. 930–45

290. Ginzburg, Vitaly L. ; Landau, Lew D.: On the theory of superconductivity. in: *Zhurnal Eksperimental'noi i Teoreticheskoi Fiziki(Journal of Experimental and Theoretical Physics)* 20 (1950), nr. 12, p. 1064

291. Abrikosov, A.A:: On the Magnetic Properties of Superconductors of the Second Group. in: *Journal of Experimental and Theoretical Physics* 5 (1957), p. 1174

292. Bardeen, J. ; Cooper, L. N. ; Schrieffer, J. R.: Theory of Superconductivity. in: *Physical Review* 108 (1957), December, nr. 5, p. 1175–1204

293. Mandl, Franz: *Statistical physics*. 2nd. Chichester West Sussex New York : Wiley, 1988. – ISBN 0471915335

294. Szymkowiak, A. E. ; Kelley, R. L. ; Moseley, S. H. ; Stahle, C. K.: Signal processing for microcalorimeters. in: *Journal of Low Temperature Physics* 93 (1993), November, nr. 3-4, p. 281–285

295. Enss, Ch.: *Cryogenic Particle Detection*. Berlin/Heidelberg : Springer-Verlag, 2005. – ISBN 3–540–20113–0

296. Efros, A L. ; Shklovskii, B I.: Coulomb gap and low temperature conductivity of disordered systems. in: *Journal of Physics C: Solid State Physics* 8 (1975), February, nr. 4, p. L49–L51

297. Friedrich, Stephan ; Funk, T. ; Drury, O. ; Labov, S. E. ; Cramer, S. P.: A multichannel superconducting soft x-ray spectrometer for high-resolution spectroscopy of dilute samples. in: *Review of Scientific Instruments* 73 (2002), nr. 3, p. 1629

298. Friedrich, Stephan: Cryogenic X-ray detectors for synchrotron science. in: *Journal of synchrotron radiation* 13 (2006), March, nr. Pt 2, p. 159–71

299. Friedrich, Stephan ; Drury, Owen B. ; Hall, John ; Cantor, Robin ; Garrett, R. ; Gentle, I. ; Nugent, K. ; Wilkins, S.: Development of Ta-based Superconducting Tunnel Junction X-ray Detectors for Fluorescence XAS. in: *SRI 2009, 10TH INTERNATIONAL CONFERENCE ON RADIATION INSTRUMENTATION*, 2010, p. 101–104

300. Mazin, Benjamin A.: *Microwave kinetic inductance detectors*, California Institute of Technology, PhD Thesis, 2005. http://resolver.caltech.edu/CaltechETD:etd-10042004-120707

301. Ullom, J. N. ; Doriese, W. B. ; Hilton, G. C. ; Beall, J. A. ; Deiker, S. ; Duncan, W. D. ; Ferreira, L. ; Irwin, K. D. ; Reintsema, C. D. ; Vale, L. R.: Characterization and reduction of unexplained noise in superconducting transition-edge sensors. in: *Applied Physics Letters* 84 (2004), nr. 21, p. 4206

302. Lindeman, MA: *Microcalorimetry and the transition-edge sensor*, Univ. of California, Davis, CA (US), PhD Thesis, 2000. http://www.osti.gov/energycitations/product.biblio.jsp?osti_id=15009469

303. Irwin, K. D. ; Hilton, G. C. ; Wollman, D. A. ; Martinis, John M.: Thermal-response time of superconducting transition-edge microcalorimeters. in: *Journal of Applied Physics* 83 (1998), nr. 8, p. 3978

304. Irwin, K. D.: An application of electrothermal feedback for high resolution cryogenic particle detection. in: *Applied Physics Letters* 66 (1995), nr. 15, p. 1998

305. Seidel, W. ; Forster, G. ; Christen, W. ; Feilitzsch, F. von ; Goebel, H. ; Proebst, F. ; Moessbauer, R.L.: Phase transition thermometers with high temperature resolution for calorimetric particle detectors employing dielectric absorbers. in: *Physics Letters B* 236 (1990), March, nr. 4, p. 483–487

306. Clarke, John (Publ.) ; Braginski, Alex I. (Publ.): *The SQUID handbook*. Weinheim : Wiley-VCH, 2003. – ISBN 3527404082

307. Irwin, K D. ; Niemack, M D. ; Beyer, J ; Cho, H M. ; Doriese, W B. ; Hilton, G C. ; Reintsema, C D. ; Schmidt, D R. ; Ullom, J N. ; Vale, L R.: Code-division multiplexing of superconducting transition-edge sensor arrays. in: *Superconductor Science and Technology* 23 (2010), March, nr. 3, p. 034004

308. Reintsema, C. D. ; Adams, J. S. ; Baker, R. ; Bandler, S. R. ; Doriese, W. R. ; Figueroa-Feliciano, E. ; Hilton, G. C. ; Irwin, K. D. ; Kelly, R. L. ; Kilbourne, C. A. ; Krinsky, J. W. ; Porter, F. S. ; Wikus, P. ; Young, Betty ; Cabrera, Blas ; Miller, Aaron: Electronics for a Next-Generation SQUID-Based Time-Domain Multiplexing System. in: *The thirteenth international workshop on low temperature detectors -LTD13* vol. 1185, 2009, p. 237–240

309. Å ström, K.J. ; Murray, R.M.: *Feedback systems: an introduction for scientists and engineers*. Princeton Univ Pr, 2008. – 424 S. – ISBN 0691135762

310. Bennett, Stuart: *A History of Control Engineering 1930-1955*. (Iee Contr. Institution of Electrical Engineers, 1993. – 1993 S. – ISBN 0863412998

311. Nof, Shimon Y. (Publ.): *Springer Handbook of Automation*. Berlin, Heidelberg : Springer Berlin Heidelberg, 2009. – ISBN 978–3–540–78830–0

312. Adams, J. S. ; Bandler, S. R. ; Brown, L. E. ; Boyce, K. R. ; Chiao, M. P. ; Doriese, W. B. ; Eckart, M. E. ; Hilton, G. C. ; Kelley, R. L. ; Kilbourne, C. A. ; Porter, F. S. ; Rabin, M. W. ; Smith, S. J. ; Stewart, D. D. ; Ullom, J. N. ; Young, Betty ; Cabrera, Blas ; Miller, Aaron: Real-Time Data Processing for X-Ray Spectroscopy. in: *The thirteenth international workshop on low temperature detectors -LTD13* vol. 1185, 2009, p. 274–277

313. Tan, Hui ; Breus, Dimitry ; Hennig, Wolfgang ; Sabourov, Konstantin ; Warburton, William K. ; Doriese, W. B. ; Ullom, Joel N. ; Bacrania, Minesh K. ; Hoover, Andrew S. ; Rabin, Michael W.: *High rate pulse processing algorithms for microcalorimeters*. IEEE, 2008. – 1130–1133 S.

314. Gifford, William E. ; R.C., Longsworth: Pulse Tube Refrigeration Progress. in: *International Advances in Cryogenic Engineering - Volume 10*. University of Pennsylvania, 1964

315. Waele, A. T. A. M.: Basic Operation of Cryocoolers and Related Thermal Machines. in: *Journal of Low Temperature Physics* 164 (2011), June, nr. 5-6, p. 179–236

316. Radebaugh, R.: Development of the pulse tube refrigerator as an efficient and reliable cryocooler. in: *Proc. Institute of Refrigeration* vol. 2000. London, 1999

317. Shirron, Peter J.: Cooling Capabilities of Adiabatic Demagnetization Refrigerators. in: *Journal of Low Temperature Physics* 148 (2007), June, nr. 5-6, p. 915–920

318. Shull, R. ; McMichael, R. ; Ritter, J.: Magnetic nanocomposites for magnetic refrigeration. in: *Nanostructured Materials* 2 (1993), March, nr. 2, p. 205–211

319. Wolf, B. ; Tsui, Y. ; Jaiswal-Nagar, D. ; Tutsch, U. ; Honecker, A. ; Removic-Langer, K. ; Hofmann, G. ; Prokofiev, A. ; Assmus, W. ; Donath, G. ; Lang, M.: Magnetocaloric effect and magnetic cooling near a field-induced quantum-critical point. in: *Proceedings of the National Academy of Sciences* 108 (2011), April, nr. 17, p. 6862–6866

320. Hölzer, G. ; Fritsch, M. ; Deutsch, M. ; Härtwig, J. ; Förster, E.: $K\alpha_{1,2}$ and $K\beta_{1,3}$ x-ray emission lines of the 3d transition metals. in: *Physical Review A* 56 (1997), December, nr. 6, p. 4554–4568

321. Porter, F. S.: *private communication*. 2004. – remeasured and added 5899.417eV from Intensity 0.005 to .018 and adding 5902.712eV with I 0.004 and the width 1.5528

322. Chechev, V. P.: Certified Reference Tables on Decay Characteristics and Radiations of Radionuclides Used to Calibrate Semiconductor Spectrometers for Photon Radiation in the Energy Range 5-140 keV. in: *Measurement Techniques* 46 (2003), December, nr. 12, p. 1202–1206. http://dx.doi.org/10.1023/B:METE.0000018733.56924.e2. – DOI 10.1023/B:METE.0000018733.56924.e2

323. Nockert, Jens: *(working title:) Features and Implementation of a parallized optimal filter for dataprocessing of microcalorimeter data.*, Bachelor thesis. – defence Jan 20th 2012

324. Kinnunen, K.: *Studies of Transition-edge Sensor Physics, Thermal Models and Noise*, University of Jyväskylä, PhD, 2011

Acknowledgments

I owe my deepest gratitude to my thesis supervisor Professor Villy Sundström. His support and encouragement gave me the chance to develop into a new world of science and gain knowledge in a wide variety of topics that can not be sufficiently represented by this thesis. The german name for supervisor is "Doktorvater" (doctor father) and is definitely the best description for what you were. Supportive, encouraging and always there when needed to ask a question or to give me a little push in a better direction. Thank you Villy.

To Wilfred: "I just wanted to put this thought in your head" will be the sentence i gone miss most after this thesis. It would be hard to believe if somebody would say that there is a more dedicated and at the same time open minded scientist out there than Wilfred Fullagar. With his thinking "outside the box" and expertise in many a subject he is the mastermind behind much that was achieved in this project. Thanks for all your time, especially during the thesis writing weeks and your working "holidays". This thesis would not exist without you.

I am thankful to my opponent Professor Thomas Elsässer, and the thesis committee members: Professor Karin Schillén, Professor Tony Hansson and Professor Emad Mukhtar for accepting to evaluate this work.

I would like to thank Niklas Gador, Monika Walczak and Sophie Canton for their time and contributions to the project. Dimali Vithanage and Pavel Chabera had to fight the laser with me for many hours and i would like to thank them for their efforts and their friendship. Arkady Yartsev and Ivan Scheblykin had always an open ear and often just the right advice or lacking this a Russian joke that made things look brighter, thank you guys! Torbjörn Pascher deserves my gratitude for all the little electronic things he build and the hours we spent discussing. Yingyot, Thomas, Donatas, Ramunas, Oleg, Lotta Daniel, Tönu, Per and Ebbe and can only stand as examples for all the special peoples that are united in our department and i had the privilege to learn from. I enjoyed the time with all of you.

I would like to give my thanks to Professor Claes-Göran Wahlström for that we could perform the measurements at Lunds High Power Laser Facility and for some really interesting discussions and insights afterwards. I would like to thank Professor Anne L'Huillier who started and chaired the MAXLAS program that brought me to Lund and financed me the first years.

Marko Swoboda, Nino Cutic, Ralph Nüske, Guillaume Genoud, and Jörg Schwenke became much more then just fellows in the same European project. Thank you guys for all the nice hours. Thomas Björkman, Maria Levin, Jan Wegner, Anki Wikander, Tommy Ljungdell, Stefan Jonason and Rickard Holst took care of all the administrative sides and are as important to any science.

Kimmo Kinnunen and Ilari Maasilta brought us into the game of low temperature detectors and shall be thanked for this. Kimmo, it was quite a time in Boulder. Thanks for all the help and company.

I would like to thank the whole team in Boulder that built this nice detector for and with me. Joel Ullom, Randy Doriese, Dan Swetz and Joe Fowler traveled all the way over the big lake and carried the largest piece of work while developing this system. Joe and Joel you had to stand all my questions and demands during the last month, thanks for staying so patient. I'm looking forward to work with you guys.

My thanks goes also to the MAXLAS project that financed me the first years and to Villy who used parts of his ERC grant to support this research.

My special thanks to my new family Eriksson that gave me a home in this country from the very beginning.

Lisa, how many time have I been frustrated and found a save haven at home with you. Where would SAM be without you? I hope we hold together for the good and bad times that might come. I love you.

Last but not least: Mutsch, Pa, es ist ein tolles Gefühl zu wissen, das man immer eine Stelle in der Welt hat an der man zu Hause ist. Was auch immer ich für verrückte Pläne auheckte, es gab immer Euch, mit Eurer Liebe und Unterstützung. DANKE!

Comments on the Papers

I **A broadband laser plasma x-ray source for application in ultrafast chemical structure dynamics.**
I took part in most of the experiments and contributed substantial parts to the manuscript.

II **The use and characterization of a backilluminated charge-coupled device in investigations of pulsed x-ray and radiation sources.**
I took major part in all experiments and contributed substantial parts to the manuscript.

III **Lab-based Ultrafast Molecular Structure**
I a took major part in all experiments and contributed to the manuscript.

IV **Laser generated 300 keV electron beams from water**
I was responsible for the experiments, data analysis and writing of the manuscript.

V **Table-top ultrafast x-ray microcalorimeter spectrometry for molecular structure**
I was responsible for the experiments, data analysis and writing of the manuscript.

Papers

Paper I

A broadband laser plasma x-ray source for application in ultrafast chemical structure dynamics.

W. Fullagar, M. Harbst, S. Canton, J. Uhlig, M. Walczak, C.-G. Wahlström, V. Sundström.

Review of Scientific Instruments **78(11)**, 115105 (2007).

REVIEW OF SCIENTIFIC INSTRUMENTS **78**, 115105 (2007)

A broadband laser plasma x-ray source for application in ultrafast chemical structure dynamics

Wilfred Fullagar, Michael Harbst, Sophie Canton, Jens Uhlig, Monika Walczak, Claes-Göran Wahlström, and Villy Sundström
Division of Chemical Physics, Lund University, P.O. Box 124, SE-22100 Lund, Sweden and Division of Atomic Physics, Lund Institute of Technology, P.O. Box 118, SE-22100 Lund, Sweden

(Received 24 July 2007; accepted 16 October 2007; published online 20 November 2007)

A plasma source free from characteristic emission lines is described, based on laser irradiation of a water jet in a helium atmosphere. Various key aspects of the laser interaction are presented along with practical characterization of the observed isotropic ~4–10 keV x-ray emissions, measurements of which indicate subpicosecond duration. Observations are consistent with a vacuum heating plasma mechanism at the helium-water interface and indicate strong potential for in-house ultrafast chemical structure dynamics application when coupled to contemporary detector developments. © *2007 American Institute of Physics*. [DOI: 10.1063/1.2813340]

INTRODUCTION

At the present time, a strong motivation for the development of laser-based x-ray sources is the possibility of in-house measurement of molecular changes on picosecond and faster time scales, using x-ray absorption spectroscopy[1] and, where beam properties allow it, Laue crystallography.[2] Both techniques require polychromatic radiation. In ultrafast experiments using monochromatic radiation (by angular dispersion of momentum transfer in powder[3] or diffuse[4] diffraction) there is an implicit need for collimation or focusing.[5] Reflectometry also offers interesting possibilities.[6] These experiments have in large measure only been implemented given a very high level of synchrotron development access, to date generally with pulse durations of ~100 ps that motivate continuing development of short pulse electron sources, time-slicing schemes, and streak cameras at large scale facilities. While x-ray generation from condensed matter targets has been explored by many groups for several decades,[7,8] much attention has recently been directed to the possibility of more or less collimated laser-generated broadband beams obtainable by relativistic electron acceleration,[9–11] high harmonic generation,[12,13] and reverse Compton scattering.[14] The latter approaches are undergoing intensive development at the present time, and the possibility of in-house pump-probe Laue crystallography[2] using the low shot rates but high collimated fluxes of broadband femtosecond betatron beams[15] may be worth particular suggestion. Meanwhile the extreme laser power requirements, low flux soft x-ray beams, and need for implementation of a relativistic electron beam in these respective sources motivates ongoing work with simpler laser-based sources.

Temporal structure of plasma sources has in some instances been found to be much longer than hoped for ultrafast applications,[16] likely because the emission of line radiation has the reacquisition of electrons by stripped atoms as a relatively slow prerequisite,[17] this being dependent on plasma properties in the particular circumstances. The present work avoids production of detectable emission lines for reasons of source temporal duration, characterization, and application by exploiting bremsstrahlung from a water jet target.[18–20] The choice of a low-Z target for bremsstrahlung production is generally counterintuitive,[21] however, we note that the total bremsstrahlung radiation yield from a fast electron brought to rest in water is only about an order of magnitude less than from the same electron brought to rest in denser, higher Z materials such as mercury.[22] The electron stopping length is greater in water (with potential consequences for pulse duration that we address later), but the escape depth of x rays is also greater.[23] Such matters aside, the nontoxicity, high solvent power, ease of supply and handling, extremely smooth target surface, opportunities for debris-free continuous operation, and relatively relaxed safety considerations owing to the lack of intense hard emission line radiation make water a somewhat overlooked but nevertheless extremely attractive target material.[24] In practice x rays have been observed from laser plasma targets in air[18,19] or preferably helium[25] atmospheres, and x rays above ~1 keV have excellent transmission through the latter gas. The use of helium provides the opportunity to avoid vacuum systems and the corresponding remote control infrastructure in experimental setups, as well as permitting the study of vacuum incompatible samples. These features are all enjoyed in the apparatus described below.

Regarding detection, array detection methods not based on diffraction are vastly more efficient than single crystal diffraction-based energy dispersion, since the latter operate by discarding all photons in energy/angular phase space that do not meet the Bragg condition. Extended x-ray absorption fine structure (EXAFS) measurements are envisaged as an initial approach to combine such an array detector with a kilohertz repetition rate version of this source, in which its inherent beam divergence would be used to advantage. In such an arrangement, the extremely efficient detection would otherwise lead to detector saturation by "worthless" emission lines. For this and the various other reasons already given,

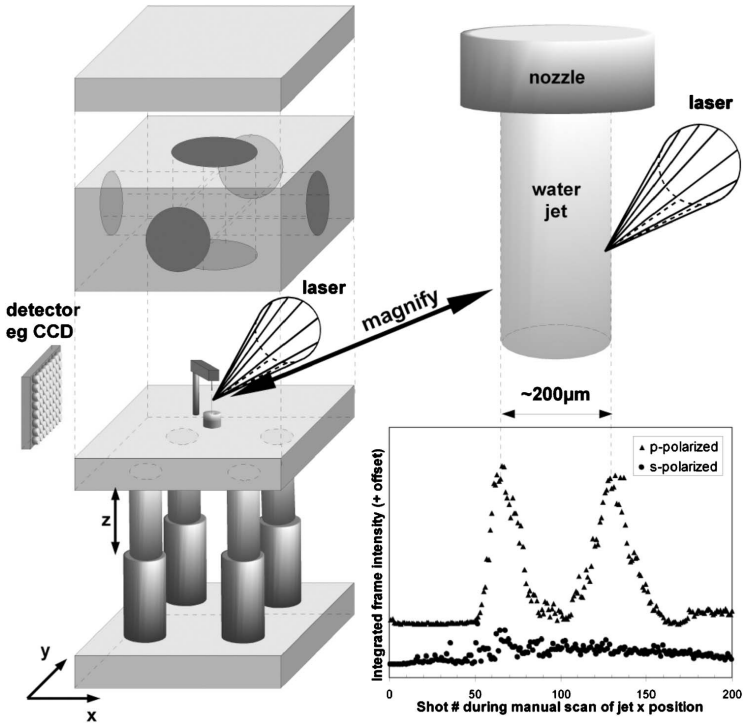

FIG. 1. Schematic of the laser plasma source. A horizontally polarized laser beam is focused to the tangent of a vertical water jet under helium in grazing incidence, resulting in isotropic x-ray bremsstrahlung emission. The lead block surrounding the water jet has dimensions of 48 mm×96 mm ×96 mm. Variants of this block permit evacuability, access of laser beams from additional angles, and placement of other items very close to the point of x-ray emission.

and with the relevant detection developments underway, the source we describe deliberately avoids the generation of monochromatic hard x rays.

APPARATUS

Essential requirements for the x-ray generator were adequate radiation shielding, close access to the source, rapid dismantling and reconstruction, independent movement of target and focusing optics, and no electronic remote control. Target chambers for different experiments were made by machining lead bricks, a typical example of which is illustrated in Fig. 1. Common features are a small hollow central region (typically ~125 cm^3) for the target, various holes to allow laser entry and x-ray exit through suitable windows, provisions for accommodation of a small styrofoam diffuser block in the diverging laser beam, and admission and drainage of the target material through a lead base plate. The latter feature allows immediate access to the target jet by lifting away the upper part of the structure. The base plate is mounted on an *xy*-translation table on an optical table. Most variants have had deliberate small leaks, for example, where the water drains out of the chamber. This allows flooding of the internal cavity with helium by slight overpressure using a few l/m. Alternatively, by aspirating the water out of the drainage port using an aspirator pump, the jet can be pressurized by atmospheric pressure and operated close to water's vapor pressure at room temperature (~25 torr). This increases x-ray fluxes and temperatures very substantially, but requires further provisions to ensure jet stability; as such we choose to focus on the helium experiments here. Typical external linear dimensions of the lead constructions are 100–120 mm. One variant allows a closest external approach of ~15 mm.

Ordinary tap water is used in the jet, since the concentration of contaminants is negligible in the context of x-ray generation. A jet diameter of 150–200 μm is usually used and can be either gravity fed or pumped. The laser is directed onto the jet 2–3 mm downstream from the nozzle, before it breaks into drops. Thicker jets increasingly lead to splattering. Thinner jets have not been tried by us, in the interests of maintaining good control of the laser interaction geometry. Occasional difficulties of internal condensation buildup on optical or x-ray windows are simply addressed by directing the incoming helium onto the offending optic.

The 10 Hz 800 nm Ti:sapphire laser of the Lund Laser Centre is used to generate the x rays. Light pulses traverse the following sequence of components: oscillator, acousto-optical modulator, (saturable absorber preamplifier), stretcher, regenerative amplifier, (2×) cleanup Pockels cells, multipass amplifier, beam expansion telescope, compressor, variable polarizing beamsplitter. The saturable absorber preamplifier can be used to substantially reduce amplified spontaneous emission (ASE) from the oscillator and may be flipped in and out of the circuit at will; in addition a beam position stabilization circuit was installed during this work at the input to the butterfly amplifier. A specific consequence of

these ongoing developments is that the present studies have enjoyed unusually low levels of prepulses and ASE pedestals ($<10^{-8}$ contrast ratio), both of which critically affect x-ray production in laser plasma sources.[26,27] Key matters related to these aspects of the temporal quality of the laser beam are the temporal structure of the x-ray generation, optimal target interaction geometry, and the production of energetic electron beams. Associated maximum energies available to our experiments have varied from ~40 to ~300 mJ/pulse, while shot to shot stability is obtained by gain depletion in the final multipass amplifier stage. In combination with higher order compensations the compressor permits variable pulse durations from <40 fs to ~1 ps with positive or negative chirp. The ~3 cm diameter output beam is variably polarized by a half-wave plate before transmission through a vertical Brewster plate to give a horizontally polarized transmitted beam used in these experiments, the intensity of which is varied by rotating the half-wave plate. The final focusing optic is a 50.8 mm diameter 90° off-axis parabolic metal mirror with effective focal length of ~100 mm. The essential interaction geometry is shown in Fig. 1.

Our primary x-ray detector is a direct-detection, thinned, back illuminated, peltier cooled charge coupled device (CCD) consisting of 512×512 24.8 μm pixels (Princeton Instruments). In use, the CCD camera unit is positioned in air a few millimeters distant from the exit window of the x-ray source, typically in the horizontal plane orthogonal to the converging laser beam. Incident x rays traverse a 250 μm Be window and a few millimeters of vacuum before impinging directly on the CCD, the latter typically being ~7 cm from the source (~0.032 sr). Background-subtracted exposures of less than 6 s ensure that exposure-independent (e.g., preamplifier) noise is the dominant source of noise in the resulting frames. Distances and filters can be arranged such that individual pixels are single-photon detectors with energy resolution of ~150 eV. When operated in this way, a histogram of the pixel intensities allows low resolution x-ray energy spectra on a single shot basis, after allowance for filters, events that span multiple pixels, and the CCD's spectral redistribution function.[28,29] The practical rapidity of these measurements has enabled an extensive survey of fluxes and temperatures versus laser pulse energies and chirp. On the other hand, the available resolution is too poor for EXAFS and shot rates must be reduced to match the full frame CCD readout time. Moreover, an adequate account of the necessary data interpretation is at odds with the present intention of source characterization, so we choose instead to present the relatively very limited results obtained using a germanium point detector (below). The spectral results obtained from the two detectors are nevertheless in excellent quantitative agreement. For now it suffices to indicate the general utility of the multidetector array approach but also caution that the integrated CCD response should generally not be considered a proportional indicator of single shot x-ray flux, since the source temperature may also vary, while different photon energies have different propensities to shift to lower energies in the course of spectral redistribution. This said, the utility of direct-detection CCDs for work of this nature must not be underestimated. Full frame readout of single shot x-ray spectra requires 3–4 s, so a synchronous vertical hardware binning scheme is generally used to monitor the general x-ray production in real time at the 10 Hz laser repetition rate. Spectral information is lost in this process. The resulting one dimensional array may then be summed in software to give the integrated detector response for the corresponding laser shot. Scans of observable yield versus arbitrary experimental variables can thus be made in real time on a shot by shot basis, while one dimension of spatial resolution can be retained if needed.

To confirm spectral observations made initially using the CCD in individual shots, much slower photon counting measurements were made at selected points in laser parameter space using a liquid nitrogen cooled germanium detector (ORTEC Canberra GUL0105 with EG&G ORTEC 429 3 MCA card). Despite a poorer energy resolution than the CCD and only a single "pixel," this detector has the advantages of response to harder x rays (up to ~200 keV) and much less spectral redistribution. It was carefully starved into single-photon counting mode using a 300 μm pinhole in a lead sheet taped in front of the detector, which was variably positioned ~10–30 cm from the source, with known thicknesses of aluminium for additional attenuation. Background counts were eliminated using temporal coincidence gating (20 μs gate at 10 Hz) and pileup was then arranged to be ~10% by adjusting distances and filtering to give ~1 event/s from the 10 Hz source. A few hours of measurement was sufficient to obtain the spectra presented here.

An x-ray streak camera (Kentech) was used to obtain an upper bound of x-ray pulse durations. The experiments described here used a ~10 nm Au photocathode spaced 3 mm from the extraction grid, allegedly giving ~0.1% quantum efficiency at 3–4 keV with temporal resolution of ~25 ps. The latter value is consistent with the 1 mm photocathode slit width and ~11 ps/mm maximum sweep rate. A low jitter timing pulse derived from the oscillator but gated by entrapment of the optical pulse in the regenerative amplifier was used for sweep triggering. Swept photoelectrons impinged on a phosphor coupled by a fiber plate to a temporally gated image intensifier (FlameStar multichannel plate and CCD).

EXPERIMENTAL

To align the off-axis parabolic focusing mirror, the horizontally polarized laser beam is brought to a focus in air and the mirror adjusted to produce a spark at the minimum possible energy. The laser self-focuses to different extents in windows and different gases, so the focal point shifts somewhat after placing the lead target chamber over the jet and admitting helium. The jet is moved into the spark (audible) and its position adjusted in real time so as to optimize the vertically binned CCD signal. Radiation incident on the beryllium window of the CCD camera is filtered by ~6 cm of helium gas at ambient temperature and pressure, a beryllium or thin Mylar exit port, and a few millimeters of air. Other detectors (e.g., scintillator/photomultiplier tube, photodiodes, ion chambers, etc.) also give useful real time signals. When selecting a signal to optimize it is essential to be aware of

electron beams with associated secondary radiations that we observe under particular laser conditions, or the various possible sources of ions in the chamber.[30–33]

Under the described experimental conditions, grazing incidence in *p* polarization is necessary for significant x-ray production. Thus when scanning the jet through the focus of the horizontally polarized laser focus, two distinct positions give similar yield, corresponding to the laser grazing either side of the jet, as shown in Fig. 1. Very little x-ray production can be observed when striking the jet normally or at intermediate angles. To confirm the grazing geometry, a thicker jet 830(±10) μm (microscope observation, circular jet cross section) was used and required a micrometer translation of 840(±30) μm between the two x-ray maxima. The dependence of the x-ray yield on laser polarization is also shown in Fig. 1; when the previously intense and obvious x-ray signal is again sought using vertically polarized light (*s*-polarized interaction), only very weak and erratic x-ray emission is observed. Indeed it is clear that the slow decay of weak emission after passing through the beam is largely due water vapor remaining from the previous shot, which can build up locally when the helium flow rate is relatively low, as it was for the illustrated measurements. This was confirmed by repeating a given scan in the opposite direction, also by increasing the flow rate of helium. The erratic emission by the vapor is independent of the laser polarization.

The observable x-ray yield depends critically on laser pulse duration (chirp) for pulse durations from the shortest value up to a few hundred femtoseconds. The integrated x-ray intensity scans shown in Fig. 2 were obtained by manually scanning the distance between the gratings in the laser pulse compressor through the value corresponding to the shortest pulse. Such scans are very valuable for diagnostic purposes and are performed routinely. The full width half maximum of the optical pulse was measured independently using an autocorrelator and is shown in the same graph. From this it is apparent that the laser pulse duration corresponding to the edge of the x-ray yield plateau (for either positive or negative chirp) is ~200 fs, or ~80 field cycles. Shorter pulses have a stronger tendency to self-focus, so that it was not possible to perform simple scans of this nature in which the position of the jet was constantly optimized. As a result, such scans were done after first optimizing the jet position at a particular grating separation. This said, the transform limited pulse invariably gives relatively very poor yield, while the x-ray yield typically shows maxima or plateaus on either side of the shortest pulse. Such behavior is evident in all scans where the jet position is not first optimized for very short pulses, while the appearance of distinct yield maxima versus plateaus depends at least in part on the chirp at which the jet position is optimized prior to making such scans. Other experiments we describe typically involve use of a chirp corresponding to the edge of the x-ray yield plateau, this giving best x-ray yield without unnecessarily compromising the laser (and therefore potentially also x-ray) pulse duration.

Shot to shot x-ray production is very stable, enabling real time scans of various parameters and negating pileup problems that would otherwise require more extensive

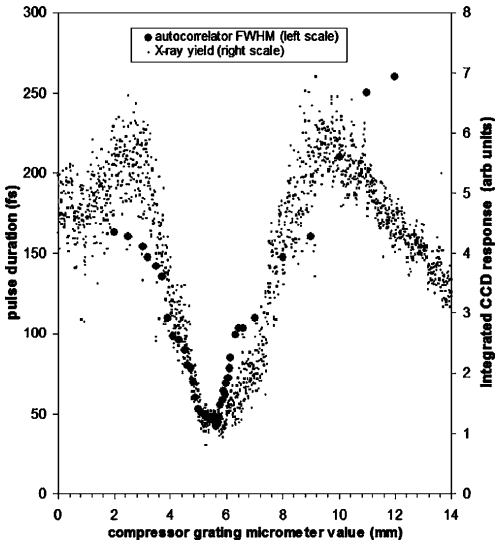

FIG. 2. Typical scan of x-ray yield vs laser chirp, with overlaid measurement of laser pulse width using an optical autocorrelator. Indicated micrometer values are an offset from the full compressor grating separation of approximately 1 m. For the x-ray yield data, the distance between the gratings was scanned manually while recording the integrated frame by frame CCD response in real time (see text). Bremsstrahlung yield is significantly reduced with optimally compressed laser pulses, an observation that remains true even after adjusting the jet position to compensate for self-focusing at the shorter pulse durations.

precautions[34] in the multishot germanium point detector experiments described shortly. A root-mean-square stability of 5%–6% (shot-shot deviation of integrated CCD signal) is typical. This is believed to be due to a combination of shot noise for detection of x-ray events on the CCD with pulse to pulse stability of the laser energy.

When operated as described in this work, the source is essentially isotropic. This is evidenced in single shot CCD frames, multishot images, also films wrapped in aluminum foil lining the inside of the chamber. High-contrast small objects of known dimensions positioned close to the source cast shadows whose edge blurring allows geometrical estimates of the source size, being ~30 μm in both horizontal and vertical dimensions (CCD positioned orthogonal to the converging laser beam and jet direction). Analogous measurements, but with the camera repositioned in line with the converging laser beam, show that the depth of the x-ray radiating region in the water jet is ~16 μm. To date experiments have not been performed to assess the source size on a single shot basis. Despite this, the alignment stability and vibration-free, laminar operation of the jet give confidence that the measured multishot source size is a close upper bound for the single shot size. We also observe that biological samples with thicknesses of hundreds of microns to millimeters can produce highly satisfactory images, since these "sample" depths are a fair match to the extinction lengths of the detected x rays in aqueous and organic material.

X-ray energy spectra initially obtained using the direct-

detection CCD as an array of energy dispersive detectors permitted extensive and rapid assessment of x-ray flux and temperature within the laser pulse energy and chirp parameter space. These explorations show that integrated observable flux and spectral temperature both increase with energy per laser pulse at a fixed (optimized) laser chirp. Perhaps counterintuitively, flux and spectral temperatures also increase when the pulse duration is increased (chirped) away from the transform limited value at a fixed laser pulse energy. Such observations were without exception for pulse durations within the maximum x-ray yield plateaus shown in Fig. 2, and for pulse energies up to the pulse energy available from the laser at the time of the CCD spectral measurements (100 mJ/pulse). These observations were confirmed using the germanium point detector in measurements that permitted simultaneous use of both detectors. A CCD x-ray spectrum demands at most a few shots, while the corresponding germanium point detector spectrum requires several hours. Quantitative spectral and flux agreement of the two detectors is testament to both the long term stability of the source and adequate modeling of the CCD behavior. The long measurement times required by the point detector necessitate a very sparse and selective sampling of the laser's chirp and power parameter space. A selection of point detector spectra after compensation for filters, solid angle, and measurement time are shown in Fig. 3, where simultaneously measured data from the CCD are overlaid in one instance to illustrate the region of quantitative agreement and motivate relevant cautions in the spectral interpretation.

To date we have only seen evidence for a single exponential expression for the flux, modeled as $N=N_0 \exp(-h\nu/kT)$, where h, ν, and k have their usual significance, and N_0 and T are fitted flux and temperature parameters. Pileup manifests as a shallower slope at higher energies in the linear-log plot, being especially prominent in the illustrated CCD spectrum. A component with steeper slope can be apparent at the low energy end of spectra due to partially registered events and preamplifier noise in combination with ill conditioning (high filter normalization of low count rates). This is again most prominent in the CCD spectrum (in which events spanning multiple pixels were integrated using imaging software). The steeply declining ability of low energy photons to reach and stimulate the CCD (response function) is shown as partial motivation for this explanation, which finds further support in peripheral work with this detector using ^{55}Fe and ^{241}Am radioactive sources. When using titanium and copper foil filters of known thicknesses (results not shown), our ability to quantitatively model the magnitudes of the absorption edges is an assurance that other detectable radiations are not simultaneously present. Fitted values for the illustrated spectra are tabulated in Table I. Trends of temperature versus power and temperature versus chirp evident in the table verify the much more extensive CCD measurements; note the quantitative agreement of the corresponding CCD and germanium point detector spectra, measured at the same time. X-ray flux continues to be very appreciable even at the lowest pulse energy shown in the table, indicating that the results are transferable to high pulse repetition rate (kilohertz) laser systems.

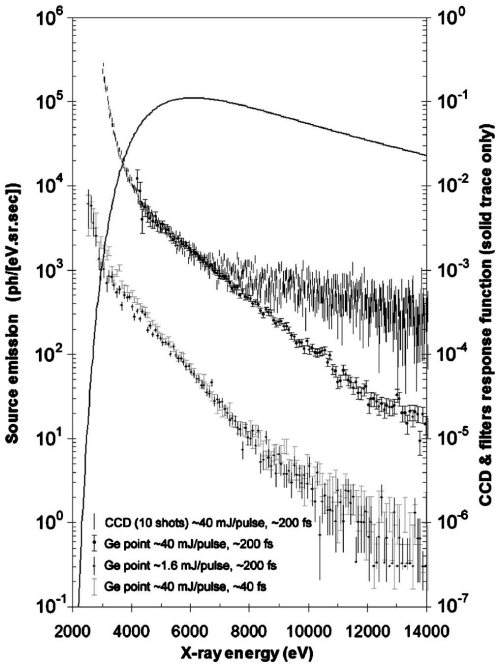

FIG. 3. Source spectra after normalization by filters, ADC binning interval, solid angle, and measurement time. A linear region is apparent in all cases from 4–7 keV and extends to higher energies depending on the degree of pileup. The response functions of the CCD and filters used in the associated spectrum are shown on a comparable scale. The data only support modeling of a single temperature component for each spectrum (see text).

An upper bound on the x-ray pulse duration was obtained using the streak camera. In practice it was possible to position the photocathode ~12 cm from the plasma source. Optimization of the source permitted typically several tens of x-ray events to be observed per laser shot. Following examination of the unswept photocathode image, the sweep was stepwise increased to its fastest value, with fine tuning of the delay at each step to temporally window the swept pulse. The image of the slit width did not significantly increase at any point during this procedure and the number of observed photons did not appreciably change. Significant timing jitter was observed on the fastest sweeps, as anticipated. This is shown in Fig. 4, where we also show an effective compilation following manual compensation of jitter in individual frames. As far as is possible to determine, the x-ray pulse obtained in this way is symmetrical, moreover narrower than

TABLE I. Fitted source flux and temperatures corresponding to Fig. 3.

Energy/pulse (mJ)	Optical pulse duration (fs, estimate)	N_0 (ph/[ev sr s])	T (K [eV])
40	~200 (max x rays)	17.5×10^3	17.4×10^6 [1500]
1.6	~200 (max x rays)	14.7×10^3	12.7×10^6 [1090]
40	~40 (shortest pulse)	29.2×10^3	11.5×10^6 [990]

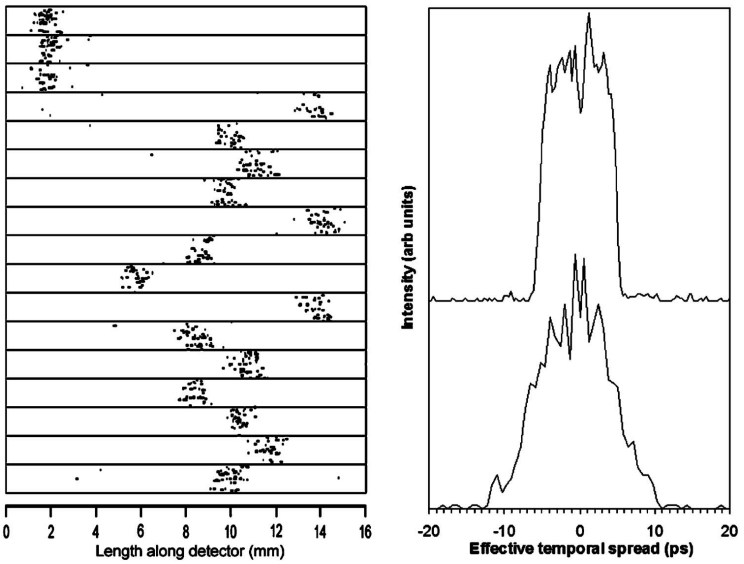

FIG. 4. Summary of streak camera results. Typically several tens of events were registered per shot. On the left are examples of unstreaked (top three) and streaked images at the fastest rate of ~11 ps/mm. Trigger jitter causes differences in the positions of the swept photocathode images at this sweep rate. The upper right trace shows the breadth of the unswept photocathode image, while the lower trace shows apparent broadening that could be inferred by subjective manipulation of 22 swept images.

the ~25 ps resolution function previously ascribed to this instrument. Various instrumental matters can contribute to such spreading in the streaked images, but on the other hand the observation of only a few photons per shot could potentially reduce the width in the compilation. Determination of what limits the camera's x-ray temporal response function lies outside the goals of the present work. We believe these measurements indicate an upper bound for the x-ray pulse duration, whose actual duration is presumed to be considerably shorter, as discussed below.

To motivate ongoing developments leading to applications, Fig. 5 shows CCD shadow images obtained in several hundreds of shots, indicative of the practical flux and isotropicity, also a single shot absorption spectrum of a 5 μm titanium foil measured using the CCD. The *K*-absorption edge at 4.97 keV in the latter is clearly evident. To our knowledge, this is the first literature presentation of a single shot, presumed subpicosecond absorption edge measurement using an in-house vacuum-free laser plasma system.

DISCUSSION

Unusually low prepulse and ASE pedestal ratios in our laser system ($<10^{-8}$) indicate a sharp plasma density gradient during laser-target interaction at the water surface. Such conditions are required for the vacuum heating mechanism of Brunel,[35] which we invoke as the mechanism for electron acceleration preceding x-ray bremsstrahlung generation. Strong evidence is found in the grazing angle of incidence and polarization requirements[36] on the extremely smooth target surface, in x-ray measurements that are not complicated by the simultaneous observation of emission line radiation. Pulse durations corresponding to the edge of the plateau (~200 fs) along with estimates of the laser spot size and measurement of laser power (~100 mJ/pulse) indicate target

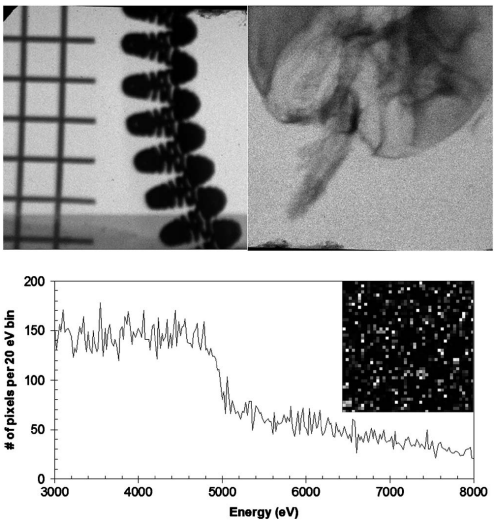

FIG. 5. Motivations for source applications. Shadow imaging applications demonstrate an abundance of isotropic x rays with a small source size. Upper left image shows a 254 mm nickel mesh a 60 W incandescent lamp filament, showing its supercoil structure, here measured in the horizontal plane orthogonal to the converging laser beam. A total exposure time of 2 min was used. The high contrast of such objects permits estimates of the source size in three dimensions. At upper right is the head of a housefly, for which a reasonable match of the extinction depths of observable x rays to sample dimensions permits good contrast of internal features. An aluminum filter (12 μm) was used in this total 4 min exposure. The lower image is a *K*-edge absorption spectrum of a 5 μm titanium foil obtained as a direct histogram of pixel intensities in a single, presumed subpicosecond burst (see text). The inset gives an impression of the fairly high degree of pileup in this measurement.

intensities of $\sim 10^{17}$ W/cm^2 for our experiments, an intensity range in which this heating mechanism is well established.[7] Also importantly, we observe x-ray temperatures that increase as the laser pulse duration is extended while maintaining constant laser pulse energy, an observation consistent with resonant heating of electrons in the laser field. The present combination of observations is thus a clear practical indication of this mechanism.

In addition to spectral properties, temporal aspects of the source are vital to its development, since longer pulse laboratory sources requiring less infrastructure can also be constructed.[37,38] At the present time there are four independent handles on this question. The first is the streak camera measurements, which merely permit the statement that the observed x-ray pulse duration is less than or at most comparable to that instrument's temporal resolution function. Secondly, there is the duration of the optical pulse, whose envelope is observed to be 200–300 fs when x-ray generation is optimized. As shown in Fig. 2 this can be reduced while still obtaining appreciable x-ray production. Thirdly, we infer electron temperatures from the x-ray spectra (typically ~ 1 keV). While acknowledging the potential for misinterpretation, this suggests a fast rate of blackbody radiation loss through the Stefan-Boltzmann law in combination with the measured source size. The energy of a 100 mJ laser pulse would then be dissipated in <10 fs, assuming complete conversions. Fourthly, the electron attenuation length in water, divided by the velocity of electrons capable of producing high energy x rays, indicates the time scale of the interaction. The continuous slowing down approximation electron penetration distances[22] suggest approximate time scales of 42, 330, and 760 fs for the bremsstrahlung interactions of 10, 50, and 100 keV electrons in a 200 μm water jet. In the same vein, our multishot x-ray radiation depth estimate of ~ 16 μm associated with registry of mostly 4–5 keV x rays suggest a time scale of ~ 400 fs. From such arguments it would appear that either the electron stopping depth or perhaps the optical pulse duration determines the x-ray pulse duration. Since water jets can be arranged that are thinner than the electron stopping length, while buildup of electron energies requires several field cycles, the latter bounds are subject to practical manipulation and further interpretation, respectively. Access to an x-ray streak camera with subpicosecond temporal resolution or careful single shot radiation depth measurements could perhaps give a practical answer to which bound is more appropriate in particular circumstances. In either case it appears that x-ray pulses are around two orders of magnitude briefer than typically obtained in synchrotron storage rings, this being a range that renders them of particular interest for molecular chemical structure-dynamics studies. As such, and with the relevant detection developments underway, it is presumed that application-based pump-probe experiments will provide a fifth and independent practical indication in due course. Synchronization of the x-ray pulse with the laser in the associated pump-probe topologies will be essentially free from temporal jitter.

The number of broadband x-ray photons emitted in an experimentally accessible solid angle is already quite adequate when considering essential numbers needed by applications such as pump-probe transmission EXAFS. Detection schemes based on conventional diffraction topologies are the only restriction to this application. The essential truth of this assertion is quickly appreciated from Fig. 5, where we show images involving necessarily large numbers of photons obtained in very reasonable experimental times at 10 Hz, along with an absorption edge observation simply obtained using a single laser shot. Associated work with our CCD detector confirms that the addition of many such histograms is of no practical value with this kind of detector. Nevertheless it is clear that one approach to ultrafast EXAFS on such a laser plasma based source is to subtend a sufficient solid angle around the source with a suitable number of high-resolution detectors that are capable of readout at the laser repetition rate, such that the dramatic losses associated with analyzer crystals are completely avoided. In such a setup the water jet itself might be a very inviting solvent matrix for certain EXAFS samples if x rays are generated on the side of the jet such that they must traverse it to reach the detector; alternatively a second jet or other sample apparatus is easily arranged in the closest possible proximity to the source. In either case, the volume of sample requiring optical excitation needs to have dimensions only slightly larger than the ~ 30 μm $\times$ 30 μm x-ray source, enabling high levels of optical sample excitation using available ultrafast lasers, while in principle requiring very little sample material and leading to very small temporal dispersion due to geometrical considerations. The lack of x-ray focusing optics in this scheme (in particular, before the sample) eliminates issues related to alignment and temporal dispersion in such components. Our source is extremely well suited to such a detection scheme, since suppression of energies outside the range of interest involves nothing more than simple foil filters, removal of unwanted emission lines is unnecessary, and the isotropic nature of the x-ray emission would be used as an advantage. Given sufficient pixel readout rate, it is readily appreciated that the rate of data acquisition is proportional to both the number of pixels and the laser repetition rate. We have demonstrated that laser pulses do not need to be unusually brief or powerful, so that standard kilohertz repetition rate lasers can be used, if necessary with tight focusing and measures to improve the contrast ratio.

Direct-detection CCD detectors are presently giving way to much higher resolution microbolometric array detectors[39] which will obviate the need for wasteful crystal diffraction-based analyzers hitherto associated with suitably resolved energy dispersion at "hard" x-ray energies. Foreseeable availability of microbolometric array detectors[40] is a key motivation for ongoing exploration of this source. The millikelvin temperatures required by such detectors gives cause to reflect on the extraordinary temperature range these experiments would involve. In combination with in-house sources such as described here and by others,[12] these detectors should enable ultrafast molecular structure studies in any suitably equipped ultrafast kilohertz laser laboratory. To assist the necessary developments, a few precautions of particular relevance to the source described here are outlined in the remaining paragraphs. We further point out that with the contemporary development of collimated broadband laser-

generated x-ray beams, such array detectors will enable x-ray momentum transfer measurements, this being the essential measurement required for structural measurements by diffuse scattering, crystallography, and reflectometry. As such, the development of fast readout high-resolution array detectors in photon-starved ultrafast x-ray science should offer benefits comparable to the development of time of flight techniques in neutron science.

In a somewhat shorter term, conventional extremely lossy but technically straightforward diffraction-based technologies[41,42] are lately enjoying a renaissance[43,44] which might also permit practical ultrafast x-ray absorption spectroscopy applications. The latter developments motivate awareness of source parameter spaces that can be used to enhance the bremsstrahlung, but also of the practical complications that may ensue. For example, we observe that hard x-ray fluxes and temperatures increase considerably when using a water aspirator vacuum instead of helium, an approach in which it is necessary to degas and slightly cool the water in order to maintain jet stability. Also, when using diffraction-based detection the generation of hard emission line radiation is not in itself an issue (indeed such lines are useful energy calibrants). Thus higher-Z materials or concentrated solutions of high-Z compounds are typically attractive targets because of their higher bremsstrahlung yields. In practice, it proves difficult to avoid problems associated with debris.

The controlled insertion of a prepulse with s-polarized interaction geometry (capable of generating a preplasma without itself generating significant x rays) introduces an enormous parameter space displaying very rich behavior. In a simplistic view, prepulses generate a more gradual local plasma density gradient that causes refraction of the subsequent pulse away from the higher density regions at greater depths. One consequence is that x-ray generation by the subsequent p-polarized pulse is optimal at a nongrazing angle of incidence. Indeed we observe that the controlled introduction of prepulses is associated with dramatic changes in the interaction geometry leading to x-ray generation. In this context we note that 30°–60° angles of incidence have often been cited in the literature,[7,25,45] in clear contrast to the grazing incidence required by the present very low prepulse experiments and the sharp density profile vacuum heating mechanism invoked to explain our specifically bremsstrahlung results. In addition, upon the introduction of prepulses or when the contrast of our laser system is impaired, additional caution is needed to distinguish x rays generated at the target from collimated ~20–200 keV electron beams[31,32,45] and secondary emissions these can give rise to, both of which we have unambiguously observed under those specific conditions. While indicating potential pitfalls for the unwary, this also indicates the feasibility of controlled electron beam generation desirable in related contemporary developments. As a result, such beams are the subject of peripheral investigations.

The approximate brilliance of the source when operating under helium is inferred from Table I and the observed multishot source size of 30 μm, which perhaps varies under different laser conditions. Thus the first entry in the table corresponds to ~397 photons/s mm^2 mrad^2 0.1% bw at 5 keV. Such low values give an initial impression of woeful inadequacy compared with contemporary synchrotron and other emerging sources. However, the comparison is not a meaningful one. The reason is that such sources normally aim for increasingly tight collimation and narrow bandwidths for the purposes of satisfying grazing incidence mirror requirements and crystallographic Bragg conditions in analyzer optics, such that the corresponding normalizations dramatically favor them. As we indicate, diffraction based energy dispersion is not viewed as the best way to proceed with chemical structure studies using this source. Topologies that address large solid angles are clearly essential, along with low temporal dispersion before traversing samples, and we have indicated how both can be achieved. Fluxes from our source will scale linearly with laser repetition rate and can be made to increase by adjustment of several independent laser parameters as we have shown.

In closing we point out that earlier solid target plasma sources involved mechanisms to address target replacement, debris handling, remote control, and target and/or sample evaporation in evacuated chambers, as well as pumping equipment and necessarily more extensive radiation safety precautions. Given such infrastructure, typical shot to shot fluctuations from solid targets could still be several orders of magnitude.[34] Many observations indicate substantial intensity increases when shooting into nanostructures,[46] existing craters,[47] and (very early in this work) lead smoke from laser ablation of the target chamber itself, collectively demonstrating the criticality of reliable interaction geometry in reproducible experiments. The source we describe has sought to address all these matters in simple and robust ways, this being a prerequisite for foreseeable applications in chemical structural dynamics. Substantial alterations and additions to the laser system as well as construction of several variants of the x-ray generator during the two years of these developments confirm the robustness of the observations presented.

CONCLUSIONS

An x-ray laser plasma source is presented whose novelty lies in its broadband spectral qualities free from observable emission lines, practical simplicity with complete avoidance of vacuum systems, or remote control, temporal duration suitable for ultrafast applications, good shot to shot stability and transferability to lower power, higher repetition rate laser systems. To our knowledge this work is the first to demonstrate a clear requirement for grazing incidence of p-polarized laser fields for the generation of few keV bremsstrahlung in the absence of significant prepulses or ASE. This gives strong indications of a vacuum heating mechanism, which finds further support in quantitative measurements of yield and x-ray temperatures versus laser chirp. We indicate prepulse based approaches that may allow the source to be made brighter without sacrificing the associated x-ray temporal structure. A single shot observation of a Ti foil absorption edge is presented to stimulate foreseeable spectrometer and detector developments in anticipation of ultrafast structural dynamics applications. In association with contempo-

rary detector developments, and along with other existing laser-based x-ray sources, we believe the source we describe points the way to in-house picosecond chemical structural dynamics in essentially any modern ultrafast laser laboratory operating at kilohertz laser repetition rates.

ACKNOWLEDGMENTS

We thank A. Persson, E. Pourtal, F. Lindau, O. Lundh, T. Hanson, and J. Larsson for assistance with laser operation, optical characterizations, discussions, and general developments during this project. This work has enjoyed financial support from the Knut and Alice Wallenberg Foundation, the Kungliga Fysiografiska Sällskapet, and the Swedish Research Council.

[1] C. Bressler and M. Chergui, Chem. Rev. (Washington, D.C.) **104**, 1781 (2004).
[2] V. Srajer, Z. Ren, T. Y. Teng, M. Schmidt, T. Ursby, D. Bourgeois, C. Pradervand, W. Schildkamp, M. Wulff, and K. Moffat, Biochemistry **40**, 13802 (2001).
[3] S. Techert, F. Schotte, and M. Wulff, Phys. Rev. Lett. **86**, 2030 (2001).
[4] H. Ihee, M. Lorenc, T. K. Kim, Q. Y. Kong, M. Cammarata, J. H. Lee, S. Bratos, and M. Wulff, Science **309**, 1223 (2005).
[5] A. Franks, Proc. Phys. Soc. London, Sect. B **68**, 1054 (1955).
[6] R. F. Garrett, J. W. White, D. J. King, T. L. Dowling, and W. Fullagar, Nucl. Instrum. Methods Phys. Res. A **467**, 998 (2001).
[7] P. Gibbon and E. Forster, Plasma Phys. Controlled Fusion **38**, 769 (1996).
[8] S. C. Wilks and W. L. Kruer, IEEE J. Quantum Electron. **33**, 1954 (1997).
[9] W. P. Leemans, E. Esarey, J. van Tilborg, P. A. Michel, C. B. Schroeder, C. Toth, C. G. R. Geddes, and B. A. Shadwick, IEEE Trans. Plasma Sci. **33**, 8 (2005).
[10] A. Rousse, K. T. Phuoc, R. Shah, A. Pukhov, E. Lefebvre, V. Malka, S. Kiselev, F. Burgy, J. P. Rousseau, D. Umstadter, and D. Hulin, Phys. Rev. Lett. **93**, 135005 (2004).
[11] W. P. Leemans, B. Nagler, A. J. Gonsalves, C. Toth, K. Nakamura, C. G. R. Geddes, E. Esarey, C. B. Schroeder, and S. M. Hooker, Nat. Phys. **2**, 696 (2006).
[12] E. Seres, J. Seres, and C. Spielmann, Appl. Phys. Lett. **89**, 181919 (2006).
[13] J. Seres, P. Wobrauschek, C. Streli, V. S. Yakovlev, E. Seres, F. Krausz, and C. Spielmann, New J. Phys. **8**, 251 (2006).
[14] K. Chouffani, F. Harmon, D. Wells, J. Jones, and G. Lancaster, Laser Part. Beams **24**, 411 (2006).
[15] K. T. Phuoc, F. Burgy, J. P. Rousseau, V. Malka, A. Rousse, R. Shah, D. Umstadter, A. Pukhov, and S. Kiselev, Phys. Plasmas **12**, 023101 (2005).
[16] J. Larsson and A. Sjogren, Rev. Sci. Instrum. **70**, 2253 (1999).
[17] A. K. Shuaibov, L. L. Shimon, A. I. Dashchenko, I. V. Shevera, and M. P. Chuchman, Plasma Phys. Rep. **27**, 82 (2001).
[18] K. Hatanaka, T. Miura, and H. Fukumura, Appl. Phys. Lett. **80**, 3925 (2002).
[19] K. Hatanaka, T. Miura, and H. Fukumura, Chem. Phys. **299**, 265 (2004).
[20] R. J. Tompkins, I. P. Mercer, M. Fettweis, C. J. Barnett, D. R. Klug, L. G. Porter, I. Clark, S. Jackson, P. Matousek, A. W. Parker, and M. Towrie, Rev. Sci. Instrum. **69**, 3113 (1998).
[21] M. Lamoureux, P. Waller, P. Charles, and N. B. Avdonina, Phys. Rev. E **62**, 4091 (2000).
[22] M. J. Berger, J. S. Coursey, M. A. Zucker, and J. Chang, ESTAR: Electron Stopping-Power and Ranges, http://physics.nist.gov/PhysRefData/Star/Text/ESTAR.html
[23] X-ray interactions with matter, http://www.cxro.lbl.gov/optical_constants/
[24] A. Thoss, Ph.D. Thesis, Fachbereich Physik der Freien Universität Berlin, 2003.
[25] F. Benesch, T. W. Lee, Y. Jiang, and C. G. Rose-Petruck, Opt. Lett. **29**, 1028 (2004).
[26] A. Rousse, P. Audebert, J. P. Geindre, F. Fallies, J. C. Gauthier, A. Mysyrowicz, G. Grillon, and A. Antonetti, Phys. Rev. E **50**, 2200 (1994).
[27] J. Steingruber, S. Borgstrom, T. Starczewski, and U. Litzen, J. Phys. B **29**, L75 (1996).
[28] M. W. Bautz, G. Y. Prigozhin, M. J. Pivovaroff, S. E. Jones, S. E. Kissel, and G. R. Ricker, Nucl. Instrum. Methods Phys. Res. A **436**, 40 (1999).
[29] G. Prigozhin, S. Jones, M. Bautz, G. Ricker, and S. Kraft, Nucl. Instrum. Methods Phys. Res. A **439**, 582 (2000).
[30] P. Gibbon, Phys. Rev. Lett. **73**, 664 (1994).
[31] X. Y. Peng, J. Zhang, T. J. Liang, Z. M. Sheng, Z. Jin, Y. T. Li, Z. H. Wang, Q. Z. Yu, Z. Y. Zheng, Y. Q. Liu, H. C. Wu, Z. Q. Hao, X. H. Yuan, and Z. Y. Wei, Chin. Phys. Lett. **21**, 693 (2004).
[32] X. Y. Peng, J. Zhang, Z. Jin, T. J. Liang, J. Y. Zhong, H. C. Wu, Y. Q. Liu, Z. H. Wang, Z. L. Chen, Z. M. Sheng, Y. T. Li, and Z. Y. Wei, Acta Phys. Sin. **53**, 2625 (2004).
[33] J. Zhang, Y. T. Li, Z. M. Sheng, Z. Y. Wei, Q. L. Dong, and X. Lu, Appl. Phys. B: Lasers Opt. **80**, 957 (2005).
[34] A. Sjögren, M. Harbst, C. G. Wahlstrom, S. Svanberg, and C. Olsson, Rev. Sci. Instrum. **74**, 2300 (2003).
[35] F. Brunel, Phys. Rev. Lett. **59**, 52 (1987).
[36] K. Eidmann, R. Rix, T. Schlegel, and K. Witte, Europhys. Lett. **55**, 334 (2001).
[37] C. N. Boyer, G. E. Holland, and J. F. Seely, Rev. Sci. Instrum. **76**, 035109 (2005).
[38] L. Soto, Plasma Phys. Controlled Fusion **47**, A361 (2005).
[39] *Nuclear Instruments and Methods in Physics Research Section A: Accelerators, Spectrometers, Detectors and Associated Equipment* (Elsevier, New York, 2006) Vol. 559, pp. 329–860.
[40] I. J. Maasilta, K. M. Kinnunen, A. K. Nuottajärvi, J. Leppäniemi, and A. Luukanen, Supercond. Sci. Technol. **19**, S242 (2006).
[41] P. Beiersdorfer, R. E. Marrs, J. R. Henderson, D. A. Knapp, M. A. Levine, D. B. Platt, M. B. Schneider, D. A. Vogel, and K. L. Wong, Rev. Sci. Instrum. **61**, 2338 (1990).
[42] A. P. Shevelko,Proc. SPIE **91**, 3406 (1998).
[43] M. Kaburagi, Y. Z. Bin, D. Zhu, C. Y. Xu, and M. Matsuo, Carbon **41**, 915 (2003).
[44] H. Legall, H. Stiel, V. Arkadiev, and A. A. Bjeoumikhov, Opt. Express **14**, 4570 (2006).
[45] S. Bastiani, A. Rousse, J. P. Geindre, P. Audebert, C. Quoix, G. Hamoniaux, A. Antonetti, and J. C. Gauthier, Phys. Rev. E **56**, 7179 (1997).
[46] P. P. Rajeev, P. Taneja, P. Ayyub, A. S. Sandhu, and G. R. Kumar, Phys. Rev. Lett. **90**, 115002 (2003).
[47] M. Grätz, Ph.D. Thesis Lunds Universitet, 1998.

Paper II

The use and characterization of a backilluminated charge-coupled device in investigations of pulsed x-ray and radiation sources.

W. Fullagar, J. Uhlig, M. Walczak, S. Canton, I. Maasilta, V. Sundström.
Review of Scientific Instruments **79(10)**, 103302 (2008).

REVIEW OF SCIENTIFIC INSTRUMENTS **79**, 103302 (2008)

The use and characterization of a backilluminated charge-coupled device in investigations of pulsed x-ray and radiation sources

Wilfred Fullagar,[1,2] Jens Uhlig,[1] Monika Walczak,[1] Sophie Canton,[1] and Villy Sundström[1]
[1]*Division of Chemical Physics, Kemicentrum Lund University, P.O. Box 124, SE-22100 Lund, Sweden*
[2]*Monash Centre for Synchrotron Science, Monash University, Clayton, VIC 3800, Australia*

(Received 7 April 2008; accepted 23 September 2008; published online 29 October 2008)

Examinations of bremsstrahlung and energetic electron beams from a novel laser plasma source motivate and assist characterization of a backthinned, backilluminated direct detection x-ray charge-coupled device (CCD), a topology that is uncommon in hard x-ray work. Behavior toward pseudomonochromatic (^{55}Fe) and multichromatic (^{241}Am) sources is briefly reviewed under optimized noise conditions. Results collectively establish the previously unknown functional depth structure. Several modes of usage are illustrated in ~4–20 keV x-ray laser plasma source investigations, where the significance of the characterization is briefly discussed. The spectral redistribution associated with this CCD topology is unfavorable, yet appropriate analysis ensures that sufficient spectral information remains for quantitative determination of broadband x-ray flux and spectra in essentially single laser shot measurements. The energy dependence of nascent electron cloud radii in silicon is determined using broadband x-rays from the laser plasma source, turning the narrow depletion depth to advantage. Finally, the characterization is used to quantify recent x-ray spectral explorations of the water jet laser plasma source operating under aspirator vacuum. These results will have key value for establishment of laboratory based ultrafast extended x-ray absorption fine structure experiments using microbolometric detectors. © *2008 American Institute of Physics.* [DOI: 10.1063/1.3000003]

I. INTRODUCTION

Charge-coupled devices (CCDs) are a mature technology.[1] The use of direct detection CCDs is fairly widespread in x-ray communities requiring single photon sensitivity at energies up to ~20 keV and moderate resolution of photon energies within each pixel. They permit high spatial resolution imaging capability with the convenience of electronic data acquisition, making them a popular choice for x-ray studies in plasma physics,[2] astronomy,[3,4] x-ray imaging,[5,6] and diffraction[7] applications. Many accounts of direct detection CCDs in a laser plasma context have substantially attended to observation of x-ray emission lines,[2,8,9] or their use in spectral imaging modes.[10,11] Often, an understanding of the x-ray source is sought, with limited attention to detector details.

A backilluminated, non-deep-depleted direct detection CCD has been available to us for the evaluation of radiations from a novel laser plasma source.[12] Its extended use[13–16] in a fundamental research environment[17] has led to a continual demand for its characterization, in the face of limited technical information about the particular device. Its topology is unusual in the hard x-ray field of study. We evaluate its energy resolution limit, strong x-ray spectral redistribution and declining sensitivity to high energy x-rays using pseudomonochromatic and multichromatic sources. These allow an outline of its depth structure that are subsequently fine-tuned using results from our broadband laser plasma x-ray source, with calibration by a Ge point detector. The same measurements allow estimation of thermalized electron cloud radii over a continuum of x-ray energies, with a simple and empirical outcome that may find applicability from visible energies to ~60 keV. Several important plasma source experiments that have benefited from the CCD characterization are illustrated. Finally, we use our findings to quantitatively measure ~4–20 keV ultrafast broadband x-ray spectra that should be obtainable using kilohertz repetition laser systems in developments that are currently underway. Detector limitations and their causes realized in this work led us to suggest the incorporation of microbolometer arrays in associated ultrafast molecular structure dynamics developments.[12]

An overview of the processes occurring during direct x-ray detection indicates the limitations encountered in this work. The photoelectric cross section dominates the interaction of x rays with Si (the CCD material) for x-ray energies up to ~60 keV.[18] The initial outcome is an ionized atom and an energetic photoelectron. The former may generate further electrons by Auger and shakeup processes, while these new electrons and the energetic photoelectron cause further excitations on length scales of approximately a micron and less.[19] The electronically measurable outcome is a localized cloud of thermalized electrons in the semiconductor's conduction band. Thermalized electron cloud radii are an increasing function of x-ray photon energy. The clouds diffuse in all directions, following local electric field gradients. Another relaxation channel for the excited atom is x-ray fluorescence; energy that escapes detection by this mechanism gives rise to escape peaks. Also, if x-ray photon capture occurs sufficiently close to the surface, nonthermalized electrons can

carry energy out of the detector as photoelectrons if their energy is still above the material's work function. Recombination or trapping may occur, also it may not be possible to quantitatively bring the entire charge cloud into a readout amplifier. In the course of the overall process, most of the original x-ray energy is in fact converted to heat. The microscopically stochastic nature of the heat versus conduction electron outcome leads to a fundamental (Fano)[20] limit for the energy resolution of nonbolometric detectors.[21]

With these provisos, the number of measurable electrons arising from an event is generally proportional to the original x-ray photon energy so that from a CCD user perspective, and if all goes well, a discrete x-ray event translates to a single bright pixel in the associated CCD readout. The corresponding charge is proportional to the energy of the x-ray photon. A histogram of pixel intensities can be interpreted as the energy spectrum, given allowances for the many potential losses just described, as well as the possibility of pileup. Circumstances permit good signal to noise ratio for these measurements, indeed sufficient to directly appreciate the Fano limit. The CCD pixels, and the event charges they contain, are read out sequentially. This approach is extremely valuable when events strike the detector in different pixels, but simultaneously from an electronic perspective; it enables one-shot spectral assessment of arbitrarily short pulse, noncollimated x-ray sources.

We take a symptomatic approach to the CCD characterization. The reason is simply that the device we possess continues to be extremely versatile in numerous experiments, yet technical information has been scarce. As mentioned at the outset, CCDs are a mature technology so sophisticated and successful models exist for electron cloud diffusion in different detector regions and electronic biasing conditions in various CCD topologies. For these the reader is directed elsewhere.[1,22–24] Here a general awareness suffices, coupled to practical observation; the outcome is consistent with general expectations. It has long been apparent that the nondeep-depleted, backilluminated topology is not an ideal CCD topology for hard x-ray detection, for reasons that are clear in this work. Consequently, this work presents a rather unique look at the behavior of this CCD topology in the hard x-ray spectral region. We turn its thin depletion layer to advantage when studying the cloud radius versus x-ray photon energy variation. We go on to quantify extremely useful and contemporary laser plasma x-ray results that used the CCD, required its characterization, and could not be generated using other detectors available at the time.

II. APPARATUS

The CCD is a backthinned, backilluminated 512 $\times$512 pixels, 24.8 μm$\times$24.8 μm direct detection device (model SXTE/CCD-512TKB1, Scientific Imaging Technologies). It lies 10 mm behind a 250 μm Be window in an evacuated, triple Peltier stage, water cooled camera head, and is coupled to a computer controller interface (ST-130, 16 bit, 200 000 samples/s, Princeton Instruments). This work uses a stable gain setting corresponding to $\sim$20.2 eV of x-ray energy per analog to digital converter (ADC) unit, calibrated using emission lines from an ^{55}Fe source. The preamplifier output and ADC input are relatively biased such that null output from the preamplifier is $\sim$120 ADC units. This provides adequate resolution and dynamic range to characterize noise functions as well as individual x-ray photons, including high energy or pileup events. Specific information regarding CCD construction and performance has been obscured by the commercial environment surrounding its manufacture and subsequent integration (the CCD manufacturer has ceased operations). This work builds on the following indications. Quantum efficiency curves for an apparently similar CCD (PIXIS-XO 512B) in the 1–9 keV range can be reverse engineered to suggest an attenuating layer of 0.1 μm Si followed by a sensitive depth of $\sim$14.9 μm Si. Backilluminated, backthinned CCDs of $\sim$15 μm thickness were available from the CCD manufacturer prior to the delivery of our apparatus in 1994. In these, a bias-dependent potential valley extends several microns in the vicinity of the gate electrodes.

A Ge point detector (ORTEC Canberra GUL0105 with EG&G ORTEC 429 3 MCA card) was used to calibrate each of the x-ray sources examined. It is characterized elsewhere.[25] For present purposes we take its detection efficiency to be 100% in the entire spectral region examined in this work (25 μm Be in front of a Ge detector crystal with active thickness of 5 mm). Relative to the CCD, it is associated with very little spectral redistribution, but has a relatively poor energy resolution that is a function of shaping times.

The noise floor of the CCD was established, and the detector always operated in this region. In particular, for our examinations of pulsed sources, CCD exposure times can be arbitrarily short. The presented spectral measurements arise from two readout frames of equal exposure; the first (blank) functioning as a flat field correction. A new blank background measurement is made at the commencement of any measurement. Dark current variation is, in fact, low enough that a potentially $\sqrt{2}$ increase in base line width incurred by two measurements does not necessarily justify the flat field subtraction. However, the procedure ensures symmetry of the baseline peak about zero. It also effectively corrects a stick-jump problem[26] with the ADC, since the flaw is uncorrelated with pixel position and falls well within the noise envelope observed in subsequent pixel intensity histograms. The nature of this problem is that as the input voltage to the ADC is continuously increased, the digital output sticks at particular values for longer than it should, eventually jumping over the correct value to the next higher value. This can happen to the extent that certain values of the digital output are observed twice as often as they should be, while adjacent values are not observed at all.

III. RADIOACTIVE SOURCE WORK

Figure 1 condenses a representative fraction of the radioactive source work. It shows:

(a) Spectra from ^{55}Fe, showing a histogram of all pixel values, another histogram of the same data after thresholding and grouping pixels into events (to reinte-

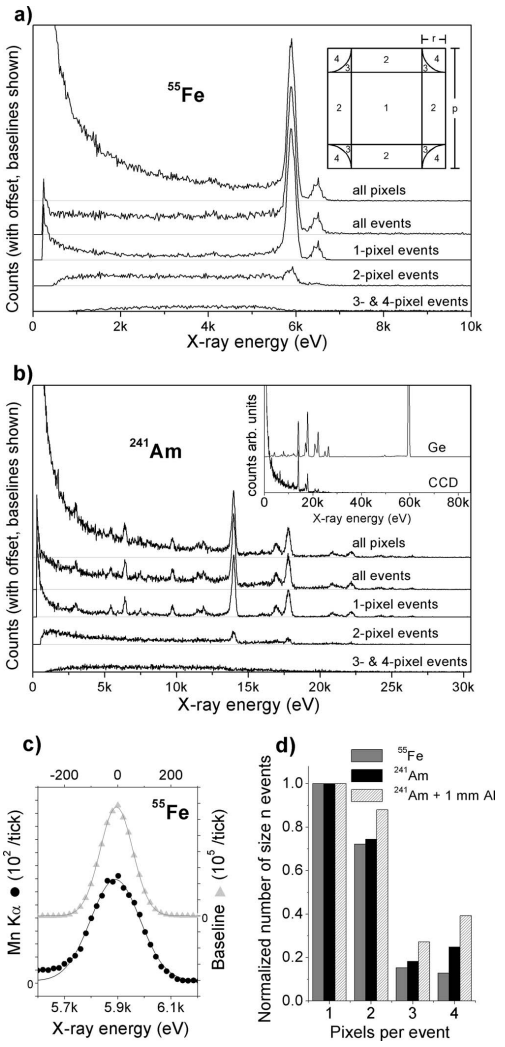

FIG. 1. (a) Pixel histogram, event histogram, and n-pixel event histograms of an ^{55}Fe source measurement. The base line is shown in each case. (b) Analogous histograms from a measurement of an ^{241}Am source. The inset compares the CCD histogram with data obtained using a Ge point detector, showing the rapidly deteriorating high energy response of the CCD. (c) Comparison of the base line and 5.9 keV widths in the same ^{55}Fe data set. (d) High energy events tend to span more pixels. The inset to panel (a) is an aerial sketch of a pixel, showing regions where an event of radius r will span 1, 2, 3, and 4 pixels, applicable in the case of fully registered ^{55}Fe events.

grate distributed charge), the histogram of 1 pixel events (those in which thresholded events are in isolated pixels), the histogram of 2 pixel events, and the histogram of 3 and 4 pixel events. A base line is shown in each case. It is clear that 1 pixel events provide the "best" spectrum and that no spectral improvements can be made by consideration of other events.

TABLE I. Event counts obtained by thresholding ^{55}Fe data obtained using the CCD.

	1 pixel events	2 pixel events	3 and 4 pixel events	≥5 pixel events	Total
≥268 eV	21 354	15 123	5514	608	42 599
≥5704 eV	9343	1953	1041	407	12744
≥6856 eV	28	319	796	336	1479

(b) A corresponding set of histograms for ^{241}Am. The same deduction can be drawn. Fluorescence and escape peaks are visible as well as the source emission lines. The inset compares the CCD with the Ge detector, showing the former's deteriorating response at higher x-ray energies. A faint trail leading up to but not beyond the 59.5 keV line is visible in the CCD data on close analysis.

(c) A comparison of the spread of empty pixels (base line) with the spread of ^{55}Fe's Mn K_α line. It is an unresolved doublet (5889.1 and 5900.3 eV), yet the observed broadening relative to the baseline [full width half maximum (FWHM) of 144 eV] requires convolution with a Gaussian of FWHM of 161 eV to account for the observed Mn $K\alpha$ breadth of 216 eV. This observation guarantees that our measurements are essentially Fano limited. As a result, there is no reason to further pursue questions of electronic noise.

(d) The lateral extent of events increases with the average event energy. All observed events are considered, since it is generally not possible to ascribe the true energy to an arbitrary event in the multiline ^{241}Am spectra. The average event energy from the ^{241}Am source is further raised by filtering; 1 mm of Al strongly suppresses the emissions below ~20 keV.

(e) (Inset to the ^{55}Fe histograms.) An overhead sketch of a pixel, showing the regions in which an event (assumed circular) will be registered in one, two, 3 or 4 pixels. Because it is not possible to confidently assign the true energy to an arbitrary event in nonmonochromatic spectra, this will only have meaning when applied to the pseudomonochromatic ^{55}Fe data, and events whose total charge corresponds to the known x-ray energy. By classifying events as 1 pixel, 2 pixel, etc., generating a histogram in each case, and counting the number of events that exceed particular thresholds, the numbers of fully registered n-pixel events can be established (>268 eV=above detection noise, between 5704 and 6856 eV=fully registered). Table I shows counts corresponding to these thresholds. The ratios of 1 pixel to 2 pixel to 3 and 4 pixel fully registered events best fits the algebraic ratios derivable from the sketch for a lateral cloud radius of ~1.1 μm.

The ^{55}Fe histograms in Fig. 1 demonstrate that the partial registry (spectral redistribution to apparently low energies) in our backilluminated CCD has at least two causes. One is the potential for events to span multiple pixels. However, the weakness of the emission line peak in the 2 pixel and 3 and 4 pixel event histograms show that by itself, this

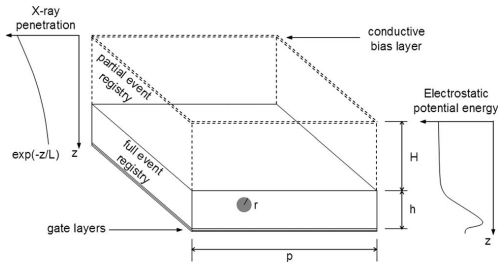

FIG. 2. A simplified sketch of a pixel volume in the CCD. Photons approach from above and are attenuated exponentially. The surface layer (h) is associated with weak field gradients, allowing diffusion of electron clouds both vertically and laterally, and resulting in partial registry of electron clouds forming in this layer. The depletion layer (h) is associated with strong field gradients and a potential minimum (buried channel) in the vicinity of the gate layer. Thermalized electron clouds contained within this layer cannot diffuse out, and are fully registered.

does very little to account for the many partial events. Instead, we see that the more pixels spanned by an event, the lower the likelihood of complete registry at the known peak energy. The same situation clearly also applies to the higher energy ^{241}Am spectra. An explanation[27] can be found in the presumed depth structure of the CCD, as follows. Seen by the source, and sketched in Fig. 2, our backilluminated topology starts with an $\sim$0.1 μm superficial conductive layer that applies the CCD substrate bias. Next comes a layer several microns deep, characterized by weak vertical field gradients, which we refer to as the surface layer. Electron cloud diffusion occurs in all directions in this layer, owing to the weak field gradients. The part of the cloud that diffuses toward the superficial layer is lost as far as measurement is concerned, while lateral diffusion means that the remainder of the cloud can be spread over several pixels. The partial loss of electron clouds in this layer means that the inferred event energies will be falsely low; they have been spectrally redistributed.[28] The exponentially decaying likelihood of x-ray penetration, and the surface layer's relative thickness leads to numerous partial events and the extensive spectral redistribution observed in our CCD. The problem can be quantified in conjunction with physical models; however, that has not been the objective in the present work. Deeper in the structure (close to the readout gates in the backilluminated device) is the depletion layer. Here the vertical field gradients are sufficient to counter vertical diffusion. Electron clouds formed in this region are quantitatively swept into a potential minimum (buried conduction channel) associated with the gate layer, from whence they are eventually read out with very low losses.[1]

In terms of practical use, it is clear that we must confine our attention to 1 pixel events to best avoid spectral redistribution. We must also accept the reality that some 1 pixel events are also partially registered, to an extent dependent on cloud radius and therefore photon energy. The ^{55}Fe and ^{241}Am 1 pixel spectra in Fig. 1 demonstrate these points, showing tolerably low levels of partial registry except at energies in the range $\sim$260–2000 eV. Although it is above the readout noise, this region is powerfully attenuated by the 250 μm Be window on the CCD, so there is little risk of confusing these partial events with real events.

Comparison of the total number of ^{55}Fe events observed using the CCD versus the Ge detector (absolute source calibration) confirms the $\sim$15 μm total thickness of the Si in our CCD. The number of fully versus partially registered events (Table I) then gives a first estimate of the surface and depletion layer thicknesses. They are $\sim$10.6 and $\sim$4.4 μm, respectively, here with the assumption of negligible charge cloud radii.

Observable cloud size is a function of where in the CCD's depth the cloud forms and the nature of the measurement. Depth and lateral field gradients are functions of three dimensional location in the CCD structure, as is readily appreciated from Fig. 2. Depth field gradients tend to be strong compared to lateral gradients, so given otherwise isotropic diffusion, electron cloud sizes inferred from depth measurements are generally smaller. As we have seen, lateral measurements are based on the charge cloud spanning multiple pixels. On the other hand, depth measurements must rely on how much of the charge cloud falls within the depletion layer. This can be done by generating a model that contains the relevant layer dimensions and cloud radii as parameters. Fitting a large number of observed events to the model establishes the dimensions. Below we present a novel variation on this approach.

We now turn to measurements involving the laser plasma source.

IV. PLASMA SOURCE WORK

An $\sim$200 μm water jet under 1 atm He gas provides the basis of our laser plasma source, described elsewhere.[12] The arrangement has great promise for in-house subpicosecond transmission extended x-ray absorption fine structure (EXAFS), given the microbolometric detection scheme we are developing for it.[12,29] Here, unless otherwise stated, we describe its x-ray bremmstrahlung emissions when operated under aspirator vacuum. Such a vacuum is naturally constrained to water's vapor pressure, obviating boiling of the slightly cooled, degassed water that is fed from a reservoir under 1 atm He. A prototype apparatus can operate stably for hours at a time, but to date has been somewhat less reliable than the original pumped water jet under 1 atm He. X-ray spectral measurements using the vacuum apparatus have necessarily been based entirely on the CCD, since its use does not require exceptional long term stability. Characterization of the CCD has clearly been of critical importance in this approach. Observable x-ray yields are significantly increased under vacuum, and short laser pulses are relatively effective at producing hard x rays, motivating improved constructions.

The Ge detector in single photon mode can provide a spectrum of the 10 Hz repetition rate source. Long term shot to shot source stability and a few hours per spectrum are used to avoid pileup, but also requires the more reliable water jet in He arrangement for this particular measurement. At intervals during measurement, the Ge detector can be replaced with the CCD, which needs at most a few laser shots to generate a useful spectrum. The 1 pixel CCD events are

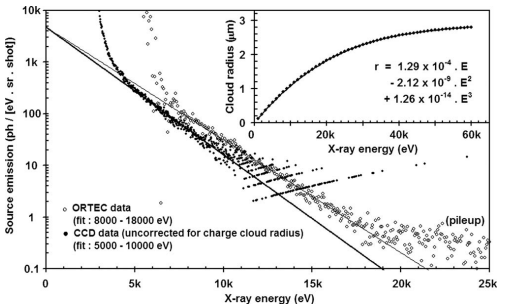

FIG. 3. Parallel measurement of an X-ray spectrum of the broadband laser plasma source using the He using the Ge point detector and the CCD, after normalizations for filters, pileup, energy binning interval, solid angle, and number of laser shots. Slope differences are due to larger electron clouds from high energy events being less able to fit in the CCD's depletion layer thickness. The CCD's depletion depth is adjusted to give a common zero energy extrapolation for both detectors, where the cloud size is expected to vanish. This interpretation allows quantitative estimation of the cloud size variation with energy, shown in the inset (see text).

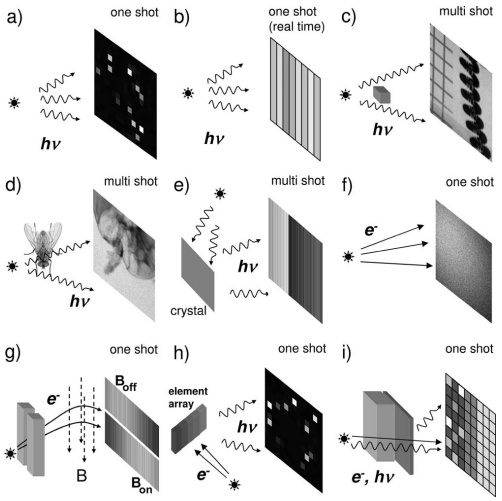

FIG. 4. Selection of laser plasma source experiments motivating CCD characterization. Requirement for single or multiple shots is indicated in the panels. Data measured using the CCD are shown in each case, except as follows; (a) X-ray photons impinge on the CCD in discrete pixels enabling histogram spectra. (b) Aggressive hardware binning allows real time optimization of x-ray flux (impression only, vertical binning sketched). (c) Blurred shadow edges of high contrast objects reveal source dimensions. (d) Biological specimens can be imaged by x-ray absorption. (e) Crystal dispersion of x-ray energies (von Hamos, absorption edge of Ti foil is illustrated, vertically binned). (f) Energetic electron beams are produced when using double or impaired temporal contrast laser pulses, traversing filters (with scatter and secondary radiation) to impinge directly on the CCD. (g) Magnetic deflection confirms electron beam polarity and energy. (h) Indirect observation of electron beams by x-ray fluorescence from element arrays. (i) Single shot distinction of x rays vs electron beams (CCD half obscured by thick absorber, other half by thin element foil; x rays produce sharp edge shadow with absorption edge in foil transmission, electrons give a diffuse shadow (scatter) with x-ray emission lines from the foil in the shadow; impression in figure applies to electron beam).

isolated in software. Filters, pileup, energy binning intervals, solid angles, and number of laser shots are normalized for both detectors. The relatively insensitive surface layer of the CCD is included as an additional filter for the 1 pixel events, since these are associated with the thin depletion layer of the CCD. The earlier indication of 10.6 and 4.4 μm obtained in the ^{55}Fe measurement provides a first guess of these thicknesses. Figure 3 presents parallel Ge and CCD spectra obtained in this way. Here, respective thicknesses of 9.2 and 5.8 μm are applied to the CCD model, constraining the combined thickness to 15 μm. This choice is based on extrapolation of both spectra to a common point at the limit of low energy, where cloud radii are expected to vanish. We note that incorrect filter normalization leads to apparent nonlinearities at low energies (when shown on the log scale). Variation of the CCD depletion layer thickness in the range of 2–10 μm does not cause this effect to an objectionable extent (filters other than the CCD's surface layer dominate the low energy attenuation), but instead mostly determines the height of the CCD data on the plot, as it should.

Electron cloud radii and their variation with energy can be estimated from Fig. 3, as we now show.

The different detector slopes of the two detectors in Fig. 3 can be attributed to the fact that higher energy photons cause larger electron clouds, which are less likely to fall completely within our CCD's narrow depletion layer. To bring CCD spectra into agreement with corresponding Ge spectra requires increasing the number of observed 1 pixel events by an energy dependent factor $\exp(dE)$, where d ($\sim$0.066 keV^{-1}) is the difference of the two fitted gradients in the log plots. This factor, which we apply in all subsequent spectra, is expected to equal $p^2h/[(p\text{-}2r)^2(h\text{-}2r)]$ (model in Fig. 2), being the ratio of volumes within a pixel that describe the 1 pixel full registry losses when considering a cloud of finite size. Equality gives an analytical expression for electron cloud radius versus energy. The expression is cumbersome, but its validity is limited by data quality and assumptions. We therefore provide a simple polynomial fit to the analytical electron cloud radius over an extended energy range where it might be of interest to do so, and urge a suitable level of awareness when using the result (inset of Fig. 3). The size of the cloud radii outside the fitted regions cannot be presumed with confidence. However, we note that extrapolation predicts $\sim$2.8 μm cloud radius for the 59.5 keV photons provided by ^{241}Am. Such events could be fully contained within the proposed $\sim$5.8 μm potential well depth of the CCD and so be fully registered, though this would happen only rarely. Qualitatively, this is precisely what we observe.

At this point, we are in a strong position to apply the CCD to new and unknown x-ray sources, which can show diverse and exciting behavior.[30–36] As Fig. 4 illustrates, laser plasma sources[12] can fit this description very well, where we show a selection of our data obtained using this CCD. The characterization in this work assists in many ways. When working with x-ray spectra, we have the necessary knowledge of the CCD's stopping power, spectral resolution, and limitations. Primary and secondary x-ray radiations are instantly recognizable, with clear identification of responsible

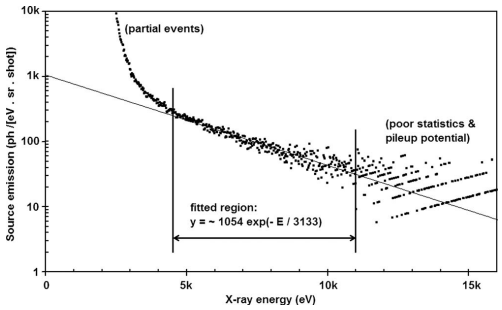

FIG. 5. Example of an x-ray spectrum from the laser plasma source when operated under aspirator vacuum, here using 38 laser shots at 4.0 mJ/pulse with estimated pulse duration ~118 fs (see text).

elements in both emission and absorption measurements. In quantitative spectral flux work, we know to isolate 1 pixel events to minimize spectral redistribution, and have determined the functional depth structure associated with these (and multiple pixels) events. There is an appreciation of the effects of charge cloud size and its variation with energy. Observed spectra can be suitably compensated, enabling correct deduction of the source spectra. Noise levels can be anticipated in different operation modes. The extent of edge blur associated with the detector is known. If dealing with x-ray images, we know that high levels of partial registry must be borne in mind when addressing intensities. Partially registered events that may be dispersed as a spectrum over the CCD area can be confidently interpreted. There can be no mistake when new radiations enter the picture, for example, energetic electron beams. In our work, their initial observation[12] was made using this CCD, and their study in a forthcoming publication has been significantly assisted by it, as illustrated. The CCD depth structure determined in this work is a prerequisite for calculations of the observable signals generated by the new electron-Si interactions.

We close with some recent measurements of laser plasma x-ray spectra generated under aspirator vacuum. The following measurements are valuable in applications presently under development and are entirely reliant on this CCD characterization.

Earlier laser plasma source work under He established that polarization, interaction geometry, and temporal contrast play critical roles for the bremsstrahlung x-ray (and electron beam) generation.[12] To date the double laser pulse structrue[37] that we have used[12] to generate electron beams has not led to dramatic increases in primary x-ray generation from our water jet target. Investigation of this matter has required careful distinction of the two radition types and their secondary radiations, which is enabled by the CCD as shown in Fig. 4. The same observations apply under vacuum. Figure 5 is representative of x-ray generation from a water jet under vacuum, applying all the CCD corrections discussed above to a 4 mJ/pulse, ~118 fs duration, 780 nm Ti:sapphire generated x-ray spectrum, here compiled from 38 laser shots. Excluding the known detector limitations at either end of the fitted region, such fits are invariably excellent fits to a simple

TABLE II. Fits to $N=N_0 \exp(-E/T)$ (photons/ per eV bandwidth per sr per laser shot) under aspirator vacuum, with fixed laser pulse duration (estimated ~118 fs). The apparent anomaly at 6.0 mJ is noted in the text.

Laser energy per pulse (mJ)	N_0 (ph/eV sr shot)	T (eV)	Fit range (eV)
1.0	420	1840	4500–8500
2.0	560	2300	4500–9000
3.0	850	2710	4500–10 500
4.0	1050	3130	4500–11 000
6.0	840	1800	4500–9000
10.0	1324	3290	5000–12 000
20.0	1560	2750	5000–12 000

exponential: $N=N_0 \exp(-E/T)$. Compared to operation under He, vacuum operation of the water jet gives significant increases in observable ~4–20 keV x-ray yields, as observed previously.[12] The temperature parameter (T) plays the dominant role in this increase. The enhancement is particularly useful at low laser pulse energies (such as when adapting to kilohertz repetition rate lasers), and when using near transform limited pulse durations.

The fit parameters listed in Tables II and III should guide the establishment of new x-ray sources of this kind. Laser pulse duration estimates are based on occasional calibrations of the optical compressor using an optical autocorrelator.

In Table II, fitted prefactors (N_0) and temperatures (T) are given for a range of laser pulse energies, at a constant laser pulse duration of ~118 fs. Such laser pulse energies are typically encountered in conventional optical laboratories using amplified 780 nm Ti:sapphire lasers. An interesting trend is that the production of x rays may begin to plateau above ~4 mJ/pulse. This is welcome news when setting up on a kilohertz laser system, where the energy per pulse may otherwise be restrictive.

The duration of the laser pulse is another critical metric, partly because it affects the hard x-ray yield, and partly because it potentially determines the duration of the x-ray pulse.[12] In Table III, prefactors (N_0) and temperatures (T) are given for several laser pulse durations, at a constant laser energy of 4 mJ/pulse. Here an interesting observation is that the shortest available laser pulses give only slightly reduced yields of observable hard x rays. This contrasts with the situation under He, where the same action leads to relatively dramatic reduction in observable x-ray yields.[12] The presence of He gas evidently plays a role that goes beyond self-focusing, since the position of the jet in the laser focus was

TABLE III. Fits to $N=N_0 \exp(-E/T)$ (photons/eV bandwidth per sr per laser shot) under aspirator vacuum, with fixed laser energy per pulse (4.0 mJ).

Pulse duration (fs; estimate)	N_0 (ph/eV sr shot)	T (eV)	Fit range (eV)
38	640	3590	4500–10 000
43	840	3330	4500–10 000
54	1110	3550	4500–10 000
65	1030	3340	4500–10 000
118	1270	3090	4500–10 000

optimized with regard to observable x-ray yield in every spectral measurement. At the same time, the observation indicates that measurable electron stopping ranges in the target are likely to determine the x-ray pulse duration.[12]

Clearly, one seeks to map out the x-ray spectra as functions of many laser and experiment variables. Reproducibility is essential, and often obtained. For example, independent 4 mJ, ~118 fs measurements appear in Tables II and III. They were made an hour apart, and are in reasonable agreement. However, practical difficulties delay such efforts and account for anomalies in the tabulated data. Thus, the 6 mJ N_0 and T parameters shown in Table II would not be interpolated from the corresponding 4 and 10 mJ values; indeed some unexplained but temporary difficulties were noted with that measurement. Variability in experiments to date is believed to be dominated by the following causes. In our prototype vacuum apparatus, stability and reproducibility of the jet cannot be taken for granted, although the tiny stream appeared smooth and laminar on nearly all occasions when it was visually inspected. Proper degassing, slight cooling of incoming water, and leak-free plumbing are essential. Occasional small air leaks into the vacuum chamber or partial jet blockages might in principle lead to instability of the jet position and/or affect the laser focusing. Several degrees of freedom are needed in the critical manual alignment of the off-axis parabola. Once optimized (by generating a visible spark in air at the lowest possible energy at the start of each campaign), it is normally left alone, subsequently translating the target into the focal point; variations can be expected from one campaign to the next. Temporal aspects of the laser operation are known to critically affect laser-matter interactions and have led to constant maintenance and evolution of the laser system since its inception.[17] Temperamental behavior of the laser system's many active components often do correlate with anomalous experiments in ways that can be more or less subtle, erratic or intermittent, and are not always easy to identify or remedy. Experimental variability clearly is a problem that can be improved in future work, meanwhile a degree of caution needs to be exercised when inferring trends.

V. CONCLUSION

Characterization of a backthinned, backilluminated CCD has enabled quantitative investigation of ~4–20 keV x-ray emissions from a laser plasma radiation source. Its responses to monochromatic and multichromatic radioactive x-ray sources, as well as pulsed isotropic broadband x rays from the laser plasma source have been optimized, interpreted, and quantified for practical use. Collectively, results lead to appreciation of a partially sensitive surface layer of 9.2 μm, beneath which is a quantitatively sensitive depletion layer of 5.8 μm. This is consistent with limited available manufacturer information and other descriptions of CCDs where the internal structure was known. The particular CCD topology is uncommon within the x-ray single photon community, since the relatively thick and exposed surface layer scrambles events to lower energies, while the depletion layer is rather thin and deeply buried. Nevertheless we successfully extract quantitative hard x-ray spectra by directing attention to events isolated in single pixels. Further, we infer the variation of nascent electron cloud radii in Si by x-ray photons spanning a continuum of energies, by observations of broadband spectra from the laser plasma source. The approach takes advantage of the thinness of the depletion layer. We illustrate the CCDs use in a range of laser plasma x-ray experiments, where we indicate the significance of the present characterization. Finally, we show valuable new x-ray spectral flux measurements that are entirely reliant on the CCD and its characterization. These measurements are of immediate value when setting up similar laser plasma sources using ultrafast lasers capable of a few millijoules per pulse. Such developments, in conjunction with microbolometer detectors, are expected to enable laboratory based ultrafast EXAFS on a very widespread scale.[12]

ACKNOWLEDGMENTS

We wish to thank C.-G. Wahlström and Lund Tekniska Högskolans, Department of Atomic Physics for access to the Terawatt Laser Facility and the CCD used in this work. We especially wish to thank the following individuals, who have been particularly helpful in assisting with day-to-day laser operation over a period of several years: A. Persson, E. Pourtal, O. Lundh, F. Lindau, Y. Glinec, G. Genoud, and M. Harbst. This work has benefited through the Swedish Consortium for Artificial Photosynthesis, Sweden's Kungliga Fysiografiska Sällskap, the Swedish Energy Agency (STEM), the Knut and Alice Wallenberg Foundation, and a Linneus grant awarded to Lund's Laser Centre. J. Uhlig and M. Walczak acknowledge financing through the MAXlas project, under the Sixth European Framework Programme (contract number MEST-CT-2005-020356).

[1] J. R. Janesick, *Scientific Charge-Coupled Devices* (SPIE, Bellingham, WA, 2001).
[2] L. Labate, A. Giulietti, D. Giulietti, P. Koster, T. Levato, L. A. Gizzi, F. Zamponi, A. Lubcke, T. Kampfer, I. Uschmann, and E. Forster, Rev. Sci. Instrum. **78**, 103506 (2007).
[3] B. E. Burke, J. A. Gregory, M. W. Bautz, G. Y. Prigozhin, S. E. Kissel, B. B. Kosicki, A. H. Loomis, and D. J. Young, IEEE Trans. Electron Devices **44**, 1633 (1997).
[4] H. Tsunemi, E. Miyata, H. Ozawa, D. Matsuura, H. Tomida, H. Katayama, and K. Miyaguchi, Nucl. Instrum. Methods Phys. Res. A **579**, 866 (2007).
[5] C. M. Laperle, P. Wintermeyer, J. R. Wands, D. Shi, M. A. Anastasio, X. Li, B. Ahr, G. J. Diebold, and C. Rose-Petruck, Appl. Phys. Lett. **91**, 173901 (2007).
[6] S. C. Mayo, P. R. Miller, S. W. Wilkins, T. J. Davis, D. Gao, T. E. Gureyev, D. Paganin, D. J. Parry, A. Pogany, and A. W. Stevenson, J. Microsc. **207**, 79 (2002).
[7] C. Broennimann, E. F. Eikenberry, B. Henrich, R. Horisberger, G. Huelsen, E. Pohl, B. Schmitt, C. Schulze-Briese, M. Suzuki, T. Tomizaki, H. Toyokawa, and A. Wagner, J. Synchrotron Radiat. **13**, 120 (2006).
[8] A. Rousse, P. Audebert, J. P. Geindre, F. Fallies, J. C. Gauthier, A. Mysyrowicz, G. Grillon, and A. Antonetti, Phys. Rev. E **50**, 2200 (1994).
[9] F. Zamponi, T. Kampfer, A. Morak, I. Uschmann, and E. Forster, Rev. Sci. Instrum. **76**, 116101 (2005).
[10] T. Lee, Y. Jiang, C. G. Rose-Petruck, and F. Benesch, J. Chem. Phys. **122**, 084506 (2005).
[11] J. Chen, H. Zhang, I. V. Tomov, M. Wolfsberg, X. Ding, and P. M. Rentzepis, J. Phys. Chem. A **111**, 9326 (2007).
[12] W. K. Fullagar, M. Harbst, S. Canton, J. Uhlig, M. Walczak, C. G. Wahlstrom, and V. Sundstrom, Rev. Sci. Instrum. **78**, 115105 (2007).
[13] C. Tillman, PhD Thesis, Lunds Universitet, 1996, LRAP-204.
[14] G. Grätz, PhD Thesis, Lunds Universitet, 1998, LRAP-236.

[15] A. Sjögren, PhD Thesis, Lunds Universitet, 2002, LRAP-288.
[16] E. Danielsson, Masters Thesis, Lunds Universitet, 2003, LRAP-309.
[17] S. Svanberg, J. Larsson, A. Persson, and C.-G. Wahlström, Phys. Scr. **49**, 187 (1994).
[18] XCOM, Photon Cross Sections Database, http://physics.nist.gov/PhysRefData/Xcom/Text/XCOM.html
[19] M. J. Berger, J. S. Coursey, M. A. Zucker, and J. Chang, ESTAR: Electron Stopping-Power and Ranges, http://physics.nist.gov/PhysRefData/Star/Text/ESTAR.html
[20] U. Fano, Phys. Rev. **72**, 26 (1947).
[21] Ch. Enss, *Cryogenic Particle Detection*, Topics in Applied Physics (Springer, New York, 2005), Vol. 99.
[22] G. C. Holst and T. S. Lomheim, *CMOS/CCD Sensors and Camera Systems* (JCD, Winter Park, FL/SPIE, Bellingham, WA, 2007).
[23] S. E. Holland, D. E. Groom, N. P. Palaio, R. J. Stover, and M. Wei, IEEE Trans. Electron Devices **50**, 225 (2003).
[24] G. Prigozhin, N. R. Butler, S. E. Kissel, and G. R. Ricker, IEEE Trans. Electron Devices **50**, 246 (2003).
[25] A. Shariff, B. G. Martinsson, V. Auzelyte, M. Elfman, P. Kristiansson, K. G. Malmqvist, C. Nilsson, J. Pallon, and M. Wegden, Nucl. Instrum. Methods Phys. Res. B **219**, 110 (2004).
[26] W. Kester, Which ADC Architecture is Right for Your Application? http://www.analog.com/library/analogdialogue/archives/39-06/architecture.html
[27] M. W. Bautz, G. Y. Prigozhin, M. J. Pivovaroff, S. E. Jones, S. E. Kissel, and G. R. Ricker, Nucl. Instrum. Methods Phys. Res. A **436**, 40 (1999).
[28] G. Prigozhin, S. Jones, M. Bautz, G. Ricker, and S. Kraft, Nucl. Instrum. Methods Phys. Res. A **439**, 582 (2000).
[29] I. J. Maasilta, K. M. Kinnunen, A. K. Nuottajärvi, J. Leppäniemi, and A. Luukanen, Supercond. Sci. Technol. **19**, S242 (2006).
[30] A. Rousse, K. T. Phuoc, R. Shah, A. Pukhov, E. Lefebvre, V. Malka, S. Kiselev, F. Burgy, J.-P. Rousseau, D. Umstadter, and D. Hulin, Phys. Rev. Lett. **93**, 135005 (2004).
[31] E. Sato, E. Tanaka, H. Mori, T. Kawai, T. Ichimaru, S. Sato, K. Takayama, and H. Ido, Med. Phys. **32**, 49 (2005).
[32] C. N. Boyer, G. E. Holland, and J. F. Seely, Rev. Sci. Instrum. **76**, 035109 (2005).
[33] L. Soto, Plasma Phys. Controlled Fusion **47**, A361 (2005).
[34] E. J. Lerner and A. Blake, U.S. Patent No. 20070201598A1 (2007).
[35] H. Daido, Rep. Prog. Phys. **65**, 1513 (2002).
[36] J. Seres, P. Wobrauschek, Ch. Streli, V. S. Yakovlev, E. Seres, F. Krausz, and Ch. Spielmann, New J. Phys. **8**, 251 (2006).
[37] K. Hatanaka, H.. Ono, and H. Fukumura, Appl. Phys. Lett. **93**, 064103 (2008).

Paper III

Lab-based Ultrafast Molecular Structure

W. Fullagar, J. Uhlig, N. Gador, K. Kinnunnen, I. Maasilta,
C.-G. Wahlström, V. Sundström.

AIP Conference Proceedings **1234(1)**, 919-922 (2010).

Lab-based Ultrafast Molecular Structure

Wilfred Fullagar[1,4], Jens Uhlig[1], Niklas Gador[1], Kimmo Kinnunen[1,3], Ilari Maasilta[3], Claes-Göran Wahlström[2], Villy Sundström[1]

[1.] *Division of Chemical Physics, Lund University, P.O. Box 124, SE-22100 Lund, Sweden*
[2.] *Department of Physics, Lund University, P.O. Box 118, SE-22100 Lund, Sweden*
[3.] *Nanoscience Center, P.O.Box 35, FI-40014 University of Jyväskylä, Finland*
[4.] *Monash Centre for Synchrotron Science / Monash School of Physics / Centre of Excellence for Coherent X-ray Science, Monash University, Clayton, VIC 3800, Australia (subsequent employers)*

Abstract. The proliferation of various laser-driven approaches to sub-picosecond hard X-ray and short-wavelength radiation generation in the past few decades has opened many avenues for the laboratory-based development of traditionally facility-based short wavelength ultrafast molecular structure science. Together with the introduction of microcalorimeter detection schemes, this opens the floodgates to widespread, decentralized implementation of what were until recently specialist short wavelength techniques. Solar energy capture, optical transducers, molecular evolution and energy transfer processes, coherent control experiments and lasers themselves can benefit from accessible molecular structure dynamics, much as biochemistry benefits from determination of biomolecular structures. In what follows, a few ultrafast molecular structure developments and their rationale are briefly recounted.

The ubiquitous phase problem aside, it is a long established fact that the diffraction-based observation of a 3-dimensional object requires the Ewald sphere to be presented throughout a substantial volume of the sample's reciprocal space. For present purposes, the objects are molecules, requiring that the probing radiation possesses short wavelengths - comparable to interatomic bond lengths. In routine steady state crystal analyses using collimated monochromatic beams the necessary presentation is accomplished by steadily rotating the sample during data collection. In pulsed ultrafast measurements the same approach is not possible, thus motivating a disordered (powder or solution/diffuse) arrangement of molecules [1, 2], convergent/divergent monochromatic beams, a short wavelength beam containing multiple wavelengths (Laue crystallography [3]), or some combination of the latter. Given the definition of source brilliance : ph/[s.bandwidth.area.divergence], it is clear that the source-manipulation approaches just described effectively amount to a reduced brilliance requirement for the beam – for reasons demanded by the sample. Extended X-ray absorption fine structure spectroscopy (EXAFS) is also an intrinsically broadband technique [4], being in effect an energy-dispersed electron holography measurement. This criticality of using reduced-brilliance (especially polychromatic) beams can be counter-intuitive to those accustomed to seeking information through phase-sensitive short-wavelength imaging techniques, but is otherwise well established in ultrafast X-ray and neutron scattering communities [5-8]. Particularly in the latter case, the relevant techniques have been the basis for numerous and various major user facility developments for many decades.

For pulsed pump-probe measurements a complicating factor is that the pumping stimulus (typically optical excitation by a laser) must produce a significant percentage of excited molecules, usually leading to rapid sample destruction. Many tricks are in common use to alleviate this, for example aggressive cooling [9], the use of host-guest chemistries to dissipate energy in inert matrices [10, 11], dissipation in protein scaffolds [12], excitation in the red wing of absorption spectra [13] or the use of fluid samples to allow continuous replacement [4].

Given any radiation beam diffracting from a sample, the key point is to know the momentum transfer from the sample to the radiation quanta. This - with allowance for different scattering factors and mechanisms for different radiations - allows direct comparison of X-ray, neutron, electron and other diffraction data. The momentum transfer is connected to the nature of the radiation (neutrons, X-rays, electrons, etc), the geometry of the scatter, and the

energy of the particles or photons. Thus for monochromatic beams the situation is relatively simple. Given a polychromatic beam, the trick is to also keep track of the energy of individual quanta. For particle radiations such as neutrons, time-of-flight techniques provide this information. Charged particles can further employ energy-determination techniques based on their charge and mass. Polychromatic X-rays enjoy neither luxury!

However, the energy of X-ray events can be measured. The classical approach is Bragg reflection, which effectively amounts to the use of extremely narrow bandpass filters, with typical throughputs of $\Delta E/E = \sim 10^{-5}$ (Darwin width [14]). There is a corresponding loss of flux when using this approach, which is the death of many an ultrafast experiment. The loss can be avoided if the X-ray detector is directly able to register individual photon energies (for momentum transfer one also needs to know the position where they strike the detector). Semiconductor and many other detectors (fluorescence, photoelectric, ion chamber, etc) can do this reasonably well, but their energy resolution is in each case ultimately compromised because the measured energy does not represent all possible energy decay channels. The stochastic nature of energy dissipation among multiple decay channels limits the observable photon energy resolution; this is the basis of the Fano limit [15].

To avoid this Fano limit for photon energy resolution, one needs to bring all the photon energy into a common channel, avoiding energy trapping and loss mechanisms (such as electron promotion to semiconductor conduction bands, defect formation and fluorescence emissions). The obvious common channel to aspire to is phonon production – heat. Accurate heat measurement requires low thermal masses and heat capacities. Thus the optimum conditions for X-ray event measurement occur in materials such as bismuth at ultracryogenic temperatures well below the Debye temperature, with its poor metallic behaviour and correspondingly low Sommerfeld parameter [16]. Material dimensions of tens to hundreds of microns allow complete entrainment of thermalised photoelectric X-ray events [17], while the necessarily accurate thermal measurements can be accomplished using superconducting transition edge [18, 19] or other sensors [20]. A potential new approach is to quantitatively observe the activity in feedback loops of actively damped mechanical microresonator arrays [21-23], which has a conceptual parallel in the indirect measurement of temporal jitter in synchrotron-based pump-probe experiments [24]. The direct relationship of X-ray photon energy resolution to chemical structure measurements assures the continued rapid development of ultracryogenic position and energy sensitive array detectors.

In polychromatic Laue crystallography, such as the laser wakefield driven scheme first attempted by us in 2007 (Fig. 1) [4], it is worth noting that the job of energy resolution is very substantially done by the sample itself, thanks to its known crystal lattice and independently established ground state structure. The very finite longevity of sample crystals has been mentioned and is awkward, rendering this and other photocrystallography techniques only pseudo-stroboscopic [3, 9, 25]. This motivates the necessary X-ray properties, also a good supply of crystalline material.

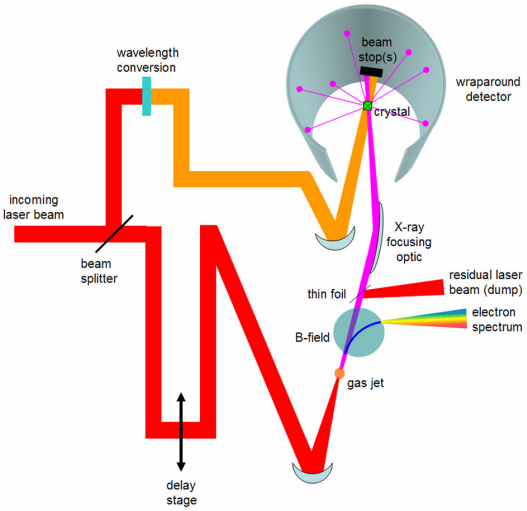

FIGURE 1. The sketched prototypical femtosecond Laue crystallography topology was pursued (2007). A sample crystal with a suitable detector subtending a large solid angle (wraparound image plate in first instance) is stimulated by a light pulse (orange). An optically delayed pulse then wakefield-generates a broadband few-keV X-ray beam [26-30]. Arrangements were made for a crossed venetian blind (lobster eye) lens [31] for compactness reasons, despite its spatial aberrations and temporal dispersion. Regrettably the gas jet and laser system proved too unstable during the experiment's brief window of opportunity.

Many fluorescence and transmission topologies exist for EXAFS experiments. In steady state measurements, fluorescence has significant advantages in terms of sensitivity and sample concentration. However, its adaptation to ultrafast experiments requires ultrabrief and easily tuneable monochromatic X-ray stimulation beams. Synchrotron time-slicing schemes may provide this at large facilities. Here, Fano limited energy dispersive single photon semiconductor detector arrays can allow fluorescence windowing either in software [17, 32] or hardware [33], if necessary with the usual suppression of elastic scatter using absorption edge filters. Transmission EXAFS does not require this tuneability of the X-ray beam, provided one can disperse broadband photon energies after passing the sample. Thus we have at times proposed use of a white synchrotron beam, with the necessary energy dispersal by Debye-Scherrer scatter from diamond powder, or better, a uniaxial "powder" such as carbon fiber [34]. The angularly dispersed scatter is directed onto a streak camera to give the spectrum as one dimension, and temporal evolution the other. The duration of a "typical" 100 ps synchrotron pulse can thus be stretched out to sub-ps resolution in an arrangement that does not demand a great deal of beam conditioning infrastructure. The sample excitation laser can provide a temporal fiducial on the streak camera to later compensate temporal jitter. As for lab-based ultrafast EXAFS, the arrangement of approximately 1/e attenuating samples in moderate to high concentrations is often straightforward in chemical research contexts, as is the arrangement of filters to suppress X-ray energies outside the spectral range of interest. Thus, bearing in mind the availability of ultrashort pulsed broadband X-ray sources and the emergence of microbolometric detectors, a transmission EXAFS geometry can be a practically viable and extremely exciting approach to in-house ultrafast chemical structural dynamics research [4]. This is especially important given many contemporary interests in molecules for solar energy capture [35-37] and the foreseeability of measurements that further incorporate in-situ coherent control of chemical reactions [38, 39].

The arguments that have been presented in favour of polychromatic beams apply very generally, such that one can in principle consider polychromatic adaptations of ultrafast diffuse scatter (pair distribution function) measurements, powder crystallography, grazing incidence surface scattering, surface reflectometry (Fig. 2), coherent X-ray diffractive imaging, and ultimately also phase contrast imaging, given adequate individual photon energy resolution for their respective tasks. Depending on the application, temporal aspects may not be a priority, for example when using temporally stochastic or pseudo-steady state sources (eg tubes, synchrotron) to study details of static samples. Much of the work outlined here took place during 2004-2008, in which it supported the scientific case for the MAX-IV short pulse X-ray facility in Lund, Sweden [40] and argued for the availability of broadband ultrabrief hard X-ray beams [41]. This work also lent support to Lund's successful bid for the European Spallation Source [42, 43], in which polychromatic neutron beams can be taken for granted.

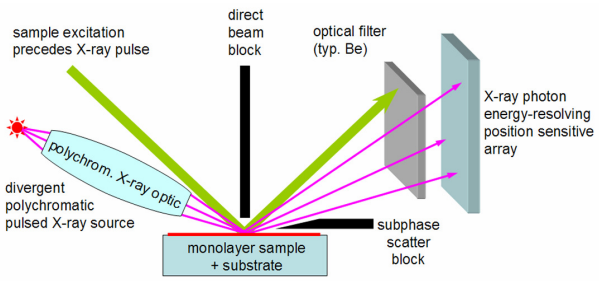

FIGURE 2. Stroboscopic arrangements such as this have been evaluated for ultrafast polychromatic pump-probe specular reflectometry [4, 7]. There are close parallels in neutron work [8, 44].

While recognizing that many observations above will be familiar to readers with neutron scattering backgrounds, it is hoped that repeating them here will further stimulate development of high resolution energy and position sensitive detectors within the X-ray community. This allows capitalization on the affordability of internationally mature and maturing laser-generated ultrashort pulse polychromatic hard X-ray schemes. Their combination [4] opens the door to rapid, diverse and widespread lab-based studies of ultrafast chemical structural dynamics.

ACKNOWLEDGMENTS

Developments were funded by the Swedish Consortium for Artificial Photosynthesis, the Knut and Alice Wallenberg Foundation, the Kungliga Fysiografiska Sällskapet, and the Swedish Research Council. Insights and opportunities extended by John White (ANU, Canberra, Australia), Philip Coppens (SUNY at Buffalo, USA),

Jörgen Larsson, Anders Persson and other members of the Lund Laser Centre (Lund, Sweden) are gratefully acknowledged. WKF is thankful for occasional oversight of housing rent by the Gynning family in Björnstorp (Genarp, Sweden), the Williams family (Mt Waverley, Australia) and other personal kindnesses that have at times enabled this work in recent decades. The Australian Research Council's Centre of Excellence for Coherent X-ray Science, and Monash University's School of Physics, have subsequently permitted academic access during pursuit of other X-ray studies [45]. Thanks to Richard Garrett and Chris Hall for encouraging this glimpse of earlier and ongoing work undertaken during previous international postdoctorates.

REFERENCES

[1] S. Techert, F. Schotte, and M. Wulff, Physical Review Letters **86**, 2030 (2001).
[2] H. Ihee *et al.*, Science **309**, 1223 (2005).
[3] V. Srajer *et al.*, Biochemistry **40**, 13802 (2001).
[4] W. Fullagar *et al.*, Rev. Sci. Instrum. **78**, 9 (2007).
[5] R. Durand *et al.*, Mol. Phys. **86**, 1 (1995).
[6] W. K. Fullagar, *Molecular Fullerides*, (PhD thesis, Australian National University 1997), http://thesis.anu.edu.au./public/adt-ANU20010831.150750
[7] R. F. Garrett *et al.*, Nucl. Instrum. Methods Phys. Res. Sect. A-Accel. Spectrom. Dect. Assoc. Equip. **467**, 998 (2001).
[8] W. K. Fullagar *et al.*, Biophysical Journal **85**, 2624 (2003).
[9] W. K. Fullagar *et al.*, J. Synchrot. Radiat. **7**, 229 (2000).
[10] S. L. Zheng, and P. Coppens, Cryst. Growth Des. **5**, 2050 (2005).
[11] P. Coppens *et al.*, CrystEngComm **4**, 302 (2002).
[12] Z. Ren *et al.*, Biochemistry **40**, 13788 (2001).
[13] R. I. Epstein *et al.*, Nature **377**, 500 (1995).
[14] J. Als-Nielsen, and D. McMorrow, *Elements of Modern X-ray Physics* (J. Wiley, New York, 2001).
[15] U. Fano, Physical Review **72**, 26 (1947).
[16] H. P. Myers, *Introductory Solid State Physics* (Taylor and Francis, London, 1990).
[17] W. Fullagar *et al.*, Rev. Sci. Instrum. **79**, 8 (2008).
[18] I. J. Maasilta *et al.*, Superconductor Science and Technology **19**, S242 (2005).
[19] K. M. Kinnunen *et al.*, Journal of Low Temperature Physics **151**, 119 (2007).
[20] C. Enss, *Topics in Applied Physics 99 - Cryogenic Particle Detection* (Springer, Berlin, 2005).
[21] D. Kleckner, and D. Bouwmeester, Nature **444**, 75 (2006).
[22] W. Hu *et al.*, Rev. Sci. Instrum. **80**, 085101 (2009).
[23] S. Kelling *et al.*, Rev. Sci. Instrum. **80**, 093101 (2009).
[24] M. Harbst *et al.*, Appl. Phys. A-Mater. Sci. Process. **81**, 893 (2005).
[25] P. Coppens, Angew. Chem.-Int. Edit. **48**, 4280 (2009).
[26] A. Rousse *et al.*, Physical Review Letters **93**, 135005 (2004).
[27] F. Lindau, *PhD thesis : Laser-driven particle acceleration. Experimental investigations.*, thesis, Lund University LRAP-378 2007),
[28] O. Lundh, *PhD thesis : Laser-driven beam soft fast ions, relativistic electrons and coherent X-ray photons*, thesis, Lund University LRAP-391 2008),
[29] P. Gibbon, *Short Pulse Laser Interactions with Matter. An Introduction.* (Imperial College Press, London, 2005).
[30] D. A. Jaroszynski, R. Bingham, and R. A. Cairns, *Laser-Plasma Interactions* (CRC Press, London, 2009).
[31] A. V. Baez, Journal of the Optical Society of America **50**, 1127 (1960).
[32] P. Denes *et al.*, Rev. Sci. Instrum. **80**, 5 (2009).
[33] M. Fiederle *et al.*, Nucl. Instrum. Methods Phys. Res. Sect. A-Accel. Spectrom. Dect. Assoc. Equip. **591**, 75 (2007).
[34] D. J. Johnson, and C. N. Tyson, J. Phys. D-Appl. Phys. **2**, 787 (1969).
[35] G. Benko *et al.*, Journal of the American Chemical Society **125**, 1118 (2003).
[36] J. Kallioinen *et al.*, Journal of Physical Chemistry B **106**, 4396 (2002).
[37] R. Brimblecombe *et al.*, Angew. Chem.-Int. Edit. **47**, 7335 (2008).
[38] A. Assion *et al.*, Science **282**, 919 (1998).
[39] B. Bruggemann *et al.*, Physical Review Letters **97**, 4 (2006).
[40] S. Werin *et al.*, Nucl. Instrum. Methods Phys. Res. Sect. A-Accel. Spectrom. Dect. Assoc. Equip. **601**, 98 (2009).
[41] *Scientific Evaluation of the MAX IV Proposal. Vetenskapsrådet rapportserie 20:2006* (Vetenskapsrådet, Swedish Research Council, 2006).
[42] T. Feder, Physics Today **June**, p22 (2008).
[43] G. Brumfiel, Nature **459**, 626 (2009).
[44] W. K. Fullagar, S. A. Holt, and I. R. Gentle, Biophysical Journal **95**, 4829 (2008).
[45] W. K. Fullagar, D. M. Paganin, and C. J. Hall, New Journal of Physics, ("Revisiting Bragg's Xray microscope : scatter based optical transient grating detection of pulsed ionising radiation" under revision following review Nov 2009).

Paper IV

Laser generated 300 keV electron beams from water

J. Uhlig, C.-G. Wahlström, M. Walczak, V. Sundström, W. Fullagar.

Laser and particle beams **29-4**, 415-424(2011).

Laser and Particle Beams (2011), *29*, 415–424.

doi:10.1017/S0263034611000516

Laser generated 300 keV electron beams from water

JENS UHLIG,[1] CLAES-GÖRAN WAHLSTRÖM,[2] MONIKA WALCZAK,[1] VILLY SUNDSTRÖM,[1] AND WILFRED FULLAGAR[1]

[1]Department of Chemical Physics, Lund University, Lund, Sweden
[2]Department of Physics, Lund University, Lund, Sweden

(RECEIVED 20 February 2011; ACCEPTED 9 July 2011)

Abstract

300 keV electron beams with energy peaked in the range 280–390 keV were generated by focusing a high contrast ratio but temporally double pulsed 800 nm ultrafast laser onto a flowing water jet under both helium atmosphere at ambient pressure and water aspirator vacuum conditions, using laser intensities in the range 10^{15}–10^{18} Wcm^{-2}. Their characteristics have been investigated as functions of inter-pulse delay, incidence geometry and laser pulse chirp. Shot-to-shot variation of the beams' equatorial and azimuthal distributions was also recorded in real time. Measurements of the emitted charge and energy have been performed. Secondary X-ray emission arising from impingement of the electron beams on the target chamber walls and other parts of the apparatus have been identified. Preliminary results after transition to a high repetition rate laser system have shown similar behavior. Approaches for improvements and applications are suggested.

Keywords: Fast electrons; Laser-plasma wakefield acceleration; Multi-pulse structure; Plasma source; Table top X-ray source

INTRODUCTION

In recent years, the interest in table top laser based hard X-ray sources for laboratory based applications has increased dramatically (Dorchies *et al.*, 2008; Gizzi, 2010; Guo, 2009; Hatanaka *et al.*, 2008; Hou *et al.*, 2008; Kugland *et al.*, 2008; Lee *et al.*, 2005; Silies *et al.*, 2009; Tarasevitch *et al.*, 2009; Zamponi *et al.*, 2009; Fullagar *et al.*, 2010; Chen *et al.*, 2008, 2010; Mangles *et al.*, 2006). Temporal multi-pulse regimes have been assessed in attempts to increase X-ray yields (Ahn *et al.*, 1996; Anand *et al.*, 2006; Hatanaka *et al.*, 2008). Several publications report collimated electron beams with narrow energy distributions generated with femtosecond lasers in the several mJ class, using solid or micro droplet targets in high vacuum (Anand *et al.*, 2007; Bastiani *et al.*, 1997; Li *et al.*, 2006; Ruhl *et al.*, 1999; Zhang *et al.*, 2005; Nakano *et al.*, 1996). Their use has been proposed in electron scattering experiments and for accelerator injection (Hu *et al.*, 2010; Mordovanakis *et al.*, 2010; Fullagar *et al.*, 2007*a*; Centurion *et al.*, 2008; Reckenthaeler *et al.*, 2009; Centurion *et al.*, 2009). This report surveys our work on laser plasma generated electron beams based on water jet targets performed at the Lund Laser Center's terawatt laser system (Svanberg *et al.*, 1994; Mangles *et al.*, 2009). The use of a water jet target, under helium atmosphere at ambient pressure or water aspirator vacuum, is motivated by foreseeable chemical ultrafast X-ray applications (Fullagar *et al.*, 2007*b*, 2008). The work described herein strongly supports long-standing evidence (Max, 1980) that the existence of a pre-plasma — formed by the first pulse of a temporal multi-pulse structure — is critical for the generation of electron beams by subsequent laser pulses, and that these must be *p*-polarized. Indeed the appearance of electron emission has been symptomatic for occasional problems with the laser system. In this work, two collinear orthogonally polarized pulses of comparable energy are arranged, and focused to strike a circular cross section water jet at a predetermined angle, usually at grazing incidence. The constraint of equal laser energy in both pulses was used merely to simplify the exploration of laser parameter space. However, electron beams were identified at different intensity ratios too. In the context of laser generated X-rays from condensed matter targets, the electron beams must be recognized in interests of radiation safety, optimization of X-ray emission from the intended target, and elimination of secondary emissions. Controlling their directionality, angular spread, charge and energy is of critical interest for

Address correspondence and reprint requests to: Jens Uhlig, Department of Chemical Physics, Lund University, Lund University, P. O. Box 124, 22100 Lund, Sweden. E-mail: jens.uhlig@chemphys.lu.se

subsequent applications. At the same time, exerting the necessary control has been a major obstacle in the characterizations described here. Laser-plasma interaction is a complex and extremely active field of research whose theoretical and numerical treatments lie outside the scope of this work, which aims at a symptomatic description.

EXPERIMENTAL SETUP

For the results presented, we used about 800 nm parasitic pulses from the 10 Hz multi-terawatt laser at the Lund Laser Centre with typically about 40 mJ pulse energy and chirp controlled durations of about 46 fs up to several picoseconds. These typically have excellent temporal contrast ratio as described elsewhere (Lindau, 2007). We have also observed electron beams with a 3 mJ 1 kHz system with lower temporal contrast, results of which will be discussed in the remark section. For the deliberate generation of high temporal contrast pre-pulses, the arrangement sketched in Figure 1 was used.

In this arrangement, the *p*-polarized pulse passes through two Brewster type polarizer's. Laser chirp scans (of the inter-grating spacing in the optical compressor) have been routinely performed throughout our experimental campaigns to find the shortest pulse duration for the *p*-polarized pulse at the target position, thus compensating for group velocity dispersion in this and other glass downstream from the compressor (e.g., target chamber windows). The compressor settings of the shortest pulse duration is determined by using optical autocorrelator traces or by the generation of white light in air at low laser energy per pulse and by the form of the resulting X-ray curves (see Fig. 4a). In the configuration used, the *s*-polarized pulse is not compensated in the same way, and thus obtains a slightly different chirp and pulse duration. However, this and associated work (Fullagar *et al.*, 2007*b*) show that the *s*-polarized pre-pulse does not itself lead to any significant hard radiation (X-rays or electrons) — its function is merely to generate a plume of expanding matter at the target surface. In this role, optimum group velocity dispersion compensation of the *s*-polarized pulse is not critical. Inter-pulse delays of up to ± 1.5 ns could be realized. The two pulses are tightly focused by the same off-axis parabolic mirror. Laser intensity at the target was varied in the region 10^{15}–10^{18} Wcm^{-2}. The water jet target has a circular cross section with about 180 μm diameter and is directed vertically downwards in a helium atmosphere at atmospheric pressure, alternatively drawn into a vacuum close to the vapor pressure of water. Stable vacuum operation of the water jet is achieved by degassing the water and by drawing it into the chamber by use of a water aspirator pump, whose vacuum is automatically limited to water's vapor pressure at room temperature. In addition to degassing, a stable jet requires that the water is cooled a few degrees prior to its introduction to the chamber. The necessity of doing so confirms that the chamber pressure is close to the room temperature vapor pressure of water (about 23 mbar at 20°C).

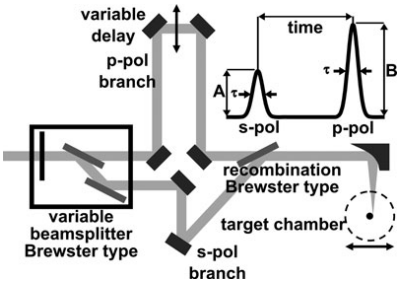

Fig. 1. A 3 ns delay stage varies the relative timing between two variably split beams of opposite linear polarization, the power division of which is controlled using a 1/2-wave plate. After their recombination using a Brewster type mirror the beam is tightly focused by a 90° off axis parabolic metallic mirror onto the target. The target is moved relative to the focus and consists of a ~ 3 ms^{-1} water jet in laminar flow conditions.

The primary radiation detector was a 512×512 pixel direct detection charge-coupled device (CCD)(Princeton Instruments SX-TE/CCD-512TKB/D), whose characterization and operation is described in a previous paper (Fullagar *et al.*, 2008). A particularly useful mode of operation for these electron beam studies is the vertically (hardware) binned, laser-synchronous mode. This allows data capture at the laser repetition rate while preserving one axis of spatial information. Much of the data presented below integrates this remaining axis, so that individual data points show the integrated frame intensity corresponding to individual laser shots. This permits straightforward graphical presentation of scans of the many variables in the laser and experimental parameter space (jet position, laser chirp, inter-pulse delay, intensity ratio, etc). At the same time, the additional data dimension is retrievable from the original data. For charge measurements, we observed the induction caused by the electron beams through a calibrated ferrite toroid. Wide-angle beam divergence and its real time shot-to-shot stability was externally observed as fluorescence generated in Kodak Lanex Gd_2O_2S:Tb fluorescent screens lining the inside of transparent vacuum cylinders, in contact with 110 μm of aluminum on the target side to filter target-generated X-radiation softer than about 7 keV and scattered laser light (Glinec *et al.*, 2005). Magnetic deflection of the beams after passage through a collimating aperture is observable on the screen and confirms the charge polarity, electron energy, and the absence of detectable co-propagating X-ray beams such as potential betatron radiation (Rousse *et al.*, 2007). When operating in the single pulse mode, X-ray emission is isotropic, with insufficient energy to substantially penetrate the aluminum filter. Thus, and in practice, the fluorescent screen is not perceptibly illuminated during X-ray generation as described in our account of this X-ray source (Fullagar

et al., 2007*b*). Details about the respective detectors and their choice are given below.

OBSERVATIONS

Scanning the delay between the two orthogonal polarized pulses reveals dramatically different behavior on either side of simultaneous arrival. If the *s*-polarized pulse arrives first, it generates no substantial X-rays from the undisturbed target (Fullagar *et al.*, 2007*b*), but nevertheless interacts with the surface leading to formation of a plume that rapidly expands away from the surface. The subsequent *p*-polarized pulse enters the density gradients presented by this plume, and interacts with it. It is this situation in which high energy electron emissions are observed. If, on the other hand, the *p*-polarized pulse arrives first, it can stably generate hard X-rays from the target. In this case, the subsequent s-polarized beam does not lead to hard X-rays or hot electrons that we have been able to observe.

This behavior is shown in Figure 2a where the relative delay was scanned several hundred picoseconds on either side of simultaneous pulse arrival. The electron beams that form the subject of this paper, and whose identity is confirmed later, appear as high intensity data points at negative delay times.

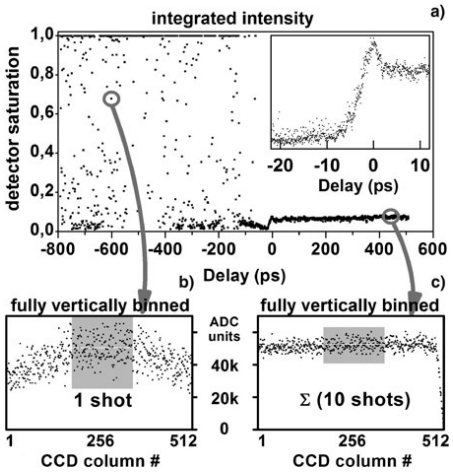

Fig. 2. (**a**) shows the integrated frame signal of the laser synchronous X-ray CCD, *vs.* delay between *s*- and *p*-polarized laser pulses. The inset shows the transition to stable X-ray production when the *p*-pulse precedes the *s*-pulse (positive delay). Destruction of conditions for efficient X-ray generation occurs within 5 ps both in helium (main scan) and in vacuum (inset), for which the general behaviour is similar. (**b**) expands the indicated non-saturating electron beam shot into the corresponding CCD columns (see text). (**c**) sums 10 consecutive shots during stable X-ray production in order to give a result with comparable average intensity in the shaded CCD columns. Substantially higher shot noise is evident in (b) than in (c), illustrating the higher energy of the radiation quanta in (b) (see text).

In these measurements, radiation passed through about 5 cm of helium gas at atmospheric pressure, about 50 μm of Beryllium, about 7 mm of air, and about 500 μm of Beryllium, before partial or complete registry at different depths in about 15 μm thick Silicon CCD, which is described elsewhere (Fullagar *et al.*, 2008). The X-ray photon energy of about 3–10 keV is unaltered by transit through matter, whereas individual electrons lose energy, so that the energy of detected electron quanta deposited in the thin Silicon detection layers is a fraction (F) of the electrons' original energy. We can anticipate that F will be rather small for electrons with energies on the order of 100 keV, for which we might expect $F = 0.1 - 0.5$ (Berger *et al.*, 1998). Nevertheless, the electron generated charge clouds often saturate the CCD preamplifier, which was at its lowest gain setting for this measurement. This and other comparable scans indicate that inter-pulse delays of 15 ps — 1.5 ns produce electron emissions in the direction of the CCD camera, here mounted in the horizontal plane at 90° from the incoming laser beam. The fixed and small angle of detection and generally erratic nature of the intensity spikes suggest that even shorter inter-pulse delays may be effective for their generation. The inset of Figure 2a shows the steep drop in X-ray production that occurs on a timescale of ~5 ps when the s-polarized pulse precedes the *p*-polarized pulse. It indicates the timescale of disruption of the sharp plasma gradient conditions that are a prerequisite for stable X-ray generation. The X-ray pulse itself is likely shorter than this (Fullagar *et al.*, 2007*b*).

Figures 2b and 2c show the data retained within individual points of Figure 2a when using the synchronously binned CCD procedure and can be used to estimate the electron energy. Noise is observable in the intensity distribution along the horizontal axis of the CCD for each laser shot. Its interpretation as quantum shot noise indicates that the energies deposited by detected electron radiation quanta are substantially higher than for typically 3–10 keV X-rays. Thus, for a particular non-saturating electron beam shot, we observe a standard deviation of $\sigma = 7500$ analog to digital converter units (ADCU) in Figure 2b, with average intensity $I = \sim 52000$ ADCU/column. In the region of stable X-ray production, the summation of 10 shots in Figure 2c leads to a comparable intensity, but with $\sigma = 2900$ ADCU. For the electrons, Poisson statistics indicates $\sigma/I = N^{-1/2}$, implying an average of $N = \sim 48$ events/column. The observed average intensity is $I = N{\cdot}E{\cdot}F/k$, where E is the unknown radiation quantum energy, F was defined previously, and $k = \sim 40$ eV/ADCU is the calibration factor (gain setting) of the CCD in the experiment. Rearrangement gives $E = (I{\cdot}k/N)/F = \sim 43000/F$ electron-volts. Thus, about 43 keV is a lower bound for the original electron energy (corresponding to $F = 1$), however, based on our anticipations concerning F in the previous paragraph, the measurement implies electron energies in the 100s of keV range. A better estimate by this approach would require quantitative assessment of F (bearing in mind that electrons may not be monoenergetic) and treatment of the scattering and secondary radiations

caused by such energetic electrons (primarily bremsstrahlung and X-ray fluorescence). The steep intensity drop above CCD column 500 in Figure 2c is due to shielding by a lead block. The smearing of this edge in Figure 2b shows the property of the electron beams to scatter on transit through air and the CCD's beryllium window. Similar scattering can also be seen in our earlier magnetic deflection data (Fullagar *et al.*, 2008).

Scans of the jet through the laser focus are shown in Figure 3, with and without the prepulse. In these scans, as in all data obtained using the CCD, the position of the jet was first adjusted to give grazing laser incidence on the side of the water jet closer to the CCD. Single *p*-polarized pulses were then used to optimize the observable X-ray signal in real time. In Figure 3, after establishing the optimum position, the jet was translated away from the CCD, before commencing data recording and manually scanning it at a steady rate towards the CCD, all the way through the laser focus. In the single pulse mode, two radiation peaks are invariably observed, corresponding to focusing on the near and far side of the jet. The second peak is somewhat smaller because the essentially isotropic, few keV broadband X-ray radiation is attenuated by its passage through the jet. Figure 3 also suggests the approach by which we can reliably generate electron emission; by first optimizing the stable X-ray emissions in a grazing incidence geometry on the CCD side of the jet with a single *p*-polarized pulse, then admitting a prepulse. The shape of the trace observed during the scan then changes dramatically. Erratic sharp peaks at about 0 μm and about 170 μm on the abscissa correspond to electron emission normal to the target surface for grazing laser-target interaction geometry. Erratic electron beams can also be observed at other, apparently arbitrary incidence angles, where their appearance can be optimized by translating the jet downstream in the converging laser beam, thus returning the water jet surface to the laser focus. This adjustment was not made in Figure 3, where we note instead that the electron beams appear capable of traversing the water jet (occasional flashes at about 170 μm on the abscissa; minor contributions from secondary radiations may also contribute). When striking the center of the water jet with the double pulse, radiations are again observable, in contrast to the single pulse measurement. If the simple double-peak X-ray behavior is not observed when a single ultrafast laser pulse is used, then experience has shown to expect impaired laser temporal contrast. Indeed, changes of this double-peak X-ray behavior, often accompanied by electron beams, have proven to be convenient indicators when troubleshooting occasional temporal problems of the laser systems.

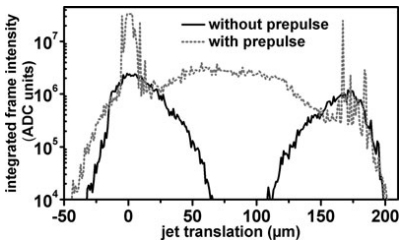

Fig. 3. Radiation observed using the X-ray CCD when scanning the water jet through the laser focus. The black trace uses a single *p*-polarized laser pulse, producing stable X-ray emission at grazing incidence on either side of the jet. The grey dotted trace adds an *s*-polarized prepulse, here showing erratic electron emissions at grazing incidence on either side of the jet. In addition, X-ray emission is observed at normal incidence (see text).

When striking the water jet at normal incidence in Figure 3, the circular cross section of the water jet surface lies slightly before the laser waist. In this geometry, the concepts of *s*- and *p*-polarized incidence cease to have meaning, although it is conceivable that the direction of emissions depends on the polarization (i.e., not isotropic), and the practical equivalence of the two pulses remains to be confirmed by delay scans such as in Figure 2, perhaps with appropriate equalization of the chirp in both pulses. In Figure 3, this normal incidence, double pulse arrangement appears capable of somewhat increasing the X-ray emission from the source over the single pulse grazing incidence geometry, which might be of interest in future applications. The observed radiation (in the abscissa range about 50–130 μm in Fig. 3) requires the second pulse for its generation, and shows quantum shot noise comparable to the X-rays generated by the single *p*-pulse in grazing incidence, noting also its relatively stable behavior and moderate average intensity in this scan.

Here the situation appears to be that of coronal hole punching and associated ponderomotive electron acceleration to the critical density, as proposed for fast ignition schemes in inertial confinement fusion (Tabak *et al.*, 1994; Mulser & Bauer, 2004, 2010). However, at this stage, our investigations of this double pulse, normal incidence geometry have not been taken further, and so contain the possibility of secondary radiations arising from the target chamber. Shadow images, spectrally resolved data, and temporally resolved X-ray streak camera measurements could resolve these questions in future experiments.

Figure 4 shows the X-ray production under helium (Fig. 4a) and electron beam production under vacuum (Fig. 4b) as functions of laser chirp on either side of its shortest value, as indicated by an optical autocorrelator. Note the change of vertical scale in the panels for the radiation data and frequent CCD saturation by the electron beams. For X-rays, the maximum radiation yield corresponds to a laser pulse duration of about 150–200 fs (Fullagar *et al.*, 2007*b*). The different behavior of the X-ray and electron emission with respect to laser pulse duration indicates different mechanisms for their generation. Both kinds of radiation emission appear symmetrical about the shortest pulse duration (about 46 fs), implying that chirp polarity is not a critical aspect of either generation process. This symmetric chirp behavior and optimal reliability at shortest pulse durations implies that pulse intensity is essential for electron beam formation.

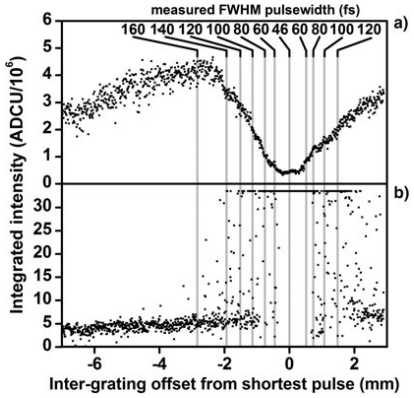

Fig. 4. (**a**) shows a scan of the X-ray yield observed by the CCD *vs.* inter-grating distance (chirp). The inset numbers give the approximate pulse duration in femtoseconds with the shortest pulse corresponding to about 46 fs. The X-rays were generated using a high contrast ratio single *p*-polarized pulse. In (**b**) a prepulse is added, leading to production of fast electrons. Note the change of intensity scale, including frequent CCD saturation by the electrons, and apparent symmetry of radiation yield with regard to sign of the chirp.

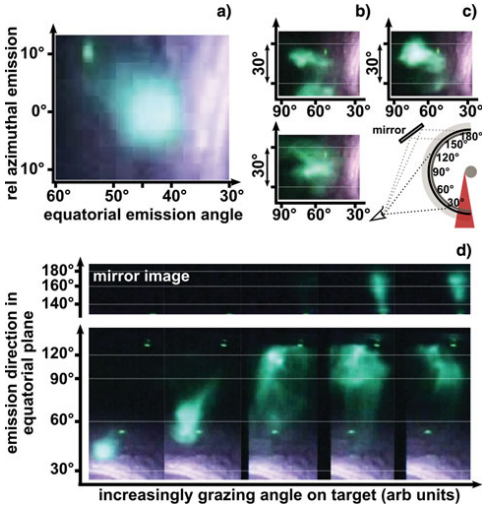

Fig. 5. (Color online) Video stills of a visually fluorescing screen wrapped inside a transparent Perspex vacuum cylinder, centered on the target jet. (**a**) shows a selected shot whose brightest fluorescence just saturates the camera. (**b**) shows three consecutive shots after an attempt to optimize the beam position (see following). (**c**) sketches the setup; from the jet outwards, components are: 6 cm aspirator vacuum, 110 μm aluminum, fluorescent screen, vacuum cylinder. The camera is mounted in air, with a mirror to increase observable angles around the cylinder. In (**d**) the jet is translated to give increasingly grazing laser-target incidence angles (these individual images are rotated sideways to allow more convenient display).

To ensure shot-to-shot reproducibility of the preplasma plume structure and associated directional instabilities of the electron beams, excellent pointing stability is desirable, as the following measurements show. Instability in the direction of the emitted electron beams is a contributing aspect of the erratic electron intensity observations in Figures 2, 3, and 4.

In Figure 5, the lead target chamber and CCD are replaced by a wrap-around Lanex screen, viewed externally using video cameras and mirrors positioned in the horizontal plane as shown in Figure 5c. In conjunction with visual observation, the fluorescent screen thus allows simultaneous real time observation of a very large solid angle around the source on a shot-to-shot basis. Approximately collimated beams have been observed around the equatorial plane from about 30° to about 150° with respect to the incoming laser. Figure 5a shows such a shot with the indicated emission angles. The observable distribution is not greatly smeared by interactions in the aluminum filter and the 1.5 mm thick fluorescence screen (which are essentially in contact with each other), as can be judged by the amount of structure in the images. Figure 5b shows three consecutive shots, during which laser intensity fluctuations were in the range of a few percent. The electron beams have only been observed in the horizontal plane, with a visually estimated azimuthal spread of at most about 40°. Once conditions for their appearance have been established, the electron beams are observable in most shots. They can be generated under various angles of target incidence; moreover a degree of beam steering is possible in this way, by translating the water jet within the laser focus (Fig. 5d). However, the jet and its translations are small enough that the exact angles of target incidence cannot be reliably ascertained. Fluorescence above 140° on the equator is observable in the mirror. Close to grazing incidence the stabilization of the collimated beams becomes nearly impossible and the beam diffuses. In this region, complex and non-reproducible distribution of the electron emission on an individual shot basis appear to vividly illustrate laser plasma instabilities (see also text to Fig. 8).

The X-ray source size is not necessarily connected to the electron beam source size. However, we are able to observe the X-ray source size, both with and without prepulses, which is important for applications (Loupias *et al.*, 2009; Pikuz *et al.*, 2010). In Figure 6, the CCD is arranged in line with the converging laser beam, to give indications of the X-ray source depth in the target, also its vertical extent. Approximately 300 laser shots were needed to produce the images, which yield multi-shot average measurements. Without a prepulse, and by fitting a Gaussian error function to the edge blur, the observable single pulse X-ray source size full width half maximum (FWHM) is 6.77 μm (vertical dimension) and 11.3 μm (deep, in the target). The first of these values is a bound of the laser pointing stability (an issue

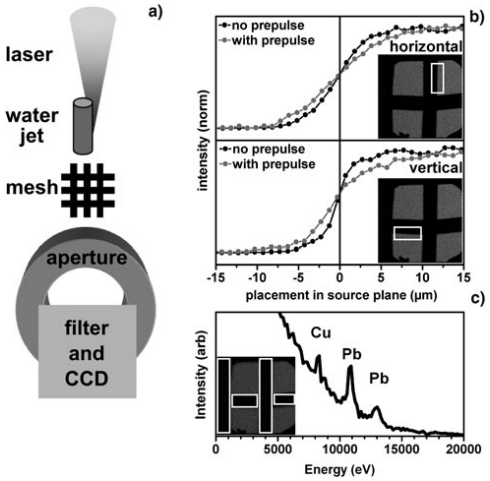

Fig. 6. Inline measurement of multi-shot average X-ray source size. (**a**) shows the arrangement used to generate shadow images of a wire mesh on a CCD. (**b**) illustrates the edge blurring for the respective edges, shown as insets, from which the average source size is deduced (see text). (**c**) shows a histogram of events that appear in the inset region of interest (i.e., in the shadows of the wire mesh) when using a double pulse structure.

that has been refined over the years on this laser system) (Genoud *et al.*, 2011), while the second is mostly attributed to the stopping range of few-keV electrons in water (Fullagar

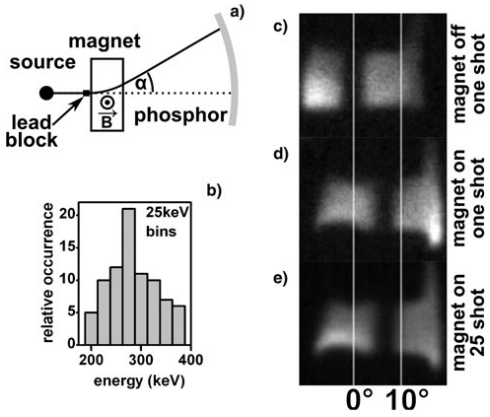

Fig. 7. Magnetic deflection of electron beams, projected on a fluorescent screen. (**a**) sketches the experimental setup, using a 15 cm diameter transparent cylinder, a 10 mm long, 27 mT electromagnet and a lead block placed before the magnet that casts a shadow through it. (**b**) histograms the inferred energy of individual shots. The relativistically corrected energy was determined from displacement of shadow edges. (**c**) and (**d**) show examples of single shots used in this approach. (**e**) shows the average of 25 shots, in which the essentially modest broadening of the edge shadow supports the energy histogram in panel b).

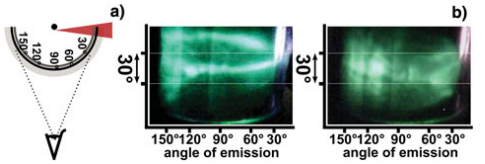

Fig. 8. (Color online) Externally viewed video stills of electron distributions, using grazing laser incidence on the target jet. (**a**) sketches the setup, with water jet, 110 μm aluminum filter and optically fluorescent screen in a transparent vacuum cylinder with 6 cm diameter. (**b**) shows examples of complex single shot electron distributions.

et al., 2007*b*). The addition of the prepulse increases the average FWHM source size to 14.7 μm (vertical) and 17.1 μm (deep). In these images, the pointing stability of the laser can be assumed identical both with and without the prepulse. The observed increases in the average X-ray source size on addition of the prepulse indicate one or both of the following: (1) the region of X-ray emission has increased on a single shot basis, (2) the position of X-ray generation in space has been made more random by the prepulse. The second interpretation is consistent with expected laser plasma interaction instabilities. Figure 6c shows secondary X-ray radiations, caused by the electron beams striking objects within the chamber and the chamber wall. These are not evident when using a single pulse. X-ray fluorescence lines from lead (chamber) and copper (riser pipe for the water jet, and mesh) are apparent in the histogram.

The charge of the beam per laser shot was estimated by positioning a 3.5 mm internal diameter ferrite toroid about 5 mm from the target in the path of the electrons, with two turns of wire on the toroid serving as a readout coil. After calibration and when generating electron emission using prepulses (allowing for radiofrequency pickup from synchronous components of the laser system, typically Pockels cells), the observed voltage transients indicated an emitted charge of as much as about 6 pC through the solid angle of the toroid which agrees well with the results found by Wang *et al.* (2010). Other charged particles, their absorption in the residual gas and disturbances due to the plasma explosion can influence these measurements (Hidding *et al.*, 2007); nevertheless the signal polarity was as expected for electrons, and the measurement gives at least an indication of the charge.

A lower bound on the electron energy is easily obtained by observing X-ray fluorescence lines excited from different elements as observed using the CCD (Fullagar *et al.*, 2008). The beams' ability to penetrate different materials (Berger *et al.*, 1998), and the angular properties of associated scatter gave further indications, consistent with the magnetic deflection method below.

The shadow of a rectangular lead wire was projected onto a Kodak Lanex screen filtered by 110 μm of aluminum, with a 10 mm long, 27 mT calibrated electromagnet between the

wire and the screen (Fig. 7). The spectral sensitivity of a similar arrangement has been characterized by others and is maximal in the approximate range 300–900 keV (Glinec *et al.*, 2006). For this experiment, we used 17 mJ in each laser arm with minimum duration *p*-pulse, about 20 ps relative delay, and aspirator vacuum in a 15 cm diameter transparent chamber. The shadow edge is observed to shift by up to 7.7°, corresponding to relativistically corrected electron energy of about 280 keV. The instabilities seen in earlier figures make these measurements challenging, yet they provide a clear demonstration of the nature of the beam, also a direct indication of its energy. The comparable level of shadow edge blurring when the magnet is switched on and off, or its polarity reversed, indicates that the single-shot electron energy distribution is narrow compared to the sensitive energy range of the screen. Also, the observed deflected shadow edges show surprisingly little positional variation from one successful shot to the next. The corresponding energy analysis leads to the result in the histogram inset in Figure 7. Although modest, these shot-to-shot energy differences substantially account for the edge blurring observable when the magnetically deflected images are averaged, also shown in Figure 7.

We have repeated this experiment, with similar results, though in which experimental differences led to 6.3° beam deviation when applying the same field, corresponding to 390 keV electron energy. These energies correspond well with the observations of Wang and co-workers under high vacuum with an aluminum target (Wang *et al.*, 2010).

REMARKS

During the transition from a high power, high contrast ratio but low repetition rate laser system to a commercially available 3 mJ 1 kHz system with a 10% temporal prepulse due to leakage in the cavity we observed similar collimated electron beams. The experimental setup was otherwise comparable. These reduced intensity conditions suggest continued exploration of the electron beams for a range of applications, though they should also be recognized as a radiation safety hazard and potential source of secondary radiations when studying laser plasma X-ray sources. Low atomic number materials are advisable on the inner walls of target chambers, to minimize hard secondary radiation and slow the electrons to rest.

For further experiments, the round water jet has proven to be entirely satisfactory in terms of stability, target smoothness, controllability of laser-target interaction geometry and simplicity of operation.

The mechanistic origin of the fast electron beams is not fully understood. It can be assumed that a continuum of plasma densities is encountered by the second laser pulse. Also, based on increases in the X-ray source size measurements, as shown in Figure 6, it appears that length scales on the order of about 10 μm are operative in the laser-plasma interaction region on the timescale of the interpulse delay, corresponding to supersonic plasma expansion. The data in Figure 2 shows that conditions required for effective X-ray production by Brunel (vacuum) heating (Brunel, 1987; Fullagar *et al.*, 2007*b*) are disrupted on a timescale of only about 5 ps, which together with the undisturbed X-ray source size of 6.77 μm implies velocities on the order of 1.4×10^6 ms^{-1}. While the laser waist is doubtless somewhat smaller on a single shot basis, this high velocity indicates that, with regards to destroying the conditions necessary for the Brunel mechanism, the prepulse merely perturbs the motion of electrons at the sharp plasma gradient, which seems consistent with the presumed mechanism for the X-ray generation (Fullagar *et al.*, 2007*b*). Given inter-pulse delays of the order 10–100 ps there is sufficient time for the establishment of a plasma plume of the required dimension. For the second (*p*-polarized) pulse at increasing depths within the plasma plume, different mechanisms exist that can lead to pulse self-modulation, self-compression, and filamentation (Max, 1980; Sjögren, 2002).

In Figure 8, the laser-target interaction is at almost grazing incidence, with the second pulse in the usual *p*-polarization. The pattern of accelerated electrons striking the fluorescent screen indicates the directionality of the electron acceleration process occurring in the target, likely also the electron density perturbations and intense local electromagnetic field gradients immediately before, during and after the acceleration. It is apparent that the fluorescence intensity pattern represents a potentially quantifiable observation of the complex and unstable dynamics associated with the transversal of the second pulse through the preplasma and its interaction with the critical surface (Naumova *et al.*, 2004). The future use of few cycle pulses with carrier envelope phase stabilization (Mathur *et al.*, 2008; Sansone *et al.*, 2006) might be critical for such studies and could perhaps lead to satisfactory control of the electron beams.

The conditions obtained have long been recognized as suitable for the absorption of light by its conversion to electron plasma waves near the critical density (Kruer, 1975). Plasma wave breaking, associated with critical surface rippling and cavity formation may occur in these circumstances (Tajima & Dawson, 1979; Estabrook, 1976; Estabrook *et al.*, 1975). Our observed electron acceleration to about 280–390 keV in apparent distances of about 10 μm (50 GeV/m) is comparable with laser plasma wakefield acceleration experiments (Jaroszynski *et al.*, 2009; Lundh, 2008; Steinke *et al.*, 2010). With these considerations in mind, it is not unlikely that our double pulse experiments have certain aspects of underlying physics in common with laser plasma wakefield acceleration.

CONCLUSION

Double laser pulses impinging on a water jet target with the second pulse in *p*-polarized geometry, create about 280–390 keV electron beams when using inter-pulse delays in the range from tens of picoseconds to nanoseconds and

longer. The beams are generated at laser intensities in the range of about 10^{15}–10^{18} Wcm^{-2} in a helium atmosphere at ambient pressure or water aspirator vacuum and are favored by laser pulses of near transform-limited duration. Their appearance can be symptomatic of poor temporal contrast in laser systems of the kind often used for X-ray plasma generation. Conditions for angularly reproducible generation of the fast electron beams are far harder to achieve than for stable X-ray generation using a temporally isolated *p*-polarized laser pulse. The high electron energies represent a significant radiation hazard and motivate the use of low-Z materials for the inner walls of future target chamber constructions. They also represent a potential source of confusion if only point radiation detectors are available, and if care is not taken to discredit secondary radiations. If a suitable degree of control can be obtained, the observed about 280–390 keV electron beams are likely to prove useful in ultrafast electron imaging and scattering applications.

ACKNOWLEDGEMENTS

We especially thank the following individuals, who assisted in day-to-day laser operation over the period from 2005 to 2008 when the experiments took place: A. Persson, E. Pourtal, O. Lundh, F. Lindau, Y. Glinec, G. Genoud, and M. Harbst. This work has received funding from the Swedish Consortium for Artificial Photosynthesis, the Swedish Kungliga Fysiografiska Sällskap, the Swedish Energy Agency, the Knut and Alice Wallenberg Foundation, the Swedish Research Council, a Linneus grant awarded to the Lund Laser Centre and the ERC Advanced Investigator Grant No 226136. J. Uhlig and M. Walczak acknowledge financing through the MAXlas project, under the Sixth European Framework Programme contract number MEST-CT-2005-020356.

REFERENCES

Ahn, H., Nakano, H., Nishikawa, T. & Uesugi, N. (1996). Simultaneous measurement of absorption and x-ray emission from preformed plasma generated by ultrashort prepulse. *Jap J. Appl. Phys*. **35**, L154–L157.

Anand, M., Gibbon, P. & Krishnamurthy, M. (2007). Hot electrons produced from long scale-length laser-produced droplet plasmas. *Laser Phys*. **17**, 408–414.

Anand, M., Kahaly, S., Kumar, G.R., Krishnamurthy, M., Sandhu, A.S. & Gibbon, P. (2006). Enhanced hard X-ray emission from microdroplet preplasma. *Appl. Phys. Lett*. **88**, 181111–1

Bastiani, S., Rousse, A., Geindre, J.P., Audebert, P., Quoix, C., Hamoniaux, G., Antonetti, A. & Gauthier, J.C. (1997). Experimental study of the interaction of subpicosecond laser pulses with solid targets of varying initial scale lengths. *Phys. Rev. E* **56**, 7179–7185.

Berger, M.J., Coursey, J.S., Zucker, M.A. & Chang, J. (1998). Stopping powers for electrons and positrons. http://physics.nist.gov/PhysRefData/Star/Text/ESTAR.html.

Brunel, F. (1987). Not-so-resonant, resonant absorption. *Phys. Rev. Lett*. **59**, 52–55.

Centurion, M., Reckenthaeler, P., Fuss, W., Trushin, S., Apolonski, A., Krausz, F. & Fill, E.E. (2009). Ultrafast imaging with electron pulses. *Proc. Conference on Lasers and Electro-Optics and Quantum Electronics and Laser Science Conference*, pp. 1093–1094.

Centurion, M., Reckenthaeler, P., Trushin, S.A., Krausz, F. & Fill, E.E. (2008). Picosecond electron deflectometry of optical-field ionized plasmas. *Nat. Photon*. **2**, 315–318.

Chen, L.M., Kando, M., Xu, M.H., Li, Y.T., Koga, J., Chen, M., Xu, H., Yuan, X.H., Dong, Q.L., Sheng, Z.M., Bulanov, S.V., Kato, Y., Zhang, J. & Tajima, T. (2008). Study of X-ray emission enhancement via a high-contrast femtosecond laser interacting with a solid foil. *Phys. Rev. Lett*. **100**, 045004.

Chen, L.M., Liu, F., Wang, W.M., Kando, M., Mao, J.Y., Zhang, L., Ma, J.L., Li, Y.T., Bulanov, S.V., Tajima, T., Kato, Y., Sheng, Z.M., Wei, Z.Y. & Zhang, J. (2010). Intense high-contrast femtosecond k-shell X-ray source from laser-driven ar clusters. *Phys. Rev. Lett*. **104**, 215004.

Dorchies, F., Harmand, M., Descamps, D., Fourment, C., Hulin, S., Petit, S., Peyrusse, O. & Santos, J.J. (2008). High-power 1 kHz laser-plasma X-ray source for ultrafast X-ray absorption near-edge spectroscopy in the keV range. *Appl. Phys. Lett*. **93**, 121113.

Estabrook, K. (1976). Critical surface bubbles and corrugations and their implications to laser fusion. *Phys. Fluids* **19**, 1733.

Estabrook, K.G., Valeo, E.J. & Kruer, W.L. (1975). Two-dimensional relativistic simulations of resonance absorption. *Phys. Fluids* **18**, 1151.

Fullagar, W., Uhlig, J., Walczak, M., Canton, S., Wahlström, C.-G. & Sundström, V. (2007*a*). Radiations from a water jet plasma source. http://www.maxlab.lu.se/emergingsources/images/wilfred_fullagar_poster_A2.pdf.

Fullagar, W.K., Harbst, M., Canton, S., Uhlig, J., Walczak, M., Wahlström, C.-G. & Sundström, V. (2007*b*). A broadband laser plasma X-ray source for application in ultrafast chemical structure dynamics. *Rev. Sci. Instr*. **78**, 115105.

Fullagar, W.K., Uhlig, J., Gador, N., Kinnunen, K., Maasilta, I., Wahlström, C.-G. & Sundström, V. (2010). Lab-based ultrafast molecular structure. *Proc. AIP Conference Proceedings*. pp. 919–922. Melbourne: Australia American Institute of Physics.

Fullagar, W.K., Uhlig, J., Walczak, M., Canton, S. & Sundstrom, V. (2008). The use and characterization of a backilluminated charge-coupled device in investigations of pulsed X-ray and radiation sources. *Rev. Sci. Instr*. **79**, 103302.

Genoud, G., Wojda, F., Burza, M., Persson, A. & Wahlström, C.-G. (2011). Active control of the pointing of a multi-terawatt laser. *Rev. Sci. Instr*. **82**, 033102–033102.

Gizzi, L.A. (2010). Progress in Ultrafast Intense Laser Science. In (Yamanouchi, K., Giulietti, A. and Ledingham, K., Eds.), Vol. **98**, pp. 123–138. Berlin, Heidelberg: Springer Berlin Heidelberg.

Glinec, Y., Faure, J., Guemnie-Tafo, A., Malka, V., Monard, H., Larbre, J.P., De Waele, V., Marignier, J.L. & Mostafavi, M. (2006). Absolute calibration for a broad range single shot electron spectrometer. *Rev. Sci. Instr*. **77**, 103301.

Glinec, Y., Faure, J., Pukhov, A., Kiselev, S., Gordienko, S., Mercier, B. & Malka, V. (2005). Generation of quasi-monoenergetic electron beams using ultrashort and ultraintense laser pulses. *Laser Part. Beams* **23**, 161–166.

Guo, T. (2009). More power to X-rays: New developments in X-ray spectroscopy. *Laser Photon. Rev*. **3**, 591–622.

Hatanaka, K., Ono, H. & Fukumura, H. (2008). X-ray pulse emission from cesium chloride aqueous solutions when irradiated by double-pulsed femtosecond laser pulses. *Appl. Phys. Lett.* **93**, 064103.

Hidding, B., Pretzler, G., Clever, M., Brandl, F., Zamponi, F., Lübcke, A., Kämpfer, T., Uschmann, I., Förster, E., Schramm, U., Sauerbrey, R., Kroupp, E., Veisz, L., Schmid, K., Benavides, S. & Karsch, S. (2007). Novel method for characterizing relativistic electron beams in a harsh laser-plasma environment. *Rev. Sci. Instr.* **78**, 083301.

Hou, B., Easter, J., Mordovanakis, A.G., Krushelnick, K. & Nees, J.A. (2008). Vacuum-free X-ray source based on ultrashort laser irradiation of solids. *Opt. Express* **16**, 17695.

Hu, G.-Y., Lei, A.-L., Wang, W.-T., Wang, X., Huang, L.-G., Wang, J.-W., Xu, Y., Liu, J.-S., Yu, W., Shen, B.-F., Li, R.-X. & Xu, Z.-Z. (2010). Collimated hot electron jets generated from subwavelength grating targets irradiated by intense short-pulse laser. *Phys. Plasmas* **17**, 033109.

Jaroszynski, D.A., Reitsma, A. & Ersfeld, B. (2009). Laser-Plasma Interactions. In (Jaroszynski, D.A., Bingham, R., and Cairns, R.A., Eds.), pp. 110–169. New York: Taylor & Francis Group.

Kruer, W.L. (1975). Theoretical interpretations of enhanced laser light absorption. *Proc. Progress in Lasers and Laser Fusion*. pp. 5–26. New York: Plenum Press.

Kugland, N.L., Constantin, C.G., Neumayer, P., Chung, H.-K., Collette, A., Dewald, E.L., Froula, D.H., Glenzer, S.H., Kemp, A., Kritcher, A.L., Ross, J.S. & Niemann, C. (2008). High Kα X-ray conversion efficiency from extended source gas jet targets irradiated by ultra short laser pulses. *Appl. Phys. Lett.* **92**, 241504.

Lee, T., Jiang, Y., Rose-Petruck, C.G. & Benesch, F. (2005). Ultrafast tabletop laser-pump-X-ray probe measurement of solvated Fe(CN)(6)(4-). *J. Chem. Phys.* **122**, 084506.

Li, Z., Daido, H., Fukumi, A., Sagisaka, A., Ogura, K., Nishiuchi, M., Orimo, S., Hayashi, Y., Mori, M., Kado, M., Bulanov, S.V., Esirkepov, T.Z., Oishi, Y., Nayuki, T., Fujii, T., Nemoto, K., Nakamura, S. & Noda, A. (2006). Measurements of energy and angular distribution of hot electrons and protons emitted from a p- and s-polarized intense femtosecond laser pulse driven thin foil target. *Phys. Plasmas* **13**, 043104.

Lindau, F. (2007). *Laser-driven particle acceleration: Experimental investigations*. PhD Thesis (LRAP-378). Lund University.

Loupias, B., Perez, F., Benuzzi-Mounaix, A., Ozaki, N., Rabec, M., Gloahec, L.E., Pikuz, T.A., Faenov, A.Y., Aglitskiy, Y. & Koenig, M. (2009). Highly efficient, easily spectrally tunable X-ray backlighting for the study of extreme matter states. *Laser Part. Beams* **27**, 601.

Lundh, O. (2008). *Laser-driven beams of fast ions, relativistic electrons and coherent* X-ray *photons*. PhD Thesis (LRAP-391). Lund University.

Mangles, S.P.D., Genoud, G., Kneip, S., Burza, M., Cassou, K., Cros, B., Dover, N.P., Kamperidis, C., Najmudin, Z., Persson, A., Schreiber, J., Wojda, F. & Wahlström, C.-G. (2009). Controlling the spectrum of X-rays generated in a laser-plasma accelerator by tailoring the laser wavefront. *Appl. Phys. Lett.* **95**, 181106.

Mangles, S.P.D., Walton, B.R., Najmudin, Z., Dangor, A.E., Krushelnick, K., Malka, V., Manclossi, M., Lopes, N., Carias, C., Mendes, G. & Dorchies, F. (2006). Table-top laser-plasma acceleration as an electron radiography source. *Laser Part. Beams* **24**, 185–190.

Mathur, D., Rajgara, F.A., Dharmadhikari, A.K. & Dharmadhikari, J.A. (2008). Strong-field ionization of water by intense few-cycle laser pulses. *Phys. Rev. A* **78**, 023414.

Max, C.E. (1980). Laser Plasma Interaction. *Proc. Les Houches Summer School Proceedings*. pp. 301–410. Amsterdam: Elsevier Science Ltd.

Mordovanakis, A.G., Masson-Laborde, P.-E., Easter, J., Popov, K., Hou, B., Mourou, G.r., Rozmus, W., Haines, M.G., Nees, J. & Krushelnick, K. (2010). Temperature scaling of hot electrons produced by a tightly focused relativistic-intensity laser at 0.5 kHz repetition rate. *Appl. Phys. Lett.* **96**, 071109.

Mulser, P. & Bauer, D. (2004). Fast ignition of fusion pellets with superintense lasers: Concepts, problems, and prospective. *Laser Part. Beams* **22**, 5–12.

Mulser, P. & Bauer, D. (2010). *High Power Laser-Matter Interaction* (Höhler, G., Fujimori, A., Kühn, J., Müller, T., Steiner, F., Trümper, J. and Wölfle, P., Eds.). Berlin, Heidelberg: Springer.

Nakano, H., Nishikawa, T., Ahn, H. & Uesugi, N. (1996). Effects of an ultrashort prepulse on soft X-ray generation from an aluminium plasma produced by femtosecond Ti:sapphire laser pulses. *Appl. Phys. B* **63**, 107–111.

Naumova, N., Sokolov, I., Nees, J., Maksimchuk, A., Yanovsky, V. & Mourou, G. (2004). Attosecond electron bunches. *Phys. Rev. Lett.* **93**, 195003.

Pikuz, S.A., Chefonov, O.V., Gasilov, S.V., Komarov, P.S., Ovchinnikov, A.V., Skobelev, I.Y., Ashitkov, S.Y., Agranat, M.V., Zigler, A. & Faenov, A.Y. (2010). Micro-radiography with laser plasma X-ray source operating in air atmosphere. *Laser Part. Beams* **28**, 393–397.

Reckenthaeler, P., Centurion, M., Fuss, W., Trushin, S.A., Krausz, F. & Fill, E.E. (2009). Time-Resolved Electron Diffraction from Selectively Aligned Molecules. *Phys. Rev. Lett.* **102**, 213001.

Rousse, A., Phuoc, K.T. & Albert, F. (2007). Progress in Ultrafast Intense Laser Science II. In *Progress in Ultrafast Intense Laser Science II*, Vol. 85, pp. 215–230. Berlin, Heidelberg, Springer Berlin Heidelberg.

Ruhl, H., Sentoku, Y., Mima, K., Tanaka, K. & Kodama, R. (1999). Collimated Electron Jets by Intense Laser-Beam–Plasma Surface Interaction under Oblique Incidence. *Phys. Rev. Lett.* **82**, 743–746.

Sansone, G., Benedetti, E., Caumes, J.-P., Stagira, S., Vozzi, C., De Silvestri, S. & Nisoli, M. (2006). Control of long electron quantum paths in high-order harmonic generation by phase-stabilized light pulses. *Phys. Rev. A* **73**, 053408.

Silies, M., Witte, H., Linden, S., Kutzner, J., Uschmann, I., Förster, E. & Zacharias, H. (2009). Table-top kHz hard X-ray source with ultrashort pulse duration for time-resolved X-ray diffraction. *Appl. Phys. A* **96**, 59–67.

Sjögren, A. (2002). *Laser-Matter Interactions at Extreme Irradiance:* X-ray *Generation and Relativistic Channeling.* PhD Thesis (LRAP-288). Lund University.

Steinke, S., Henig, A., Schnürer, M., Sokollik, T., Nickles, P.V., Jung, D., Kiefer, D., Hörlein, R., Schreiber, J., Tajima, T., Yan, X.Q., Hegelich, M., Meyer-ter-Vehn, J., Sandner, W. & Habs, D. (2010). Efficient ion acceleration by collective laser-driven electron dynamics with ultra-thin foil targets. *Laser Part. Beams* **28**, 215.

Svanberg, S., Larsson, J., Persson, A. & Wahlström, C.-G. (1994). Lund high-power laser facility – systems and first results. *Phys. Scripta* **49**, 187–197.

Tabak, M., Hammer, J., Glinsky, M.E., Kruer, W.L., Wilks, S.C., Woodworth, J., Campbell, E.M., Perry, M.D. & Mason, R.J. (1994). Ignition and high gain with ultrapowerful lasers. *Physics of Plasmas* **1**, 1626.

Tajima, T. & Dawson, J. (1979). Laser Electron Accelerator. *Phys. Rev. Lett*. **43**, 267–270.

Tarasevitch, A., Gibbon, P., Mašek, M., Teubner, U., Lu, W., Nicoul, M., Shymanovich, U., Zhou, P., Sokolowski-Tinten, K. & Linde, D. (2009). Modelling and optimisation of fs laser-produced K α sources. *Appl. Phys. A* **96**, 23–31.

Wang, W., Liu, J., Cai, Y., Wang, C., Liu, L., Xia, C., Deng, A., Xu, Y., Leng, Y., Li, R. & Xu, Z. (2010). Angular and energy distribution of fast electrons emitted from a solid surface irradiated by femtosecond laser pulses in various conditions. *Phys. Plasmas* **17**, 023108.

Zamponi, F., Ansari, Z., Korff Schmising, C., Rothhardt, P., Zhavoronkov, N., Woerner, M., Elsaesser, T., Bargheer, M., Trobitzsch-Ryll, T. & Haschke, M. (2009). Femtosecond hard X-ray plasma sources with a kilohertz repetition rate. *Appl. Phys. A* **96**, 51–58.

Zhang, J., Li, Y.T., Sheng, Z.M., Wei, Z.Y., Dong, Q.L. & Lu, X. (2005). Generation and propagation of hot electrons in laser-plasmas. *Appl. Phys. B* **80**, 957–971.

Paper V

Table-top ultrafast x-ray microcalorimeter spectrometry for molecular structure

J. Uhlig, W. Fullagar, J. Ullom, W.B. Doriese, N. Gador, S. Canton, K. Kinnunen, J. Fowler, C. Reintsema, D. Swetz, D. Bennett, G. Hilton, K. Irwin, D. Schmidt, V. Sundström.

Physical Review Letter **110(13)**, 138302(2013).

PRL **110,** 138302 (2013) PHYSICAL REVIEW LETTERS week ending 29 MARCH 2013

Table-Top Ultrafast X-Ray Microcalorimeter Spectrometry for Molecular Structure

J. Uhlig,[1,2] W. Fullagar,[1] J. N. Ullom,[2] W. B. Doriese,[2] J. W. Fowler,[2] D. S. Swetz,[2] N. Gador,[1] S. E. Canton,[1,3] K. Kinnunen,[1,4] I. J. Maasilta,[4] C. D. Reintsema,[2] D. A. Bennett,[2] L. R. Vale,[2] G. C. Hilton,[2] K. D. Irwin,[2] D. R. Schmidt,[2] and V. Sundström[1]

[1]*Department of Chemical Physics, Lund University, Lund, Sweden*
[2]*National Institute of Standards and Technology, 325 Broadway MS 817.03, Boulder, Colorado 80305, USA*
[3]*Department of Synchrotron Radiation Instrumentation, Lund University, Lund, Sweden*
[4]*Nanoscience Center, Department of Physics, P.O. Box 35, FI-40014 University of Jyväskylä, Jyväskylä, Finland*

(Received 18 October 2012; published 26 March 2013)

This work presents an x-ray absorption measurement by use of ionizing radiation generated by a femtosecond pulsed laser source. The spectrometer was a microcalorimetric array whose pixels are capable of accurately measuring energies of individual radiation quanta. An isotropic continuum x-ray spectrum in the few-keV range was generated from a laser plasma source with a water-jet target. X rays were transmitted through a ferrocene powder sample to the detector, whose pixels have average photon energy resolution $\Delta E = 3.14$ eV full-width-at-half-maximum at 5.9 keV. The bond distance of ferrocene was retrieved from this first hard-x-ray absorption fine-structure spectrum collected with an energy-dispersive detector. This technique will be broadly enabling for time-resolved observations of structural dynamics in photoactive systems.

DOI: 10.1103/PhysRevLett.110.138302 PACS numbers: 82.80.Ej, 07.85.-m, 61.05.cj, 78.47.D−

Observing and understanding the motion of atoms and electrons on pico-, femto-, and attosecond time scales is a frontier of contemporary science and the motivation for vigorous development of ultrafast time-resolved spectroscopic techniques based on hard x rays [1]. These techniques are often flux-limited, particularly with laboratory pulsed laser x-ray sources. Long accumulation periods are required to achieve the necessary energy resolution owing to the involvement of Bragg reflection with its generally narrow-bandpass characteristics and consequent dramatic flux losses [2–6]. Direct energy-resolving detectors such as calorimeters or charge-coupled devices have a much higher quantum yield and a long history in radiation studies [7,8]. Recent technological developments in microcalorimetric detectors [9] have improved the energy resolution and count rates of these highly efficient direct photon-measurement schemes sufficiently to enable useful measurements in reasonable time frames.

The novel combination of a pulsed-laser-generated, broadband, hard x-ray source with a photon-measuring cryogenic microcalorimeter array has been motivated previously [10–13]. It promises spectroscopic ultrafast structural measurements with photon-counting rates that, in the prototype version discussed in this Letter, are comparable to established techniques such as electron-beam slicing at synchrotrons and focusing-crystal geometries [1,14]. The strength of this new approach lies in its straightforward scalability combined with very high collection efficiency. X-ray absorption fine structure (XAFS) features are observable and quantifiable, as are extended range modulations that result from the influence of adjacent atoms on the absorption dipole strength, and contain molecular structure and valence orbital spectroscopic information. The setup allows simultaneous observation of multiple absorption edges and considerable flexibility for binning during and after the experiment. This demonstration is a critical development in the advancement of inhouse molecular structure analysis, particularly for subpicosecond pump-probe studies in condensed phases [3,10–12,15]. This publication aims to demonstrate the new opportunities and presents, for the first time, a hard x-ray absorption fine-structure spectrum recorded with a highly efficient energy-dispersive detector.

The x-ray plasma source is based on isotropic continuum bremsstrahlung generated when focusing 1 kHz, 800 nm Ti:sapphire laser pulses with 2.5 mJ/pulse and ~50 fs duration onto a flowing water jet. The jet is operated at water aspirator vacuum pressure (~ 25 torr at 21 °C) and enclosed by a target chamber constructed from 8 mm thick aluminum. The flux, spectral, and temporal properties of the x rays emitted at this laser pulse energy were described previously [10,11]. Efforts were made to ensure sufficient temporal contrast when operating the laser, to avoid generation of high-energy electron beams and concomitant reduction of target-generated x-ray flux [16]. The laser system provides up to 6 mJ/pulse and thus has sufficient additional energy to enable optical stimulation of samples in a pump-probe arrangement.

Calorimetric event detection is based on the thermalization of single photons in an absorber and the observation of the subsequent thermal flow. The particular detector array used here is based on bismuth absorbers with transition-edge-sensor (TES) thermometers operating at millikelvin temperatures [17]. Pixels are read out in a

time-division-multiplexing scheme [18], asynchronously to the laser pulses, and with signal-record lengths of ≈ 12 ms, during which pileup had to be rejected. The laser source can provide x-ray events in each pixel at up to the laser repetition rate (1 kHz), but the source-detector distance and intervening filters were adjusted to limit the count rate. The record length is a compromise between energy resolution and readout speed. It is not a fundamental parameter, but rather reflects the current state of the readout electronics, pixel recovery periods, and pulse-processing approach. Each of these quantities is the subject of current development, and significant improvements are anticipated. The bismuth x-ray absorber in each pixel has dimensions of $350 \times 350 \times 2.5$ μm and stops $\approx 53\%$ of the arriving photons at 7.2 keV. From the installed array with 160 pixels, 22 detectors contributed to the presented spectra. A system with all 160 pixels and shorter record lengths is currently under characterization and will provide more than 16 times shorter accumulation periods. Pixel centers are positioned on a square 665 μm grid in a roughly circular array, with each absorber masked by a 320×305 μm aperture.

The emission lines from Mn-$K\alpha$ at 5.9 keV measured with the 22 pixels detector show an average energy resolution of $\Delta E_{\mathrm{FWHM}} = 3.14$ eV. During laser operation, the average resolution was 3.4 eV. The difference between these values is explained by a higher count rate from the laser as well as electromagnetic pickup from laser operation. The absorber and thermometer parameters are chosen to give the best energy resolution up to a maximum working energy of ≈ 10 keV, where the TES is thermally saturated by a single event. For a given device the energy resolution is roughly constant over the full working range of the device. The maximum working energy E_{max} is chosen during device design by adjusting film thicknesses and other TES parameters. The resolution ΔE of different designs scales as $\sim\sqrt{E_{\mathrm{max}}}$ [9,17]. The detector array is cooled by a two-stage adiabatic-demagnetization refrigerator (ADR) that is in turn backed by a cryogen-free pulse-tube cryocooler. The ADR can provide a ≈ 35 mK base temperature but is typically operated at 85 mK. Each sensor, which has a critical temperature of 120 mK, is maintained in its resistive transition via Joule heating from an applied voltage bias. The average operation period before recycling the ADR is 14 h preceded by a ≈ 1 h adjustment and calibration period. The recycling period is 2–3 h.

For the very first spectrum, ferrocene $Fe(C_5H_5)_2$ was chosen. Ferrocene was studied in the early days of x-ray absorption spectroscopy [19,20] and remains a subject of interest in studies of organometallic compounds [21] and solar-cell applications [22]. With its weakly scattering carbon atoms it can serve as a model complex for many metal-containing organic compounds.

Figure 1 shows the first hard x-ray absorption fine-structure spectrum collected by an energy-dispersive detector with sufficient resolution and statistics to retrieve molecular structure information. After digital filtering and rejection of pileup and other artifacts it contains $\sim 8.9 \times 10^6$ events accumulated at ~ 175 counts/s. Of these, $\sim 7.3 \times 10^6$ lie outside the energy range of interest

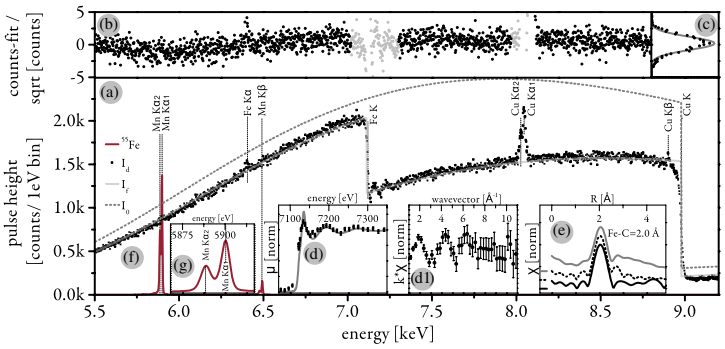

FIG. 1 (color online). (a) Laser plasma absorption spectrum of ferrocene in transmission mode. Included are emission lines and absorption edges of metal filters (see text). Dashed line (I_0) is the fitted spectrum without the sample. (b) Difference between measured spectrum (I_{d}) and the reference fit (I_{f}) of all involved materials, normalized to the Poisson error. Areas of emission lines and fine structure modulation (gray) were excluded. (c) A histogram of the normalized difference, with a Gaussian 1 σ curve superimposed. (d) Absorption fine structure of ferrocene, normalized to a measured background spectrum and the edge jump with indicated Poisson-limited error bars. The gray line is a synchrotron reference measurement from the same compound. (d1) $k\chi$ presented in k space to show the quality of the data. The error bars were generated using the statistical fluctuation expected for the number of samples per bin. (e) $|\chi|$ as function of R from the data (black line), single path fit (dotted black line) and synchrotron comparison data (gray line). Curves are offset vertically and the zero levels are marked; for details see text. (f) Additional calibration lines measured prior to the absorption spectrum; the Mn-$K\alpha$ splitting is clearly resolvable as shown in (g).

for XAFS, showing the importance of suppressing unwanted x-ray energies. In this experiment some suppression was accomplished by a stack of aluminum and copper foils, but significant improvement is possible.

The combination of source spectrum, copper, and aluminium filters, and the sample material accounts for the overall features of the spectrum in Fig. 1 (see the Supplemental Material [23] for a sketch of the experiment). Multiple absorption edges are observable simultaneously in a given measurement, a valuable feature for future experiments. The spectral range could be extended down to ≈ 200 eV, which includes the whole class of sulphurous materials, the K and L edges of the 3d transition metals, and the L edges of many heavier elements. The 200 eV lower bound is determined mainly by transmission through three infrared filter windows and one vacuum window on the cryostat. The region of primary interest in this experiment was 7000–8000 eV. The obvious lines in the spectra arise from fluorescence from a copper foil (whose position was close to the detector). The Mn-$K\alpha$ lines from a ^{55}Fe source shown in Figs. 1(f) and 1(g) were recorded prior to the absorption spectrum, and are essential for the energy and temperature calibration of the detector. Each pixel is calibrated separately, and its energy resolution can be retrieved from the known fine structure of the emission lines [24]. This calibration has to be done either on features of the measured spectrum or during a separate short calibration period. Sparse calibration features can introduce small systematic errors in the detected energies.

Fine-structure oscillations above the Fe $K\alpha$ (ferrocene) and Cu $K\alpha$ (filter) edges are visible in the data and show that two widely separated edges can be observed simultaneously. Figure 1(a) also shows a fit (gray solid line) to the baseline (using an estimate of the absorption of a free Fe atom). Residuals divided by their Poisson error are shown in Fig. 1(b), areas omitted from the noise histogram shown in Fig. 1(c) are marked in gray. The excellent agreement between the histogram and a superimposed Gaussian curve with $\sigma = 1$, shown in Fig. 1(c), demonstrates that Poisson noise associated with the number of photons per bin is the dominant noise source. Figure 1(d) shows the absorption fine structure of ferrocene, after normalization to a spectrum without the sample and the edge jump. The error bars for each bin (equidistant in k space) were obtained from the Poisson error of the recorded number of photons. The gray line in this panel shows the excellent agreement with the synchrotron reference measurement taken from the same compound. The data converted into k space are presented in Fig. 1(d1). Again the error bars are the Poisson error of the number of photons per bin. This spectrum shows the influence of the limited statistics in this very first spectrum. In Fig. 1(e) the data have been converted into R space with a window from $k = 1$–8 Å^{-1}, which is suitable for first-shell analysis and corrected for the Fe-C phase shift (solid black line). Calculation of the single scattering path from the iron to the nearest carbons in ferrocene by use of FEFF6 [25] and optimization in k space by use of single k weight with the fitting routine in ARTEMIS [26] of the IFEFFIT [27] package yielded the fit shown by the black dotted line; synchrotron data from the same compound are shown for comparison (gray line). The latter two graphs are offset vertically and the zero values are marked. All show agreement with the known Fe-C bond distance of 2.0 Å [19,28].

The extended x-ray-absorption fine structure spectroscopy (EXAFS) function $\chi(E) = [\mu(E) - \mu_0(E)]/\mu_0(E)$ and its error follow from the absorption coefficients $\mu(E) = \ln[I_0(E)/I_d(E)]$ and $\mu_0(E) = \ln[I_0(E)/I_f(E)]$, where I_d = data = integer, transmitted number of counts (experimental noise = $\sqrt{I_d}$), I_f = fitted free-atom spectrum, including sample contribution (no experimental noise), and I_0 = fitted free-atom spectrum, excluding sample contribution (no experimental noise).

These give

$$\chi(E) = \frac{\ln(I_f/I_d)}{\ln(I_0/I_f)}, \quad \text{with error: } \sigma(\chi) = \frac{1}{\ln(I_0/I_f)}\frac{1}{\sqrt{I_d}};$$

$\chi(E)$ is a ratio of intensities and an intrinsic property of the sample that distinguishes the true sample from its free-atom approximation. If it has amplitude A evaluated at the energy where a feature of interest is present, the signal-to-noise ratio (SNR) for measurements is then

$$\mathrm{SNR} = \frac{A}{\sigma(\chi)} = A\sqrt{I_d}\ln(I_0/I_f).$$

By choosing the sample thickness and concentration such that $I_d (\approx I_f) \approx I_0/e^2$, and thus $\ln(I_0/I_f) \approx 2$, an optimum signal is obtained [29]. Incorporating this, and expanding I_d gives

$$\mathrm{SNR} = 2A\sqrt{t_{\mathrm{meas}} N_{\mathrm{pix}} \rho S(B)},$$

where t_{meas} is the measurement period, N_{pix} is the number of pixels, and ρ is the average pixel event rate over the entire measured spectrum. The function $S(B) = I_{d,B}/I_{d,tot}$ is the relative spectral density of the measured spectrum, where we have a recording whose total integrated intensity is $I_{d,tot}$, and whose intensity is $I_{d,B}$ in a particular bin of energy width B, chosen to contain the feature of interest. $S(B)$ shows the advantages of selective binning and the importance of filtering out unwanted energies from the measurement. As EXAFS chemical interpretations are done in the photoelectron momentum (k) space, $k \sim \sqrt{(E - E_{\mathrm{edge}})}$, the choice of linear binning in k space improves the SNR at higher k values compared to linear binning in E. This can be easily optimized during data analysis, since the data are not prebinned by the data-acquisition method.

For steady-state measurements, amplitude A is the change in absorption between the actual sample and a

free-atom description of the sample, normalized by the depth of the edge jump. For pump-probe x-ray-absorption spectroscopy (XAS) measurements, which are the motivation of the present lab-based developments, the signal scales with the fraction of molecules that were excited into the desired state. In selected systems, the signal can be in the range of several percent normalized to the edge jump; for the strongest feature during the low spin-high spin conversion of $Fe(bpy)_3$ a change of $\sim 2.6\%$ in a 25 mM liquid jet under otherwise similar experimental condition was observed [1]. The ferrocene measurement presented in this work should be comparable: here we have $t = \sim 5 \times 10^4$ s, $N_{\mathrm{pix}} = 22$ pixels, $\bar{r} = \sim 8/\mathrm{s}$, $I_{\mathrm{d,B}} = \sim 1500$ events/1 eV bin, and $I_{\mathrm{tot}} = \sim 8.94 \times 10^6$ events, suggesting SNR ≈ 0.9. For the 5 eV bin as at 7150 eV in Fig. 1(d) (binned to equal k steps), the SNR improves to 2. With the next upgrades, the measurement period for data such as in Fig. 1 will be reduced to below 30 min. For the foreseeable future, the signal-to-noise ratio of the XAFS signal will be limited by the number of pixels, because the peak count rate (if indifferent to pileup) is limited to 1 photon/pixel/laser pulse. Future iterations will increase the fill factor and efficiency of the detector to allow experiments with even lower flux or stronger filtering. X-ray optics such as polycapillary or other broadband lenses [30] might increase the captured solid angle and decouple the sample from the generation environment with slight loss of temporal resolution [31]. Temporal smearing is not an issue if the optic is placed between sample and detector but has to be considered if placed between source and sample.

The approach described here is compatible with a broad range of samples and sample phases. When combined with an optical pump in a pump-probe arrangement as being developed, it can observe fundamental ultrafast chemistry at atomic resolution. For these reasons, and because of its compatibility with a conventional laboratory setting, the technique is well suited for dissemination. All detector parameters have been dramatically surpassed in recent developments. For example, detectors with energy resolution as good as 1.6 eV at 5.9 keV have now been demonstrated [32]. Improved multiplexing techniques such as code-division multiplexing (CDM) and the integration of CDM with microwave resonant techniques promise continued increases in array scale into the megapixel regime [33,34]. Such arrays will reduce integration periods by 10^5 compared to the results shown here.

To conclude, a cryogenic microcalorimeter array has been coupled to a laser-generated radiation source. A hard x-ray absorption fine-structure spectrum with sufficient energy resolution to extract intermolecular bond lengths has been collected for the first time with an energy-dispersive technique. The observed EXAFS oscillation and the retrieved bond length are consistent with synchrotron data within error bars [19,28]. The detectors do not suffer from narrow-band acceptance losses, do not require careful mechanical alignment, and are in a state of rapid development. These facts distinguish them from conventional detection topologies based on Bragg reflection. An excellent free-atom fit to the data was obtained, from which the incident spectrum and absence of excess noise sources were confidently established. The source spectrum is well described by a simple functional form over a multi-keV energy range, thus establishing the suitability of the source for broadband-absorption spectroscopies. A general expression for the signal-to-noise ratio in measurements of this type was derived and applied to the data. The prospects for lab-based molecular structure studies are excellent and imminent using this and related approaches, particularly for ultrafast studies [12], and are advancing in step with widespread implementations of laser-driven sources and contemporary developments of cryogenic microcalorimeter arrays.

The system was developed in the collaborative environment of the Lund Laser Centre and the Quantum Device Group of NIST Boulder, and acknowledges funding from the Swedish Consortium for Artificial Photosynthesis, the NIST Innovations in Measurement Science program and an ERC Advanced Investigator Grant No. 226136 to V. S. J U. acknowledges a scholarship under the Marie Curie Early Stage Researcher Training Site MAXLAS that was financed by the European Commission under the 6th European Framework Program.

[1] C. Bressler and M. Chergui, Chem. Rev. **104**, 1781 (2004).
[2] F. Ráksi, K. R. Wilson, Z. Jiang, A. Ikhlef, C. Y. Côté, and J.-C. Kieffer, J. Chem. Phys. **104**, 6066 (1996).
[3] T. Lee, Y. Jiang, C. G. Rose-Petruck, and F. Benesch, J. Chem. Phys. **122**, 084506 (2005).
[4] L. v. Hamos, Naturwissenschaften **20**, 705 (1932).
[5] T. Missalla, I. Uschmann, E. Förster, G. Jenke, and D. von der Linde, Rev. Sci. Instrum. **70**, 1288 (1999).
[6] V. A. Arkadiev, A. A. Bjeoumikhov, M. Haschke, N. Langhoff, H. Legall, H. Stiel, and R. Wedell, Spectrochim. Acta B Atom. Spectros. **62**, 577 (2007).
[7] J. Tyndall, *Heat: A Mode of Motion* (D. Appleton, New York, 1895).
[8] R. Balian and J.-C. Adam, *Proceedings of the Les Houches Summer School* (North-Holland, Amsterdam, 1982).
[9] J. N. Ullom, J. A. Beall, W. B. Doriese, W. D. Duncan, L. Ferreira, G. C. Hilton, K. D. Irwin, C. D. Reintsema, and L. R. Vale, Appl. Phys. Lett. **87**, 194103 (2005).
[10] W. K. Fullagar, M. Harbst, S. Canton, J. Uhlig, M. Walczak, C.-G. Wahlström, and V. Sundström, Rev. Sci. Instrum. **78**, 115105 (2007).
[11] W. Fullagar, J. Uhlig, M. Walczak, S. Canton, and V. Sundström, Rev. Sci. Instrum. **79**, 103302 (2008).
[12] W. Fullagar, J. Uhlig, N. Gador, K. Kinnuen, I. Maasilta, C.-G. Wahlström, and V. Sundstrom, AIP Conf. Proc. **1234**, 919 (2010).

[13] W. K. Fullagar, D. M. Paganin, and C. J. Hall, arXiv:1102.4680.
[14] F. Benesch, T. Lee, Y. Jiang, and C. G. Rose-Petruck, Opt. Lett. **29**, 1028 (2004).
[15] I. V. Tomov, D. A. Oulianov, P. Chen, and P. M. Rentzepis, J. Phys. Chem. B **103**, 7081 (1999).
[16] J. Uhlig, C.-G. Wahlström, M. Walczak, V. Sundström, and W. Fullagar, Laser Part. Beams **29**, 415 (2011).
[17] K. D. Irwin and G. C. Hilton, *Cryogenic Particle Detection*, edited by C. Enss (Springer-Verlag, New York, 2005) p. 81.
[18] P. A. J. de Korte, J. Beyer, S. Deiker, G. C. Hilton, K. D. Irwin, M. MacIntosh, S. W. Nam, C. D. Reintsema, L. R. Vale, and M. E. Huber, Rev. Sci. Instrum. **74**, 3807 (2003).
[19] S. P. Cramer, T. K. Eccles, F. Kutzler, K. O. Hodgson, and S. Doniach, J. Am. Chem. Soc. **98**, 8059 (1976).
[20] M. F. Ruiz-Lopez, M. Loos, J. Goulon, M. Benfatto, and C. R. Natoli, Chem. Phys. **121**, 419 (1988).
[21] M. Balasubramanian, M. T. Giacomini, H. S. Lee, J. McBreen, and J. H. Sukamto, J. Electrochem. Soc. **149**, D137 (2002).
[22] T. Daeneke, T.-H. Kwon, A. B. Holmes, N. W. Duffy, U. Bach, and L. Spiccia, Nat. Chem. **3**, 211 (2011).
[23] See Supplemental Material at http://link.aps.org/supplemental/10.1103/PhysRevLett.110.138302 for a detailed description of the experimental setup.
[24] G. Hölzer, M. Fritsch, M. Deutsch, J. Härtwig, and E. Förster, Phys. Rev. A **56**, 4554 (1997).
[25] S. Zabinsky, J. Rehr, A. Ankudinov, R. Albers, and M. Eller, Phys. Rev. B **52**, 2995 (1995).
[26] B. Ravel and M. Newville, J. Synchrotron Radiat. **12**, 537 (2005).
[27] M. Newville, J. Synchrotron Radiat. **8**, 322 (2001).
[28] P. Seiler and J. D. Dunitz, Acta Crystallogr. Sect. B **35**, 1068 (1979).
[29] R. G. Shulman, P. Eisenberger, and B. M. Kincaid, Annu. Rev. Biophys. Biophys. Chem. **7**, 559 (1978).
[30] M. Kumakhov, Phys. Rep. **191**, 289 (1990).
[31] M. Bargheer, N. Zhavoronkov, R. Bruch, H. Legall, H. Stiel, M. Woerner, and T. Elsaesser, Appl. Phys. B **80**, 715 (2005).
[32] S. R. Bandler *et al.*, in *Proceedings of SPIE 7732, Space Telescopes and Instrumentation 2010: Ultraviolet to Gamma Ray* (SPIE, San Diego, 2010), p. 38.
[33] K. D. Irwin, H. M. Cho, W. B. Doriese, J. W. Fowler, G. C. Hilton, M. D. Niemack, C. D. Reintsema, D. R. Schmidt, J. N. Ullom, and L. R. Vale, J. Low Temp. Phys. **167**, 588 (2012).
[34] G. M. Stiehl, W. B. Doriese, J. W. Fowler, G. C. Hilton, K. D. Irwin, C. D. Reintsema, D. R. Schmidt, D. S. Swetz, J. N. Ullom, and L. R. Vale, Appl. Phys. Lett. **100**, 072601 (2012).